Centre for Sensors, Instruments and Systems Development
UNIVERSITAT POLITECNICA DE CATALUNYA
Shaping light to your needs

Doctoral Thesis

For obtaining the Doctoral Degree
in the field of Optical Engineering from the

Technical University of Catalonia
UPC-BarcelonaTech
Terrassa School of Optics and Optometry FOOT

Implementation of Differential Self-Mixing Interferometry Systems for the Detection of Nanometric Vibrations

---

Author:
Francisco Javier Azcona Guerrero

Thesis Director:
Dr. Santiago Royo Royo

Tribunal members:

Presented in Terrassa, Spain, July 2018

Abstract

Since the appearance of laser technology, man has been interested in its application on daily life and in scientific progress. The appearance of the laser diode, and the massification of miniaturized electronic devices drove further this agenda by allowing the creation of portable systems capable e.g. of storing and reading large amounts of data, or producing high resolution optical measurement systems.

In this Thesis, we explore Self-mixing Interferometry (*SMI*), a method capable of producing high resolution optical path related measurements in a simple, compact and cost effective way. Even with a notably less complex setup than traditional interferometric methods, SMI is able to produce measurements with a resolution well below the micrometric scale ($\lambda/2$) which is sufficient for most industrial applications.

The SMI effect is produced when a small part of the laser power impacting a target is back-scattered and re-injected into the laser cavity. As a result, the phase and amplitude of the laser wave is modified generating a signature beat which can be "easily" related to different optical path-related dynamics. The main advantage of this method in relation to other interferometric methods is the simple setup consisting mainly of a single mode laser diode (*LD*) equipped with a simple electronic system readout. A simple optical system may be used to collimate/focus the beam allowing measurements at larger distances. As a result of the small amount of reflected optical power required to allow the effect, the technique is able to produce high resolution measurements even with diffusive targets.

While the SMI method has been largely studied in the last three decades, there are still several topics worth the development of further research. One of those topics, how to increase the resolution on displacement measurements, is one of the main topics covered in this work.

Classical SMI methods allow the reconstruction of displacement measurement with a resolution of $\lambda/2$. The use of special processing algorithms can push further this limit reaching values in the order of e.g. $\lambda/32$. In this work, we propose a method to increase even further this limit to reach values better than $\lambda/100$. The idea discussed, differential self-mixing interferometry (*DSMI*) proposes the use of a reference modulation (mechanical or electrical) to be used as a reference for the measurement. Simulated results have shown that under ideal conditions, it may be possible to reach resolutions in the order of $\lambda/1000$. In practice, however, this limit is much smaller ($\lambda/100$) as a result of LD dynamics, and different practical limitations present in the amplification and readout electronics. Experiments and measurements are presented along the second chapter of this work to present proof of the proposed method.

After exploring the basics of DSMI, possible applications for classic SMI and DSMI were pursued. The obtained results are presented in the following sections.

First, a review on potential biomedical measurements using SMI is discussed. The obtained results suggest that it is possible to obtain some key values related to biomedical constants (e.g. APW) using a displacement SMI measurement. The method, however, may not be reliable enough especially on long time measurements. Moreover, the use of certain wavelengths must be avoided during long exposures as they may prove harmful to the soft tissue due to the requirements of a small laser spot. It is observed that SNR may lead to difficulties during the signal processing stage which may impact the results of the reconstructed signal.

Next, the DSMI method was tested in an AFM-like cantilever system. The results suggest that is possible to follow the motion of a micrometric size cantilever oscillating at low frequencies with a high resolution. Higher frequencies may be achieved by using an electronic reference modulation configuration. The proposed system was able to detect some artifacts on the motion which may be attributed to possible deflections on the cantilever surface. Possible enhancements to the method are suggested for any researcher who wants to expand the topic.

Keywords: Interferometry; Self-mixing Interferometry; Displacement, High resolution measurements; Metrology; Photonics engineering.

Resumen

Desde la aparición de la tecnología láser, el hombre ha estado interesado en su aplicación en la vida diaria, así como en el progreso científico. La aparición del diodo láser, así como la masificación y miniaturización de dispositivos electrónicos ha facilitado tal desarrollo permitiendo la creación de sistemas portátiles capaces de, por ejemplo, guardar y leer datos, o producir sistemas ópticos de medición con alta resolución.

En esta Tesis, se explora la interferometría auto-mezclante, mejor conocida por su nombre en inglés Self-mixing interferometry (SMI), un método capaz de producir mediciones relativas al cambio del camino óptico en un haz laser. La técnica está caracterizada por su tamaño compacto, bajo coste y alta resolución. Pese a su simplicidad, la resolución alcanzada por sistemas basados en SMI se encuentra por debajo de la escala micrométrica ($\lambda/2$), lo cual es suficiente para la mayoría de las aplicaciones industriales.

El efecto SMI se genera cuando una pequeña parte de la potencia óptica del láser es retro reflectada por un blanco y reinyectada en la cavidad láser. Como resultado, se genera una modulación de la amplitud y fase del láser, la cual puede ser "fácilmente" relacionada con diferentes efectos relativos al camino óptico del láser. La principal ventaja del método SMI es la simplicidad del sistema de medición el cual está compuesto de un diodo láser (LD) equipado con una tarjeta de procesamiento electrónico. Una lente de enfoque o colimación puede ser utilizada con el fin de regular la reinyección de potencia y la distancia al blanco. Debido a que el SMI se genera con una pequeña cantidad de potencia es posible realizar mediciones incluso en blancos con reflexión difusa.

Si bien el método SMI ha sido estudiado ampliamente durante las 3 últimas décadas, aún existen diversos puntos de interés en su estudio. Uno de estos puntos corresponde a la mejora de resolución en la medida de desplazamiento, el cuál es uno de los temas abordados en el presente trabajo. Los métodos clásicos SMI para la medición de desplazamiento permiten alcanzar una resolución en el orden de $\lambda/2$. El uso de algoritmos de procesamiento especializados puede permitir mejorar el límite de la técnica alcanzando resoluciones (por ejemplo) en el orden de $\lambda/32$. En este trabajo proponemos un método que teóricamente permitiría alcanzar resoluciones mejores que $\lambda/100$. La discusión en este punto se sitúa sobre la técnica differential self-mixing interferometry (*DSMI*), la cual hace uso de una modulación de referencia (mecánica o electrónica) para realizar la medición. Los resultados de diversas simulaciones sugieren que, en condiciones ideales, la técnica es capaz de producir una resolución superior a $\lambda/1000$. En la práctica, el límite encontrado es menor ($\lambda/100$), lo cual puede ser atribuido a condiciones de ruido y efectos de no linealidad en el láser. Para apoyar la idea propuesta diversas medidas simuladas y experimentales son presentadas a lo largo de esta Tesis.

Después de explorar las ideas básicas de DSMI, un grupo de posibles aplicaciones para SMI y DSMI fueron exploradas en este trabajo.

Una revisión de posibles aplicaciones bio médicas utilizando SMI fue explorada. Los resultados obtenidos sugieren que es posible obtener valores relacionados con constantes biomédicas de interés (por ejemplo APW) utilizando medidas de desplazamiento basadas en SMI. El método, sin embargo, no es lo suficientemente confiable como para producir medidas estables en un uso prolongado. Además, el uso de ciertas longitudes de onda debería ser evitado pues las mismas podrían causar daños a ciertos tipos de tejidos debido a los requerimientos del tamaño del spot. El SNR de la señal puede introducir complicaciones durante el procesado SMI que puede derivar en errores de reconstrucción de la señal original.

El método DSMI fue probado en un prototipo de sistema AFM equipado con un cantiléver. Los resultados obtenidos sugieren que la técnica es capaz de medir movimientos producidos por un cantiléver de dimensiones micrométricas con alta resolución en bajas frecuencias. La medición de oscilaciones de mayor frecuencia podría ser alcanzada utilizando una configuración basada en modulación electrónica. El sistema propuesto fue capaz de detectar artefactos en el movimiento que podrían ser atribuidos a deflexiones en el cantiléver. Algunas posibles mejoras a esta implementación son sugeridas como puntos para futuras investigaciones alrededor de este tema

Palabras clave: Interferometría; Interferometría auto mezclante (SMI); Desplazamiento, Mediciones de alta resolución; Metrología; Ingeniería fotónica.

Acknowledgements

When someone finishes a long journey, such as the one I embarked when I applied to start working on the PhD research, it is always good to look back and try to measure how much that someone has grown in all aspects. Every step on the journey is a lesson learnt sometimes in company of "blood and tears", sometimes full of joy. Therefore, I wish to give a word of advice to any reader considering to embark in the quest of pursuing a PhD before getting into acknowledgments.

Pursuing a PhD is not for those faint of heart. It may sound like a joke, but during research you can expect anything. You will feel the adrenaline of running into a deadline (specially when a congress is approaching), you will fill the thrill of getting your first publication accepted and published, and of course the disappointment when your paper gets rejected. Sometimes it will be a roller-coaster of feelings which you must be prepared to face off. Of course, in this trip, you are not alone and you will find that all the people around you who will help you to face most of the issues you come through along the path. And then, when you are finally reaching your goal, you will notice that your work would have not been the same if all those people around you would not have taken the time to help you, guide you and encourage you. And thus, they also deserve an acknowledgement in the conclusion of the work.

In my case, as in many others, there are a lot of people who have helped in the development of the current work. Sometimes their help has come in an indirect fashion, but the worth of their advises has been quite significant, nonetheless. If I miss any names along this acknowledgement please keep in mind that your contribution have also been important but at the moment I wrote this I was probably a bit distracted to include everyone. Also take into account that the order in which I present the acknowledgments does not reflect a higher importance in the advises, talks, or help provided to this work, but rather the order in which memories came into my mind.

First of all, I would like to give a special acknowledgement to the reviewers of this thesis. During the development of my PhD dissertation I was able to review the work of other researchers and I am aware of some of the issues at hand during this task. Thanks for all your inquiries, positive and negative comments. Only through a good peer review it is possible to take science a step further, and I expect that with my work and your comments, we will be able to contribute at least a spec of dust in the large sandbox that is science this days.

Next I would like to thank my tutor Dr. Santiago Royo for coaching me and encouraging me along this process. I am aware that there might have been several hardships along the way but he was always ready to help with ideas or comments. His entrepreneurial spirit allowed the SMI team, in which I was working, to attempt some market solutions for different problems and to develop different patents which in the future may be used in a system development.

I would also like to help the administrative team at CD6 (Rosa, Cristina, Jordi, etc). You were all of great help at different steps of this journey. Sorry for any of the inconveniences I may have caused by paperwork (I know sometimes I am a bit of a mess in administrative procedures). Thanks for the talks and all the morning coffees. You helped to keep the moral high even when sometimes the environment felt grim. A mention is also here in place for Alba Rubies and Montserrat Arjona who were always attentive on the university procedures and let us know when to fill a given form, and in some cases bought us some time to comply with some of the regulations.

To the mechanical and electronic team also a big thank you. I will always consider teachers to Xavi, Fermin, and Jesus. Even after several years of study you are not knowledgeable enough in a given trade. Specially Xavi and Fermin who taught me different skills on the trade which I know will become useful in the future. All the tips of do's and dont's were really appreciated as one can only learn from the experts. I just hope I could have returned your help and teachings with at least attitude (yes Xavi, I am aware that a Spanish ham would be better).

To the SMI team (Reza, Carlos, Ajit), thanks for all the interesting talks and discussions. I know that we might have been at odds at some times due to our different ways of looking at the technique but most of the time I feel everything was constructive. I think now many of us are continuing on a different path but the things we have learned from each other will always be there.

To Vincent an Jordi, thanks for those initial days when I arrived at CD6 and I was working with you in the telescope project. I will always remember those moments. It was quite fun to work with you guys.

To the people in the PhD room. If I needed to say all things here this section would be endless. I were with all of you guys almost since the beginning of the journey, and I have created so many memories that it would not be possible to thank you for everything. I guess a special note here goes to Anna, Ciscu, Selena, Alfonso, Pepe, Esther, and Cristina (yep, I am aware some of you were not at the room at the same time but the easiest way for me to thank you is to set you in the same group). Thanks a lot for the conversations, coffees, encouragement words, and for those time you hold me up when I needed it. As I said at the beginning the PhD may be a roller-coaster and sometimes the personal life may not help to make the ride easier. Thanks for being there when I needed you the most, and thank you for being my family in Europe. I will always cherish all those moments we had together. Thanks for help me grow, and for allowing me being there for you when possible. Achieving this work would have not been possible if you were not there. Also thanks to the rest of the people that came later into the PhD room, the conversations were always of help and encouraged me to complete this work.

Last, but not least, thanks to my family in Mexico who encouraged me during this work. Possibly, many times my attitude was not the best for all their encouragement but it was a result of the feelings at a given time. Thanks for all your love and support. Sin ustedes, esto no habría sido posible.

Contents

List of Figures

List of Tables

1. Introduction

The understanding of matter and its interactions has changed dramatically during the course of the last century. A clear example of these changes is easily observed when light and electromagnetic waves are studied. Knowledge in these fields has experienced a remarkable evolution, resulting in the development of new technologies which have found different niches of application including almost anything from low cost presence detection sensors to sophisticated state of the art devices capable of determining e.g. the presence of Higgs' bosons.

Knowledge, as it happens in most cases, has not come by mere chance but by the hard work of brilliant minds who have had the ability of describing nature with the universal language of mathematics. However, mathematical models, by themselves, are not enough to probe a concept since it is only a plausible explanation of a phenomenon within a defined set of boundaries and conditions which, to be generalized, requires to be demonstrated through experimentation. In order to produce such demonstration, it has always been necessary to attain one or several measurements using a reliable instrument capable of quantifying a defined property of the studied phenomena in an objective manner.

Metrology, thus, plays a crucial role on science and life in general, since it allows to quantify the properties of a physical phenomenon. From a practical point of view, metrology is not only limited to the creation of quantification methods and patterns; it is also devoted to the development of techniques and sensors compliant with current and future technological needs. Optical metrology, metrology using light, adds to such benefits the ability to measure relevant properties of matter without even getting in contact with it, preventing the sample from contamination while providing different working principles involving amplitude, intensity, phase or polarization of light which may be applied to different real-world problems.

1.1 Motivation

In recent years a trend in the use of micro and ultimately nanometric scale systems has been observed not only on laboratory applications but also into everyday life applications. This is observed for example in the case of the microelectromechanical system market (MEMS) which has doubled its market share in the last decade and which expects to keep growing in the next years. Similarly the nanotechnology market has observed a large increase of value making it a niche of interest to develop new technologies to characterize and/or use in real life applications.

In many cases, it is not possible to perform direct measurements on micro and nanometric applications due its size and to restrictions in the system construction or the measured phenomena. While many technologies offer non contact measurement methods, few, in a personal opinion, offer the versatility observed in self-mixing interferometry. Self-mixing interferometry is an optical measurement method which uses the properties of single wavelength, single mode light to characterize optical path related characteristics of the measurement media. Therefore, in a general sense, self-mixing can be considered as a ruler to measure different types of processes which may range e.g. from displacement characterization to biomedical sensing. Moreover, due to the size of modern laser diodes, the size of a self-mixing interferometer can be reduced resulting in a highly compact measurement tool (a TO package) with a fraction of the cost

of traditional interferometric methods.

I first became aware of the existence of self-mixing interferometry by the end of 2010 after finishing my MSc degree. I became attracted by the method after considering it could provide a suitable alternative to measure displacements in MEMS-based applications which I had approached during my MSc, and an interesting approach to measure cantilever motion e.g. for AFM or other high resolution material characterization tools which I had also approached during my education. From that early beginning, the characteristics of the self-mixing interferometer (compactness, high cost-effectiveness, and low alignment requirement) presented themselves as a desirable component for any micromechanical system that required an external sensor control.

After an initial research, it was possible to observe the vast extension of the field which yielded the question of the limits of the method an whether it would be possible to expand these limits further. As a result of a talk with a fellow PhD student, it was observed that by applying an special modulation, it would be possible to bend the limits of the method and reach higher resolutions than the ones typically observed for displacement measurement. After a few preliminary simulations, it was observed that the proposed method allowed the possibility of measuring not only the amplitude or vibration frequency, but also the complete form of the wave produced by a target moving within the nanometric scale ($\leq 20nm$) with a high precision. After this initial step, we continued with the experiments which lead to the results ultimately presented in this work.

As it will be presented further on, the proposed method is capable of measuring experimentally target displacements with resolutions in the order of $3nm$ depending on the reference modulation. During the course of the work, it was also discovered that other configurations could also be applied. Using this configurations it is possible to reduce the cost and size of the initial proposed method.

After testing the technique with a suitable gold standard, it was possible to start proposing applications for the new developed sensor. For this work, the focus is set into two applications driven by the new method and further research of the self-mixing interferometry method for measuring in in-vivo conditions.

The results of this work show that the proposed method can be used as a suitable alternative for measuring optical path changes with high resolution, with a significant reduction of cost when compared to traditional interferometric methods. Moreover, it is our belief that with some mechanical adjustments it might be possible to apply the method outside the optical laboratory environment, thus increasing its potential number of applications. The most important drawback of the method, in our opinion, is related to the amount of noise that may need to be filtered as a result of the large sensitivity obtained by measuring in the nanometric scale.

1.2 Aims and content overview

The aim of this Thesis is to describe, develop and test a method capable of measuring optical changes with amplitudes below half-wavelength and resolution in the nanometric scale, based on self-mixing interferometry. As it will be shown, the proposed method relies on using a controlled laser stimulus to generate a desired fringe pattern which is then used as a reference to produce sub-$\lambda/2$ amplitude measurements. Thus, in comparison with classical SMI, a “reference arm" is artificially generated allowing the measurement of optical path changes in the order of few nanometers, without adding further complexity to the setup if the single laser setup proposed in this Thesis is used. It is the first time, to the best of our knowledge, that sub-$\lambda/2$ amplitudes of displacement are precisely measured using self-mixing interferometry.

The Thesis is structured as follows:

- This Ch.1 is intended to show the reader the motivation of pursuing this Thesis as well as to show some of the classic sensors and technologies available for the measurement of the nanoscale, and introduce the organization and interest of the work.
- In Ch.2, a review of the self-mixing interferometry phenomena and its most common applications in metrology is presented to produce a background for differential self-mixing interferometry. In the first section of the chapter, we will start by taking a look at self-mixing interferometry from a historical perspective. Then, the discussion will be focused in discussing the main characteristics of laser diodes, which make them a suitable tool for designing self-mixing sensors. Next, we discuss the theoretical basis of SMI using both the well known Lang-Kobayashi set of equations, and the more intuitive three mirror Fabry-Perot cavity model. The most common applications of SMI will then be discussed. Finally, we will sketch the main efforts realized in the past to improve the resolution of the self-mixing technique and registered in the literature.
- In Ch.3 the main contribution of this dissertation is introduced: differential self-mixing interferometry (DSMI). In the first section of the chapter, the technical specifications of the method (amplitude resolution and bandwidth) are discussed in depth. As it will be shown, the flexibility of the method is one of its greatest strengths since it allows to reach measurements of extremely low amplitude and high bandwidth just by introducing small changes in the reference excitation, thus tailoring easily the measurement technique to the physical problem to be measured. The next section of this chapter covers the simulation tests as well as the experimental data acquired using the differential self-mixing method in the differential and single laser diode configurations. Finally, a third method, only covered by simulations in this Thesis, is presented. This method will be further extended in a future Thesis work. Finally the section concludes remarking the main advantages and problems of the technique as well as a brief summary of the chapter contents.
- On Ch.4 two different measurement problems from different fields, based on the SMI and the DSMI methods, are presented. In the first section of the chapter, a technique to estimate the arterial pulse wave based in SMI is presented. After this, the use of DSMI in the characterization of microcantilever sensors is explored. In each case, a short conclusion of the experimental results is presented within each section.
- Finally in Ch.5, a set of general conclusions for the DSMI approach and the explored applications is presented. A short overview of some possible lines of work and recommendations to future researchers on this topic is also provided within this chapter.

1.3 Scholar and industrial interest

The work performed during this Thesis has allowed the publication of different documents with scholar and industrial interest. It has also allowed the participation on different workshops (including an entrepreneurship course imparted by personal of the Berkeley University), short term scientific missions, research projects, and partnering activities funded by the Generalitat de Catalunya (AGAUR 2012FI_BI 00240), the Spanish Ministry of Science and Technology, and the European Union (COST Project).

As a part of the scientific divulgation activities along this Thesis, it was possible to participate with manuscripts in at least 5 national conferences and 7 international conferences. In 8 of this conferences it

was possible to participate as a speaker and actively discuss the results with the attendants.

The developed work also allowed to present manuscripts to different national and international journals, resulting in 9 publications, being the main author in 3 of them, and actively participating as a co-author in the rest of them.

This work has also resulted in the publication of 3 patents, two of them currently under exploitation by Beamagine S.L. (see: Publications Patents 2), and BCB electrónica (see: Publications Patents 3).

A detailed list of the publications can be found before the Appendix section of this Thesis.

2. Self-Mixing Interferometry: A Historical and Technical Review

Interferometry and interferometric methods are a well known set of techniques in Optical Metrology which have been employed for the characterization of diverse properties of matter, using the study of light waves that interact with a sample. In general, interferometric methods rely on the superposition of at least two electromagnetic waves which combine in amplitude and phase to produce an interferometric pattern. Interferometric patterns are typically observed in the form of fringes as a result of the additive coherent effects of the light waves and their corresponding phases along an optical path.

The appearance of interferometric methods can be dated back to the beginning of XIXth century with Young's work on light wave theory [1] and his celebrated double slit experiment, and to Malus' work on polarization, which would led to discussions on the nature of light. The work of other scientists such as Fresnel and Arago [2] who worked in the effects of polarized light and interference, or Fizeau and Foucault who were able to produce interference fringes for long optical path changes on a single wavelength, settled the basis for today's interferometric technologies. Some years later, Michelson and Morley would continue working on developing different apparatus for the measurement of the velocity of light [3, 4] based on the ideas set by the Fizeau interferometer, which led the way for the measurement of star disk sizes in 1920 [5].

From Michelson's experiments to date, different interferometric arrangements have been proposed and implemented (e.g. Sagnac, Moiré, Fabry-Perot, or Mach-Zehnder, among others) leading to the measurement of various physical parameters in different areas of knowledge (e.g. displacement, distance, topography and refractive index), reaching in some cases resolutions in the sub-nanometer range, given a selected set of conditions is present [6, 7].

Typically, in order to reach such very high resolutions (the sub-nanometer scale is at the atom level), systems need to be constituted by bulky and expensive equipment, such as the instrument shown in Fig.2.0.1. Besides these difficulties, with such a demanding resolution it is also necessary to control different environmental variables such as pressure, temperature, or any subjacent mechanical vibration to which the room might be subjected to. A change in any of these features usually hampers severely the result of the measurement. Also, due to the high number of materials and elements involved in the instrument, it is necessary to perform a careful alignment of all the optical components of the setup and of the corresponding optical sensor. This leads to lengthy and sensitive alignment procedures which need be done periodically in order to obtain satisfactory results.

Besides these high resolution methods, about 60 years ago a new interferometric technique named self-mixing interferometry (*SMI*), also known as optical feedback interferometry *OFI*, appeared in the panorama of interferometric methods leading to more affordable, compact and simple to align interferometric measurements. For the work presented in this Thesis, SMI is a cornerstone as all the analysis to be performed is based on it. While this chapter is not intended as an exhaustive description of all possible applications and detection techniques used on SMI, it will try to show some of the most representative application examples, as well as the fundamental theoretical basis of the method. Thus, this chapter is proposed as a starting

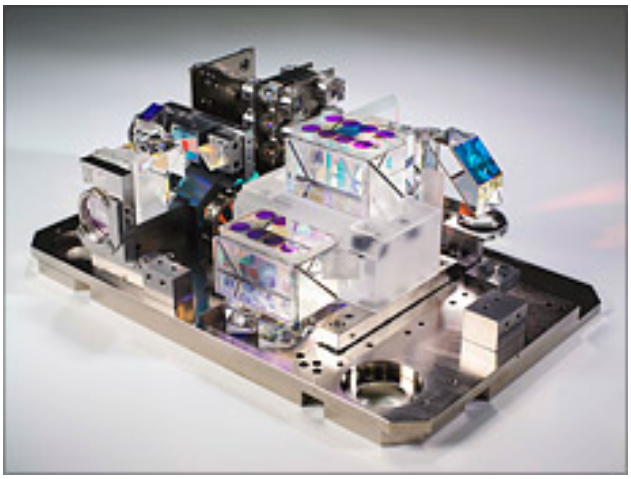

Figure 2.0.1: Example of a commercial interferometer from ZYGO. The instrument shows a complex optical, mechanical, and thermal control structure when compared to an SMI setup. ([8]).

background to understand the main concepts behind SMI and set the basis of the Differential Self-Mixing Interferometry (*DSMI*) technique proposed in this Thesis, and of its applications.

In the first section of this chapter, relevant historical and technical aspects of the SMI method are introduced. After briefly covering the historical developments that gave rise to SMI, a short explanation of the working principle of the laser diode (*LD*) and its relevance for SMI is presented.

Further, along Sec.2.2, the two most common strategies to model the SMI phenomena and its interactions with matter will be studied. First, in Sec.2.2.2, the Lang-Kobayashi (*LK*) model, which includes almost a full description of the electrical characteristics of the laser, is presented. Next, in Sec.2.2.3, the popular (and simpler) three cavity Fabry-Perot (*FP*) model is introduced.

Next, in Sec.2.3 a review of the classical SMI applications, as well as an explanation of its working principles and limitations is presented. In this Section the four classical applications which include most of the results of the method will be covered: displacement/vibrometry, absolute distance, laser Doppler velocimetry (*LDV*) based measurements, and different attempts of SMI imaging will be covered.

Finally, in the last section, we will cover the state of the art regarding the different attempts to increase the resolution of SMI and the limitations of such approaches. This section can be understood as one of the motivations for starting the development of this work and, as well, the topic that was studied during a large majority of the current Thesis.

2.1 Historical development

Since its appearance in the 1960's [9,10], laser systems have proved their utility in diverse fields of research. For instance, metrology and telecommunication have largely benefited from the appearance of these devices due to the characteristics of the available light sources.

For the case of metrology, the use of laser-based systems is widespread and many optical measurement devices and techniques, going from simple triangulation sensors, to light detection and ranging sensors (*LIDAR*), or interferometric sensors use laser as their primary light source because of its characteristics. The characteristics of laser light [11] involve high collimation with small divergence, high spatial and time coherence, narrow spectral linewidth and high intensity. It is also important to notice that laser light

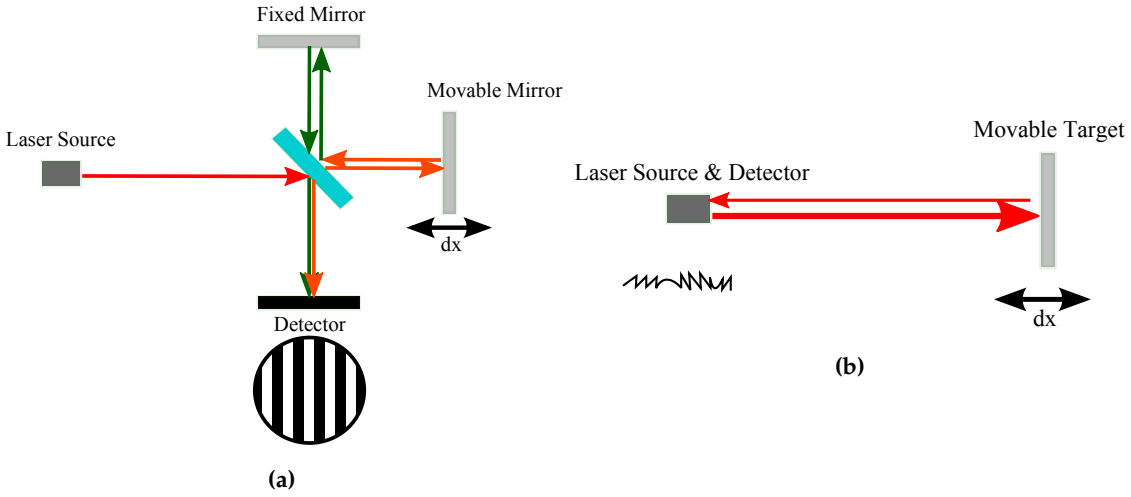

Figure 2.1.1: Two types of interferometry: (a) Schematics of a Michelson interferometer with the laser beam following two different optical paths and combining on a detector. (b) Schematics of a SMI sensor where the light follows the same optical path and recombines in the laser cavity.

propagation in an optical system preserves the features of the input wave (e.g. coherence, spectrum and polarization) in general-purpose optical systems unless well-known special situations (such as e.g. strong focusing, metamaterials...) are present.

Interferometric methods allow the measurement of displacement, vibration and velocity, among several other parameters, as a function of the interaction between two coherent light waves of the same wavelength and polarization. While in the classical case (e.g. Michelson interferometry, Fig.2.1.1a) the superposition comes from two waves following two different optical paths which overlap on a single point or imaging detector, in the case of SMI the combination emerges on the same path and takes place within the cavity of the laser diode, as shown in Fig.2.1.1b. Also, it is important to remark that, while most interferometric techniques can provide point and area measurements, SMI is restricted to pointwise measurements. Nevertheless, as it will be explained in Sec.2.3, different research groups have worked with possible solutions to this issue, in general working around different scanning strategies.

The feedback phenomena, underlying what later on became SMI, was first documented in 1958 by King and Steward [12], who observed small amplitude modulation effects in the optical power of a MASER system with back-reflections in the order of 2% of the initial radiation. In 1964, Crowe and Craig showed that optical feedback could reduce the linewidth or suppress the presence of multiple axial modes in the optical spectrum of a semiconductor laser [13]. Yet, the first description of a practical approach for the SMI phenomena with a laser corresponds to Rudd [14] who implemented a laser Doppler velocimeter (*LDV*) using a He-Ne laser on scattering particles.

Other early implementations of the optical feedback phenomena can also be found in early descriptions of laser-based communications and compact discs (*CD*), where the effects caused by optical feedback were classified as noise and typically disregarded, as presented in [15–17]. Coherence collapse is also a particular feature observed in lasers under large feedback levels. In such cases, the increase of spectral linewidth results in the collapse of the coherence length to a few millimetres, as demonstrated by Lenstra et al. [18] using a Michelson interferometer.

After the first descriptions of feedback in 1962, diverse theoretical and practical applications of LDs

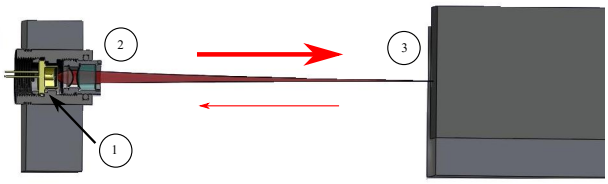

Figure 2.2.1: Classical self-mixing interferometry setup. 1) Laser diode, in some cases the encapsulation can include a PD. 2) Focus or collimation lens. 3) Partially reflective target.

were studied and developed [19–23]. Nevertheless, it was not until 1980, thanks to the studies of Lang and Kobayashi [24], that the first attempts to explain weak optical feedback and its possible applications were explored in detail [25]. The LK paper set a milestone in the field leading different research groups to the development of a number of different applications based on the optical feedback effect. Dandridge et al. [26], for example, reported in 1980 an application for acoustic wave detection using a LD. Later, in 1984, reports of velocimetry measurements using CO_2 lasers were demonstrated using a photodiode *PD* placed at the rear of the laser [27]. In this paper, the author also shows that it is possible to obtain the feedback effect when the laser is operated well above its threshold; also a narrow band of operation close to the laser threshold in which enhanced sensitivity appeared was reported [27].

In 1986, the possibility of producing a small LDV was documented by Shinohara et al. [28] either by detecting the changes of optical power using an external PD or by measuring the variations in the LD junction voltage. Based on this work, in 1987, other effects such as the capacity for detecting the direction of the motion were discussed by Shimizu et al. [29] based on the phase of the second harmonic of the sawtooth signal produced under a defined set of feedback conditions. In 1995 Donati et al. [30] suggested that working on moderate regime would allow the reconstruction of displacements without ambiguity by applying the fringe counting method, which later would become a standard of the technique, and looking at the slope of the sawtooth signal created.

2.2 Description

The SMI effect (Fig.2.2.1) is generated whenever a small amount of power of a coherent wave is backscattered from a partially reflective target. A portion of the back-reflected power then re-enters the laser cavity interfering (or "self-mixing") with the standing wave inside the cavity, causing a variation in the output power. The change of power can be then proportionally related to the changes in the optical path caused e.g. by the motion of a target, as will be shown in Sec.2.3.

In comparison with other interferometric techniques, SMI methods are known to be more responsive to the amount of back-reflected power that produces the interference effect. It has been theorized by S. Donati [31] that the effect may be achieved and used with a feedback in the order of up to $-90dB$ in the case of the photodiode measuring approach, and up to $-50dB$ in the case of the junction voltage measurement approach. In both cases, quantum noise and electronic noise caused by the amplification circuitry [32] are the main limiting factors for detection in the technique.

Some of the main distinctive features of SMI-based methods in practical applications can be listed as:

- **Small size**: As shown in Fig.2.2.1, the most basic SMI configuration is formed just by a laser source (in the case of Fig.2.2.1, a LD), a collimating or focusing lens, and a target. While in practice it is

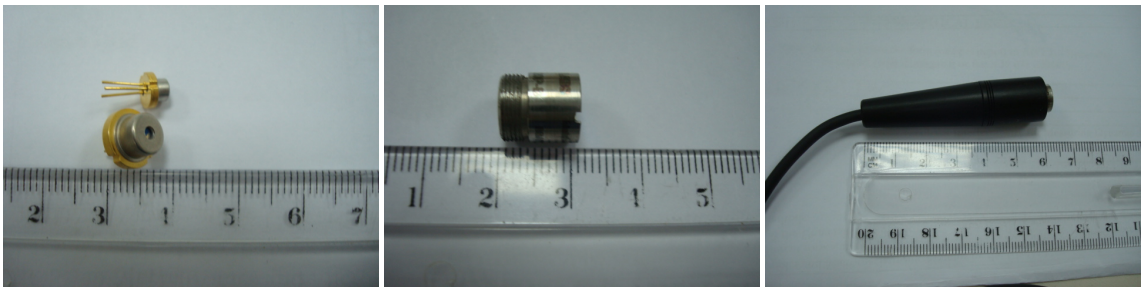

(a) (b) (c)

Figure 2.2.2: Example of a SMI probe using a FP LD. The probe is composed by three elements: the LD (which contains a monitor photodiode), a focusing lens, and a mechanical tube for placement of the setup. (a) Examples of 9mm and 5.9mm FP-LD cans. (b) Thorlabs focusing lens C220230P-B. (c) SMI laser probe.

commonly preferred to use a power detector (e.g. a PD) placed within the electronic encapsulation of the LD in order to increase the dynamic range of the sensor, this detector is not strictly required, thus allowing to capture the effect even using surface mount devices (*SMD*) not equiped with a monitor photodiode. This also has been exploited in other type of measurements such as in THz based setups, where as a result of wavelength or cost, the use of external detectors is not feasible [33]. In such cases, using the changes in optical power it is possible to sense the SMI signal directly using the laser junction voltage. Typically the LDs preferred for SMI applications include, among others, 5.9 mm, 9 mm, and TO-46 package encapsulations typically used for discrete low power transistors. Thus, the size of the SMI interferometer is mainly determined by the required optics and the distance to the target. In some cases, for close distance approaches, the lens might even be removed as presented in [34]. The distance to the target plays then a key role in the quality of the signal. This issue will be described in detail in a following section within this chapter. An example of a typical SMI probe is presented in Fig.2.2.2.

- **Self-alignment**: As explained before, conventional interferometric systems are composed by a large number of optical elements that require delicate alignment. In the case of SMI, since all the interference effects are produced *inside* the LD, virtually no alignment is required. In a majority of cases, however, a focusing or a collimating lens is added to the design in order to have some control on the spot size at the target (related to the measurement area), and subsequently on the amount of feedback in the cavity, which, as we will see, severely affects the properties of the signal. The problem of alignment between the LD and the lens is typically solved using cylindrical mounts which allow the lens to be concentric relative to the laser window. Some care should be taken, however, with the angle relative to the surface of the sample at which the measurement is performed, which may become a key parameter affecting the accuracy of the measurement. This feature of the method is typically disregarded in some types of measurements (usually in direct interferometric vibrometry), but is routinely used in velocimetry setups as described in Sec.2.3.

- **Simple structure**: The SMI effect, as discussed above, originates directly in the cavity of the laser source, and could be observed and detected anywhere along the complete optical path. While most common measurements rely in the use of a monitor photodiode placed at the rear of the laser package (which is routinely used in telecommunication applications to monitor the power emission of the laser), it is possible to measure the same effect by properly amplifying the junction voltage of the

LD [28, 32, 35]. Besides these options, it is always possible to include in the setup an external power detector to increase the measurability of the signal [36], and so its quality. However, there are only a few examples of SMI systems using an external detector since this introduces added complexity to the sensor setup, removing one of the main advantages of SMI based instruments.

- **High responsivity**: Since the method is typically applied using LDs, and the amount of feedback required to produce a significant interference effect is reduced, the resulting sensors are typically highly responsive to power, allowing coherent measurements even on diffusive targets. This degree of responsivity, however, can also be a severe drawback in the case of highly reflective targets, where the signal can become chaotic due to the presence of too large amounts of feedback.
- **Large bandwidth**: SMI sensors are only limited, theoretically, by the electronic elements used for sensing. In the case of photodiodes, electronic bandwidths can typically go from a few MHz to a couple of GHz depending upon their size and structure as shown in [37]. A more hampering effect is introduced by the operational amplifier used on the transimpedance and in the gain amplification stages of the sensor. Therefore, choosing the right operational amplifier (*OPAMP*) for each stage can be a critical factor to describe the total bandwidth of the complete sensor. It is also important to remark that the analog to digital conversion (*ADC*) used in most SMI systems will also affect the effective bandwidth of the sensor.
- **Non-contact:** As almost all optics-based sensors, SMI is a technique suitable for non-contact measurements. The maximum range of the sensor may vary depending upon the optical elements used on it (focusing or collimating lenses). While typically it would be advisable to perform the measurements at close distance to prevent large environmental effects, and to keep a reduced setup, SMI has been shown to perform properly at long distances (in the order of 7 to 8 meters), being limited only by the coherence length of the laser and the reflectivity of the target.

2.2.1 The laser diode

A laser can be defined as a medium capable of amplifying light waves at an adequate, precise frequency [38]. Semiconductor lasers difference themselves from solid state laser sources in size (e.g. a He-Ne laser has a length of some centimeters while a LD can reach a size in the order of $250\mu m$), cost, amplification media and energy efficiency. Also, laser diodes are easily mass produced as they are built using state of the art electronics equipment, applying litographic production techniques.

Semiconductor lasers are also considered “open” devices, as they allow $\sim 70\%$ of the light to escape from the main laser cavity, while conventional He-Ne lasers typically emit only 1 to 5% of their intensity. Such an "openness” is also a key feature which contributes greatly to the generation of the SMI effect, as the quantity of backscattered energy that may re-enter the laser cavity is larger than in gas lasers, thus requiring lower feedback levels in order to obtain a similar amount of signal. This property in particular has been largely exploited since the 1980s due to its possibilities in the development of different experimental non-linear dynamics methods [17, 18, 25]. The lasing medium is usually an active layer of different semiconductor materials. Due to Fresnel reflections between the active layer and air, the diode facets have reflectivities in the order of 30% which combined with the presence of high gains in the media ($\sim 50cm^{-1}$) are usually enough to avoid the presence of external mirrors. Typically combinations of materials involving indium, gallium, arsenide, or phosphorus are combined in different quantities to obtain the desired wavelength.

In order to produce lasing, a population inversion capable of overcoming all the losses in the medium

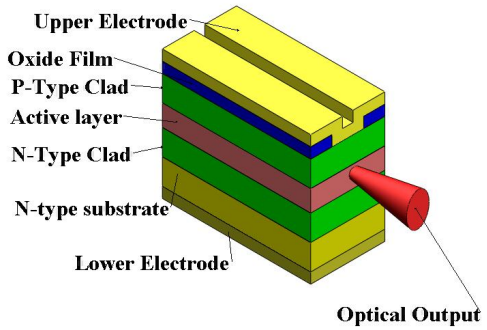

(a)

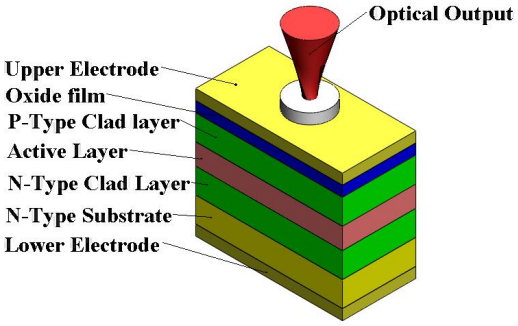

(b)

Figure 2.2.3: Simplified model of a semiconductor Fabry-Perot and VCSEL laser diodes. The top and bottom layer correspond to the electrode layers followed by the P and N doped layers, and to the active layer of the diode,respectively. Lasing occurs if enough electron-hole pairs are formed due to electrical excitation. (a) Tranverse edge emitting laser structure. (b) Vertical cavity surface emitting laser (*VCSEL*) structure.

needs to occur. In the case of LDs, this is bound to happen if a sufficient number of electron-hole pairs are formed by the electrical current exerted between the two doped layers of the semiconductor diode (Fig.2.2.3). The minimum current level to produce the population inversion level is described in the technical specifications as the threshold current I_{th} (presented e.g. in Annex A). This threshold value varies widely depending on different factors such as the construction technology of the laser, as commented, but also on temperatureand age of the laser source. As an example, threshold currents in the order of a few milliamperes are common for the case of vertical cavity surface emitting lasers (*VCSEL*), while threshold currents in the order of $20mA$–$40mA$ are common for the case of FP based laser diodes. Other thresholds can be observed in other laser geometries, which have not been included here for the sake of brevity. [39].

Due to the fast dynamics at which the electron-hole pairs are formed and recombined relative to polarization dynamics, it is usually possible to describe the lasing phenomena using a set of first order differential equations. This equations describe the relaxation oscillation between the emitted power P and the electron hole-pairs N. Furthermore, laser diodes also present phase-amplitude coupling which may lead to chirp behavior, in which small variations of the nominal laser frequency are generated. As result of the frequency

changes, an amplitude modulation may be produced which may cause an asymmetrical waveforms as a result, for instance of the presence of mode hopping effects.

The phase-amplitude coupling is typically modelled using a parameter known as the linewidth enhancement factor α, which typically varies from 3 to 7 in semiconductor LDs [38,40,41].

While there exist some examples of SMI and other optical feedback effects using multimode laser sources [42,43], the current work and the approaches studied in it are only focused on single mode LDs as they are commonly preferred for SMI applications. A single mode laser diode is characterized by presenting only one principal emission frequency. By contrast, multimode LDs present a main emission frequency with two or more sidebands. These sidebands are usually observable as harmonics of the main emission frequency in the laser power spectrum.

2.2.2 The Lang-Kobayashi Approach

In 1980, Lang and Kobayashi (*LK*) published what is considered the cornerstone of the optical feedback theory [24]. In their seminal paper, they examined previous attempts of explaining optical feedback effects with the purpose of using them in practical applications such as longitudinal mode selection [44], reduction of waveform distortion, and also SMI detection using the amplified changes in the voltage junction [45]. Their research also focused for the first time in the effects of feedback in single mode lasers, reducing the degree of uncertainty introduced by the complex behavior of the laser when a broader spectrum is involved, the sensitive dependence of the refractive index with temperature, and the strong dependence of the active medium refractive index with the carrier intensity.

The LK experiments showed for the first time the effects of having an external reflector feeding an optical field back into the laser cavity. They showed this would result in undulations in the output power emission of the LD. Such undulations would, in addition, present a periodicity proportional to the distance to the reflector. Further, some emphasis was made on the potential hysteresis effects which could appear due to the amount of feedback power, which caused a variation on the refractive index of the active region in the LD. It was also noticed that the maximum amplitude in the power modulation was registered when the total distance from the reflective surface to the LD was an integer multiple m of the LD cavity length. Other relevant effects, such as an early description of mode hopping due to optical feedback, were also briefly introduced.

The LK model [24,25,46] describes the evolution of the electric field in a single mode laser diode including the influence of feedback as a time-delayed term with a coupling strength defined by the parameter $\tilde{\kappa}$. The electric field E in the compound cavity is assumed to be the product of an envelope function $E(t)$ modulated by the rapidly oscillating optical field $e^{i\omega_0 t}$ at the angular frequency ω_0. Therefore, it is possible to equate:

$$\frac{dE(t)}{dt}e^{i\omega_0 t} = \left\{ i\omega_N(N) + \frac{1}{2}\left[G(N) - \Gamma_0\right] \right\} E(t)e^{i\omega_0 t} + \tilde{\kappa}E(t-\tau)e^{i\omega_0(t-\tau)}, \tag{2.2.1}$$

where $\omega_N(N)$ is the frequency of the longitudinal mode calculated as:

$$\omega_k(n_0) = k\pi c/(n_0 L), \tag{2.2.2}$$

with k an integer number, c the speed of light in vacuum, n_0 the refractive index of the laser cavity and L the cavity length.

The first term in the right-hand side of Eq.(2.2.1) accounts for any possible difference between the optical central frequency ω_0 and the instantaneous frequency of light ω_k. Given a fixed carrier density N,

a phase shift is produced over the field envelope inducing a change in ω_0. As a result of this variation, an instantaneous change of the laser frequency occurs due to the coupling of phase and amplitude. The second term (including the optical gain $G(N)$) is used to describe the amplification of such changes by stimulated emission, and Γ_0 describes the attenuation due to cavity losses. The last term accounts for the delayed back-reflected field getting back into the cavity with a time delay defined by τ, with a degree of coupling defined as a function of the reflectance of the internal mirror in the laser cavity and the target. Thus, it is possible to define:

$$\tilde{\kappa} = \frac{c(1-R_2)\sqrt{\frac{R_3}{R_2}}}{2n_0L} = \frac{(1-R_2)\sqrt{\frac{R_3}{R_2}}}{\tau_{in}} = \frac{\kappa}{\tau_{in}}, \tag{2.2.3}$$

where the R_x parameters represent the reflectances corresponding to the two facets of the LD limiting the active region (R_1 and R_2) and the external reflector (R_3). The total cavity losses Γ are given by:

$$\Gamma = \Gamma_w - \frac{c}{n_0L}\ln(\kappa\sqrt{R_1}) = \Gamma_0 - \frac{c}{n_0L}\ln(1+\kappa e^{-i\omega_0 t}). \tag{2.2.4}$$

Although equation (2.2.1) properly described the time-delayed equation for the electric field in a laser diode under feedback, it should be kept in mind there is a coupled rate equation for the carrier density N, which can be expressed as:

$$\frac{dN}{dt} = -\frac{1}{\tau_e}N(t) - G(N)|E|^2 + \frac{J\eta}{qd}, \tag{2.2.5}$$

where τ_e is the spontaneous lifetime of the carrier ($\tau_e = 2ns$ [47]), and the carrier injection rate is noted by the relationship between the current density J, the electron charge q, and the active layer thickness d. If the stationary lasing condition is assumed for Eq.(2.2.1), it becomes possible to divide it into its real and imaginary parts:

$$G(N) - \Gamma_0 + 2\tilde{\kappa}\cos(\Omega t) = 0, \tag{2.2.6}$$

$$\omega_N(N) - \Omega - \tilde{\kappa}\sin(\Omega t) = 0, \tag{2.2.7}$$

where Ω describes the laser oscillation frequency. Both, the gain $G(N)$ Eq.(2.2.6), and the phase $\omega_N(N)$, are dependent upon the carrier density N and therefore are mutually coupled. It is also observed that the equations are related by the time of flight t and therefore can be related to a target distance.

Next, it is necessary to study the effects of small variations of refractive index inside the LD cavity as this variable affects the instantaneous phase of the laser as depicted in Eq.(2.2.2). While different factors such as the variation of temperature T, the oscillation frequency Ω, and the carrier density N can affect refractive index, for the current analysis we are mainly interested in the effects of N. The main reason to restrict the analysis to the variation of N is related to the high dynamics at which the phenomena takes place. As a result, it is possible to use a first order approximation to define small variations of the refractive index as:

$$n(N) = n_{th} + \Delta N\frac{\partial n}{\partial N}, \tag{2.2.8}$$

where n_{th} corresponds to the refractive index under stable conditions.

Similarly, the process can be expanded to study the effects of small variations of the phase as a function of the refractive index resulting in:

$$\omega_N = \omega_{th} + \Delta n\frac{\partial \omega}{\partial n}. \tag{2.2.9}$$

By using the implicit derivation theorem and substituting the second term of Eq.(2.2.8) in Eq..(2.2.9), it is possible to equate:

$$\omega_N = \omega_{th} - \Delta N\frac{\omega_{th}}{n_{th}}\frac{\partial n}{\partial N}, \tag{2.2.10}$$

leading to a model dependent upon the variation of the carrier density. In a similar fashion, it is possible to express the effects of the variation of the carrier density as a first order approximation given by:

$$G(N) = G_{th} + \Delta N \frac{\partial G}{\partial N}. \tag{2.2.11}$$

By substituting ΔN in Eq.(2.2.10) using Eq.(2.2.11), we obtain:

$$\omega_N = \omega_{th} + \frac{\alpha[G(N) - \Gamma_0]}{2} \qquad \text{with} \qquad \alpha = -\frac{2\omega_{th}}{n_{th}} \left(\frac{\frac{\partial n}{\partial N}}{\frac{\partial G}{\partial N}} \right), \tag{2.2.12}$$

which makes possible to introduce the linewidth enhancement factor α into the proposed model.

Next, if Eq.(2.2.12) is substituted into Eq.(2.2.1), the small fluctuations of the complex field in terms of the real part of the amplitude and the phase can be considered as shown in [24,47]. Hence, it is possible to define the two rate equations getting out of the real and imaginary parts of Eq.(2.2.1) in terms of the carrier density as:

$$\frac{dE_0}{dt} = \frac{1}{2}\left\{ G_n \left[N(t) - N_0 \right] - \frac{1}{\tau_p} \right\} E(t) + \frac{\kappa}{t_{in}} E(t-\tau) \cos\left[\omega_0 \tau + \phi(t) - \phi(t-\tau) \right], \tag{2.2.13}$$

$$\frac{d\phi(t)}{dt} = \frac{1}{2}\alpha G_n (N(t) - N_{th}) - \frac{\kappa}{\tau_{in}} \frac{E_0(t-\tau)}{E_0(t)} \sin\left[\omega_0 t + \phi(t) - \phi(t-\tau) \right], \tag{2.2.14}$$

being N_0 the carrier density at transparency ($N_0 = 1.4 \times 10^{24} m^{-3}$), N_{th} the carrier density at threshold, $\tau_p = 1.6ps$ the photon lifetime, α the linewidth enhancement factor, and G_n the modal gain coefficient with a typical value of $G_n = 8 \times 10^{-13} m^3 s^{-1}$ [25,38,41,48].

If we now consider the steady state solution for Eq.(2.2.13) and Eq.(2.2.14), and we consider $E_0(t) = E_0(t-\tau)$, $N(t) = N_F$ and $\phi(t) = \Delta\omega_F = (\omega_F - \omega_0)t$ as the increase of optical frequency, it is possible to rewrite the coupled equations as:

$$\omega_0 - \omega_F = \frac{\kappa}{\tau_{in}} \sqrt{1+\alpha^2} \sin[\omega_F \tau + \arctan(\alpha)], \tag{2.2.15}$$

$$N_F = N_{th} - \frac{2\kappa}{G_n \tau_{in}} \cos(\omega_f \tau),, \tag{2.2.16}$$

where Eq.(2.2.15) shows the phase effects caused by the round trip delay, and Eq.(2.2.16) shows the effects on carrier density and the changes in gain as a result of optical feedback. The amount of optical power can be estimated using the approximation $P_F \approx |E_F|^2$.

2.2.3 The Double Cavity Fabry-Perot Approach

An alternative, very popular approach to explain small feedback phenomena in laser cavities was presented later in 1988 by de Groot et al. [49], used in 1992 by Koëlink et al. [50] and retaken by Wang in 1993 [43]. This model is not as rigorous as the LK modelling approach, as the complex effects of the delayed field in the population inversion in the gain media of the semiconductor are ignored, and in fact the dynamics of the whole semiconductor media is ignored in the model. This complicates the description of the cases under large feedback when the resonator goes into chaotic regimes, but in the smaller feedback levels giving rise to the SMI phenomena relevant to metrological applications it becomes a very simple and descriptive model whose results surprisingly are fully equivalent to the LK model just described above. Also, the simplicity of the model allows to get a better insight of the SMI process.

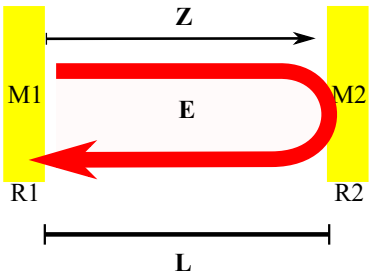

Figure 2.2.4: Diagram of a single cavity FP resonator

2.2.3.1 The single cavity resonator

As first step, a simple FP resonator such as the one shown in Fig.2.2.4 is considered, in which the main aim is to focus on the longitudinal dependence of the lasing condition in the direction of propagation z.

The cavity is formed by two mirrors $M1$ and $M2$ with reflectance coefficients $R_1 = r_1^2$ and $R_2 = r_2^2$, respectively, and a distance L between the two mirrors. Between both mirrors there exists an electric field E defined by the complex vector:

$$E = E_0 e^{i(\omega_0 t - \tilde{k}z)} \qquad \text{with} \qquad \tilde{k} = n_0 \frac{\omega}{c} - i\frac{\alpha_{abs}}{2}, \tag{2.2.17}$$

where the real part of the refractive index in the active region is represented by n_0, ω_0 is the resonance frequency of the LD in the absence of feedback, $\alpha_{abs} \ll n\omega_0/c$ is the absorption coefficient in the active media and $\tilde{k}$ is the complex propagation constant.

From the diagram in Fig.2.2.4, it is observed that the field can be divided into the wave $E_f(z)$ travelling in the forward direction, and the wave $E_b(z)$ travelling in the backwards direction, which can be expressed as:

$$E_f(z) = E_{f0} e^{-i\frac{n\omega_0}{c}z - \frac{1}{2}\alpha_{abs}z}, \tag{2.2.18}$$

$$E_b(z) = E_{b0} e^{-i\frac{n\omega_0}{c}(L-z) - \frac{1}{2}\alpha_{abs}(L-z)}, \tag{2.2.19}$$

hence, at the boundaries of the cavity, it is possible to write $E_{f0} = r_1 E_b(0)$ and correspondingly $E_{b0} = r_2 E_f(L)$ for continuity reasons.

Substituting E_{b0} in Eq.(2.2.19) and evaluating at $z = 0$ it may be obtained:

$$1 = r_1 r_2 e^{-2i\frac{n\omega_0}{c}L - \alpha_{abs}L}. \tag{2.2.20}$$

which becomes the condition for maintaining a standing wave in the cavity, and thus for lasing.

Then, the modulus of the required threshold gain can be calculated from $\alpha_{abs} = G_{thr} + \alpha_{int}$, where α_{int} is the internal loss parameter. This results in:

$$G_{thr} = \alpha_{int} + \frac{1}{L}\ln\left(\frac{1}{|r_1 r_2|}\right). \tag{2.2.21}$$

The second term of the equation is often defined as mirror loss [38], and it may be defined as α_M. From Eq.(2.2.20) it is also possible to compute the value of the phase which yields the lasing frequency as:

$$\omega_{thr} = m\frac{\pi c}{n_0 L}, \tag{2.2.22}$$

where m is an integer and ω_{thr} denotes the longitudinal mode of the FP cavity.

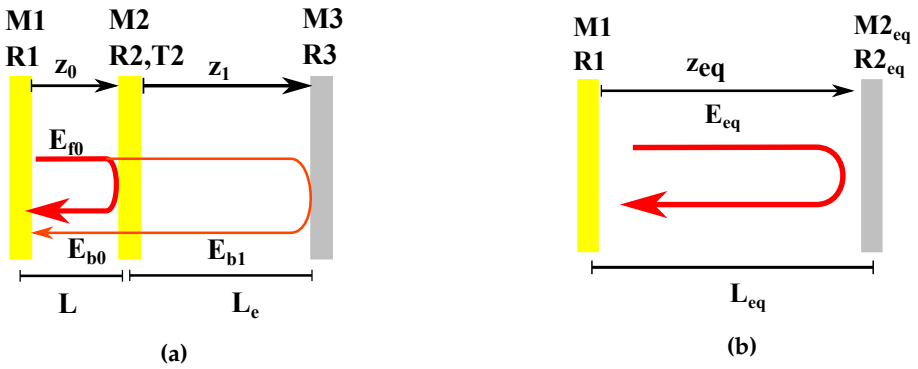

Figure 2.2.5: Double FP cavity model. (a) The model is represented by two cavities using three mirror like surfaces $M1$, $M2$, and $M3$. (b) Equivalent single cavity of the depiction presented in (a), notice that mirrors $M2$ and $M3$ have been replaced by an equivalent reflector $M2_{eq}$.

2.2.3.2 Double Cavity FP Model

As described, the single cavity model can help to describe the resulting frequency of a laser diode as well as the minimum gain to attain lasing in a quite simple manner. When a second cavity (the *external* cavity) is introduced, this parameters will change according to the length of such external cavity and the level of feedback power reintroduced in the *internal* cavity.

To continue the analysis, let's consider the effects introduced when the second, external cavity shown in Fig.2.2.5 is introduced. In this case, we define the forward-propagation wave reaching the external mirror $M3$ as:

$$E_f(z_0, z_1) = E_{f0} t_2 e^{-i\tilde{k_0} z_0 - i\tilde{k_1} z_1}, \tag{2.2.23}$$

where the sub-indexes 0 and 1 are used to differentiate between the two cavities; $\tilde{k_x} = n_x \omega_x / c + i\alpha_{absx}/2$. Similarly, for the backward-propagation wave it is possible to equate:

$$E_b(z_0, z_1) = E_{b_1}(z_0, z_1) + E_{b_0}(z_0), \tag{2.2.24}$$

$$E_b(z_0, z_1) = t_2 E_{b1} e^{-i\tilde{k_0}(L - z_0) + -i\tilde{k_1}(L_e - z_1)} + E_{b0} e^{-i\tilde{k_0}(L - z_0)}, \tag{2.2.25}$$

where L_e represents the length of the external cavity.

If we assume there is only a single reflection from the external mirror $M3$, then $r_2 \gg r_3$. Then, the reflection at $M1$ and thus the initial forward wave can be written as:

$$E_{f0} = r1 E_b(0,0) = r1(t_2 E_{b1} e^{-i\tilde{k_0} L - i\tilde{k_1} L_e} + E_{b_0} e^{\tilde{k_0} L}), \tag{2.2.26}$$

Moreover, it is also observed that:

$$E_{b1} = E_f(L, L_e) = r_3 t_2 E_{f0} e^{-i\tilde{k_0} L - i\tilde{k_1} L_e} \tag{2.2.27}$$

$$E_{b0} = r_2 E_{f0} e^{-i\tilde{k_0} z_0} \tag{2.2.28}$$

Substituting Eq.(2.2.27) and (2.2.28) in Eq.(2.2.26) we arrive to the expression:

$$1 = r_1 r_2 e^{-2i\tilde{k_0} L} \left(\frac{r_3}{r_2} t_2^2 e^{-2i\tilde{k_1} L_e} + 1 \right). \tag{2.2.29}$$

which can be directly compared to Eq.(2.2.20). Therefore, it is possible to redefine Eq.(2.2.29) as:

$$1 = r_1 |r_{2eq}| e^{-2i\tilde{k_0} L + \phi}, \tag{2.2.30}$$

where:

$$r_{2eq} = r_2\left[\frac{r_3(1-r_2)^2}{r_2}e^{-2i\left(\frac{n_1\omega_1}{c}-\frac{\alpha_{abs_1}}{2}\right)L_e}+1\right] = r_2(\kappa e^{\omega_1\tau-\frac{\alpha_{abs_1}}{2}}+1). \tag{2.2.31}$$

In this equation, typically the losses due to air absorption in near infrared (*NIR*) can be omitted for the model because they become negligible.

As in the previous case, first it is required to change the gain threshold due to the external feedback (G_{thr_F}), which is given by:

$$G_{thr_F} = \frac{\alpha_{int}}{2}+\frac{1}{L}\ln\left(\frac{1}{r1\|r_{2eq}\|}\right), \tag{2.2.32}$$

where the modulus of $r_{2eq} \approx \Re(r_{2eq})$ assuming the case of weak optical feedback. Thus, the difference in gain can be equated using Eq.(2.2.21) and Eq.(2.2.32) as:

$$\Delta G = G_{thr_F} - G_{thr} = \frac{1}{L}\ln\left(\frac{1}{\kappa\cos(\omega_F\tau)+1}\right) = \frac{1}{L}\ln(1+\kappa\cos\omega_F\tau), \tag{2.2.33}$$

Finally, using the first term of the expansion series:

$$\ln(1+x) = x-\frac{1}{2}x^2+\frac{1}{3}x^3-\frac{1}{4}x^4+\cdots, \tag{2.2.34}$$

it is possible to define the change in the gain threshold as:

$$\Delta G \approx \frac{1}{L}\kappa\cos\omega_F\tau. \tag{2.2.35}$$

Following this process it is also possible to compute the value of the phase term. In order to do so, first we compute the phase given by the term r_{2eq}. Provided that $r_2 \gg r_3$ and therefore $\kappa < 1$, only small changes on the phase are considered, thus resulting in:

$$\phi_{eq} = \arctan\left(\frac{\Im(r_{2eq})}{\Re(r_{2eq})}\right) \approx \frac{\Im(r_{2eq})}{r_2} = \kappa\sin(\omega_F\tau). \tag{2.2.36}$$

Other effects such as a change in the frequency of emission and in refractive index also induce a frequency shift that needs to be accounted for. This changes can be expressed as [51]:

$$\Delta(\omega n_e) = \omega_{thr}\Delta n_e + (\omega_F-\omega_{thr})n_e, \tag{2.2.37}$$

where n_e is the effective refractive index in the equivalent cavity. The change of refractive index can then be defined in terms of the carrier density N as:

$$\Delta n_e = \frac{\partial n_e}{\partial N}(N-N_{th})+\frac{\partial n_e}{\partial\omega}(\omega_F-\omega_{thr}) = -\frac{\alpha c}{2\omega_{thr}}\Delta G+\frac{\partial n_e}{\partial\omega}(\omega_F-\omega_{thr}), \tag{2.2.38}$$

which, using the property of the effective group refractive index $n_0 = n_e + (\partial n_e/\partial\omega)\omega_{thr}$ results in:

$$\Delta(\omega n_e) = (\omega_F-\omega_{thr})n_0-\frac{\alpha\Delta G}{2}. \tag{2.2.39}$$

Substituting Eq.(2.2.35) in Eq.(2.2.39) and adding the phase of the equivalent reflection, it is possible to obtain the excess phase equation:

$$\Delta\Phi = (\omega_F-\omega_{thr})\tau_{in}+\alpha\kappa\cos(\omega_F\tau)+\kappa\sin(\omega_F\tau), \tag{2.2.40}$$

which, after using the trigonometric property:

$$A\cos x + B\sin x = \sqrt{A^2+B^2}\sin\left[x+\arctan\left(\frac{B}{A}\right)\right], \tag{2.2.41}$$

then multiplying by the time of flight of the external cavity, and dividing by the time of flight of the internal cavity, results in the well known form of the excess phase equation:

$$\Delta\Phi = (\omega_F - \omega_{thr})\tau + \frac{\kappa\sqrt{1+\alpha^2}\tau}{\tau_{in}}\sin[\omega_F\tau + \arctan(\alpha)]. \tag{2.2.42}$$

This representation is analogous to the one presented in Eq.(2.2.15). As in the previous case, the total optical power may be calculated as the square of the electric field moduli.

2.2.4 Optical output power

As explained at the beginning of this section, SMI phenomena can be understood as a modulation of the optical output power (*OOP*) of the LD detected in different ways. Such a power modulation can be related to the excess phase induced by feedback, which also induces changes in the electron carrier density. To study the effects of optical power in terms of the previously depicted models, Eq.(2.2.16) is substituted into Eq.(2.2.5) as described in [47, 52, 53]. Equating to the square modulus of the electric field under feedback E_F, it can be obtained:

$$P_F = |E_F|^2 = \frac{\frac{Jn}{qd} + \frac{N_{th}G_n\tau_c - 2\kappa\cos(\omega_F\tau)}{\tau_e G_n\tau_c}}{G_nN_F - G_nN_{th}}, \tag{2.2.43}$$

which after using the approximation $1/\tau_p = G_n(N_{th} - N_0)$ [47] leads to:

$$|E_F|^2 = \frac{\tau_p}{\tau_e}\frac{\frac{Jn}{qd}\tau_e - N_{th} + \frac{2\kappa}{Gn\tau_c}\cos(\omega_F\tau)}{1 - \frac{2\kappa\tau_p}{\tau_c}\cos(\omega_F\tau)}. \tag{2.2.44}$$

Assuming that the expression Eq.(2.2.44) can be linearized into:

$$P_F \approx \frac{\tau_p}{\tau_e}\left(\frac{Jn}{qd}\tau_e - N_{th}\right)\left[1 + \frac{2\kappa\tau_p}{\tau_c}\cos(\omega_F\tau)\right] \tag{2.2.45}$$

and, given that initial output power can be modeled as $P_0 \propto |E_0|^2 = \tau_p[Jn/(qd) - N_{th}/\tau_e]$, it is possible to arrive to the expression:

$$P_F = P_0(1 + mF(\phi)), \tag{2.2.46}$$

where:

$$m = 2\frac{\kappa\tau_p}{\tau_c} = C\frac{2\tau_p c}{L_e\sqrt{1+\alpha^2}} \tag{2.2.47}$$

$$F(\phi) = \cos(\omega_F\tau) = \cos(\omega_F\frac{\phi}{2\pi}\frac{\lambda_0}{c}), \tag{2.2.48}$$

with λ_0 the wavelength of the LD.

Due to its nature (for SMI and telecommunication processes), optical power is typically read using a photodiode (*PD*). In the case of LDs, the PD can be placed in the same mechanical package to monitor the emission of the LD, although in some cases the PD may not be available. Still, for the SMI process, it is possible to measure the changes in optical power by reading the LD junction voltage [32, 35, 53] as:

$$\Delta V = -K\cos(\omega_F\tau), \tag{2.2.49}$$

where K is a term dependent upon the optical power. In the case of SMI applications, the use of a PD based scheme or a junction LD scheme would result in a difference of SNR [32] that can go from $-90dB$ in the PD case to $-50dB$ in the voltage junction case. Other differences in both approaches may be found in the literature for example in [54].

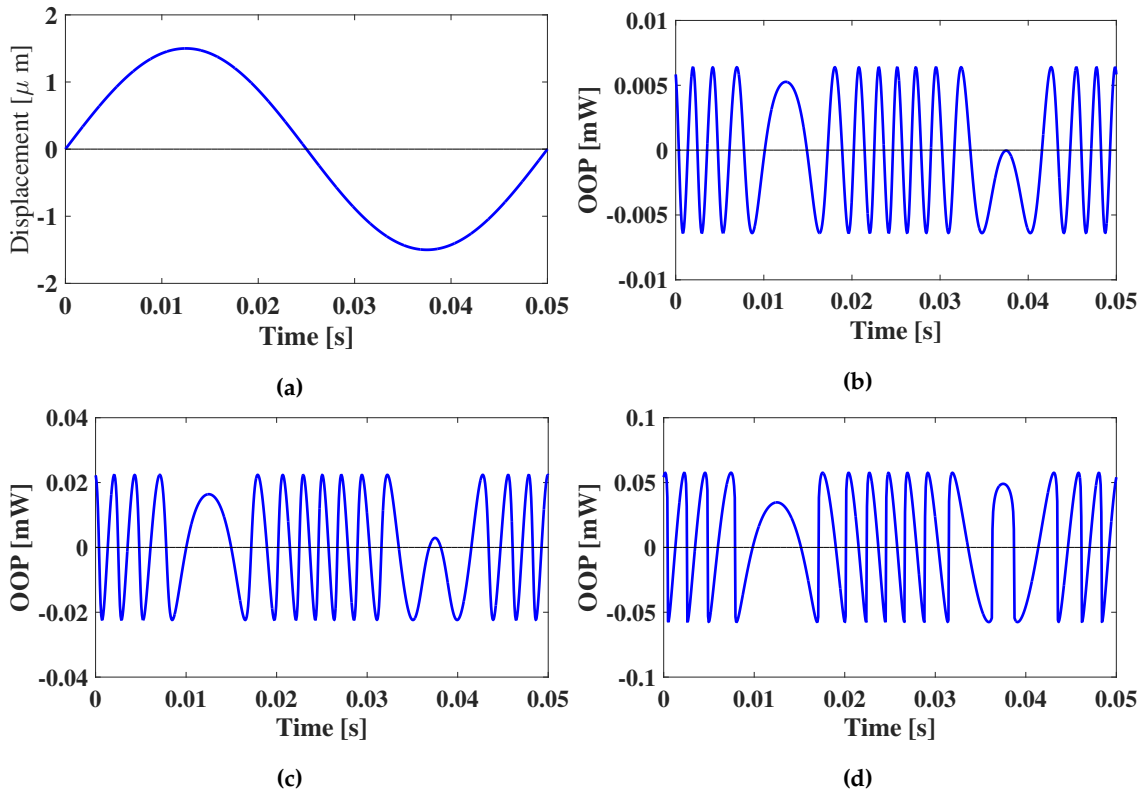

Figure 2.2.6: Examples of simulated SMI signals for different feedback regimes for a $3\mu m$ amplitude sinusoidal displacement. (a) Reference displacement used for all signal simulations; (b) Very weak regime, with $C \approx 0.1$; (c) Weak regime, with $C \approx 0.4$; (d) Moderate regime $C \approx 1.1$.

2.2.5 The Feedback Factor

Different authors [31,47,55] have directly related the behavior of the SMI signal with the amount of feedback power in the cavity using the so-called feedback factor C. As seen from Eq.(2.2.42), there exists a non-zero multiplicative factor which changes the amplitude of the sin function, depending on the reflectance and the ratio of time of flight between the internal and external cavities. Some authors [47] have included a correction to this term to take into account the losses due to the length of the cavity, therefore representing the term as:

$$C = \kappa \sqrt{1+\alpha^2}\frac{\varepsilon}{\sqrt{A}}\frac{\tau}{\tau_{in}}, \tag{2.2.50}$$

where A represents the total optical power attenuation in the external cavity, and $\varepsilon \leq 1$ is a parameter introduced by Acket et al. [55] to account for mismatch in overlap. This parameter is typically modelled with values within the range from 0.1 to 0.8 .

There have been extensive studies focused on the evaluation of the effects of the C parameter, its relation with phase shift, and the distortion introduced in SMI signal [25,31,47,53,56–60]. In general, it is possible to divide the response of the SMI signal depending upon the value of the C factor into four main feedback regimes [39]:

- **Very weak feedback regime** ($C < 0.1$): The resulting feedback signal behaves sinusoidally (Fig.2.2.6b). Typically in this form the signal to noise ratio (SNR) is low. While this type of signal is not used for displacement measurements, as it will be discussed in the following section, it can be useful in order

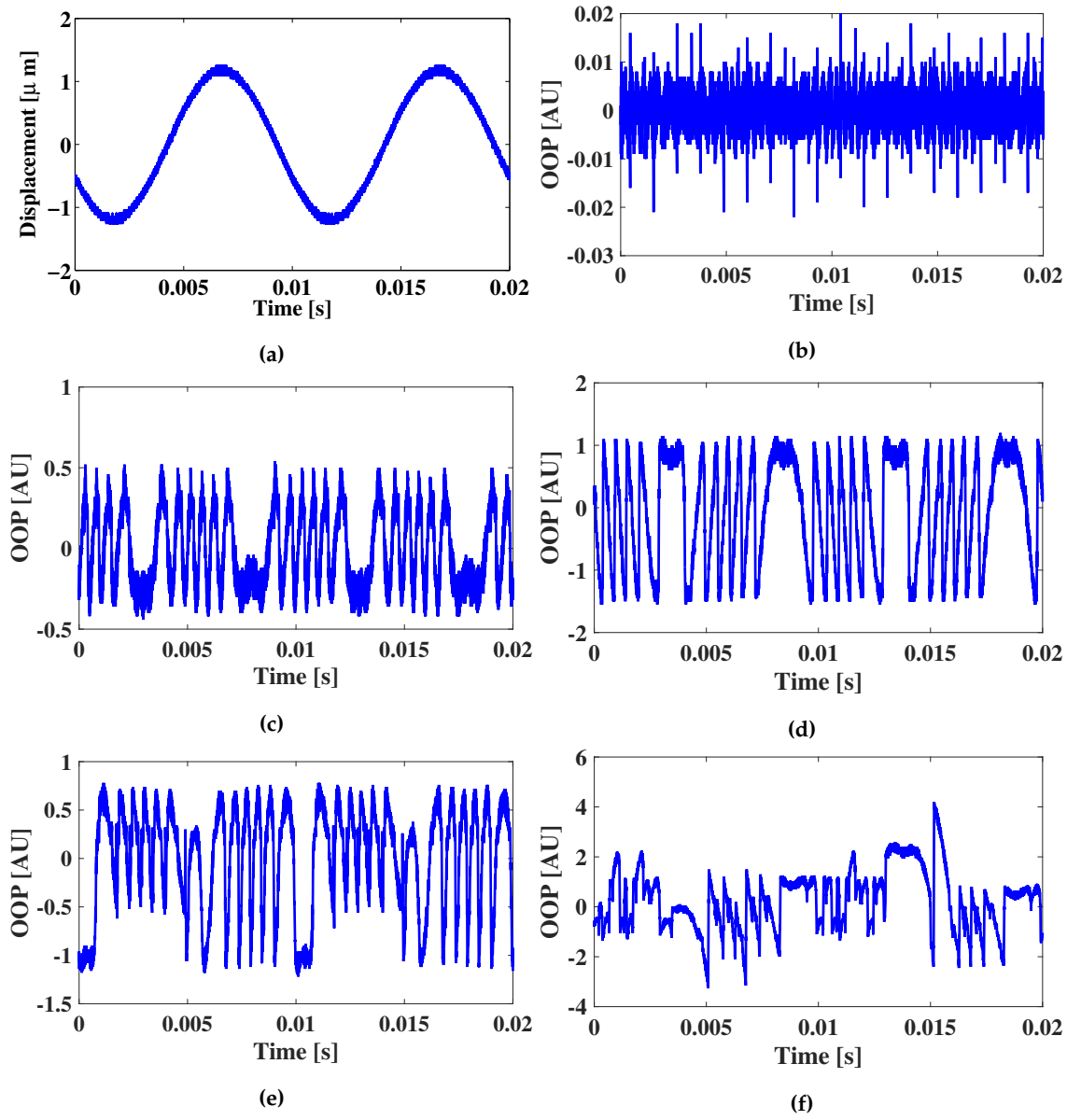

Figure 2.2.7: Example of experimental SMI signals at different feedback regimes. The feedback power back in the laser cavity is controlled using a Thorlabs focusing lens $C230220P-B$. (a) Sinusoidal displacement of the piezoelectric target used to generate the corresponding SMI signals; (b) SMI signal in the very weak feedback regime with $C < 0.1$, l; (c) SMI signal in the weak feedback regime with $C < 0.5$; (d) SMI signal in the moderate feedback regime $C > 1$; (e) SMI signal in the strong feedback regime $C > 4.7$; (f) SMI signal in the chaotic regime.

to perform velocity or flow measurements.

- **Weak feedback regime** ($0.1 < C < 1$): The sinusoidal term of the excess phase equation becomes distorted as the feedback increases (Fig.2.2.6c). It is possible to observe an increase of the signal SNR as the feedback value approaches to $C = 1$. The frequency distortion makes the signal start behaving in a sawtooth-like fashion, with a slope dependent upon the motion direction.

- **Moderate feedback regime** ($1 < C < 4.6$): The sinusoidal signal becomes totally distorted and acquires a sawtooth-like shape (Fig.2.2.6d). As the value of C increases, hysteresis effects may be observed as a

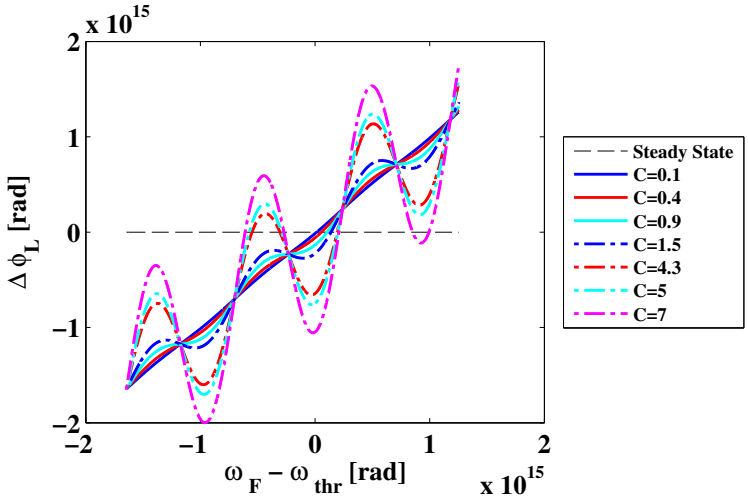

Figure 2.2.8: Effects of the feedback factor on the number of steady state solutions for the excess phase equation. As the C increases the number of zero crossings increases.

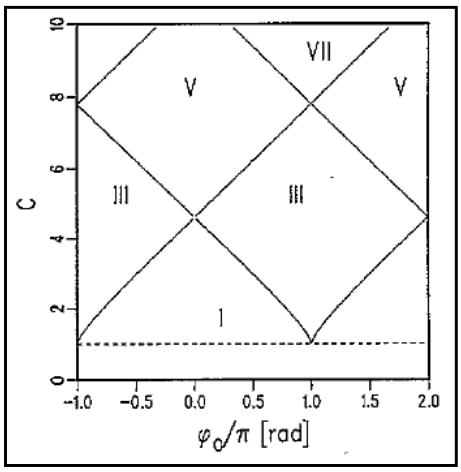

Figure 2.2.9: Number of solutions for Eq.(2.2.42) according to Eq.(2.2.51) proposed in (source: [55]).

result of mode hopping between allowed states. The SNR of the signal allows a clear detection of the interferometric fringes for displacement sensing purposes.

- **Strong feedback** ($C > 4.6$): The number of solutions in the excess phase equation and the effects increases from 3 to 5 and hysteresis effects are more evident. The SNR of the signal is reduced as the relative amplitude of the sawtooth signal experiences a reduction due to hysteresis effects. In some cases multiple mode hopping may be experienced. Further increments on the feedback level result in a chaotic signal.

It is to be noticed that the detection capabilities of a SMI sensor depend upon the amount of feedback, and also on the SNR of the detected signal. In Fig.2.2.7 some examples of experimental signals for a $2\mu m$ peak to peak amplitude sinusoidal displacement are shown. The displacement is produced using a piezoelectric transducer (PZT) equipped with an internal capacitive sensor. It can be observed how the SNR of the signal tends to increase as the amount of feedback increases. After reaching the strong feedback regime, however, the amplitude of the fringes shows dependence on the direction of motion. This changes in amplitude can be

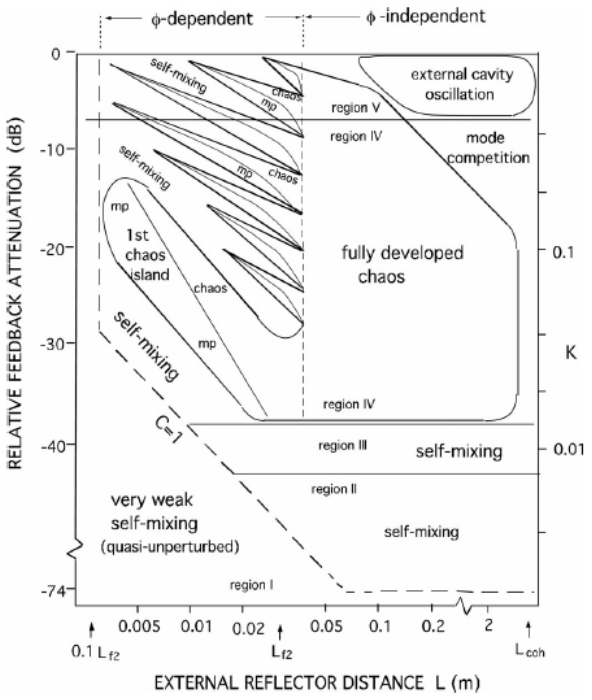

Figure 2.2.10: Feedback diagram proposed by Donati et al. The dotted lines represent the boundaries between perturbed and unperturbed operation. As observed, the amount of feedback required for a SMI behavior varies as a function of the external cavity length (source: [31]). In region *I* only very weak and weak feedback SMI can be developed ($C < 1$). Region II is characterized for having multiple solutions involving mode hopping (moderate feedback). In region III the laser returns to a single narrow line mode (this region is also characterized for showing moderate feedback conditions). Regions IV and V show chaotic conditions which are outside of the analysis presented in this Thesis.

related to hysteresis effects introduced by mode hopping between the multiple solutions of the excess phase equation, as described in [47]. If the feedback is increased further, the detection in one of the directions may become compromised as a result of digital acquisition limitations. Chaotic behavior, as described in [31], can be reached at larger feedback levels, as shown in Fig.2.2.7f.

It is possible to study the number of steady state solutions the signal would have as a result of an increase of the C factor as shown in Fig.2.2.8. As it is observed, as C increases the number of solutions will increase, resulting always in an odd number after crossing some threshold values. This behavior was studied by Acket et al [55], who observed that for $C < 1$ a single stable solution is found at a slight variation from the frequency of the solitary state laser. For $C \geq 1$, nevertheless, the number of zero crossings in the steady state solution increases according to:

$$\phi_0 = (2k+1)\pi \pm \arccos\left(\frac{1}{C}\right) \mp \sin\left[\arccos\left(\frac{1}{C}\right)\right], \tag{2.2.51}$$

where k is an integer and $\phi_0 = \omega_0\tau + \arctan(\alpha)$. As a result, it is possible to detect the space (C, ϕ_0) (Fig.2.2.9) where the number of the zone denotes the number of solutions at a defined feedback level.

The external cavity length plays a very important role on the C value, since, as observed from Eq.(2.2.50), and contrary to intuition, C *increases* proportionally with the length of the external cavity. In order to point out the effects of C as a result of the cavity length, Donati et al [58] define the limit of the cavity length as $L_{coh} = c/(2f_2)$ with f_2 the cut-off frequency of the laser modulation, and the coherence length L_{coh}.

For short cavities ($L < 0.1L_{f2}$), very weak and weak feedback regimes occur from -74 to $-30dB$ of relative optical attenuation as shown in Fig.2.2.10. However after crossing the critical $C = 1$ value, in the short cavity case, it is possible that a slight variation of the reflective conditions of the setup results in a chaotic signal. It is also to be noticed that working on a short cavity may require larger levels of feedback in order to produce a moderate level signal. In the case of working distances larger than L_{f2} , it can be observed that the moderate feedback regime (region II) is easily achieved with values close to $-74dB$ and that the signal will remain under such conditions till approximately $-45dB$, where it will enter into the strong feedback regime. Care should be taken, however, since working in this region may rapidly degenerate into fully developed chaos if the feedback level was to increase a few dBs [31] along the experiment. In case of larger distances, it is noted that after coherence length is surpassed it is still possible to get some interference effects, which in some cases would even allow reaching chaotic behavior. Nevertheless, working at such distances might be inefficient as discussed in [31].

2.3 Classical Applications

As explored in the previous section, SMI is an interesting technique capable of measuring all kinds of changes in the optical path of the laser. Taking as starting point the excess phase equation, different methods have been proposed to study, among others, displacement, velocity and absolute distance, which are in the root of the vast majority of applications of the self-mixing technique. In this section, a short overview of the methods used in such most common applications of SMI is presented.

2.3.1 Displacement measurement

There exists a variety of technologies capable to measure displacement at different scales. It is usual to divide those technologies into contact and non contact ones. Commonly the former ones allow high resolution and large bandwidths at the cost of precise positioning and potential damage to fragile samples. Some examples of this type of sensors can be found in linear variable differential transducers (*LVDT*) [61] or in extensiometric gauges [62]. Other technologies, such as capacitive [63] and inductive [64] sensing provide an intermediate alternative for non-contact displacement measurement, as in some cases the characteristics of the target may allow direct measurement of the parameter of interest or the feasibility to include some tag reactive to capacitive or inductive sensing. Finally, pure non-contact methods such as those based in acoustics and optics [65] provide a solution in those cases where size, temperature, or mass prevent from a direct contact with the measured element.

Focusing our view onto optical sensors, the most representative ones include methods based on triangulation [66], deflectometry, and interferometry. In the later case, different techniques have been proposed (e.g. Michelson interferometry [67]), relying during the processing in the well-known fringe counting method [39,68]. Several authors have discussed the capabilities of Michelson interferometry for measuring nanometric and sub-nanometric displacements [69] using special complex setups, processing algorithms, or even X-Ray based interferometry [70]. Nevertheless, in order to reach such a high resolution response it is usually required a large number of precisely aligned optical elements, thus increasing the minimum volume required for the sensor, therefore limiting the number of potential applications. In contrast, the SMI scheme provides a small volume and relatively low cost solution to that presented by classical interferometric systems, at the cost of having a resolution within the micrometric, and, under given setups, down to

the nanometric scale [53]. At the same time, SMI interferometry presents the advantage of determining the direction of the displacement by simply looking at the derivative of the SMI signal, as described by Donati et al. [30].

Different methods have been proposed in order to extract displacement information out of the SMI signal. Possibly, the best known is the so-called fringe counting method *FCM*, which consists in detecting the sharp transitions of the SMI signal corresponding to a complete period of the function $F(\phi) = 2\pi$ described in Eq.(2.2.48). The relationship of the phase with the displacement can then be easily observed by rewriting Eq.(2.2.48) in terms of the wavelength of the free running laser (λ_0) and the lenght of the external cavity L_e as [71]:

$$\left|2\pi\nu_F \frac{2L_e}{c}\right| = 2\pi \iff |\Delta L| = \frac{\lambda_0}{2}; \tag{2.3.1}$$

therefore, it is possible to calculate the total displacement in a single direction as: $\Delta L = k\lambda_0/2$, where k is an integer number representing the number of fringes detected in the OOP signal.

The algorithm in the FCM is particularly effective in the cases of weak and moderate feedback, since it is relatively simple to detect the transitions, and, at the same time, account for the direction of the displacement from the OOP value obtained. In such cases, a differentiation process is typically applied to the SMI signal (Fig.2.3.1b) resulting in positive and negative peaks which are then selected using a threshold process. Most commonly, the derivative of the signal is normalized, and a large threshold value ($thr \geq 0.5$) can be used for fringe detection due to the high SNR of the signal as depicted in Fig.2.3.1c. Finally, Fig.2.3.1d, the displacement is reconstructed by increasing or decreasing the relative displacement in $\lambda_0/2$ steps [47,53,71]. An smoothing low pass filter can be applied after the reconstruction to reduce the stepwise look of the reconstruction.

In the cases of the strong and very weak feedback regimes, the FCM technique cannot be applied without loss of precision since, in the first case, the hysteresis in the signal reduces the relative size of the fringes, making it difficult to select a threshold, and even causing loss of fringes [53]. In the later case, it is impossible to detect the direction of the displacement due to the type of signal obtained. Other detection methods to complement the FCM approach have been discussed in [72], where it is claimed that displacement detection can be performed even at very weak feedback levels.

Different practical applications have been described throughout the years based on the SMI displacement sensing scheme; some relevant contributions which set the prior art related to displacement measurement are discussed below. The works described in the items below are relevant for this Thesis since they show possible fields of application not largely exploited by SMI sensors (such as multidimensional displacement measurement), the use of multiple SMI sensors in a single setup, and possible limits on the resolution of the SMI sensor. If the reader is interested, the work presented by Taimre et al. [73] presents a comprehensive review with several applications which cannot be presented in this section for the sake of brevity.

- Haptmann et al. [74], described the use of a SMI interferometer using an optical fiber to measure the vibration of a silicon resonator. The study found that the method was limited because of the mounting methods of the resonator and the difficulty of alignment to obtain an enhanced SMI signal. It is important to stress how in this paper the authors make an emphasis in the use of multimode fibers since their use can allow a higher acceptance angle of the feedback signal.
- Tsai et al. [75] proposed the use of a SMI based sensor for the positioning and control of an optical head. Their results show that it should be possible to use multiple SMI sensors for the positioning of a 6 degrees of freedom (*DOF*) system.

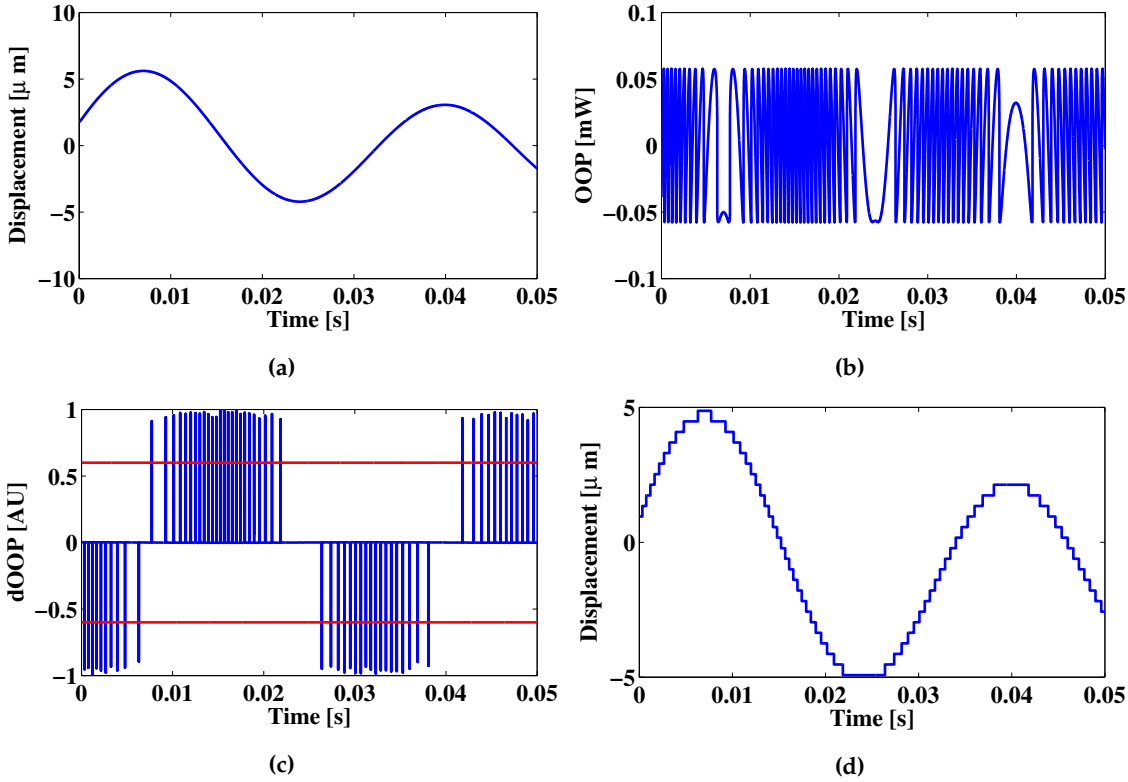

Figure 2.3.1: SMI displacement reconstruction using the FCM from a simulated signal. (a) Target displacement; (b) SMI signal at $C \approx 0.7$; (c) Normalized derivative signal and threshold value selection (red lines); (d) Signal reconstruction.

- Dabbico et al. [76] studied the use of SMI effect using an optical fiber to measure physical stress in solid bars. Their results were comparable to those obtained with commercial Fiber Bragg Grating (*FBG*) sensors.

- Lukashin et al [77] proposed the use of a SMI displacement sensor to measure cochlear vibrations in a cellular membrane. In their article, they confirm that the low power of the LD's used allows measuring *invivo* on live tissue without damaging the sample. The resolution of the method was sufficient to provide good results.

- Giuliani et al. [78] used SMI for the detection of vibration in cooperative and non-cooperative samples with an increased resolution of $\lambda/4$. In the performed tests, their instrument was able to measure vibrations with an equivalent noise around $100pm/sqrtHz$, with a maximum peak of $180\mu m$, dynamic range of $100dB$ and bandwidth of $70kHz$.

- Atashkhooei et al. [79] used and SMI sensor to measure the deflection of a structural beam and compared the results with those of a LVDT sensor. The obtained results show good agreement with available commercial sensors.

- Atashkhooei et al. [80] proposed the use of an SMI sensor for tracking the run-out of electric motor shafts for predictive maintenance. The measurement was performed using two SMI sensors placed at 90° from each other, and the total XY displacement of the motor was obtained. The sensor showed good agreement with measurements taken with other interferometric based sensors.

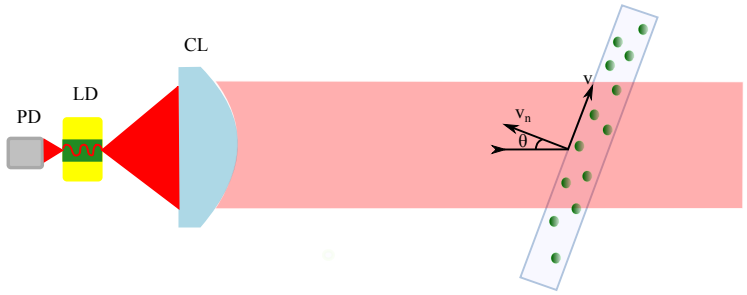

Figure 2.3.2: Diagram of a velocimetry/flowmetry setup using SMI. The resulting velocity is proportional to the frequency of the SMI signal as well as to the laser wavelength. The method can work in any of the SMI regimes, as in most cases no direction sensing is required.

2.3.2 Velocimetry, Flowmetry and Doppler-shift based methods

Doppler based detection methods have been commonly applied for processing SMI signals. Possibly, the first example of velocimetry measurements based in the self mixing effect is the one presented in [14]. A more detailed study on the use of Doppler effect for velocity measurements using SMI is proposed in [81] where the target velocity v can be related to the SMI signal frequency f_D and the beam profile properties.

In general the velocity of a solid target, or particle, moving within a measurement volume of a SMI laser sensor can be expressed as:

$$f_D = 2\frac{nv}{\lambda}\cos\theta, \tag{2.3.2}$$

where n is the refractive index of the media, typically taken as $n \approx 1$ for air interfaces, θ the angle between the normal of the target displacement vector and the LD emission axis as shown in Fig.2.3.2.

Several applications have been developed using the Doppler effect in SMI. Particularly bio-engineering applications have taken a keen interest in this kind of method since the use of low power LDs would allow the use of LDV methods through a low cost and safe approach. Some of the main applications developed in recent years using the LDV method are briefly commented below.

- Özdemir et al. [82] proposed the use of SMI for the measurement of blood flow over the skin. The study compared the flux measurements with conventional laboratory equipment and a good correlation was observed between the results obtained with both instruments.
- Tucker et al. [83] reported measuring flow of liquid using a SMI sensor without a PD. The presented measurement scheme claimed to have better bandwidth when compared to traditional SMI schemes, as the PD bandwidth is typically limited to a few kHz for optical power control purposes.
- Nagahara et al. [84] described a blood flow measurement over retinal capillaries in vivo. In the case of the 115μm radius arteries, it was found a good correlation with existent flow statistics. A question regarding the optical power required to generate the SMI signal was raised as a possible problem with the method. The main concern of the authors was the possibility of damaging samples due to long time exposition.
- Norgia et al. [85] reported an extra-corporeal blood flow sensor which could be produced at a low cost.

There are several ways to measure the velocity of a target using SMI. Possibly the most common method is described by Scalise and Paone in [86] where the detection of the main harmonic of the Fourier spectra

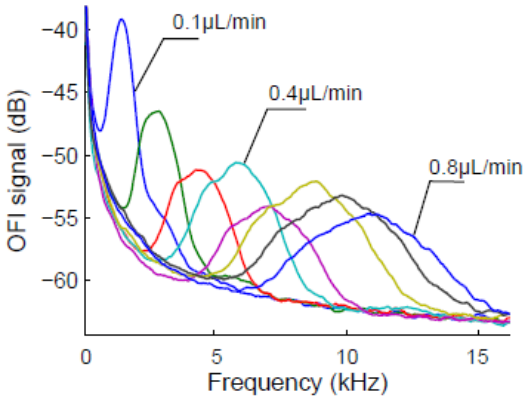

Figure 2.3.3: Example of detection of velocity using the SMI power spectra [81]. The velocity profiles correspond to different velocity profiles of water circulating through a $100 \times 20\mu m$ rectangular cross section channel. Reflectivity is enhanced using $4\mu m$ diameter latex spheres. The measurement is obtained by placing the LD with $\lambda = 667nm$ at $\theta = 80°$.

is used to detect the Doppler frequency F_D. More recently, Campagnolo [81], as shown in Fig.2.3.3 has proposed that in the cases of low SNR signals, or in the case of low feedback such as in the case of fluids with low particle reflectivity, a $3dB$ fall on the power spectra of the SMI signal can be used to detect f_D. This method is still controversial as the precision is limited to a 10% of the measurement as shown in the results of [81].

Current SMI velocimetry studies are focusing into determining the sensing volume of the sensor in order to increase the sensitivity of the method. This would be specially critical in the case of fluids where it is important to determine the number, and velocity of particles. In such cases some authors, as Wang [87,88] and Campagnolo [81] have used a Gaussian beam approximation to model the measurement volume. Wang et al. [88] claim that the power spectral density can be derived from the Fourier transform and the time correlation of two Voight functions, where the numerical results show that it is not possible to obtain a peak from the Doppler power spectral density in the case of a beam normal to the velocity vector. Mowla et al. [89] have proposed a method to use confocal microscopy and laser flowmetry to enhance skin cancer imaging by means of a Monte Carlo model.

2.3.3 Absolute distance measurement

Absolute distance measurement, also described as range finding in the literature [47,71,90,91] differs from classical SMI measurement setups since the modulation is produced in the laser's point of operation rather than in the external cavity length.

Electronic frequency modulation of a LD subjected to optical feedback was first proposed by Beheim and Fritsch [92]. The depicted range finder was able to determine the distance to the target by looking at the frequency deviation of a full phase cycle after feedback. The changes in laser current result in small variations of the LD temperature and refractive index, which create a variation of the initial wavelength $\Delta\lambda$ in the optical output. Their results show that it was possible to perform absolute distance measurements up to $1.5m$, with a resolution in the order of $4mm$, comparable to time-of-flight methods. The typical resolution of range finders based in the LD SMI method typically fall within the millimetric scale [90,91,93]. Similar results, for instance, were obtained in 1991 by Shinohara et al. in [93]. Later Goaux et al. [94] were able to obtain a $1.5mm$ resolution in a range of $0.5m$ to $2m$. It is also important to remark that Goaux discusses a

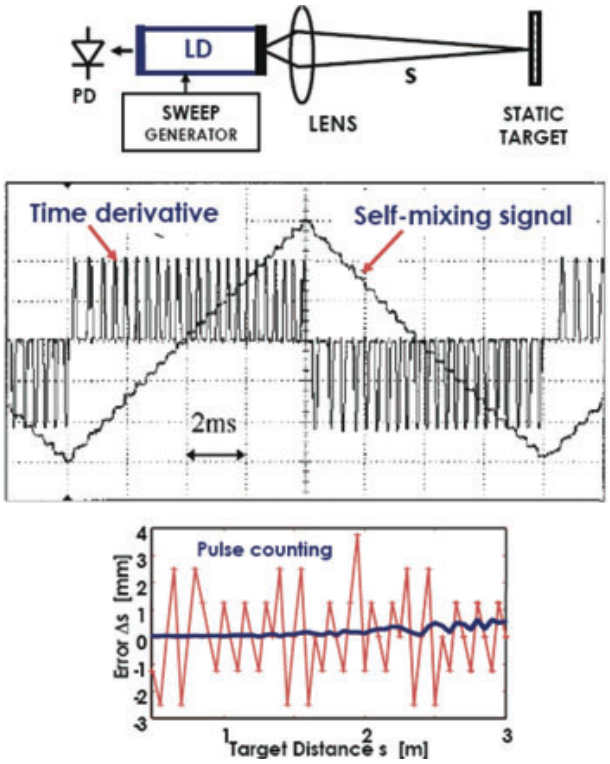

Figure 2.3.4: Example of a distance measurement using the SMI method as described in [90]. A triangular current modulation is injected in the laser. After differentiation is possible to find the beating in the signal and relate it to the absolute distance (source: [90]).

detailed theoretical model of the effects of a triangular frequency modulation on a LD with optical feedback.

In general, as described in [90], it is possible to consider the total current change in the LD operation as $I_m = I_b + \Delta I$, where I_m is the injected current, $I_b > I_{th}$ the applied bias current which by definition should be larger than the LD threshold current I_{th}, and ΔI as the induced triangular current modulation. Considering:

$$\alpha_c = \frac{d\lambda}{dI}, \tag{2.3.3}$$

as the current to wavelength coefficient, it is possible to consider the total wavelength swing caused by the change in current as:

$$\Delta\lambda = \alpha_c \Delta I. \tag{2.3.4}$$

Next, taking into account that the derivative of the wave number can be written as:

$$\Delta k = \frac{2\pi}{\lambda^2}\Delta\lambda, \tag{2.3.5}$$

it is possible to relate the number of complete periods N during half period of the frequency modulation to the distance s as:

$$s = N\frac{\lambda^2}{2\Delta\lambda}. \tag{2.3.6}$$

Some other relevant works describing applications or enhancements in the range finding method include:

- Kou et al. [95], propose the use of genetic algorithms to improve the resolution of the SMI method and claim resolutions in the order of $20\mu m$. In their experiments they focus in a range covering 2.4 to $20.4cm$ and report a standard deviation between measurements of $10\mu m$. As in many other SMI cases, the limitations of the proposed technique were given by the SNR ratio of the acquired signals.

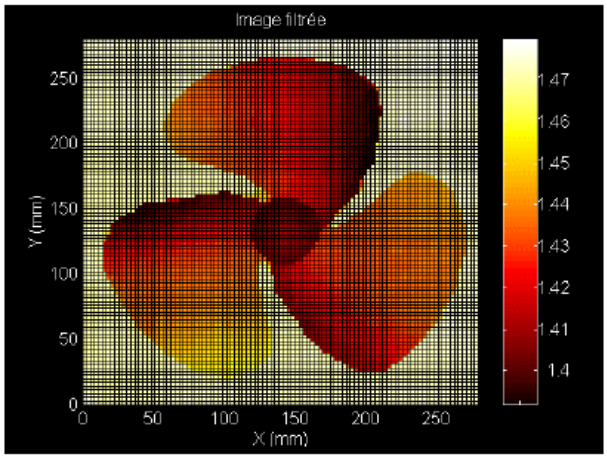

Figure 2.3.5: Example of a 3D image reconstruction in pseudo-color using a SMI range finding algorithm with an scanning stage composed by two mirrors controlled with galvanometers (source: [99]).

- In [96] Guo and Wang present an approach using a frequency current modulation method combined with an electro-optical phase modulation to perform absolute distance measurements. The value of the distances is calculated using the signal Fourier spectra, and the results show that it is possible to reach resolutions in the order or 300nm.
- Suzuki et al. [97] propose a phase locked laser diode for different SMI applications. The use of the phase-locked technique allows to fix the phase change for absolute distance measurements. Their results show a 2.58mm resolution with a noise in the order of ±25nm.

2.3.4 Imaging

Besides SMI applications for point measurements, as described in previous subsections, different research groups have developed applications capable of performing imaging using the SMI signal. In order to achieve that kind of solutions two main approaches have been taken: the use of LD arrays, and the use of scanning methods.

Bosch et al. [98] described an application using a SMI range finding sensor to build a 3D reconstruction on an object with a 0.1% resolution for a target up to a 3m range as shown in Fig.2.3.5. The scanning system consisted of a XY scanning stage of two mirrors which were rotated using iron galvanometers. To prevent temperature effects the triangular current modulation was reshaped as defined in [94]. The photoelectric current was processed using a Nagao-Median filter to improve the accuracy of the filter allowing a resolution of 1.846mm, while keeping a 0.8% distance resolution per pixel.

Zakian et al. [100] showed that it is possible to scan the velocity of a flow in in millimetric radius channels using a 2D motor stage to control the position of the measurement point. The reconstructed intensity map consisted of points spaced 500μm in a scan area of $7.5 \times 5mm$. It is also shown that the scatterers inside the tissue phantom for a thickness of 420μm can affect the measurements. The main issue in this type of mechanical configurations was the delay time between measurements at different scan points since 10s were required to provide enough mechanical stability to the laser at each position.

Within the array methods, it is possible to name the studies performed by Leng Lim et al. [101], who used VCSEL LD arrays using a voltage junction measurement scheme and measured the effects of velocity over an aluminium disk, and later in [102] enhanced their experiments to measure flow using a linear array

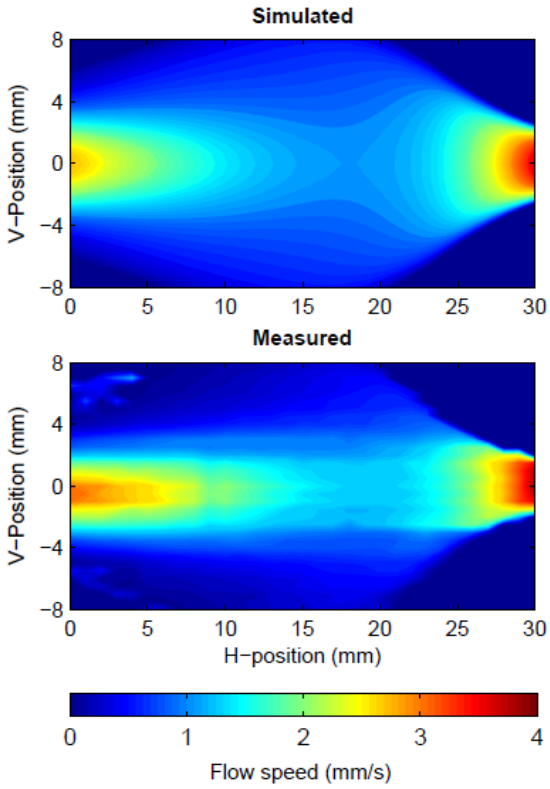

Figure 2.3.6: Comparison between simulated and measured flow in a millimetric channel for a $15mL/min$ flow rate. The measurement is achieved by using a linear array of VCSEL LDs followed by a linear mechanical scanning at different positions of the channel (Source: [102]).

as shown in Fig.2.3.6. The lateral resolution achieved with this method was $500\mu m$ due to the pitch between LD's and $1mm$ in the line scanning axis. A good correlation was found when the theoretical model and the practical results were compared. Errors in the order of 3% were observed by the authors.

More recently, Kliese [103] presented a quick scanning XY system which was able to measure the flow of liquid in a $100\mu m$ side square cross section channel with a log-periodic spacing between channels. The system demonstrated capabilities for reconstructing the flow even at an scan rate of $1mm/s$. Lateral resolution, however, seemed to be limited to the order of $100\mu m$, since the limits of flowing and non-flowing regions start vanishing when the channels where at that spacing.

Other imaging systems based on displacement measurements have been presented by Ocaña and Molina [104] using a Z displacement stage and a rotating stage to measure the displacement of a vibrating membrane. Their results show good agreement with laser sensors based on triangulation.

2.4 Limitations of the classic SMI scheme

As studied in the previous Section, SMI-based sensors present a big advantage in terms of economy, size, and alignment when compared to more traditional interferometric schemes. Nevertheless, such simplicity brings along some relevant limitations in the SMI method. The most outstanding ones, in our opinion, are speckle effects, bandwidth, real time processing, and attainable resolution. All these issues are brought on

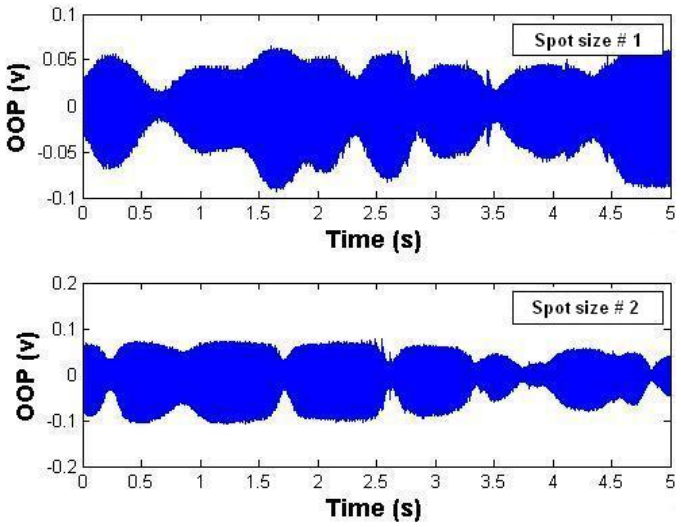

Figure 2.4.1: Example of a speckle modulation over two SMI signals with different spot size. Both lasers are pointing at the same target, but result in different amplitude modulation of the SMI signal due to their difference in spot size. (Source: [107])

by the sensing strategy and will be present in the experiments carried out in this Thesis. Our main proposal will push forward the attainable resolution limit.

2.4.1 Speckle effect

A laser speckle pattern is a random granular distribution which appears whenever a coherent light beam is reflected diffusely over an irregular surface on a scale $\gg \lambda$ [105]. The scattered coherent light then superimposes at the observation plane with random phases, yielding random local constructive or destructive interferences resulting into dark and clear speckle "grains". In the case of SMI the speckle pattern has been studied by different groups (e.g. [106], [107]) in order to limit its effects over long range displacement measurements. The speckle phenomena in SMI can be related to two main different effects [106]:

1. Amplitude modulation of the SMI signal: in a long displacement, or on a rapidly-changing phase target, the change in phase of the reflected beam may result in signal fading in the case of 1 channel interferometers, severely reducing the SNR of the signal. A typical example of such fading is observed in Fig.2.4.1, where the target is displaced along time. Some points of the acquired signal may be seen to present large drops in the signal amplitude which make them useless for measurement due to the impossibility to detect fringes.
2. Phase error: As the target moves further apart from the emission point, the phase error attributed to speckle will vary proportionally to distance. As a result, small displacements will usually result in small phase errors, which usually will be negligible in the measurement. However, as the target moves further away, the error will become larger until a point where the total phase correlation may be lost.

According to Donati et al. [106], it is possible to define the transversal speckle size as a value s_t where the correlation of the signal (also defined as the mutual intensity on the field) decreases to $C_\mu = 0.5$. Therefore,

it can be equated:

$$s_t = \frac{\lambda z}{D} \tag{2.4.1}$$

where D is the target diameter (spot size) at a defined point and z is the displacement. A similar result can be calculated for the longitudinal speckle which is given as:

$$s_l = \lambda \left(\frac{2z}{D}\right)^2 \tag{2.4.2}$$

Both s_l and s_t can be used as a reference of the value of displacement which is acceptable before incurring in a loss of signal as a result of the variance introduced by the speckle.

Several methods have been proposed in order to minimize the effects of speckle in SMI signals. In [108], Norgia et al. proposed a system based in bright speckle tracking (*BST*), in which piezoelectric actuators are used to move the laser spot on a target. Atashkhooei et al. [109] proposed two techniques: the first method consisted in the use of multiple laser diodes pointing at different spots on the target and then finding the best signal for a given time window, and a second method in which an electronically controlled liquid lens (*LL*) changed the spot size, and reduced the amount of speckle whenever the amplitude of the signal became too small. In [110], the later method is used to reduce the speckle effect on a target moving at $200\mu m/s$ over a 20 cm distance. The greatest challenge in this method are the limitations on the LL time response as this limits the method to low velocities. Other methods such as half-fringe locking (*HFL*) can also be used according to [106].

2.4.2 Bandwidth

As described in previous sections, the bandwidth of the SMI sensor is theoretically only limited by the interaction of the electric fields inside the LD cavity. Nevertheless, in practice, this restriction cannot be achieved since most electronic acquisition systems are bandwidth limited. Also, the measurement and detection schemes need to be taken into account.

According to Tucker [83], the bandwidth in a current monitor photodiode placed in the back of the LD is typically limited to $20kHz$, since its purpose is usually to control the average power of the LD. This suggests that the voltage junction approach for detection could allow a higher bandwidth. Alternatively, the use of external photodiodes can easily solve this problem as they can reach in some cases a few MHz [37], despite the compacity of the system is compromised.

Beyond the LD and PD electrical characteristics, the required analogue electronics as well as the bandwidth of the analog to digital converters (*ADC*) employed in the circuitry need be taken into account to evaluate the bandwidth of the sensor. In the first case, it is possible to design high bandwidth sensors, although the complexity of the sensor increases due to the gain bandwidth product. Due to the large amplification requirements of an SMI signal (specially in a voltage junction measurement scheme), typically a single amplification stage is not enough to provide an adequate signal level with a enough bandwidth; therefore, it is usually necessary to include several amplification stages, at the cost of an increase in the noise floor of the signal. Thus, the signal conditioning stage is of central importance in the SMI acquisition process, as it will determine the minimum requirements of the ADC stage. In the later case, the bandwidth is limited by the manufacturers, which in the case of low cost implementations are limited to a few MHz. If a large bandwidth sensor is to be designed, special care should be taken in the selection of an adequate ADC and its connection to the amplification stage. An incorrect design may lead to an increase in the noise of the readout hampering the measurement.

2.4.3 Real time processing

As it often happens with "new technologies", and specially in the field of sensors and transducers, one of the challenges to reach industrial applications is the capacity of implementing measurements in real time. In the case of SMI based methods, two diverging trends have been observed in terms of real time processing.

In the case of LDV methods based on SMI, different authors e.g. [85], have shown ways to perform real time measurements using reliable electronic interfaces, therefore allowing the construction of discrete sensors. An important part of the success of LDV methods can be attributed to the large number of electronic systems presenting the power spectra of a signal that have appeared in recent years, as it has become a general-purpose processing method in different engineering fields.

The case of displacement measurements, nevertheless, has not been as successful as the LDV case regarding a real-time implementation. In part, this is explained by the complexity of creating efficient general purpose methods for fringe detection, in special when low SNR signals are involved. In large SNR conditions the complexity of fringe detection methods can be overlooked as the combination of a simple first order derivative combined with threshold detection is enough. It is usually implemented at low computing cost and even using discrete electronic components (such as micro-controllers). However, the same approach cannot be expected in low SNR signals, where many of the amplitude variations could be misunderstood as discontinuities in the derivative. Moreover, other non-linearities such as the appearance of speckle modulation over the SMI signal also prevent from the selection of a correct threshold in some cases.

Despite the aforementioned complexities have prevented a large development and deployment of SMI displacement sensors for industrial applications, some studies have been performed (e.g. by Zabit [53]) to increase the reliability of SMI techniques for such measurements. Some of those methods rely on using diverse processing algorithms as well as special equipment such as complementary sensors (e.g. external accelerometers [53]) or automated re-focusing systems such as the one described in [110]. The use of these complementary equipment, however, requires higher processing and actuating times which could result in prohibitive time scales for some real time applications. Therefore, it can be argued that SMI displacement methods with "real-time sensing" can currently only be used in systems with slow dynamics.

Further, the complexity of signal processing in fringe detection methods has prevented the development of a large number of embedded systems. Nevertheless, some examples of SMI displacement embedded systems can be found in state of the art literature [111]. This type of embedded systems usually rely on Field Programmable Gate Array systems (*FPGA*) which allow high processing speeds.

2.4.4 Maximum attainable resolution

As mentioned in Sec.2.3.1, the classic resolution for a SMI displacement sensor is estimated as $\lambda/2$. This limit in resolution, however, has been addressed by different research groups in recent years, and has been a driver of the research in the area. due to its central role, the state of the art in SMI measurements with improved resolution is presented in a separate section.

2.5 State of the art: SMI sensors with improved resolution

As just discussed, one of the limits of SMI measurements comes from the attainable resolution in displacement measurements. In order to solve this issue, several attempts to increase the resolution in displacement

measurements have been presented by different authors along the last years. The different proposed methods may be classified into two main groups, according to their requirements of using external equipment (e.g. electro-optical modulators, phase modulators, etc.), and those techniques that are mainly based in signal processing methods (analog or digital). While the former ones often pay a price in regard to the compacity and cost of the setup, the latter ones complicate real-time sensing due to extended processing times.

In the first group, the general idea focuses on generating an external phase shift of the OOP signal which can then be modelled and used as a reference for a displacement in an order lower than $\lambda/2$. The second group focuses on the use of special processing techniques of the acquired SMI signal, which pursue to estimate phase shifts smaller than $\lambda/2$. In many cases this requires a two-stage processing procedure in which the transitions of the SMI signal are first detected, and then the estimation of the phase between transitions takes place. As it will be shown, most of the described methods have increased the resolution in an order of 5 to 10 times by applying a signal processing that takes into account different parameters affecting the SMI signal. Some relevant examples for both grops will be discussed.

2.5.1 Electro-optical modulation

Servagent et al. [112] included for the first time a phase shifting element in a SMI type sensor, extending the successful approach of phase-shifting in conventional interferometry to SMI. The basic setup of this implementation consists of a LD working in low feedback regime $C < 1$ which is then modulated using an electro-optical modulator. By using this method, the total time of flight in the external cavity can be re-defined as:

$$\tau_T = \tau + \tau_m, \tag{2.5.1}$$

where τ_m represents the induced time of flight caused by the electro-optical modulation.

Therefore, for the same amount of motion, it is possible to obtain two signals P_a and P_b, before and after the increase of phase caused by the electro-optic modulator. By looking simultaneously at these signal changes, it should be possible to reach, a $\lambda/4$ resolution [112]. Furthermore, if the modulation is extended multiple times an accuracy of $\lambda/2N$, where N is the number of induced cycles, should be possible.

To prove their method, Servagent used a crystal driven at $580kHz$, and tested the displacement of a piezoelectric stage moving in sinusoidal fashion at $1kHz$ with an amplitude of $2.3\mu m$. By using three phase shifts it was possible to recover a displacement with a resolution of $\lambda/12$. According to the authors, the sensor could be easily implemented in an embedded device such as a DSP allowing an industrial version. It is claimed that $\lambda/20$ resolutions were attained on their last experiments. It is to be said that only micrometric-scale displacements were tested and that some of the errors in the measurements of the instrument could not be attributed to a particular cause. It is also to be noticed that in the case of this sensor, higher data sampling might result in a better accuracy.

2.5.2 Correlation signal processing

Hast et al, proposed in [113] a method to increase the resolution of SMI by means of signal processing. A GaN based LD SMI sensor is depicted with capabilities of reaching the nanometer scale with a standard deviation in the order of $7nm$. According to the study, the correlation can be determined from the abscissa

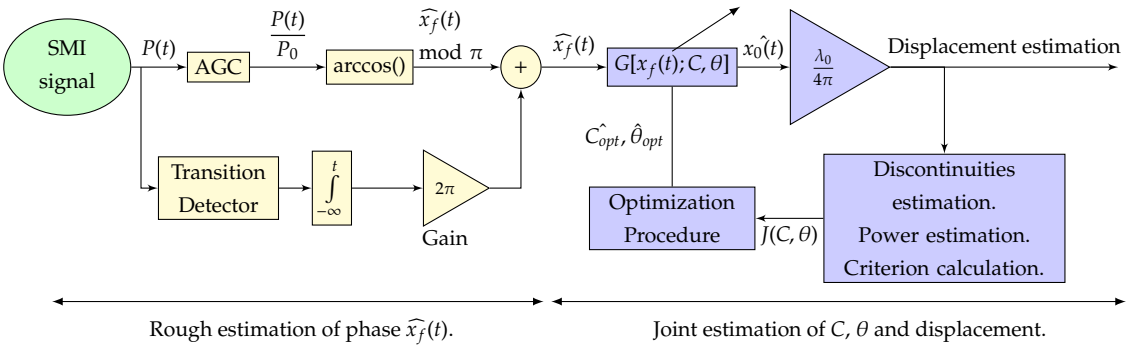

Figure 2.5.1: Signal processing for PUM displacement reconstruction method. In a first step, the transitions of the SMI interferogram are detected and the phase of the signal is roughly estimated using an arcosine function. After the initial estimation, the signal is further processed to estimate the C factor, the phase and the target displacement with enhanced resolution (Adapted from: [114]).

value of the correlation maximum. Therefore, it is possible to establish the correlation formula:

$$c_{xy} = \begin{cases} \dfrac{1}{N-\tau_c} \displaystyle\sum_{k=0}^{N-1} \dfrac{x(k)-\langle x\rangle^*}{\sigma_y^*} \dfrac{y(\tau+k)-\langle y\rangle^*}{\sigma_x^*}, \tau \geq 0 \\ \dfrac{1}{N-\tau_c} \displaystyle\sum_{k=0}^{N-1} \dfrac{y(k)-\langle y\rangle^*}{\sigma_y^*} \dfrac{x(\tau+k)-\langle x\rangle^*}{\sigma_x^*}, \tau \geq 0, \end{cases} \tag{2.5.2}$$

where τ_c is used to describe the lag, τ the time shift, N is the length of the x and y signals, the symbol $\langle\rangle$ is used to represent the mean value and σ the standard deviation. In order to use the relation, it is necessary to calculate values for $\tau_c < \tau_{max}$, where τ_{max} can be detected between the assumed maximum time shift and $N-1$.

In the experiment, an external mechanical stage was used to induce a phase shift in the SMI signal. The phase difference is then analysed using a Pearson correlation algorithm and a cubic spline interpolation allowing measurements up to a range of $110nm$ using a $405nm$ LD, thus allowing a maximum phase shift in the order of $\lambda/4$. In long time measurements (over a few minutes), the performance of the sensor was shown to be compromised as a result of several effects such as the temperature and current stability. It was estimated that the average change in phase due to this effects could introduce an error of $\lambda/8$ in the measurements.

2.5.3 Phase unwrapping method

In 2006, Bès et al. [114] proposed an efficient processing method to increase the resolution of displacement measurements using the phase unwrapping method (*PUM*) in moderate and strong feedback signals.

The principle of the PUM can be divided into two main parts consisting first in a phase estimation based on a classic fringe detection method, followed by an estimation of the phase, displacement and C parameters as shown in Fig.2.5.1. In the first estimation, it is to be noted that in the case of moderate feedback, the OOP signal suffers discontinuities with phase jumps equal to $\Delta\phi = 2\pi C/(1+C)$. Therefore, it is possible to account for a phase change of 2π every time a discontinuity is detected with its corresponding sign.

The second part of the algorithm considers that discontinuities of the signal are less frequent than the discontinuities produced by the non-linear behavior of the OOP as a result of the changes in (C, α and ΔD),

therefore allowing to rewrite the initial phase of the excess phase equation as:

$$x_0(t) = x_F(t) + C\sin(x_f(t) + \theta) \qquad \text{with} \qquad x_{0|F} = \omega_{0|F}\tau(t). \tag{2.5.3}$$

Then, an optimal set of parameters $\hat{C}$ and $\hat{\theta}$ can be used to minimize the discontinuities in $\hat{x_0}$. The parameters $\hat{C}$ and $\hat{\theta}$ are optimized using the criterion:

$$\text{Arg}\min(J(C,\theta)) = \text{Arg}\min\sum_n x_0(n) - x_0(n-1), \tag{2.5.4}$$

where $x_0(n)$ is the discrete version of $x_0(t)$, and $J(C,\theta)$ is the optimization criterion.

In a random displacement simulation, it was reported that for a $13\mu m$ displacement in a moderate regime ($C = 3$), it was possible to reconstruct the displacement with a $90nm$ error. In a practical test using a commercial vibrometer as a reference an error of $40nm$ was attained when both signals were compared. Nevertheless, this error may be biased as, according to the authors [114], the vibrometer measurement error was in the order of $100nm$, therefore requiring a better calibration process. Taking into account the best results of the method, it is possible to say that using the PUM, the resolution on displacement measurements would increase in an order of magnitude in a range between $\lambda/10$ and $\lambda/20$.

While the increase of resolution is significant, it is to be remarked that the use of a minimization algorithm suggests that the computation time required could be quite large and thus not suitable for different types of applications. Other issues might emerge in the minima detection, as saddle points in the minimized function which can affect the performance of the complete algorithm.

In [115] Bernal et al. propose an improved phase unwrapping method (*IPUM*) which, according to the authors, enhances the precision of the reconstructon and the accuracy of the oint estimation calculation, by making some enhancements in the calculation procedure.

2.5.4 Neural network algorithms

Also based on the PUM method, Wei et al. [116] proposed an application using neural networks to provide a solution for the signal filtering in conditions of weak and moderate feedback. For their method, Wei et al., described the use of a single layer of neurons with a sigmoid activation an linear output described by the function:

$$g(x,w) = \sum_{i=1}^{N_c}[w_{N_c+1,f}\tanh\left(\sum_{j=1}^{n} w_{ij}x_j + w_{i0}\right)] + w_{N_c+1,0}, \tag{2.5.5}$$

where x is the input vector and w are $(n+1)N_c + (N_c+1)$ parameters.

For the training sets of the neural network pre-processed median and mean filtered SMI signals were used, until a convergence to a threshold (selected as $0.01RMS$ error) was reached. In the cases of moderate regime, however, larger segmentation was required in order to account for the discontinuity in the function. According to the authors resolutions in the order of $\lambda/20$ to $\lambda/25$ could be achieved by this type of processing.

As in the case presented by Bès, the increase of resolution comes at the expense of a heavy data processing stage. It is to be remarked that in both cases the main limitation for the application of the algorithm is the presence of significant noise (a usual situation in practice), since it would drastically affect the determination of the position of the discontinuity. It is also to be remarked that the method was only tested for displacements with a total motion larger than $\lambda/2$, therefore showing applications only beyond that range.

2.5.5 Nanometer fringes

In 2006 Fei and Zhang [117], described a method to increase the fringe density of a SMI signal tilting a mirror. Their results claim to increase the number of detected fringes in an order of 40 times. Their experimental setup consists of a HeNe laser emitting at 632.8nm which is implemented using two high reflectivity mirrors at a distance of 15 cm. An external mirror with high reflectivity (r_{ME} = 0.993) is placed at a PZT to produce multiple reflections in the cavity. As a result the interference pattern changes increasing the number of stable fringes as the tilt of the external mirror increases with respect to the lasing axis.

According to the authors, the number of attained fringes depends upon the distance to the target, and the angle of incidence. The minimum displacement resolution shown in the article ($\lambda/80$), is retrieved at a distance of 3cm from the target and an angle of incidence θ = 1.2 for a 2μm displacement.

As a result of the high reflectivity, distance, and tilt dependence, however, the method is hard to apply outside of laboratory conditions. Also, the method requires the use of a polarized beam splitter in order to recover the direction of the motion, increasing the complexity and number of elements in the setup.

A similar approach is presented by Jiang et al in [118], where a target is tilted with respect to the emitted beam to produce an amplitude error of $\lambda/47.6$. This approach, nevertheless, is focused in only measuring the amplitude and frequency of the displacement by evaluating a N_{th} order spectral component of a Bessel function. No reconstructions of the displacement are provided in the article.

2.6 Conclusion

In this section, a review of SMI taking into account the historical and technical developments of the method has been presented. As it has been explained, SMI can be described as an inherent characteristic of LDs due to their so-called openness. While in other processes, such as in laser based communication, the LD "openness" may introduce unwanted noise-like behavior, for SMI metrology purposes it is a key factor reducing the amount of energy required to induce the optical power modulation, hence allowing the measurement of changes in the optical path in the presence of targets with low reflectivity.

As it has been shown, SMI is a versatile technique that can be used in different fields of research and technical applications. Typical applications range from displacement measurements up to complex biological sensing. Specially, the technique has shown a large success in the cases where LDV methods are applicable as in that approach the processing methods can be relatively easy to apply using discrete electronic systems used for power spectra measurements. In the later case, biological sensor systems have become a trend of research due to the capability of SMI of measuring noninvasively and to its relatively low cost (typically in the order of a few hundred euros) when compared to more classical (and bulky) interferometric equipment.

Displacement measurements, nevertheless, have not been as successful as their LDV counterparts due to the requirements of complex processing in low SNR conditions. Even taking into account the difficulties associated with displacement measurements, in the last years different teams have shown interest in creating embedded sensors capable of measuring different variables in industrial applications. Because of this interest, different authors have proposed methods for increasing the accuracy and resolution of the technique. The different proposed methods have, however, typically aimed at increasing the measurement resolution of displacements with amplitudes larger than $\lambda/2$ by complex processing techniques. In such cases, the displacement is estimated by accounting the effects of C and α over the total feedback phase. In

the rest of the cases an induced modulation is proposed, allowing to increase the resolution but only for short spans of time.

In this Thesis, a new method along the line of high resolution SMI measurements is presented. Thus, we revised which in our view were the main problems found in practice by the technique, with a focus on its limited resolution. As presented in the introduction, the methods described in the following chapters are specially interested in increasing the resolution of the method to allow, first, measurements for maximum amplitudes below $\lambda/2$ and, second, that would allow small processing times in order to try to set a milestone which, in future developments, would allow real time processing. Several aspects of the technique will be discussed trying to make reference to the possible applications in the coming sections.

3. Differential Self-Mixing Interferometry: Theory and Measurement Schemes

In the previous chapter, the theoretical model of SMI as well as its most common applications were discussed. Displacement reconstruction presents a special case of interest since it allows to obtain information on the amplitude and direction followed by a given target. At the same time, if the oscillation is repetitive, it is also possible to obtain the frequency of the target motion. In some cases, when motion information is used in conjunction with other methods, it is possible to derive diverse mechanical and physical properties of matter in a cost-effective way.

In Sec.2.3.1, the classic fringe counting method (*FCM*) and its limitations in terms of displacement resolution were presented. As it was described, a target motion can be estimated in terms of complete phase cycles of the interferometric function $F(\phi)$. Relating the phase and the displacement of a given target as shown in Eq.(2.3.1), it is possible to establish the resolution of a SMI interferometer as $\Delta d \approx \lambda/2$. Yet, it has to be wondered if this resolution is the ultimate limit for the method, and whether there exist any other methods which could result in a better resolution.

These questions have been addressed by different research groups as shown in Sec.2.5 (e.g. [112, 113]). In the majority of cases, however, the SMI resolution rested far from the limits presented by other classical interferometers, where phase shifting methods can be easily applied. The difference in terms of resolution reduces the possible number of applications for SMI sensors, making the sensor of little use in the new trends in classical industries such as non destructive testing, biomedical research, and the new micro and nano electromechanical systems (MEMS, NEMS) technologies in which nanometer and sub-nanometer resolution are required.

In [119], Donati et al. presented a diagram Fig.3.0.1 comparing the amplitude and vibration frequencies for displacement and vibrometry measurements, thus separating the typical range of applications depending on the amplitude of the motion. According to the diagram, displacement reconstruction is typically measured for amplitudes larger than a few hundred microns and up to some meters. This, however, is not always the case as e.g. in micro-cantilever based sensors the ability to measure the correct profile of the cantilever displacement would allow to have a better comprehension of the surface forces in a particular sample. Therefore, the upcoming of micrometric and nanometric manufacturing has made necessary the appearance of non-contact displacement sensors with measurement ranges not easily attainable.

As described in [119], theoretically, the SMI method is sensitive almost to the quantum state. In the case of simple vibration, where no waveform reconstruction is required, it is theoretically possible to attain measurements with errors in the order of few $fm/\sqrt{Hz}$. In practical applications, however, it is rare to find SMI based vibrometers capable of measuring below a few hundredths of nm, as presented by Giuliani et al. in [120].

While different methods have been described in order to increase the resolution of SMI displacement

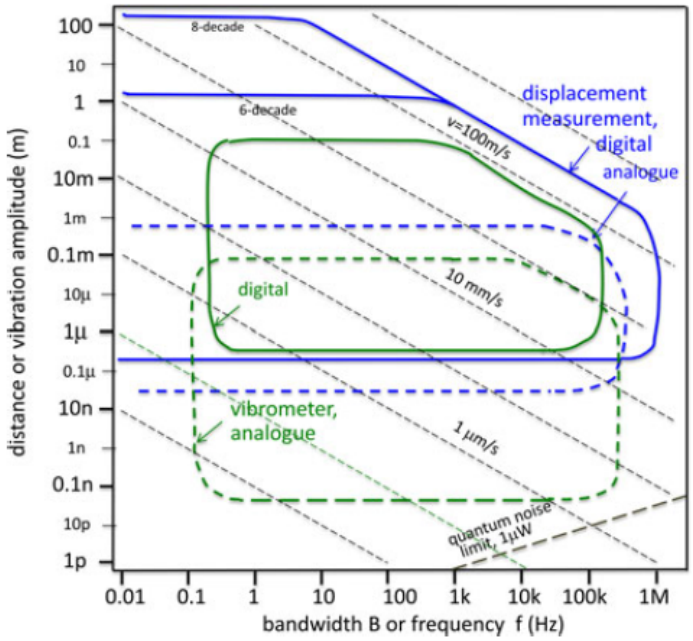

Figure 3.0.1: Wegel's diagram of performance for displacement measuring instruments and vibrometers ([119]). The upper limit is set by dynamic range and the lower limit is set by quantum noise and discretization errors.

measurements (Sec.2.5), most of the examples found on literature limit their application to displacements with a minimum amplitude larger than $\lambda/2$. In most of these cases, the SMI OOP fringes are used as a reference to determine the amount of displacement on the considered target by assuming the phase shift to be a fraction of the $\lambda/2$ relation. Some other methods [113], have allowed measurements under $\lambda/2$ using external modulators to provide a phase reference for the measurement. This method reached a $6nm$ standard deviation using a cubic spline interpolation. While this method is close to the implementation described in this work, it is to be noticed that long time stability due to laser characteristics was considered to be hard to achieve, making the measurement suitable only for small measurement intervals. Similarly in [112], the use of electro optical modulators is proposed allowing to attain resolutions in the order of $\lambda/20$.

As an attempt to solve the mentioned stability issue, differential self-mixing interferometry (*DSMI*) is proposed in this thesis as an alternative method. As it will be shown in the following sections, the described method aims to perform measurements with a resolution in the order of a few nanometers using a simple setup and a simple processing algorithm.

In the first section of this chapter, the method and its limits will be presented in terms of bandwidth and amplitude. A set of different simulations showing the limitations of working at different C factors and noise levels will be presented. Next, in a further section, practical results supporting the DSMI method for displacement measurements with amplitudes smaller than $\lambda/2$ will be presented. In this section, we include some repeatability measurements and observations of other effects. As it will be shown some limitations arise on the practical measurements as a result of the fringe detection algorithm and noise effects, including jitter.

Next, a simplified setup for a single LD DSMI method will be depicted. As it will be shown, the single LD method largely depends upon the type of modulation used for the measurement, as the reference signal can be taken in various ways. Examples on simulation and real measurements will be used to provide a comparative between the different methods. The use of a single LD system simplifies the calculations, as it is

only required to use a single fringe processing algorithm in order to acquire the measurement. Nevertheless, some inaccuracies appear in the measurement, as a result of losing the reference arm of the measurement. Such inaccuracies are also discussed in this section.

Finally, an introduction to a higher bandwidth method with similar resolution will be proposed using electronic modulation. This last scheme, however, will only be covered in its theoretical aspects, which were used as seed to the development of a complete measuring prototype, which expands beyond the scope of the present work and has been subject of a separate PhD work [121]. The chapter closes with a brief summary of the specifications of the proposed method, and how it enhances the existing measurement methods allowing to reach better resolutions and measure smaller amplitudes while still based on the SMI scheme.

3.1 Technical specifications and limitations

As discussed above, different attempts have been proposed to increase the resolution of SMI displacement measuring methods. In most of the cases the increase of resolution has been shown for displacements beyond one fringe ($> \lambda/2$). In this section, DSMI (also known as differential optical feedback interferometry *DOFI*, and as mechanically modulated optical feedback interferometry) is proposed as a method to increase the resolution of SMI displacement measurements with a sensitivity in the nanometric range.

The basic opto-mechanical setup of DSMI is shown in Fig.3.1.1. The setup consists of two laser diodes depicted with the symbol L_x. The subscript x may take the values r and m, which will be used throughout this document to denote the laser diodes acquiring the reference signal and the measurement signal respectively, or the associated OOP signals themselves. These subscripts are also used to depict any variable that depends upon the characteristics of each laser.

The LD used as reference beam (L_r) is oriented pointing towards a piezoelectric mechanical stage which produces a reference motion. The LD used as measurement beam L_m is attached to the previously mentioned piezoelectric stage and its beam is directed to the desired target, as shown in Fig.3.1.1.

The relative distance between L_r and the mechanical stage, and the distance between L_m and the target can be set arbitrarily, although in practice it is adjusted so both signals remain in a feedback level close to $C \simeq 1$, where SNR is optimized and fringe loss conditions do not occur.

Each laser is set in a collimating tube with its corresponding focusing or collimating lens, which adds an additional degree of control in the adjustment of the feedback level of the signals. It is important to notice that both lasers are pointing in opposite directions, hence allowing to obtain the same OOP signal for both lasers for a given reference motion if the target is stationary.

Let us first consider the effects of the OOP signal for each independent standalone laser diode. Let us consider that each laser has been calibrated to work in a regime $C \simeq 1$, thus allowing to obtain a high SNR OOP signal with a sawtooth-like pattern. In the case of L_r it can be easily observed that the resulting OOP is dependent only upon the the displacement of the mechanical stage Δd_r. Similarly, the resulting OOP of L_m can be related to the sum of Δd_r and the target motion ΔD.

3.1.1 Determination of the resolution in amplitude.

The analysis presented in this section estimates the resolution of the DSMI method for OOP signals close to the boundary between weak and moderate feedback regimes ($C \sim 1$). It is desirable to work close to

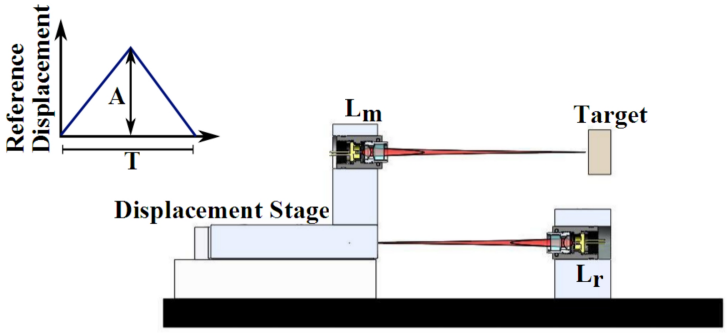

Figure 3.1.1: Differential self-mixing interferometry (DSMI) scheme. A laser diode L_r is pointed towards a linear translation stage which is mechanically coupled to the measurement laser L_m. The measurement laser is focused at a target which moves below $\lambda/2$.

this level of feedback to provide a clear fringe detection, better SNR, and to avoid possible fringe losses as described in [122].

To start the analysis, let us examine a case where the measurement target is static. When the displacement stage starts moving in a linear fashion with a velocity $v(t) = k$, where k is constant, and given two wavelengths λ_r and λ_m of similar magnitude, two SMI OOP signals are produced with constant intervals between observed transitions, proportional to each laser wavelength. Since, $\lambda_r \approx \lambda_m$, the resulting transition intervals Δt_r and Δt_m for the OOP reference and measurement signals respectively have a similar duration (in perfectly identical lasers, they have the same duration), hence enabling a comparison between resulting OOPs as shown in Fig.3.1.2.

In a second instance, the target starts moving by a small quantity with maximum amplitude $\Delta D \ll \lambda/2$ between the transition intervals. Since the movement is smaller than $\lambda_x/2$ within the interval of each transition, the number of transitions in the measurement signal remains constant. Therefore, if a reconstruction using a fringe counting method were to be implemented, the resulting displacement would correspond to that of the reference stage translation. This is clearly observed from the simulated signal shown in Fig.3.1.2d.

As observed in Fig.3.1.2a, the superposition of a small sinusoidal motion with a peak to peak amplitude of $150nm$ and with a frequency 1.5 times larger than that of the reference signal induces a small deformation onto the triangular displacement used as reference, shown in the upper trace in blue. The resulting OOP signals, depicted in Fig.3.1.2b, show an equal value of $C = 0.976$ with its corresponding sharp transition. It is also observed that at the beginning of the measurement one of the transitions might be lost as a result of windowing effects. Nevertheless, if the window were to be expanded, the same number of fringes would be detected. In Fig.3.1.2c, the points at which the transitions in the signals are detected are presented, after applying a consecutive derivative and thresholding step.

The variation in time between consecutive transitions in the measurement OOP compared to the reference OOP can then be related to the target displacement. As presented in Fig.3.1.3, the position at which each fringe appears can be related to a $\lambda/2$ displacement of each of the signals as described in Eq.(2.3.1). By accounting the time differences between the intervals in the reference and the measurement OOP signals, it is possible to measure the amplitude and sense of the target motion with very high resolution.

Thus, for the DSMI method just proposed the attainable resolution in amplitude depends mainly on two factors: the data acquisition features (in terms of frequency rate and amplitude resolution) and the wavelength of each laser.

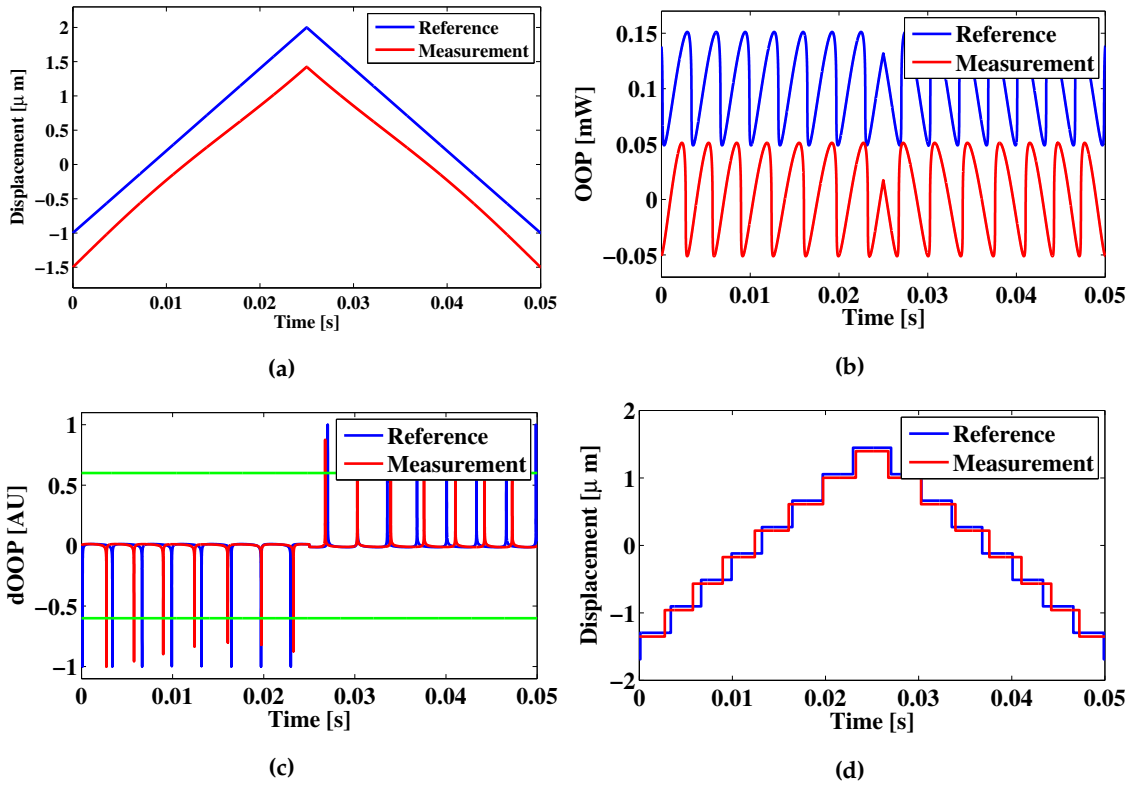

Figure 3.1.2: Example of the effects in the OOP of the reference and measurement signal. (a) Example of a reference triangular motion of amplitude $3\mu m$ and frequency $20Hz$ of the stage (upper trace in blue) and the effect of adding a small sinusoidal motion of amplitude $150nm$ and frequency $30Hz$ onto a simulated target. (b) Simulated SMI OOP signals for the reference triangular motion and the target motion. (c) Detected fringes for the reference and measurement OOP using a derivative and a thresholding algorithm; the threshold is shown by the horizontal green line. (d) Displacement reconstruction of the reference and simulated motion of the target.

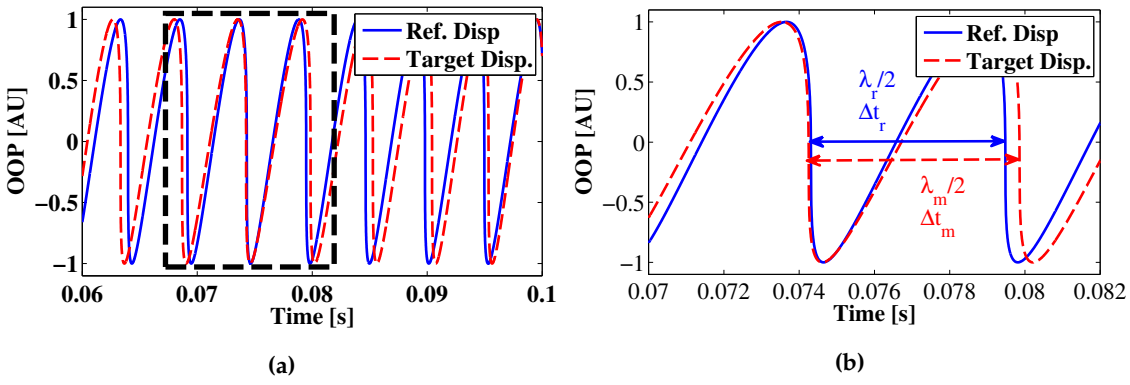

Figure 3.1.3: Detail of the time differences between the two OOP signals subject to the same reference displacement while the target is moving presented in Fig.3.1.2b. A small deviation Δt in time is observed at each fringe occurrence. (a) Representation of a simulated OOP signal of ramp-like displacements for the same wavelength. (b) Zoom of a section of (a) to remark the effects of phase change due to a simulated target motion.

The data acquisition rate (f_a) is dependent upon the acquisition electronics used for the measurement.

It will be shown that a larger f_a value will significantly increase the resolution of the method. Nevertheless, the use of large acquisition frequencies introduces limitations in terms of cost, as the complexity of the acquisition electronics increases, as well as the increased use of memory for offline processes. In terms of the amplitude resolution for the data acquisition, the system amplification needs to be designed carefully regarding both its amplification and its bandwidth. This design issue will be further studied in Sec.3.1.3.

Regarding wavelength, most LD specification sheets describe a nominal wavelength as a function of the injection current and the temperature of the casing. However, other factors such as small variations in the construction of the LD may occur, leading to physical changes in the cavity which may not allow to obtain the same wavelength output at the level of resolution required, even in the case of an equivalent current injection.

Assuming that both wavelengths (λ_r and λ_m) have a small difference between them (which is the usual situation in practice, where a few nm normally separate both wavelengths), a small additional time shift appears in the intervals of the OOP signal, proportional to the difference of both wavelengths, which will appear as a constant bias in the acquisition. To remove this bias, it is possible to use the comparison of the velocity of the reference stage rather than its direct displacement measurement, as described in [123].

In order to derive a value for the resolution of the measurement using the DSMI method let us first consider a static target. If a linear ramp-like motion in a positive direction (as shown in Fig.3.1.4a) is considered as a reference, then, it is possible to write $v_r = v_m$. Therefore, it is possible to define the difference in velocity for the reference and measurement signals as:

$$\Delta v = v_m - v_r = 0, \tag{3.1.1}$$

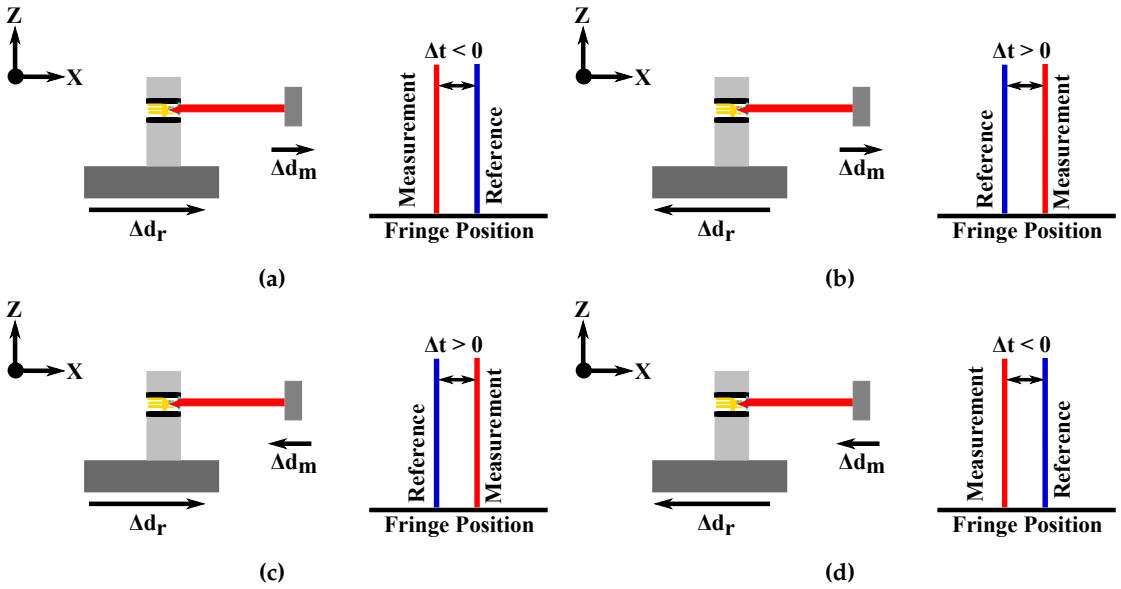

Figure 3.1.4: Representation of the expected fringe position as a result of the motion of the target. For clarity the representation considers that $\lambda_r = \lambda_m$. (a) Positive reference motion during a positive motion of the target. The resulting measurement fringe position presents an increase of the time differential (Δt) with respect to the reference fringe position. (b) Negative reference motion during a positive target motion. The measurement fringe position results in a $\Delta t > 0$. (c) Positive reference motion during a negative target motion. The measurement fringe position results in a $\Delta t < 0$. (d) Negative reference motion during a negative target motion. The measurement fringe position results in a $\Delta t < 0$.

which can also be expressed as a function of the wavelength and time intervals between consecutive OOP fringes as:

$$\Delta v = \frac{\lambda_m}{2\Delta t_{m0}} - \frac{\lambda_r}{2\Delta t_r} = 0, \tag{3.1.2}$$

where Δt_{m0} is the time between fringes on the measurement signal when the target is static, Δt_r the time difference between fringes on the reference OOP signal, and Δv is the difference in velocity between the reference and measurement signal.

To relate the measurement and reference signal time intervals for the effects of different wavelengths, it is necessary to quantify the effects of the wavelength variation in terms of Δt_r. To do so, let us define:

$$\Delta\lambda = \lambda_m - \lambda_r, \tag{3.1.3}$$

where $\Delta\lambda$ represents the variation of wavelength between the reference and measurement LDs. Substituting Eq.(3.1.3) in Eq.(3.1.2), one gets:

$$\Delta t_{m0} = \Delta t_r \left(1 + \frac{\Delta\lambda}{\lambda_r}\right), \tag{3.1.4}$$

thus relating the original fringe interval in the measurement OOP signal to the time interval in the reference OOP signal. As observed from Eq.(3.1.4) an increase in λ_m with respect to λ_r results also in an increase of the time interval between fringe positions in the measurement signal. Conversely, a decrease on λ_m relative to λ_r would decrease the duration of Δt_{m0}.

Now, let us consider a small displacement of the target in a quantity smaller than $\lambda/2$ in a positive direction as depicted in Fig3.1.4a. As a result, a positive small time differential will appear in the measurement OOP signal, with value

$$\Delta t = \Delta t_m - \Delta t_{m0}, \tag{3.1.5}$$

leading to:

$$\Delta v = \frac{\lambda_m}{2\Delta t_m} - \frac{\lambda_r}{2\Delta t_r}, \tag{3.1.6}$$

where Δt_m corresponds to the total time interval between two consecutive fringes of the measurement OOP signal. From Eq.(3.1.5) it is easily observed that the resulting Δt_m contains information of the velocity change caused by the target displacement.

By replacing Eq.(3.1.4) and Eq.(3.1.5) in Eq.(3.1.6) it is possible to derive:

$$\Delta v = -\frac{\lambda_r}{2} \frac{\Delta t}{\Delta t_r^2 \left(1 + \frac{\Delta\lambda}{\lambda_r}\right) + \Delta t \Delta t_r}, \tag{3.1.7}$$

where it is observed that the difference in the instantaneous velocity depends on the time difference between two consecutive detected fringes on the reference signal Δt_r and the wavelength of the reference LD.

It is possible to arrive to a similar equation that depends on the wavelength of the measurement laser λ_m, so the original fringe time for a static target in the measurement signal Δt_{m0} would be:

$$\Delta v = -\frac{\lambda_m}{2} \frac{\Delta t}{\Delta t_{m0}^2 + \Delta t \Delta t_{m0}}, . \tag{3.1.8}$$

In order to obtain the target displacement from Δv it is necessary to integrate the expression along the reference time interval which can be written as:

$$\Delta v = \frac{\delta \Delta D}{\delta \Delta t_{interval}}, \tag{3.1.9}$$

$$\int \delta \Delta D = \Delta v \int \delta \Delta t_{interval}, \tag{3.1.10}$$

where $\Delta t_{interval}$ corresponds to the time interval between two consecutive fringes in the measurement signal.

After substituting Eq.(3.1.7) in Eq.(3.1.10) and considering that $\Delta t_{interval} = \Delta t_r$ it is possible to arrive to :

$$\Delta D = -\frac{\lambda_r}{2}\frac{\Delta t}{\Delta t_r(1+\frac{\Delta\lambda}{\lambda_r})+\Delta t}, \tag{3.1.11}$$

where the displacement of the target ΔD is a function of the time variation Δt, the reference wavelength, λ_r, and the time interval between consecutive fringes in the reference signal Δt_r. It is possible to arrive to a similar expression by integrating Eq.(3.1.8) in the interval Δt_{m0}.

It should be noted that the equation derived above is sensitive to the direction of the reference motion. In the case of a negative reference motion, a sign inversion of the Eq.(3.1.7) and Eq.(3.1.11) has to be performed to keep the same sense of direction during the calculation. This can also be observed in Fig.3.1.4 where the dependence on the sign of Δt is depicted as an effect of the reference motion.

Looking at Eq.(3.1.11) it is observed that it may be simplified under a set of conditions. If it is considered that the wavelength difference is within $\Delta\lambda \leq 0.1\lambda_r$, which is attainable by most near infrared LDs, and also considering that $\Delta t \ll \Delta t_r$, Eq.(3.1.11) can be written as:

$$\Delta D \approx -\frac{\lambda_r}{2}\frac{\Delta t}{\Delta t_r}, \tag{3.1.12}$$

which, considering e.g. an acquisition rate $f(a) = 100kS/s$ (so the minimum theoretically detectable $\Delta t = 1\times10^{-5}s$), $\lambda_r = 785nm$, and a reference velocity of $20\mu m/s$ which yields $\Delta t_r = 1.9625\times10^{-2}s$, the theoretical resolution obtained is in the order of 2Å. In Fig.3.1.5 the effects and response of the multiplicative factor $\Delta t/(\Delta t_r(1+\Delta\lambda/\lambda_r)+\Delta)$ are plotted for a normalized interval in which $\Delta t_r = 1$ for a Δt in the closed interval $[-0.999, 0.999]$. It is observed how the resulting multiplier behaves asymptotically for negative values of Δt as it approaches to the value of Δt_r. Also, it is observed that for positive values a horizontal asymptote exist where the ratio $\Delta t/(\Delta t_r(1+\Delta\lambda/\lambda_r)+\Delta) \to 0.5$ for $\Delta t \to \infty$.

Hence, the theoretical minimal resolution of the method is limited by the minimum sampling time of the acquisition device ($\Delta t_{min} = 1/f_a$), and by the rate of change between transitions on the reference OOP (sampling frequency f_s). As a result of this dependence, it is necessary to keep a compromise between the sampling rate f_a and the attainable resolution of ΔD as, as mentioned, the use of higher acquisition rates would increase drastically the complexity and cost of the acquisition electronics.

As seen from Eq.(3.1.7) and Eq.(3.1.11), the value of the wavelength plays a central role in the DSMI measurement scheme. From Fig.3.1.5c it is observed that, as the value of $\Delta\lambda$ increases, the linearity of the curve around 0 also increases. Therefore, in case there exists some wavelength difference between the two LDs used in the measurement (which is very likely to occur in practice), the laser diode with higher wavelength should be preferred for the measurement position L_m. Large deviations in wavelength, however, should be avoided, as the number of fringes in the reference and measurement signals would start to be significantly different even at small displacements, resulting in an impossibility to provide the necessary comparison points.

The deviations or instabilities in the wavelength reference and measurement values during the capturing process introduce errors in the estimation of velocity and displacement, hence reducing the resolution and repeatability of the method. Even when the equation introduces a correction factor for the difference in wavelength between both lasers, it does not provide any correction for the dynamic variability which each wavelength may suffer due to time dependent effects such as temperature and/or current changes. Thus, it is necessary to use a robust electronic driver able to minimize the transient effects on the wavelength to avoid inaccuracies, or to assume deviations from this theoretical accuracy in practice.

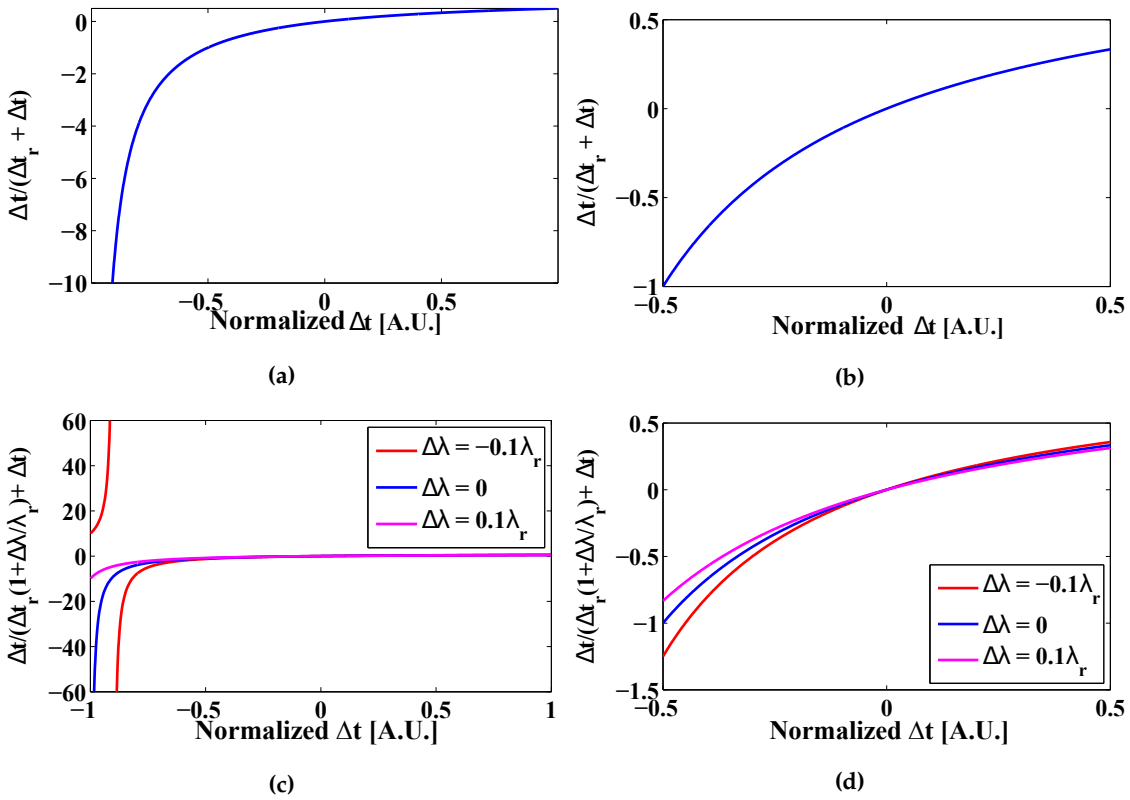

Figure 3.1.5: Example of the proportional multiplier as a result of a change of $\Delta t = 0.001\Delta t_r$ (a) in the interval $[-0.9, 0.9]$, and (b) in the interval $[-0.5, 0.5]$. The effect of using a different wavelength for the reference and the measurement LDs are plotted for the interval $[-0.9, 0.9]$ in (c) and $[-0.5, 0.5]$ in (d) in a range for $\Delta\lambda = \pm 0.1\lambda_r$. The Y-axis of all presents data corresponding to dimensionless units. The X-axis presents normalized units of time where Δt is a fraction of Δt_r.

3.1.2 Determination of the frequency limit

Regarding the sampling frequency f_s, it is important to remark that the sampling rate of DSMI is different from the acquisition rate f_a used to capture each OFI signal. In DSMI, the sampling rate is defined as the time difference between the appearance of two linked transitions in the reference OFI signal. Therefore, in order to generate a constant sampling frequency the ideal reference motion should be ramp-like. Using a ramp motion for the reference modulation allows to obtain OOP signals with fringes of the same sign throughout the acquisition process, and at the same time it prevents the appearance of the unknown phase shifts which appear wherever a change of sign (due to a change in the sense of motion) happens.

In practice, however, using pure ramp-like displacements may not be applied in many cases, since it would require large mechanical setups with inherent problems in terms of linearity and cost. At the same time, large displacements involve other undesired optical phenomena, such as speckle, which might appear on the signal increasing the complexity of the signal processing.

To come across the limitations of the ramp-like displacement just described, it is substituted in practice by a periodic triangular motion of limited amplitude (in the case of the setups discussed below the amplitude of the reference motion was set in the range from 25 to 38μm). The use of this range of amplitudes also prevents the appearance of speckle effects on the measurement signal, thus keeping a simple, well defined signal ready for processing. Taking into account that each transition in each of the signals happens whenever a $\lambda/2$ displacement is reached, as observed in Fig.3.1.3b, it is possible to calculate the sampling frequency for

DSMI (f_s) [123].

To do so, let's consider first the reference velocity of the mechanical translation stage v_r. From the velocity application described in Sec.2.3.2 it is possible to write:

$$f_s = \frac{2nv_r}{\lambda_r}\cos\theta, \tag{3.1.13}$$

where the detected Doppler frequency corresponds to the rate of fringe appearance for a given reference motion v_r, θ is the angle formed between the motion axis and the laser beam emission axis, and n is the refractive index. Since typically the measurement is to be performed in air ($n = 1.0002751 \approx 1$) and in a direction along the same axis followed by the reference motion ($\theta = 0$), it is possible to simplify Eq.(3.1.13) into:

$$f_s = 2\frac{v_r}{\lambda_r}. \tag{3.1.14}$$

Similarly, it is possible to calculate the resulting frequency as a function of the amplitude A of a symmetric triangular displacement of period T:

$$f_s = \frac{2}{\lambda_r}\frac{2A}{T} = 4A\frac{f_r}{\lambda_r}. \tag{3.1.15}$$

This representation is more suitable to be used in the cases where the amplitude and frequency of the triangular motion are known instead of the reference velocity.

It is however not possible to provide theoretical expressions for the sampling frequency in other types of modulation, as the expected sampling rate would depend upon the type of motion, e.g. in the case of a reference sinusoidal motion, the sampling frequency will decay towards 0 around the lobes (maxima and minima) of the driving motion. It is to be observed, however, that the absolute limits on the sampling rate are given by the electronic interface and the minimum and maximum attainable velocities of the reference motion actuator. For the case of the actuators used in this thesis, their reference technical sheets can be consulted in annex B. In the case of the 38μm translation stage, in the case where the full amplitude ramp is produced, e.g., it was observed that a maximum attainable frequency before loosing linearity was in the order of 10Hz (760$\mu m/s$). This leads to a maximum sampling frequency (when using $\lambda = 785nm$) of 1936.30Hz. The minimum velocity is largely affected by the quantization step provided by the available signal generator. With the equipment used along this Thesis, it was detected that using reference frequencies below 0.5Hz (38&mum/s) produced artifacts in the measurement as a result of a step like behavior of the signal generator. Considering this as a minimum velocity, the lowest sampling frequency attainable is in the order of 96.81Hz. It is to be noted that issues with the minimum velocity relative to quantization can be overcome by applying a low pass filtering stage at the output of the used signal generator or by increasing the resolution of the signal generator. In the described experimental conditions, such sampling frequencies would allow to measure a maximum velocity change in the order of 759.8$\mu m/s$ and a minimum velocity change of 37.99$\mu m/s$.

3.1.3 Signal acquisition

Two electronic schemes are suitable for the acquisition of the OOP signal as described by Donati in [32]. Both methods can also be used for the DSMI technique with its corresponding advantages and disadvantages. In the case of this Thesis, the study is focused on the PD acquisition approach because of its higher sensitivity when compared to the junction voltage approach. Small changes might be applied to the described scheme to use a junction voltage approach in the cases where the LD package does not include a PD, or if it is deemed as necessary for the proposed application.

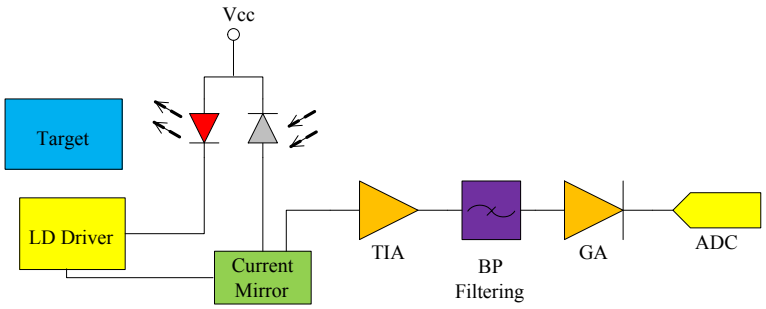

Figure 3.1.6: Block diagram of the signal acquisition on a DSMI setup. The optical feedback is recovered using a PD monitoring scheme. The current induced in the PD is sent to a current mirror which then sends the current to the LD driver and to a transimpedance amplifier (*TIA*). After a band pass filtering stage the OOP signal is amplified using a voltage gain amplifier stage (*GA*) and finally is recovered for post processing using a suitable analog to digital converter device.

One limitation of this type of approach is that typically the intended application of the PD as a control element for the LD is no longer used. As a result, the LD OOP and the corresponding wavelength may significantly vary along the measurement causing inaccuracies on the measurement. Typically, this might be overlooked in the case of classic displacement measurements, in which a resolution of $\lambda/2$ is sufficiently large when compared to the nanometric variation suffered by the LD emission. In the case of DSMI and other measurements targeting nm-scale resolutions, it is required to include a tighter control on the emitted beam, as a variation in wavelength along the measurement will introduce systematic errors in the measurement.

Therefore in some cases, specially when high resolution measurements in the nanometric or sub-nanometric scale are required, it is necessary either to use an external sensor capable of providing feedback on the wavelength to the laser driver to stabilize the wavelength of emission, resulting in an increase of the method's complexity, size, and cost; or to reproduce the PD signal to reuse it as feedback for the laser driver while it is still extracting the PD signal as output for the measurement.

Considering the measurements to be performed were of a frequency low enough, and taking into account the description of SMI noise sources for both schemes [32], it was decided that reproducing the PD signal was a better option. Thus, an electronic board with the basic electronic scheme represented on Fig.3.1.6 was assembled.

The board can be divided into the laser driver and the signal conditioning stage. In order to connect both stages, a custom made current mirror using a NPN/NPN matched double transistor BCM61b [124] and a PNP/PNP matched double transistor BCM62b [125] was designed and implemented on purpose for the application.

The driver is composed of a laser driver iC-WJZ [126] which receives feedback from the PD signal after being duplicated at a current mirror. According to the manufacturer this driver allows adjustment of the laser power, includes a soft power on start and provides protection with temperature and under voltage. A variable resistor of $10k\Omega$ is used to provide any necessary regulation of the output power. It is also to be noticed that one of the outputs of the current mirror is connected to the iC-WJZ to provide a sense of the laser diode average OOP. By controlling the output power at low values, it is expected that the laser behaves in a more stable fashion, resulting in a quasi constant wavelength value.

A second "copy" of the PD current is fed into a passive transimpedance amplifier (TIA) composed by a $2.2k\Omega$ resistor. In other designs, an active stage has been added using a LMH6601MG. Other amplifiers

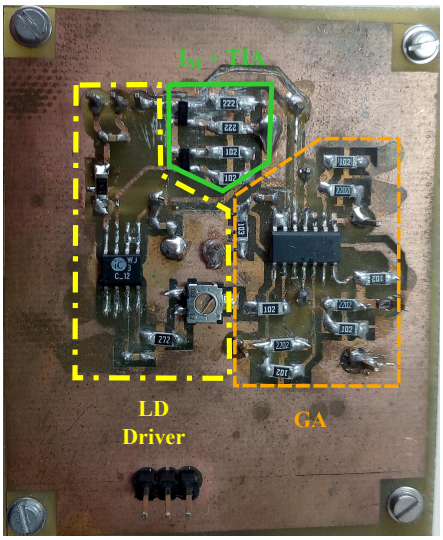

Figure 3.1.7: Example of a LD driver and OOP signal conditioning card. The card has been divided into three parts according to its operation. Inside the dot-dashed yellow section the LD driver iC-WJZ and required circuitry is presented. Inside the solid green area, the current mirror (I_M) as well as the passive TIA (uppermost resistor in the area) are shown. Finally the amplification and filtering circuitry is represented inside the dashed orange area.

may be used for this purpose as long as the bandwidth fits with the desired requirements of the instrument. It is recommended that the TIA stage has the highest possible gain in order to reduce added noise due to the subsequent consecutive amplification stages. It is to be noticed, however, that at this stage the OOP signal is several orders of magnitude smaller than the current caused by the average power of the laser. Therefore, in case of an active TIA stage, it is necessary to keep in mind the amplification limits to prevent effects related to the saturation of the amplifiers.

After the TIA stage, the signal is filtered using a high pass Butterworth filter with a cut-off frequency of $15.91Hz$ applied on a low noise operational amplifier OPA4228 recovering only the AC component of the OOP. Apart from the low noise features (lower than $90nV_{pp}$, the amplifier is selected due to its gain bandwidth product ($33MHz$), and its large open loop gain ($160dB$) [127], allowing to modify the circuit as required for different scenarios. In this stage the amplification is limited to 23 ($27.2dB$). After this stage, the signal is further conditioned using two gain stages (GA) of gain 23 ($27.2dB$) and 3.2 ($10.1dB$) thus resulting in a total amplification of 1693 ($64dB$) after the transimpedance stage. After each amplification stage an oscilloscope probe output pin is placed to provide the user a suitable acquisition test point according to the OOP signal of a given target as observed in Fig.3.1.7. After the last amplifier output, an anti-aliasing filter may be placed to reduce aliasing effects in the analog to digital signal conversion. An example of a simulation with the expected amplification outputs for a sawtooth like signal with a current amplitude of $5\mu A_{pp}$ and frequency $f_{sim} = 5kHz$ imposed over a $100\mu A$ continuous wave is presented in Fig.3.1.8.

While it is arguable that the total amplification can be applied in a single stage, thus reducing noise on the output, this would also diminish the attainable bandwidth of the circuit, and in some cases cause saturation of the amplifier. A simulation of the bandwidth achieved by the given simulated circuit is presented in Fig.3.1.9. In this case, the amplification circuit was designed with a maximum bandwidth of $\approx 1MHz$ to take advantage of the phase stable region of the OPA4228 amplifier. As it can be observed, an overshoot of the amplification is present around the region of $1MHz$, therefore limiting the application range to an order of around $600KHz$. Around this value, according to [127], the phase should also be stable. It is to be remarked

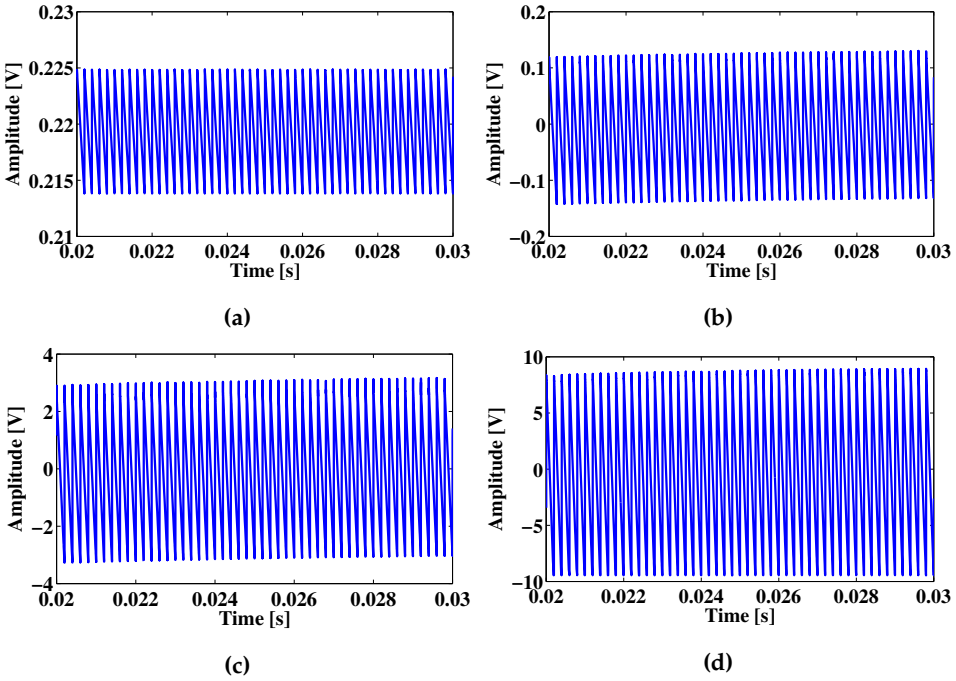

Figure 3.1.8: Simulation example of resulting amplification for the different stages in the proposed acquisition card. (a) Result of the simulation after the passive TIA stage. (b) Expected output for the simulated signal after high pass filtering and first amplification stage. (c) Output after second gain stage. (d) Total amplification of the proposed electronic card.

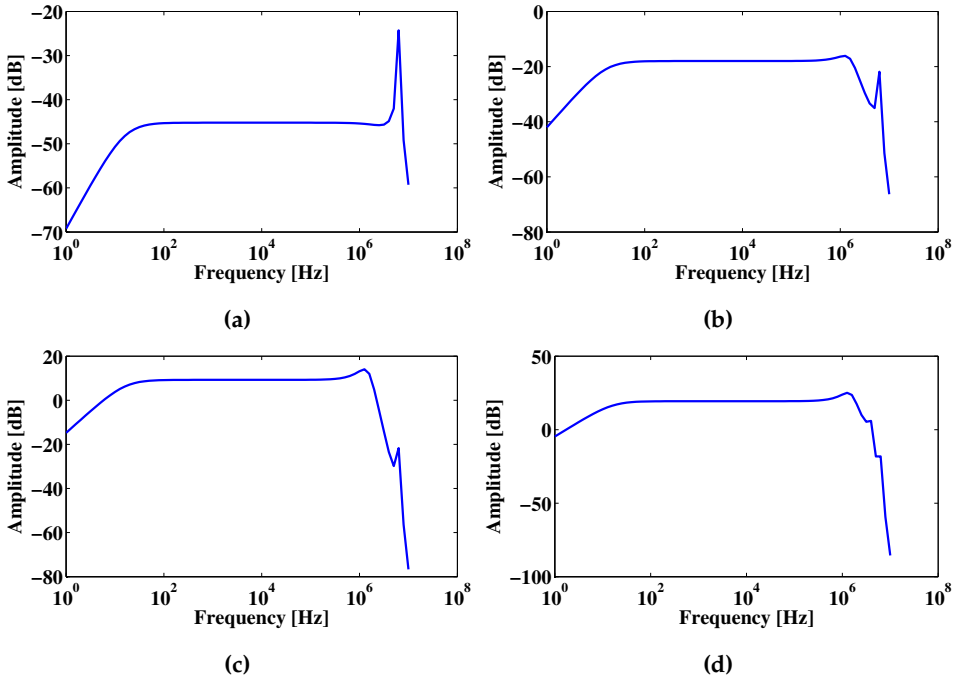

Figure 3.1.9: Simulation results of the proposed electronic acquisition card bandwidth after each amplification stage. (a) After the TIA stage. (b) After high pass filtering. (c) After the second amplification stage. (d) At the output of the electronic card.

that the proposed design was developed for a multiporpuse application and not only for the requirements of this Thesis. In the case of most of the applications covered along this Thesis, a single amplification stage would suffice to provide the necessary bandwidth.

3.2 The double diode laser method

In this section simulations and measurements based on DSMI using a configuration based on two laser diodes are presented. In the section some of the possible effects which may hinder the measurement (e.g. differences in wavelength, initial phase, and C factor) are analyzed.

The double diode laser method has been described in the previous section of the chapter and an example of the expected setup has been presented in Fig.3.1.1. Other similar alternatives of the setup would be to attach L_r to the actuator generating the reference motion while pointing it at a stationary surface. All studied cases have focused in using the same direction of displacement for the reference motion in order to obtain equivalent transitions in both the reference and measurement signals. In the case of using opposite directions for the reference motion, such variation needs be taken into account to correctly assess the direction of the displacement of the target displacement.

3.2.1 Simulation

To study theoretically the signal reconstruction capabilities of the proposed method, a simulation under standard experimental conditions is run. The values of the different parameters used in the simulation can be found in Tab.3.2.1.

The OOP signals of both the reference and measurement signal are calculated using a Schröeder-based algorithm to enhance the velocity of the convergence in the calculation of the feedback phase [128,129]. The Schröeder method in general can be described as a variation of Newton-Rhapson algorithms which allows to calculate the solution of a given equation (by zero crossing) using the first and second order derivatives

Parameter	Symbol	Value	Units
Reference wavelength	λ_r	785.0	nm
Measurement wavelength	λ_m	785.0	nm
Reference motion amplitude	A_r	38.0	μm
Reference velocity	v_r	76.0	$\mu m/s$
Sampling frequency	f_a	250.0	kHz
Simulated time	t	$[0, 0.5]$	s
Target displacement peak to peak amplitude 1	A_{pp1}	10.0	nm
Target displacement peak to peak amplitude 2	A_{pp2}	4.0	nm
Target displacement peak to peak amplitude 3	A_{pp3}	2.0	nm
Target frequency 1	f_1	5.0	Hz
Target frequency 2	f_2	20.0	Hz
Target frequency 3	f_3	2.5	Hz
Distance from measurement laser to the target	L_m	9.9	cm
Distance from reference laser to reference stage	L_r	9.9	cm
Feedback factor in the reference laser	C_r	9.7×10^{-1}	$A.U.$
Feedback factor in the measurement laser	C_m	9.7×10^{-1}	$A.U.$

Table 3.2.1: List of parameters used in the simulation of a DSMI measurement for a displacement of the target of the form $\Delta D = A_1 \sin(2\pi f_1 t) - A_2 \sin(2 * \pi f_2 t + \pi/5) - A_3 \sin(2 * \pi f_3 t + \pi/3)$.

of the considered equation. The main limitation of the method lies in the requirement of properly choosing the search intervals, since in the case of multiple solutions the method can fail to converge. For the SMI case, this implies that in the moderate and strong regimes, when $C > 1$, search intervals must be selected. An example on a method to select such intervals can be found in [60,130] where the effects of C in discontinuities of the feedback phase is discussed in detail. The simulations presented in these section will focus solely on signals with $C < 1$, therefore not requiring a selection of the intervals for the search of zeroes which converge.

The first simulation presented considers a ramp-like reference motion with a peak-to-peak amplitude of $38\mu m$, which matches the capabilities of the actuator to be used on the experimental setup discussed in Sec.3.4. Next, a target motion with the form:

$$\Delta D_{ref} = A_1 \sin 2\pi f_1 t - A_2 \sin(2 * \pi f_2 t + \pi/5) - A_3 \sin(2 * \pi f_3 t + \pi/3), \tag{3.2.1}$$

where $A_x = A_{ppx}/2$ are the amplitudes of each sinusoidal signal, f_x its correspondent frequency, and x the number of each of the sinusoidal signals used in the simulated target displacement. A complex displacement shape was chosen in order to show the capabilities of the method. The reference and measurement signals are then analyzed as described in the flow chart presented in Fig.3.2.1.

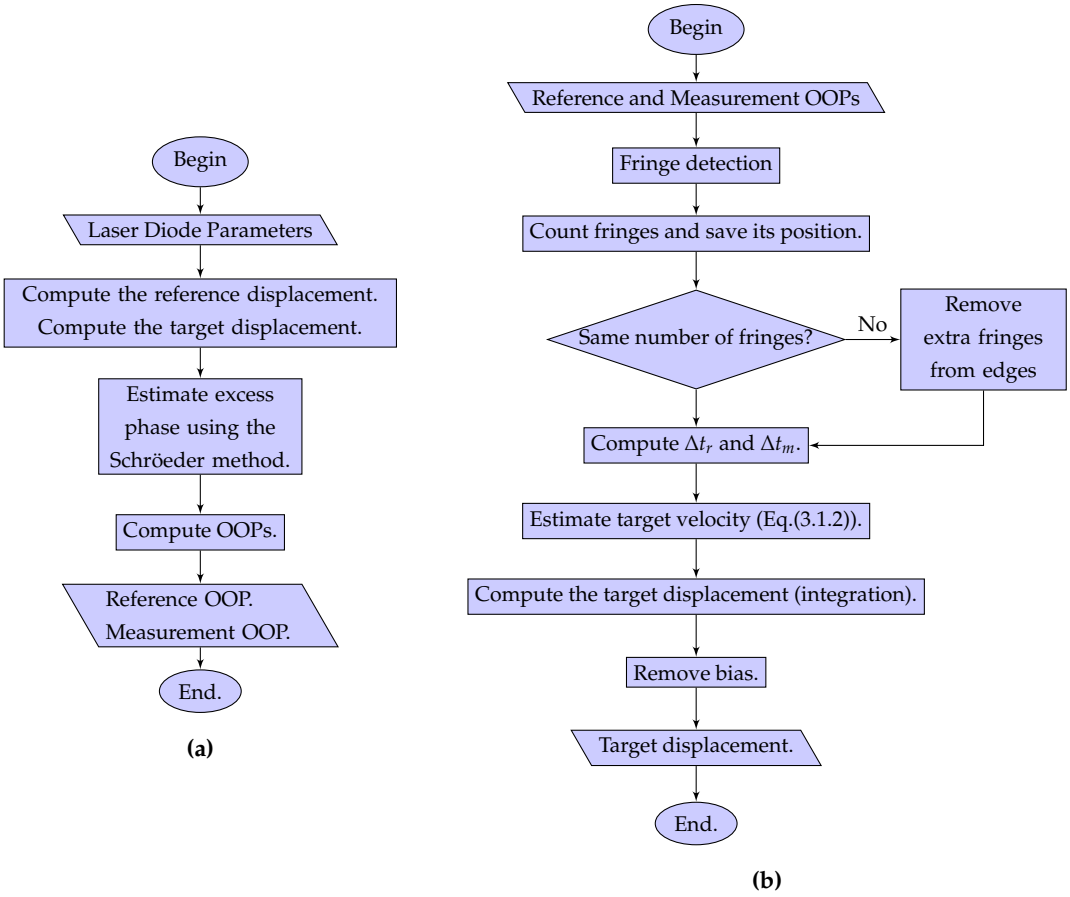

Figure 3.2.1: Flow chart used in the simulation algorithms for obtaining SMI and DSMI simulated measurements. (a) Basic flow chart used to simulate OOP signals; For the cases of DSMI simulations, the respective OOPs are generated in a 2D array. (b) Flow chart correspondent to the DSMI signal processing; after the initial fringe detection process, the velocity between fringes is detected and the target displacement can be reconstructed.

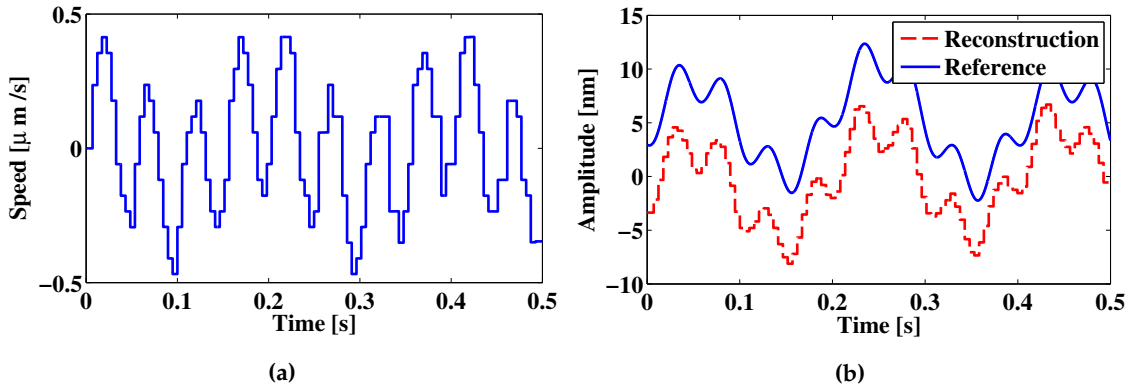

Figure 3.2.2: Results of a typical simulation of a DSMI measurement. (a) Detected velocity on the target; the points of change on the target velocity correspond to the detected position of the fringes in the reference signal. (b) Detected target displacement in dashed red and target displacement in solid blue; a constant $5nm$ offset has been included between both signals for ease of visualization.

The results of the simulation of the DSMI experiment can be observed in Fig.3.2.2 where the target displacement is presented in solid blue and the reconstructed displacement in dashed red. A constant bias of $5nm$ has been introduced for improved visualization. It may be observed how the displacement reconstructed using the DSMI method follows accurately the original displacement of the target. Some errors, however, may be detected in some sections of the measurement. After quantification (defining $Err = \widehat{\Delta D} - \Delta D_{ref}$, where $\widehat{\Delta D}$ corresponds to the displacement estimation using DSMI and ΔD_{ref} is the motion of the target), the maximum detected error magnitude had a value of $Err_{max} = 2.97nm$, within an interval between $[-2.56, 2.97]nm$ and mean value of $\overline{E_r} = 0.92nm$, with a RMS value of $Err_{RMS} = 1.08nm$ and standard deviation of $\sigma_{Err} = 1.08nm$. Similar maximum errors (in a range from 1 to $5nm$) were found for simulations with other amplitudes. The maximum error appears to be related with the maximum amplitude showing a magnitude in the order of 2 to 3% relative to the maximum amplitude.

Since the total amplitude of the target displacement is large in comparison with the displacement between consecutive transitions (measurement points), it is possible to apply a linear interpolation as shown in Fig.3.2.3. As a result of the interpolation, the error reduces to a maximum value of $Err_{Max} = 1.83nm$ within an interval between $[-1.21, 1.83]nm$, with a mean of $\overline{Err} = 3.20 \times 10^{-15}nm$, an RMS of $Err_{RMS} = 0.82nm$ and a standard deviation of $\sigma_{Err} = 0.82nm$. It should also be observed that a linear drift is present in the resulting reconstruction which can be attributed to errors along the integration step and different nonlinearities (e.g. the sampling quantization step) that are not accounted for in the formulation of DSMI here presented.

If a linear fitting is introduced in the reconstructed signal for oscillatory motions, it is possible to reduce the error in the reconstructed signal numerically even further, as presented in Fig.3.2.3, which shows a mean value of $\overline{Err} = 6.10 \times 10^{-15}$ within an interval of $[-1.09, 1.29]nm$, with a standard deviation of $\sigma_{err} = 0.56nm$ and a RMS of $Err_{RMS} = 0.56nm$.

It is to be noticed that the error varies as a function of the ratio of velocities between the target and the reference motion. This can be seen in the error bars plotted in Fig.3.2.4a. To have a better understanding of the error due to the ratio of velocities v_m/vr, a set of simulations in which the target is displaced with constant velocity are performed. The reference velocity of the simulation, as in the previous simulation, is set to $v_r = 76\mu m/s$. The errors in the displacement reconstruction as a function of the ratio of velocities are presented in Fig.3.2.4b and in Fig.3.2.5.

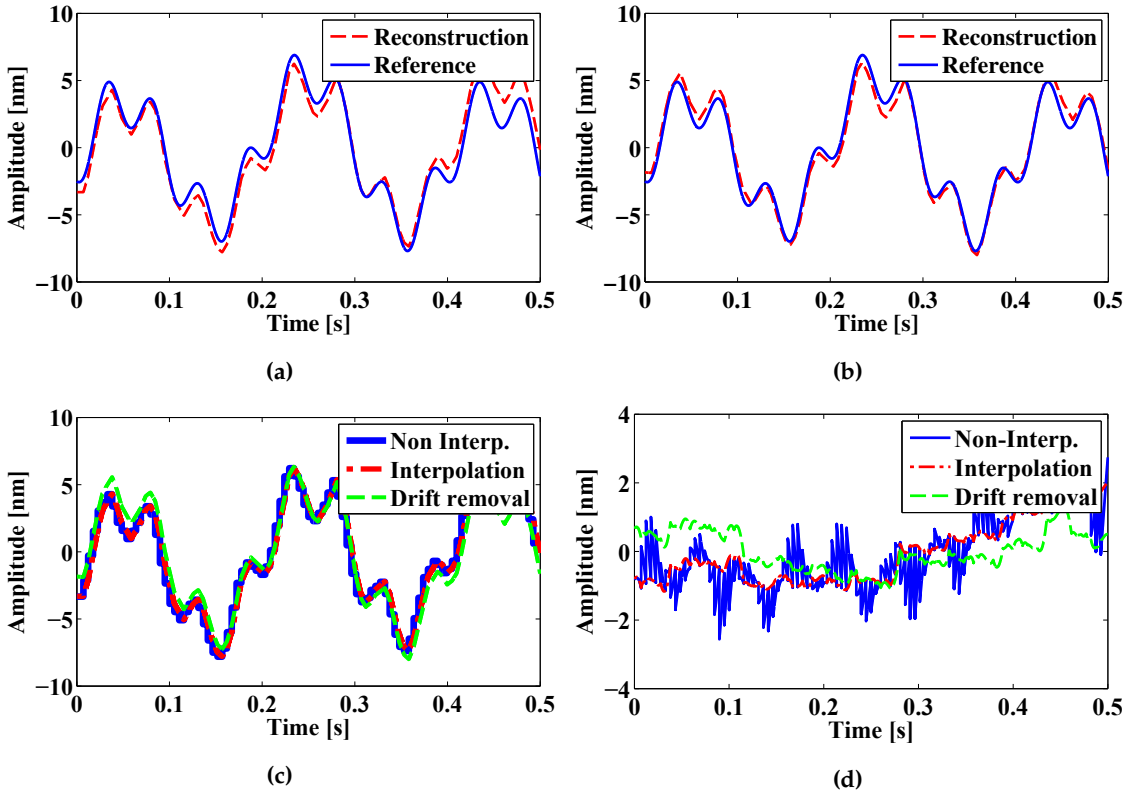

Figure 3.2.3: Results of a DSMI simulation after interpolation and drift removal and resulting errors. (a) Reconstruction of the target displacement using a linear interpolation between the DSMI measurement points. (b) Reconstruction of the target displacement after applying a linear fitting to remove drift in the measurement. (c) Comparison between reconstructions obtained after each signal processing, non interpolated (solid blue line), with a linear interpolation (dotted red line), and with a linear fit to remove drift effects (dashed green line). (d) Comparison of the errors obtained for the simulated target displacement, showing errors in the single nm range.

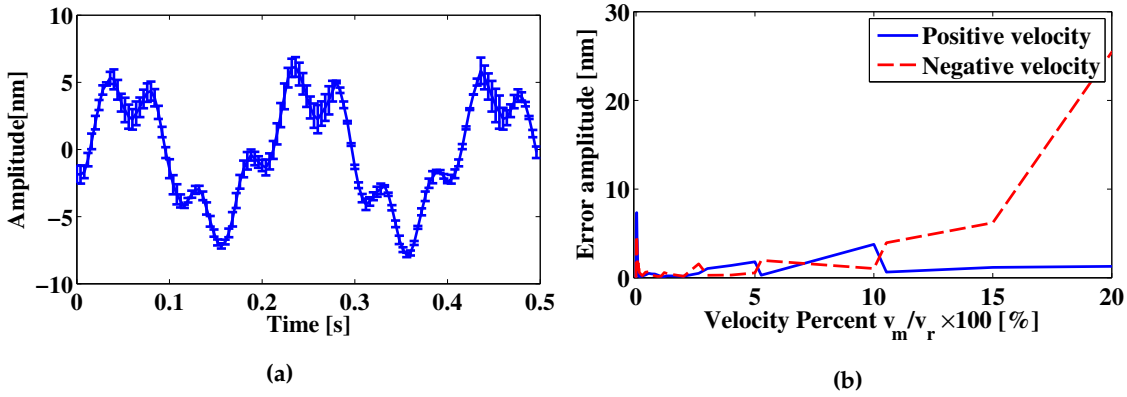

Figure 3.2.4: Measurement error introduced by the difference in velocities between the reference and target motion. (a) Example of error bars for the simulated displacement; the amplitude of the bar varies depending on the target velocity in the region between consecutive fringes. (b) Expected standard deviation of the error as a ratio of the target velocity in comparison to the reference velocity ($v_m/v_r \times 100$).

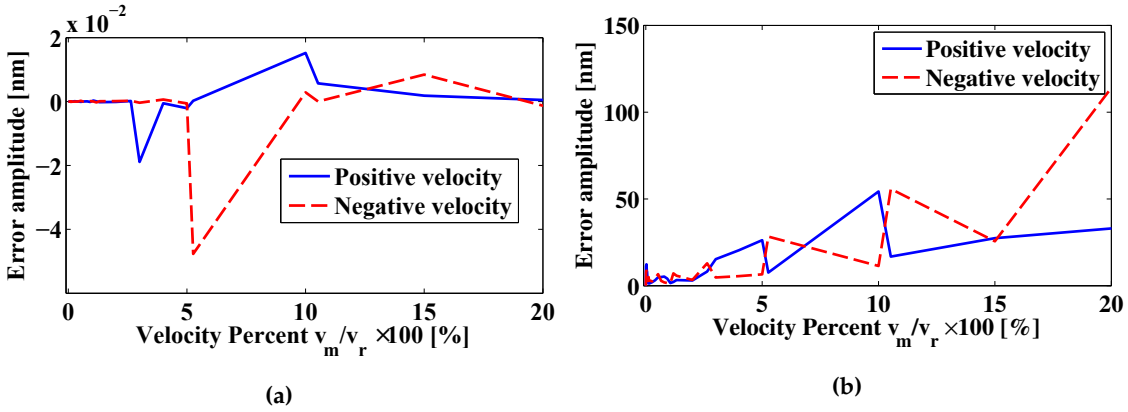

Figure 3.2.5: Measurement error as result of the difference in velocity between the reference and the target motion. (a) Mean value of the detected error. (b) Maximum value of the detected error. The X-axis in both (a) and (b) represents the ratio of velocity $v_m/v_r \times 100$.

In all studied cases it is observed that larger errors are present when the sign of the target velocity is opposite to that of the reference motion. Close to a zero velocity ratio, the error presents a peak, showing a difference around of 3.65nm for a 0.02% ratio (with a maximum value of 12.33nm). It is also noticed that larger errors compared to the amplitude of the total displacement occur for velocities around this region. After this point, a decrease on the error can be observed having a minimum around 0.1% with a mean error close to zero, standard deviation of 0.14nm and a maximum error of 1.65nm. The larger error in the case of negative velocities may be explained by the loss of linearity shown in Fig.3.1.5.

Once the minimum error is reached, a nearly constant increase in the detected error can be observed. In Fig.3.2.6 a fitting of the error is shown which has been approximated by the function:

$$\widehat{Err(v_{ratio})} = Ae^{Bv_{ratio}}, \tag{3.2.2}$$

where $\widehat{Err(v_{ratio})}$ represents the estimated error curve, $v_{ratio} = |v_m/v_r|$ is the ratio of the velocity of the target relative to the reference velocity in [%], $A = 0.4733$ with an interval $(0.1415, 0.8050)$, $B = 0.04233$ with an interval $(0.02457, 0.06010)$. The fitted function presents a sum of squares due to error $SSE = 40.91$, $R^2 = 0.919$ and $RMSE = 1.051$, showing a good agreement with the simulated data.

From these results, it is concluded that the best results are obtained for a ratio of velocities with a value between 0.5% and 5%, which typically results in a mean error close to zero, and a standard deviation in the order of 1nm (for a wavelength of 785nm). The maximum error in this interval has been found close to the 5% ratio with a peak value in the order of 20nm which corresponds to a 6.57×10^{-2}% of the total displacement amplitude. Therefore the apparent error in the total displacement may be, in some cases, negligible when compared to the total displacement. Moreover, if the method is restricted to measurements below $\lambda/2$ and the F_s rate is respected, ideally, sub-nanometric reconstruction errors may be achieved. In a typical environment, however, this limits may not be reached as other effects might appear along the measurement period.

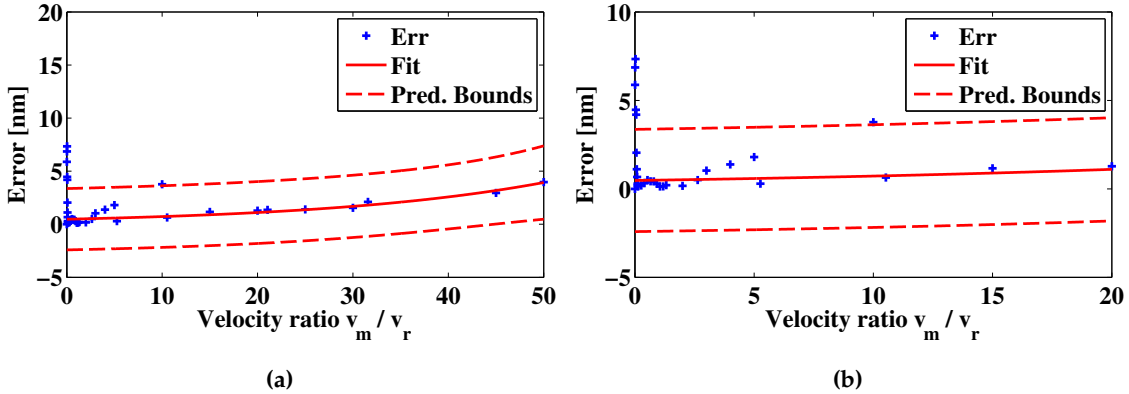

Figure 3.2.6: (a)Fitting of the standard deviation error curve resulting from the evaluation of the velocity ratio v_m/v_r. The resulting error behaves exponentially as the ratio increases. The fitting is unable to estimate the trend correctly for ratio values close to zero. (b) Zoom on the fitted curve to an interval between a 0 to 20% velocity ratio.

3.3 Theoretical analysis of experimental sources of error

It is important to keep in mind that different effects can affect the measurement, specially in the case of nanometric scale displacements. In the particular case of DSMI it is expected that different sources of noise, intrinsic or extrinsic to the sensor, will reduce the resolution and accuracy of the measurement. Further on some of this are discussed, including electronic white noise, differences in laser wavelength, and the effect of having different feedback coefficients in the analyzed OOP signals.

3.3.1 Electronic white noise

One of the possible sources of noise in the proposed method comes from the appearance of white noise due to the different electronic subsystems involved in the measurement. To investigate the limits of the proposed method a set of simulations using the parameters shown in Tab.3.2.1 are performed. In this case, after simulating the OOP waveform, white noise is added to the OOP and the DSMI signal processing is performed using the algorithm previously presented. In this case the SNR is calculated as $SNR = 20log(A_{OOP}/A_{noise})$. The SNR levels tested include: $-3dB$, $0dB$, $3dB$, $6dB$, $10dB$ and $20dB$. In all cases the reported values correspond to the reconstruction after the application of both the linear interpolation and drift removal, that is, the best reconstruction case. Due to the randomness of the noise, each simulation is repeated 10 times and the resulting mean, standard deviation, RMS and maximum values are averaged.

As it could be reasonably expected, the larger errors occur when the SNR of the signals is closer to zero or negative. It is observed that the resulting error tends to be slightly larger when it affects the reference signal. Nevertheless, this difference cannot be considered significant enough to assert that the method is more sensitive to the noise in the reference signal.

Table.3.3.1 also shows that for the case presented typical standard deviations will vary between $0.5nm$ and $2nm$, with mean values very close to zero, therefore allowing to keep at least a resolution better than $\lambda/100$. In contrast, it is also observed that the maximum error increases proportionally with the decay of the SNR. However, even accounting for the maximum error found within this simulation, the resulting reconstruction still shows a resolution within the order of $\lambda/100$, thus validating the sub-wavelength resolution claimed for the method.

SNR_r[dB]	SNR_m[dB]	$\overline{Err}$[nm]	σ_{err}[nm]	Err_{RMS}[nm]	Err_{max}[nm]
20	20	$(4.52 \pm 2.80) \times 10^{-15}$	0.50 ± 0.14	0.50 ± 0.14	1.25 ± 0.28
20	10	$(4.78 \pm 4.94) \times 10^{-15}$	0.61 ± 0.15	0.61 ± 0.15	1.59 ± 0.32
20	6	$(3.06 \pm 2.34) \times 10^{-15}$	0.75 ± 0.30	0.75 ± 0.30	2.19 ± 0.55
20	3	$(5.71 \pm 2.23) \times 10^{-15}$	0.72 ± 0.16	0.72 ± 0.16	2.18 ± 0.50
20	0	$(5.51 \pm 7.69) \times 10^{-15}$	1.23 ± 0.26	1.23 ± 0.26	3.22 ± 0.64
20	−3	$(1.58 \pm 7.24) \times 10^{-15}$	1.57 ± 0.54	1.57 ± 0.54	4.99 ± 0.54
10	20	$(3.40 \pm 2.02) \times 10^{-15}$	0.58 ± 0.23	0.58 ± 0.23	1.54 ± 0.55
10	10	$(4.17 \pm 3.89) \times 10^{-15}$	0.69 ± 0.25	0.69 ± 0.25	1.79 ± 0.54
10	6	$(4.57 \pm 4.36) \times 10^{-15}$	0.89 ± 0.44	0.89 ± 0.44	2.17 ± 0.86
10	3	$(4.54 \pm 2.98) \times 10^{-15}$	0.90 ± 0.22	0.90 ± 0.22	2.64 ± 0.82
10	0	$(1.33 \pm 8.02) \times 10^{-15}$	1.25 ± 0.57	1.25 ± 0.57	3.56 ± 1.21
10	−3	$(3.19 \pm 5.04) \times 10^{-15}$	1.65 ± 0.44	1.65 ± 0.44	5.06 ± 1.21
6	20	$(3.38 \pm 2.11) \times 10^{-15}$	0.93 ± 0.28	0.93 ± 0.28	2.36 ± 0.62
6	10	$(1.63 \pm 2.26) \times 10^{-15}$	0.83 ± 0.34	0.83 ± 0.34	2.38 ± 1.18
6	6	$(3.84 \pm 4.99) \times 10^{-15}$	0.80 ± 0.26	0.80 ± 0.26	2.50 ± 0.79
6	3	$(2.40 \pm 3.52) \times 10^{-15}$	0.91 ± 0.24	0.91 ± 0.24	3.03 ± 0.93
6	0	$(1.81 \pm 6.34) \times 10^{-15}$	1.05 ± 0.46	1.05 ± 0.46	3.87 ± 1.90
6	−3	$(-0.46 \pm 12.60) \times 10^{-15}$	0.45 ± 1.59	1.59 ± 0.45	4.91 ± 1.28
3	20	$(4.38 \pm 6.63) \times 10^{-15}$	1.06 ± 0.62	1.06 ± 0.62	2.55 ± 1.26
3	10	$(2.17 \pm 6.02) \times 10^{-15}$	0.86 ± 0.31	0.86 ± 0.31	2.88 ± 0.84
3	6	$(2.05 \pm 3.31) \times 10^{-15}$	0.97 ± 0.38	0.97 ± 0.38	2.60 ± 0.75
3	3	$(2.35 \pm 5.51) \times 10^{-15}$	1.04 ± 0.16	1.04 ± 0.16	3.35 ± 0.73
3	0	$(3.37 \pm 5.04) \times 10^{-15}$	1.20 ± 0.29	1.20 ± 0.29	3.41 ± 0.66
3	−3	$(6.35 \pm 4.91) \times 10^{-15}$	1.80 ± 0.59	1.80 ± 0.59	7.58 ± 3.89
0	20	$(1.27 \pm 4.92) \times 10^{-15}$	1.12 ± 0.33	1.12 ± 0.33	3.18 ± 0.66
0	10	$(5.93 \pm 6.49) \times 10^{-15}$	1.07 ± 0.19	1.07 ± 0.19	3.49 ± 0.76
0	6	$(1.25 \pm 5.09) \times 10^{-15}$	1.04 ± 0.46	1.04 ± 0.46	3.17 ± 1.06
0	3	$(2.15 \pm 1.79) \times 10^{-15}$	1.21 ± 0.34	1.21 ± 0.34	4.07 ± 1.24
0	0	$(2.48 \pm 3.60) \times 10^{-15}$	1.40 ± 0.44	1.40 ± 0.44	4.32 ± 1.05
0	−3	$(6.15 \pm 5.86) \times 10^{-15}$	1.63 ± 0.30	1.63 ± 0.30	6.21 ± 3.60
−3	20	$(2.55 \pm 6.37) \times 10^{-15}$	1.46 ± 0.34	1.46 ± 0.34	4.40 ± 0.98
−3	10	$(1.79 \pm 10.47) \times 10^{-15}$	1.81 ± 0.69	1.81 ± 0.69	5.67 ± 1.91
−3	6	$(2.94 \pm 4.88) \times 10^{-15}$	1.70 ± 0.27	1.70 ± 0.27	6.54 ± 2.57
−3	3	$(3.93 \pm 4.75) \times 10^{-15}$	1.61 ± 0.38	1.61 ± 0.38	7.06 ± 3.40
−3	0	$(5.00 \pm 9.96) \times 10^{-15}$	1.85 ± 0.58	1.85 ± 0.58	6.95 ± 3.18
−3	−3	$(1.95 \pm 5.56) \times 10^{-15}$	1.75 ± 0.40	1.75 ± 0.40	6.74 ± 3.14

Table 3.3.1: Estimated error of DSMI reconstructions for signals with white noise added. Different SNR values in the reference (SNR_r) and measurement (SNR_m) signals are considered. For all studied signals the noise is considered to be white and additive. All data is the average of ten independent simulations to account for randomness effects.

Further, from the table it is also clear that in order to keep a resolution in the order of $\lambda/200$, it would be necessary that both signals have a SNR above at least $3dB$. Below this value, $\lambda/100$ resolutions are still possible, if only the errors introduced by SNR are accounted for.

In the case when one of the signals has a SNR value smaller than $3dB$, it was only possible to obtain a value close to $\lambda/200$ when the opposite channel had a high SNR level, in the order of $10dB$ or better. Therefore, to obtain resolution values good enough it is necessary to satisfy a SNR better than $3dB$, although in practice larger values might be necessary.

Parameters	Symbol	Value	Units
Reference wavelength	λ_r	785	nm
Measurement wavelength	λ_m	[780, 790]	nm
Increment in measurement wavelength	$\Delta\lambda_m$	0.5	nm

Table 3.3.2: Parameters used in the simulation for differences in wavelength between the reference and measurement LD.

3.3.2 Effect of the difference in wavelength of the two channels

As described in Sec.3.1.1, the value of wavelength plays an important role in the minimum attainable resolution of the method. Even when the nominal wavelength and output power of the laser are stated in the specification sheet (see e.g. Annex A) of each LD model, those values should be only taken as a reference of the expected value of the emission. Typically, it is possible to find significant variations from this reference values, as a result of different factors such as input current, temperature, or the geometry of the laser model, among others. This variations usually fall within a constrained range of $\pm 20nm$ for FP and VCSEL LD families consulted along this research work (e.g. [131]. The corresponding specification sheets are presented in full detail in Annex A, [132], and [133]).

To analyze theoretically the effects of the differences in wavelength between the reference and measurement laser diodes, simulations with an increasing variation of $\Delta\lambda_m = 0.5nm$ in the range of $\pm 5nm$ were performed. The wavelength features used for the reference and measurement lasers used in the simulation can be found in Tab.3.3.2. The target displacement and reference motion are equivalent to those presented in Tab.3.2.1.

The initial effect of the difference in wavelength is depicted in Fig.3.3.1. As it is observed, after the initial reconstruction and interpolation, the net displacement of the target is overlapped over a constant slope which depends upon the magnitude and sign of the difference of the wavelengths, being negative when $\lambda_m < \lambda_r$ and positive otherwise.

In order to remove part of the error resulting from the mismatch on the velocity calculation, a fit correction can be applied. The results of the simulation after applying the fit correction are presented in Tab.3.3.3. From Tab.3.3.3, it can be observed that there is a trend to reduce the RMS error and the standard deviation as the value of λ_m approaches to λ_r, as one would expect. When both values are equal, however, an increase of the error from $0.12nm$ to $0.56nm$ appears on the measurement. This result, however, is contradictory as one would expect the lower amount of error at this point. A possible explanation for this last effect is related to the lack of previous knowledge on the initial position of the target (which is related to the initial LD phase), which introduces a random amount of offset in the speed measurement.

The values presented in Tab.3.3.3 show a good agreement with the expected decrease up to a close to zero $\overline{v_m}$ value when $\lambda_m \to \lambda_r$. It is important to notice, however, that a small amount of offset is present even in the case where $\lambda_r = \lambda_m$. From this information, it is also observable that it is possible to reduce some effects in the reconstruction calculation by removing the mean value of the calculated difference of velocities (Eq.(3.1.2)).

It is also to be noticed that the values of Tab.3.3.3 in terms of Err_{RMS}, σ_{Err} and Err_{Max} present an almost symmetrical behaviour showing increments in its value as λ_m moves away from λ_r. As in the previous cases, no direct relationship can be established regarding the mean error, although a trend towards lower values is observed in the interval $[784.5, 785.5nm]$.

When a similar simulation was performed for larger values of displacement ($A_{pp1} = 100nm$), similar errors to the ones presented in the table were obtained ($\sigma_{Err} = 0.31nm$ for $\lambda_m = 790nm$). It has also been found that (as expected from the theory presented in Sec.3.1.1) that larger errors can be observed when the frequency of the target motion is increased (e.g. if $f_1 = 50Hz$ the σ_{err} increases up to $3.00nm$), therefore the velocity ratio imposes a higher effect over the measurement error than the differences in wavelength. Also, the errors related to SNR seem to have a larger importance than those of a difference in wavelength as for these cases σ_{Err} increases to $0.36 \pm 0.02nm$ for $\lambda_m = 790nm$ with $SNR_m = SNR_r = 6dB$.

Thus, even when it is observed that the difference in wavelength hampers the reconstruction by adding a continuous velocity error, it is possible to remove the effect on a oscillatory signal by simply applying the linear fitting algorithm, or by removing the mean of the reconstructed velocity.

It has also been observed that the differences in velocity observed as a result of the difference in wavelength have a linear relationship of the form:

$$v_{err} \approx 96.42\Delta\lambda + 1.91 \times 10^{-9}, \tag{3.3.1}$$

where v_{err} is the error in velocity reconstruction due to the change of wavelength. This has been further simulated for a wavelength of $830 \pm 10nm$ resulting in a similar slope ($m \approx 97$). By applying this corrector factor into Eq.(2.3.2) it is possible to remove the drift caused by $\Delta\lambda$ over the velocity. Furthermore, the use

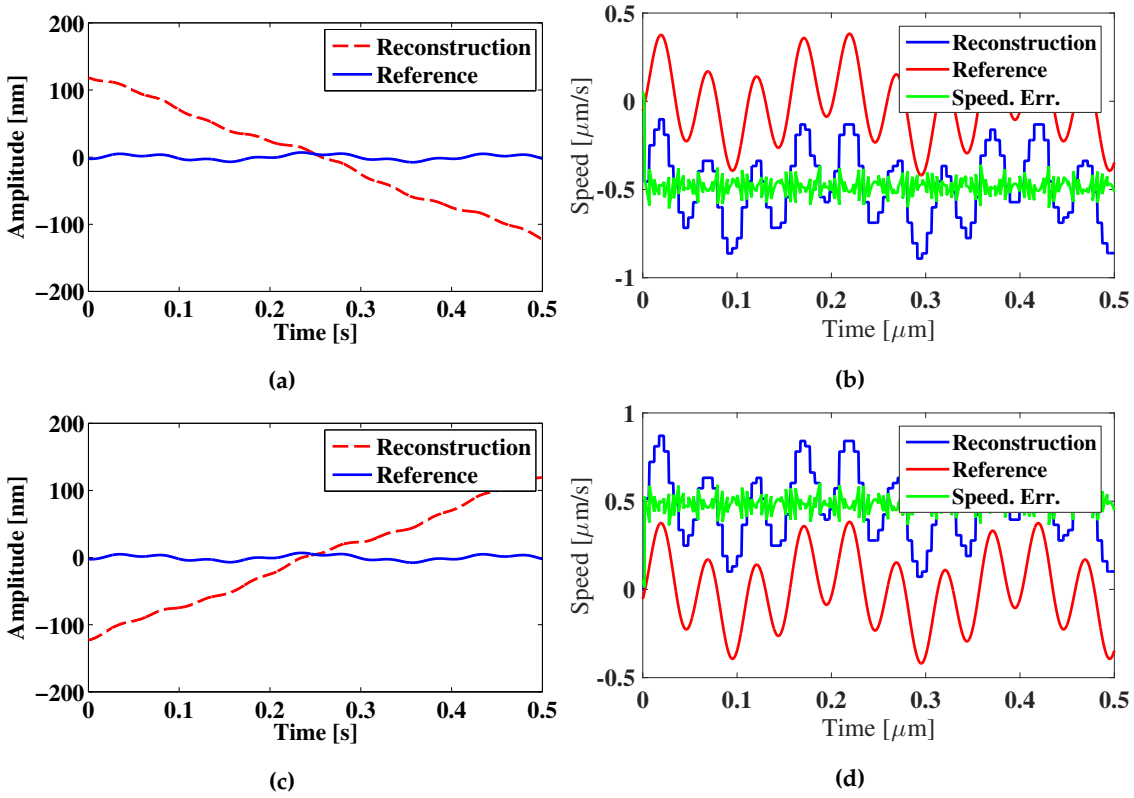

Figure 3.3.1: Effects of non-equal values of λ_m and λ_r. (a) Negative slope as a result of having $\lambda_m < \lambda_r$; the represented case corresponds to $\lambda_m = 780nm$ and $\lambda_r = 785nm$. (b) Reconstruction of the velocity of the target when $\lambda_m < \lambda_r$; the negative mean of the velocity corresponds to the slope observed in (a). (c) Positive slope as a result of having $\lambda_m > \lambda_r$; the represented case corresponds to $\lambda_m = 790nm$ and $\lambda_r = 785nm$. (d) Reconstruction of the velocity of the target for the case presented in (c).

λ_m[nm]	$\overline{Err}$[nm]	σ_{Err}[nm]	Err_{RMS}[nm]	Err_{Max}[nm]	$\overline{v_m}$[μm/s]
780.0	2.06×10^{-13}	0.13	0.13	0.70	−0.48
780.5	2.74×10^{-13}	0.13	0.13	0.60	−0.43
781.0	-1.09×10^{-13}	0.13	0.13	0.51	−0.38
781.5	5.23×10^{-14}	0.13	0.13	0.42	−0.34
782.0	5.28×10^{-14}	0.12	0.12	0.37	−0.29
782.5	-1.63×10^{-14}	0.12	0.12	0.37	−0.24
783.0	4.80×10^{-14}	0.12	0.12	0.36	−0.19
783.5	-2.53×10^{-14}	0.12	0.12	0.36	−0.14
784.0	1.40×10^{-14}	0.12	0.12	0.36	−0.10
784.5	1.81×10^{-15}	0.12	0.12	0.35	−0.05
785.0	6.10×10^{-15}	0.56	0.56	1.29	0.01
785.5	2.26×10^{-15}	0.12	0.12	0.35	0.05
786.0	1.08×10^{-13}	0.12	0.12	0.41	0.10
786.5	-5.40×10^{-14}	0.12	0.12	0.51	0.15
787.0	-6.88×10^{-14}	0.12	0.12	0.60	0.19
787.5	5.93×10^{-14}	0.12	0.12	0.69	0.24
788.0	1.88×10^{-13}	0.12	0.12	0.78	0.29
788.5	-2.95×10^{-14}	0.12	0.12	0.87	0.34
789.0	-3.14×10^{-13}	0.12	0.12	0.97	0.39
789.5	-9.82×10^{-14}	0.13	0.13	1.06	0.44
790.0	-9.38×10^{-14}	0.13	0.13	1.15	0.48

Table 3.3.3: Error effects due to difference in wavelength for a simulation with $\lambda_m = [780, 790]nm$ and $\Delta\lambda_m = 0.5$. The values correspond to the error after interpolation and drift removal. The column $\overline{v_m}$ corresponds to the mean velocity found during the reconstruction and which corresponds to the slope in the reconstruction previous to the drift removal

of this correction factor allows to reconstruct also linear displacements if no fitting is applied at the end of the process.

3.3.3 Effect of different C values

The next factor to be considered in the present study is the acquisition of signals with different feedback factors. As in the previously explored cases, this situation might be common under experimental conditions in practice. A set of different simulations is proposed using different C values, that is, different amounts of feedback, for the reference and measurement LDs. The parameters of the simulation, except for the C value, are the same ones presented in Tab.3.3.2.

To obtain a different C factor in the provided simulation file there exist two suitable possibilities: 1) to change the distance to the target, or 2), to change the external reflectivity. In the case of the simulations discussed further on, the second case is preferred over the initial one, as it is easier to keep track of the variation of C and the positioning of the equipment needs not be modified. The results of the simulation are displayed in Tab.3.3.4. All results are considered after drift removal.

Looking at the results in Tab.3.3.4, it is not possible to find a defined trend in the error as in some cases the reduction of the C value in one of the signals tends to reduce the amount of error in the final reconstruction, specially in the case of variations of C_m. In the case of the variation of C_r, it is possible to observe a small increase of the error as C_r increases. The amount of error introduced, however, does not introduce large variations when compared to the expected result as in all cases σ_{Err} is still below $1nm$.

It is important to remark that in the presented case the simulation uses a ramp motion as a reference.

With the use of this type of reference motion, it is possible to consider that the SMI transitions appear only in one direction, therefore simplifying the fringe detection algorithms and reducing possible differences in the detection of the direction of motion. It is also important to notice that the algorithm used to detect transitions uses a three step detection in all the cases discussed up to now. First, a initial estimation of the fringe position is performed over the derivative of the filtered SMI OOP signal. This detection uses a threshold which, in most of the cases, can be estimated as the RMS value of the derivative signal. Next a zero crossing detection is performed on the filtered OOP signal. Finally a comparison of the position between the derivative and the zero crossing detection is performed, allowing to detect fringes even in the case of lower C values. This would explain the small variation in the amount of error as a result of the variation of C. The described transition detection algorithm has been used along all the previous sections, and it is used for all the SMI signal processing presented in this work.

It should be noted that for all cases studied and in practical measurements, if necessary, the sensor counts with extra information as the reference motion is always controlled, thus allowing to know the direction of the reference motion even when this information cannot be extracted from the OOP signal. Therefore, in those cases where the C value is low, a correction on the sense of the detected fringes may be introduced resulting in a correct accounting of the correspondent DSMI calculation.

3.3.4 Effect of using a triangular motion

As discussed in a previous section, the use of ramp-like motions is the preferred strategy to produce the DSMI measurement. In many cases however, it might be necessary to measure over a long period of time. This would prevent from the use of a ramp-like motion, as it would require a large device to produce the reference motion. Moreover, in such a case, the OOP signal would be more susceptible to the presence of speckle noise (which is more likely to appear in long displacements), thus increasing the complexity of the detection algorithm. Therefore, a solution to this issue might be the use of a triangular motion with a fixed maximum amplitude (typically set below $100\mu m$ to prevent from potential speckle effects).

C_r[AU]	C_m[AU]	$\overline{Err}$[nm]	σ_{Err}[nm]	Err_{RMS}[nm]	Err_{Max}[nm]
0.99	0.99	3.54×10^{-15}	0.56	0.56	1.29
0.99	0.50	3.20×10^{-15}	0.43	0.43	1.12
0.99	0.32	6.48×10^{-15}	0.44	0.44	1.64
0.99	0.10	3.19×10^{-15}	0.42	0.42	2.25
0.50	0.99	-0.61×10^{-15}	0.53	0.53	6.88
0.50	0.50	8.61×10^{-15}	0.63	0.63	2.90
0.50	0.32	8.05×10^{-15}	0.60	0.60	1.70
0.50	0.10	-0.53×10^{-15}	0.79	0.79	8.61
0.32	0.99	6.54×10^{-15}	0.50	0.50	7.72
0.32	0.50	8.06×10^{-15}	0.69	0.69	6.09
0.32	0.32	6.83×10^{-15}	0.61	0.61	1.52
0.32	0.10	5.49×10^{-15}	0.63	0.63	5.47
0.10	0.99	6.26×10^{-15}	0.83	0.83	17.05
0.10	0.50	2.87×10^{-15}	0.78	0.78	10.67
0.10	0.32	3.08×10^{-15}	0.42	0.42	6.98
0.10	0.10	11.51×10^{-15}	0.62	0.62	1.37

Table 3.3.4: Error results for a DSMI displacement simulation with different values of C in OOP_r and OOP_m for a positive ramp displacement reference.

The use of a triangular motion as a reference entails, however, an expected problem inherent to calculations involving abrupt transitions, edges, or singular points, as the vertices of the triangular wave. For example, with the studied formulation, it is not possible to know the initial velocity of the motion of the target, thus causing an initial offset on the measurement. In the case of oscillatory motions, this can be easily corrected by removing the mean of the signals to be compared.

In the case of triangular motion, however, the edge boundary is present every time the reference signal changes its slope. As a result of that change the definition of the velocity stops behaving lineally so calculations may introduce an error which can oscillate from a few to several nm. To illustrate this let us consider a simulation with the parameters presented in Tab.3.2.1, expanding the simulation time as the interval $t_s = [0, 1]$. In this case, instead of a ramp reference displacement d_r, it is considered that the displacement is given by the triangular wave described as

$$d_r(t_s)\begin{cases} 2A_r t_s, & \text{if } t_s \leq 0.5 \\ -2A_r t_s + A_r & \text{if } t_s > 0.5 \end{cases} \tag{3.3.2}$$

After generating the correspondent OOP signals, it is possible to detect the corresponding fringes of the displacements observed for L_r and L_m. After the initial detection algorithm, the DSMI algorithm is run as in previous simulations, resulting in the reconstruction presented in Fig.3.3.2. It may be seen how towards the middle of the studied period a sharp discontinuity arises, as a result of the change of direction in the reference motion. This effect can be observed both in the velocity reconstruction as well as in the displacement reconstruction.

It may be observed from the error bars plotted in Fig.3.3.2c how the largest amount of error is present in the second half of the reconstruction (after the change of direction). Again this is directly related to the boundary behavior towards the change of velocity in the reference motion. Moreover, in Fig.3.3.2d, it is possible to observe more clearly the error step in the middle of the reconstruction raising from an average of $-4nm$ to $4nm$. Therefore, in this condition a mean error $\overline{Err} = 1.18 \times 10^{-15} nm$ with $\sigma_{err} = 1.50nm$, $Err_{RMS} = 1.50$ and maximum error $Err_{Max} = 3.37nm$ is obtained.

In order to mitigate the effects of the change of direction, the differences in phase of OOP_m and OOP_r around the change of direction should be accounted for. So far, however, it has not been possible to find a suitable method of accounting this change of phase even in a simulation process as in such a case the initial random phase of the LD would come into place.

Yet, it is possible to reduce the effects of the change of direction making a small modification of the quantification algorithm. To do so let us consider that the reference motion produces positive fringes along half of the signal, and negative ones along the second half of the studied time. Next, let us assume that the time of occurrence between the last positive fringe and the change of direction of the target is equal to the time between the change of direction of the target and the first negative fringe (the phase around the change of direction is symmetric). This symmetric phase assumption around the point of change of direction makes possible to equate the total velocity in the considered section as $v = 0$. Once this correction is introduced in the code, the error can be reduced significantly, as shown in Fig.3.3.3. It is to be observed that in this case the errors drop radically when compared to the results obtained before the adjustment, as now $\overline{Err} = 2.82 \times 10^{-15}$, $\sigma_{Err} = 0.70$, $Err_{RMS} = 0.70$ and $Err_{Max} = 2.13$. Even in this case (which involves a quite strong assumption), it is observed that the error is larger than the one corresponding to a ramp reference motion. It can also be observed that in this case the error has an exponential behaviour, and as a result a better fitting option might be the use of such a function. This however entails further signal processing

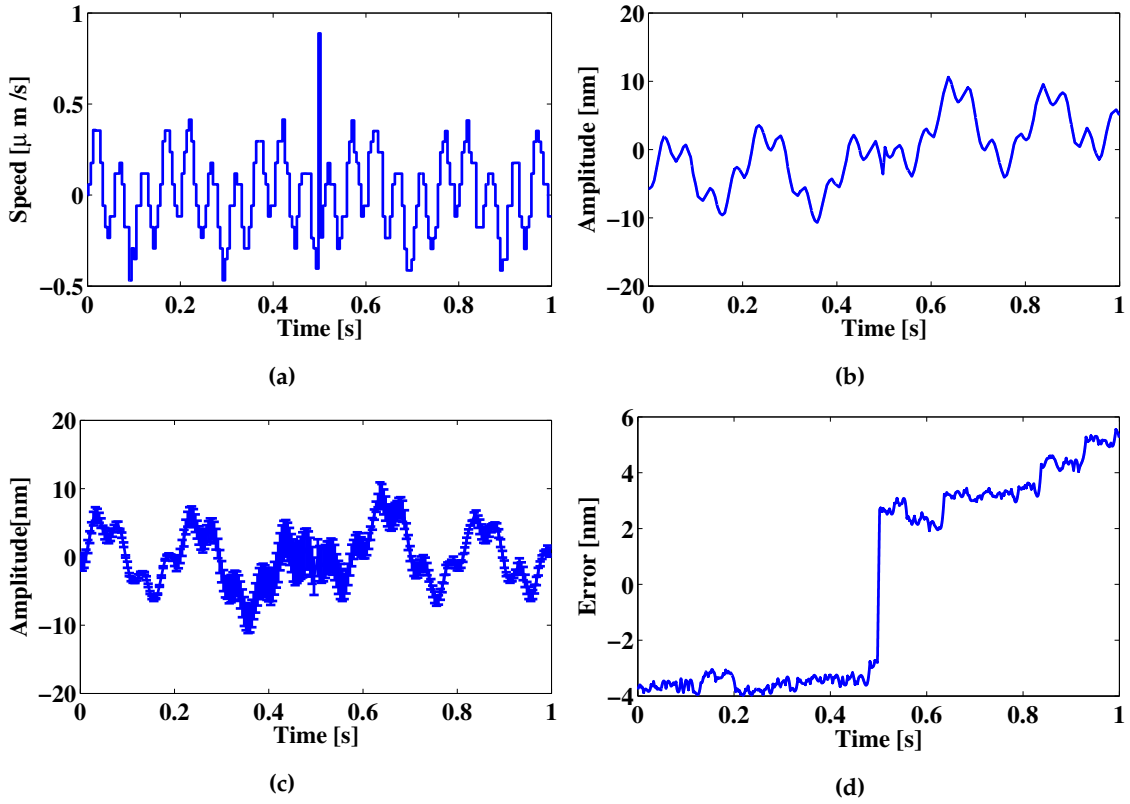

Figure 3.3.2: Reconstruction of a simulated triangular displacement and associated error. (a) Equivalent velocity measured by the DSMI algorithm. (b) Reconstruction of the simulated target motion showing a discontinuity towards the middle of the period. (c) Error bars of the resulting reconstruction, with an increase of the error visible in the second half of the signal. (d) Error introduced in the reconstruction of the displacement. A step like behavior appears at the discontinuity.

which may be prohibitive in many on-line applications.

If other parameters such as the wavelength or the *C* factor are varied in addition to this case, results comparable to the ones discussed above are obtained. For example, in the case of a difference in wavelength, the resulting reconstruction presents two slopes corresponding to the same phase of the triangular reference motion. As in the previous case, it its possible to reduce the noise by applying the correction factor discussed in Sec.3.3.3, with the sign selected as necessary and accounting for the zero position in the slope rotation point. Another possible way to reduce the error in the case of using a triangular reference motion is to apply an *n* order fitting according to the number of ramps *n* involved in the measurement instead of a linear fitting.

To summarize, different experimental effects which may be expected and which affect the performance of the DSMI method have been studied through simulation in detail. It has been found that from the studied factors the signal SNR and the velocity of the reference motion are the ones which introduce a larger amount of error in the measurement, as the former reduces the ability to correctly sense the position of the fringes, and the later reduces the resolution of the method. Other effects such as differences in wavelength, *C* factor, ramp direction, and the use of triangular motion have also been studied showing smaller effects on the resolution of the method, when compared to SNR values and reference velocity. Furthermore, in some of this cases it is possible to apply different types of corrections to account for the undesired effect, as shown,in

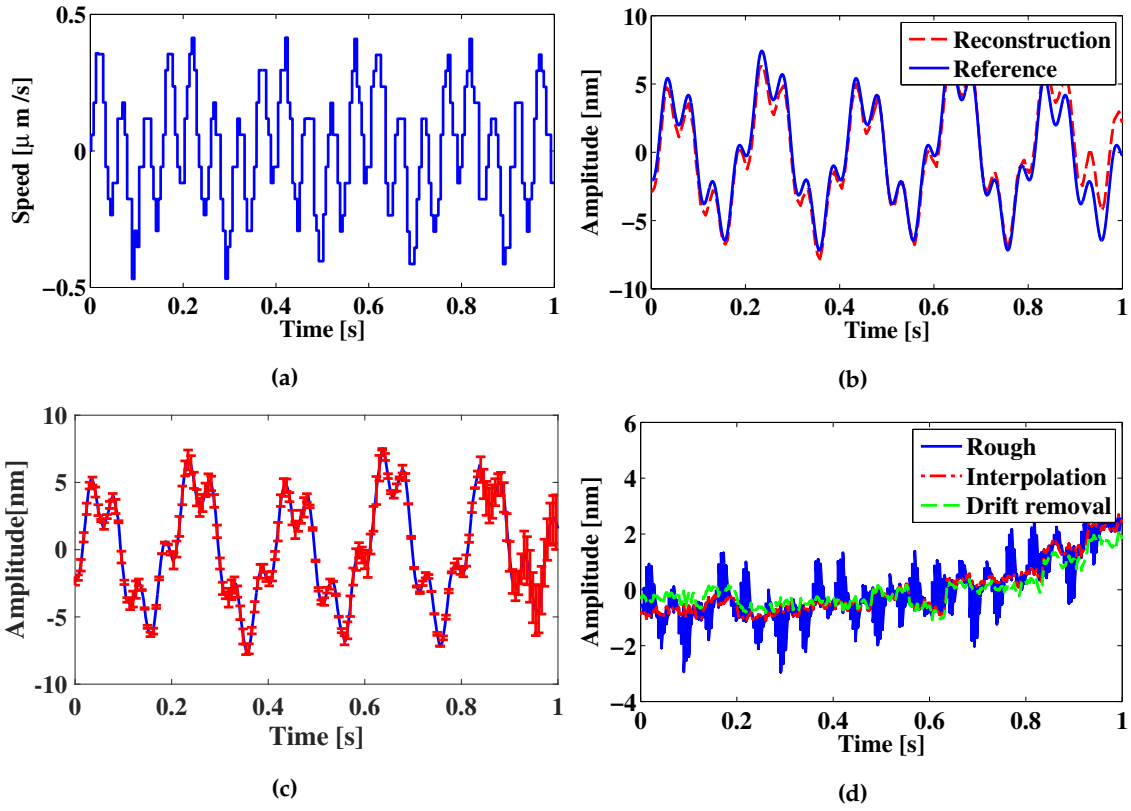

Figure 3.3.3: Example of reconstruction considering $v = 0$ during the change of direction in the reference motion. (a) Reconstruction of the velocity profile of the simulated displacement after a correction in the change of direction assuming $v = 0$ at the edge; (b) Displacement reconstruction and comparison with the originally simulated displacement. (c) Reconstructed displacement with error bars added. (d) Error calculated after the different processing stages.

e.g. the difference in reference and measurement wavelength.

3.4 Experimental results

In the previous subsection diverse effects which may affect the DSMI method have been studied isalated and theoretically to get a better understanding of their relevance in the measurement. In practice, however, it should be expected that all the effects presented, as well as some others not contemplated, will be present simultaneously in the moment of the signal acquisition, therefore reducing the practical resolution of the method below the theoretical resolution of $\lambda/1000$ discussed before. In this section a series of measurements to characterize the experimental limitations of the proposed method will be presented.

Prior to the exploration of the DSMI method in a laboratory environment, an initial characterization of the elements to be used in the sensor is performed to take into account some of the different factors such as wavelength, noise or target velocity which are expected to limit the actual resolution of the measurement.

3.4.1 Characterization of the wavelength of the laser diode

As discussed previously, the DSMI reconstruction has a dependence on the wavelength of the measurement and reference LDs. While in principle it is possible to reduce the effects of such error, to do so it is necessary

to account for the difference in wavelength values of the reference and measurement beams, or to use a fitting-based solution. Given that the former method provides better results, it is required that the LD's used in the sensor are properly characterized.

To perform the characterization of the LD, a *SPECTRO 320(D)R5 Scanning Spectrometer* device from Instrument Systems is used. The wavelength range is selected to scan in steps of $0.1nm$ focusing the measurement around the near infrared (*NIR*) wavelength in a range comprising $[780, 800]nm$. The measurements are performed under dark room conditions to prevent other sources of illumination to introduce a bias on the acquisition sensor. Previous to the start of the measurement the tested LD is placed on a Thorlabs $T220230P - B$ collimation tube and the $C220230P - B$ focusing lens is adjusted to provide a large spot to cover a large part of the $320(D)R5$ probe. Each laser is connected to a controlled current source using a Thorlabs *SR9A* ESD protection cable which contains a 3.3V Zenner diode protection and a Schottky diode for transient surge protection.

An initial test is performed changing the current input within a range ranging from 130 to $145mA$ by applying different source input voltages, as shown in Tab.3.4.1. Four Hitachi HL7851G multi quantum well laser diodes were subject to the same test in order to study possible differences on their behavior as a result of the fabrication process. It is observed that in three of the studied cases an increase of wavelength appears as the feeding current increases. In the case of LD D, however, a reduction in wavelength is observed in the

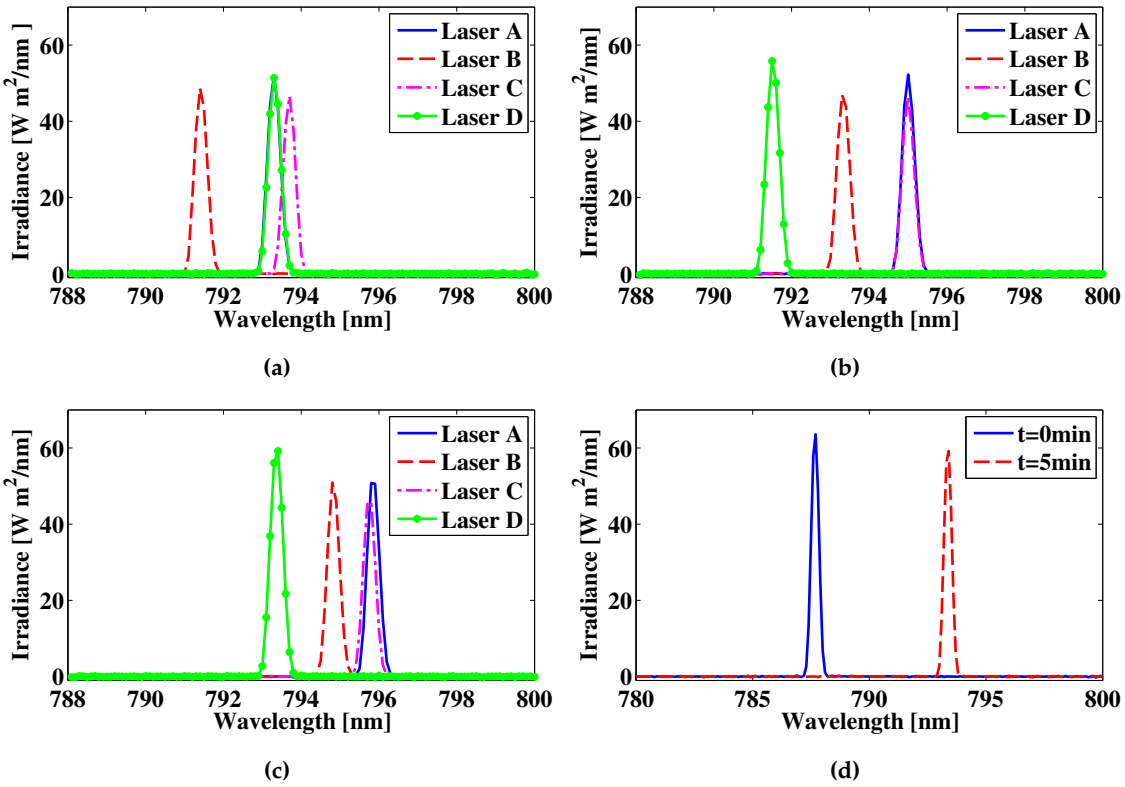

Figure 3.4.1: Example of experimental emission wavelength and resulting LD output power as a result of different injection currents. (a) Test results for four lasers for a constant current of $130mA$. (b) Test results for the four lasers for a constant current of $135mA$. (c) Test results for the four lasers for a constant current of $140mA$. (d) Effects on LD labelled as D after a working period of 5 minutes for a current around $90mA$. A relevant increase in the wavelength attributed to heating is observed.

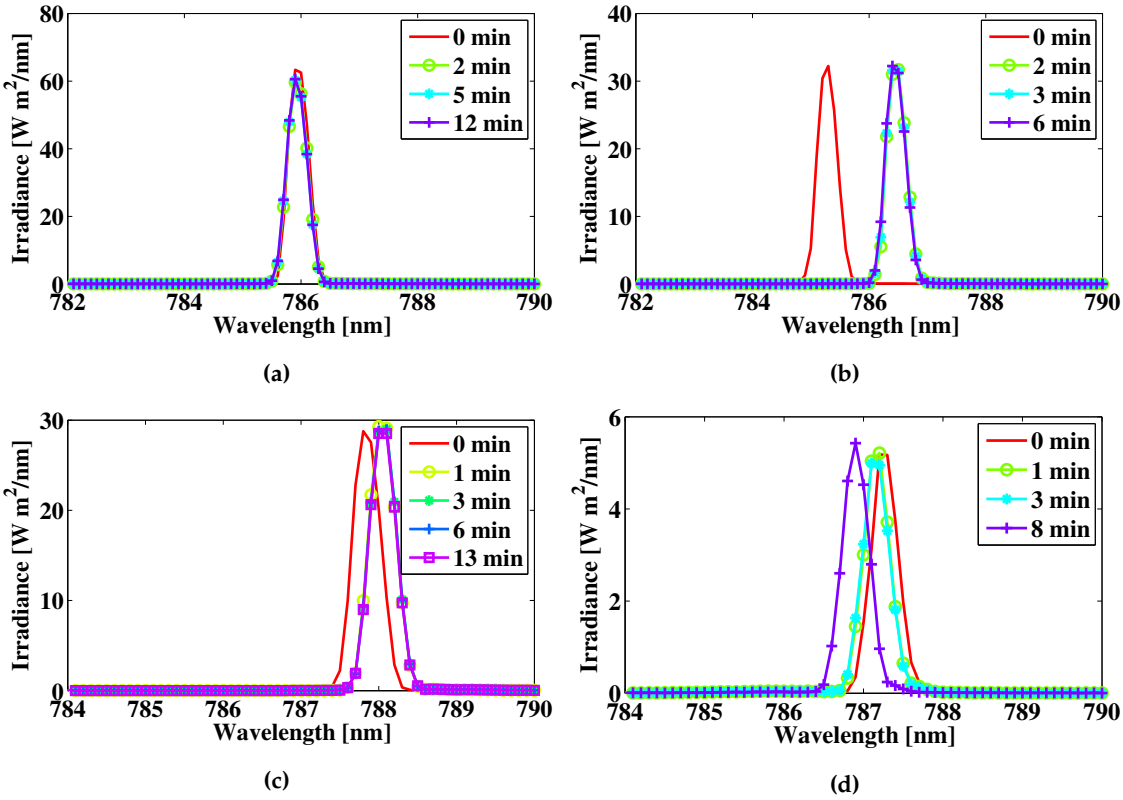

Figure 3.4.2: Wavelength variation when using a electronic card for controlling the temperature conditions in different laser diodes. (a) Laser diode A measurement under temperature control conditions. (b) Laser diode B measurement under temperature control conditions. (c) Laser diode C measurement under temperature control conditions. (d)Laser diode C measurement under temperature control conditions, with the bias point changed to show the effects at a lower output power.

	130[mA]	135[mA]	140[mA]
Laser A	793.3	795.0	795.9
Laser B	791.4	793.3	794.8
Laser C	793.7	795.0	795.8
Laser D	793.2	791.5	793.4

Table 3.4.1: Wavelength as a result of different injection currents in four laser samples of a Hitachi HL7851G laser diode.

135mA step. In all cases the LDs presented a narrow linewidth as shown in Fig.3.4.1 where the *FWHM* is in the order of 1nm.

Further, the possibility of wavelength variations as a result of thermal effects is also observed. This is shown, for instance, in Fig.3.4.1d where after a 5 minutes period an increase of wavelength of nearly 6nm is observed for the LD labeled as D, with a starting current set point around 130mA. A second sample was taken after 10 minutes, with no significant difference (increment of 0.5nm) from the 5 minutes case. An equivalent behavior with temperature was obtained in all laser diodes. In all cases, a significant increase of wavelength with temperature was observed.

After this initial test, a second test was performed using the electronic circuit proposed in Sec.3.1.3, which includes (according to the iC-WJ/iC-WJZ chip manufacturer) internal circuitry to control the laser diode

output power and a shutdown in case overheating or undervoltage are present. Different measurements for LDs A to C within an interval of approximately 10*min* were performed. The results of this test are shown in Fig.3.4.2. To reduce the variability of the experiment, the LD marked as D was dropped out of the experiment as a result of its inconsistent behaviour (compared to the rest of samples) when the current was increased. A small variability (in the order of 0.5nm) can be expected as a result of the resolution of the measurement apparatus, however, a larger drop with an increase in current would suggest a possible damage on the LD which could result in possible issues in the experimental measurements.

As shown in Fig.3.4.2, once the electronic board designed for temperature control is implemented, the LD's, specially in the case of LD A, present a much larger degree of stability in wavelength. In the particular case of LD A, no divergence from the initial wavelength of 786*nm* was detected within a test period of 10 minutes. In the other lasers, however, a small drift from the original wavelength (in the order of 1 to 3*nm*) appears. In Fig.3.4.2d it is also observed how the board allows to reduce the input intensity and is still fully operative. Nevertheless, such a decrease of output power does not seem to change the variability of the wavelength, as a small deviation from the original wavelength is observed. It is to be noticed, however, that in this last case the LD showed a reduction in the wavelength instead of the increase appreciated in the rest of the examples which would account for a decrease of the LD package temperature.

Another feature which is observed is that in order to reach a stable wavelength condition a time in the order of 1 minute might be required, although in some cases some variation might occur on larger time scales (e.g. in Fig.3.4.2d in the 8 minute mark). This issue might have some impact on the measurement depending on the time required for the measurement. As discussed previously, the resulting error may be minimized by implementing a linear fitting on the reconstructed waveform as long as the target presents an oscillatory motion.

3.4.2 Characterization of the reference displacement device

The reference displacement plays a key role in the correct implementation of the DSMI method. So far, by the analysis presented in the simulation section, it has been established that the velocity of the reference motion can be directly related to the resulting resolution of the method.

The reference displacement stage is produced by a *PI-LISA 753.3CD* piezoelectric (*PZT*) stage with a maximum travel length of 38μm. This stage is selected as reference stage due to its high linearity, described in the specs in AnnexB. It is also important to note that the stage is equipped with an internal capacitive sensor with a resolution of 2*nm* which later on will be used to compare the actual motion of the PZT with the actual response of the DSMI or the SMI sensor. While other types of stages can also be implemented for DSMI measurement applications, PZT stages may be the best suited for the task as they provide a sufficient travel and velocity range while keeping a small size on the instrument. This type of stages may also allow a relatively simple control as it is possible to operate them in a linear fashion by means of a current control loop, or enable a closed loop reference system based on a capacitive sensor which can be easily attached to the stage.

An initial linearity measurement of the PZT stage is provided by the manufacturer (see Annex B). As observed, and according to manufacturer data, the relative linearity of the measurement stays within ±0.2% (±7.6*nm*) along the total travel of the PZT. It is also noticed that the behavior of the error seems to have a sinusoidal fashion with a zero around 20μm.

Beyond linearity, it is necessary to analyze the PZT response with frequency as this would be a method to adjust the sampling frequency of the DSMI method when the maximum displacement of the target

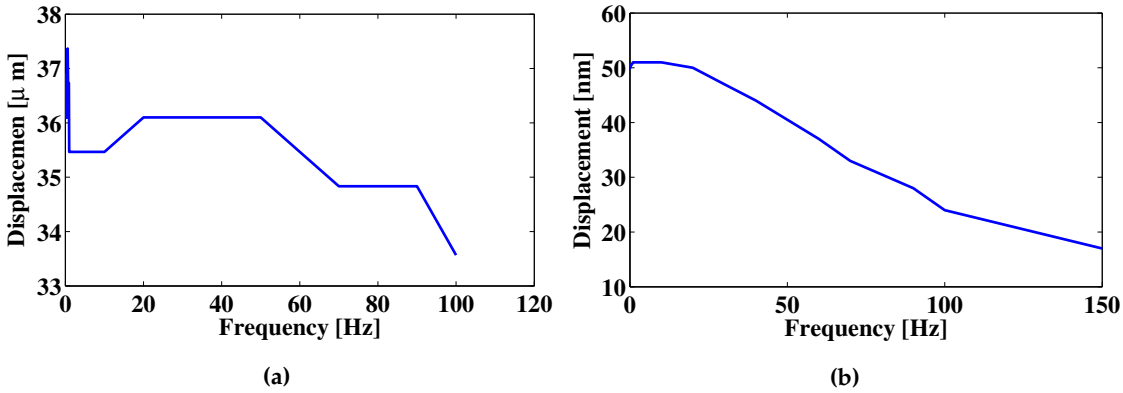

Figure 3.4.3: Frequency response test for the PZT stage used for the reference motion (a) and for the target motion (b).

is used. To test the frequency response, the PZT was subject to different sinusoidal motions with the maximum displacement for a set of frequencies between $[0.1, 100]Hz$ and the corresponding motion was recovered using the internal capacitive sensor located inside of each PZT stage. For each frequency 10 samples containing at least 10 cycles of the sinusoidal motion were acquired and the measured amplitude was calculated as the average of the maximum amplitude between the samples. Each amplitude is then plotted with respect to its corresponding frequency as depicted in Fig.3.4.3.

Fig.3.4.3 shows how the sinusoidal signal suffers of a small decrease of the total amplitude as the frequency increases. Nevertheless, for all studied cases, it is possible to obtain a displacement larger than $34\mu m$ reliably.

This is important as the displacement should be large enough to generate at least a set of 4 transitions to provide an initial measurement. When a similar test was performed using a triangular signal, it was observed that the PZT was capable of following the correct frequency with amplitudes similar to those of the sinusoidal signal, although the displacement suffered a deformation which may be attributed to the "mechanical capacitor-like" behavior of the PZT at larger frequencies. This type of behavior was specially observed for frequencies in the order of $20Hz$. Therefore, it is recommended that for this particular case the reference target stays below $20Hz$ for the complete motion.

Similarly, a test was performed to the stage to be used as a target, which was a PI LISA 753.2CD, which also includes an internal capacitive sensor with $2nm$ resolution. In this case the internal capacitive sensor has a very important role in the experimentation as it is used as gold standard for the DSMI method. It is observed that the amplitude sensed by the PZT rapidly drops for frequencies larger then $20Hz$, as expected from the behavior observed with the reference PZT. In this case the deformation at higher frequencies does not play a key role in the measurement, as the stage will be used primarily with sinusoidal-shaped motions. On the other hand it is clear that even when the amount of motion of the PZT is reduced, the capacitive sensor will provide a sufficiently accurate response to provide a comparison with the results obtained by DSMI.

In terms of the minimum displacement that can be characterized using the target PZT, the limit is not directly introduced by the PZT, but by the signal generator used to feed the PZT controller. For all the cases presented in this Thesis, the PZT driving signal is provided by a *Tektronix AFG3102C* which counts with a $14bit$ resolution and a minimum output of $25mV_{pp}$ ($62nm_{pp}$), which is well below the resolution of the capacitive sensor.

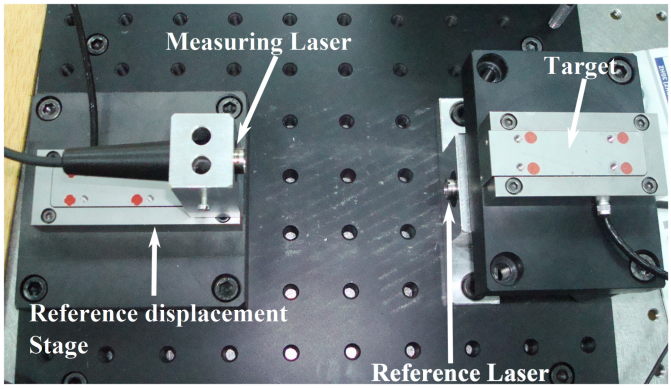

Figure 3.4.4: DSMI Experimental setup of the DSMI prototype. On the left side, L_m is placed over a PZT stage which generates the reference motion. On the right side, it is possible to observe the PZT target and L_r.

3.4.3 Experimental setup and measurements over a controlled target

In order to test the attainable resolution of the DSMI method in laboratory conditions, the prototype shown in Fig.3.4.4 was built. The proof of concept setup consists of two FP $HL7851G$ LDs, each placed inside a Thorlabs $T220230P-B$ collimation tube equipped with a $C230220P-B$ aspheric lens pair with a numerical aperture $NA = 0.55$ in the collimating lens, and $NA = 0.25$ in the focusing lens. The focal length of each of the lenses corresponds to $4.51mm$ and $11.00mm$ respectively. The thread in each tube allows to control the amount of focus obtained by each LD.

After placing the LDs inside of the collimating tube, each tube is attached to the mechanical support shown in Fig.3.4.4. The LD L_r fixation (shown on the right side of the image) is placed directly over an optical board which can be attached or detached from a pneumatic optical table. The LD_m fixation (shown in the left side of the image) is directly fixed on the reference displacement stage (PI-LISA 753.3CD). Next, the target, a PI-LISA 753.2CD, is placed at a distance of approximately $10cm$ from the position of the reference laser. In this case, the setup is built in a way that the distance from the reference LD to the reference displacement stage, and the distance from the measurement LD to the target is nearly equal. This distance, however, can be varied as necessary for a given DSMI measurement and it does not require to be equal for both LDs. Once the setup is placed, both focusing lenses are adjusted to produce an OOP with $C \simeq 1$. As discussed before, the use of this feedback level prevents potential fringe loss as well as provides a good SNR value.

During the measurement process, the reference displacement stage is oscillated in a triangular motion with a peak to peak displacement of $38\mu m$ at different frequencies. The triangular shaped signal presents linear ramps which make easier the processing of the DSMI signal afterwards, as discussed. As explained, measurement is performed only along the positive ramp of the reference motion to reduce possible bias due to change of direction. The OOP signal acquisition is performed using the custom electronic card discussed in Sec.3.1.3. Finally, the signal is acquired using a Tektronix DPO2024 oscilloscope with a $125kS$ window. All of the signals are acquired using a $76\mu m/s$ reference velocity within a time window of $0.4s$ ($f_a = 312.50kHz$). Before the start of the measurement the wavelengths of each laser are measured to be $\lambda_r = 784.95nm$ and $\lambda_m = 777.78nm$.

During the first test, the target is moved in a sinusoidal fashion with fixed peak to peak amplitude of $40nm$ and frequency of 5, 10, 20 and $50Hz$ respectively. Each of the frequencies is acquired at least 10 times in order to test the repeatability of the measurement as well as to evaluate the response of the technique in comparison to the response of the capacitive sensor. The measurement of the error is initially calculated

Freq.[Hz]	$\overline{\text{Err}}$[nm]	σ_{Err}[nm]	Err_{RMS}	Err_{Max}
5	-0.10 ± 1.00	6.49 ± 3.39	6.60 ± 3.30	16.84 ± 8.38
10	-0.47 ± 1.07	6.73 ± 2.69	6.82 ± 2.71	18.83 ± 8.31
20	-0.05 ± 0.46	6.38 ± 2.54	6.40 ± 2.55	17.36 ± 8.93
50	0.07 ± 0.14	7.69 ± 2.02	7.69 ± 2.02	24.19 ± 9.61

Table 3.4.2: Detected error after reconstruction of $40nm$ peak to peak sinusoidal signals with frequencies $5Hz$, $10Hz$, $20Hz$, and $50Hz$. The result shows an average standard deviation error equal or lower than $\lambda/100$.

as the difference between the capacitive sensor response and the DSMI reconstruction, from this difference, the mean, standard deviation, RMS and maximum error are calculated.

A summary of the results obtained with the algorithm discussed above is presented in Tab.3.4.2. It is observed that for the 4 studied frequencies, the average standard deviation of the error (σ_{Err}) and RMS (Err_{RMS}) of the error is below a $\lambda/100$ value. This result, however, is still 1 order of magnitude larger than the ideal value obtained in the simulation stage.

One of the possible causes of this difference is the appearance of shot noise close to the position of the fringes and the appearance of jitter in the OOP signal of the reference laser, as presented in Fig.3.4.5. To limit the effects of noise in the measurement we used a bandpass filter with cut-off frequencies on a fast fourier transform (FFT) band pass filter selected as $fc_{high} = 0.2 f_{SMI}$ for the high pass filter and $fc_{low} = 5 f_{SMI}$ for the low pass filter, where f_{SMI} is the main frequency of the OOP signal and which depends directly on the reference velocity as $f_{SMI} = 2v_{ref}/\lambda_x$.

After applying the bandpass filter, the transitions of the OOP signal are obtained using the previously described threshold on the OOP derivative as well as the zero crossing method. Next, the DSMI signal processing is performed. As it is explained earlier the DSMI processing includes a linear fitting in order to reduce the effects relative to the differences in wavelengths of the LDs. To test the repeatability of the method, 10 samples of each frequency are acquired and analyzed.

An example of the result of a typical reconstruction procedure is illustrated in Fig.3.4.6. When compared with the capacitive sensor readings, the reconstructed waveforms show standard deviations in the order of $7nm$. It is observed that a small delay appears on the reconstructed signal as a result of the fitting process as observed on Fig.3.4.7 where the reconstruction of two amplitude modulated signals is shown. The larger errors on the reconstructed signals are located around the delay areas, but once the delay is removed, the errors are largely decreased.

If the delay in the reconstruction is removed for comparison purposes, it is possible to obtain the results presented in Tab.3.4.3. The results show that when the delay is removed from the reconstruction the errors decrease by almost $2nm$ in the case of σ_{Err} and Err_{RMS} for repetitive motions. In this measurements, it has been noticed that the SNR obtained with the given electronics tends to be better as the reference velocity increases.

Fig.3.4.7 shows a second test performed using a variable modulation depth signal to drive the target. The driving signal is composed by a $10Hz$ sinusoidal displacement of amplitude $300nm$ and modulation depth of 90%. The reference displacement is selected as a ramp-motion with speeds ranging from $38\mu m/s$ to $152\mu m/s$.

The results obtained for this test show comparative values with those presented in the previously studied sinusoidal case, showing in average $\sigma_{Err} = Err_{RMS} \approx 8nm$. It should be stated, however that in some of the studied cases a fitting of order 2 or higher was required to remove the baseline of the reconstructed

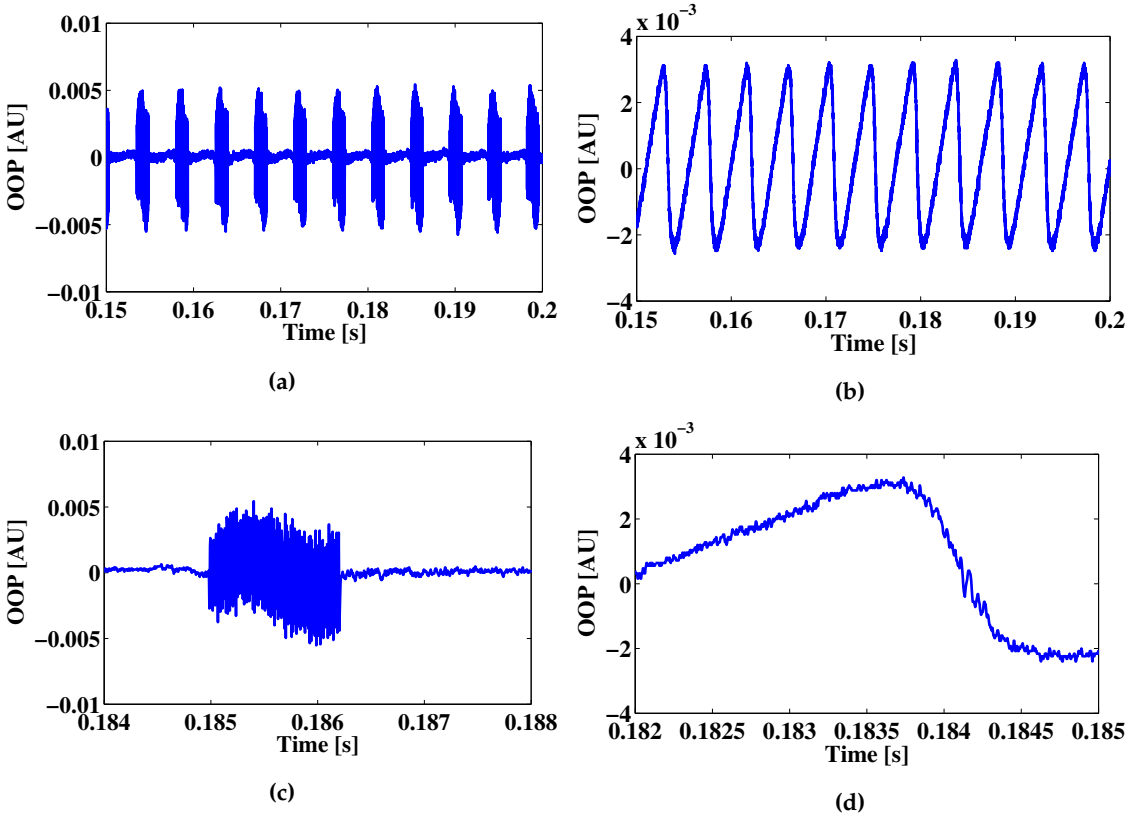

Figure 3.4.5: Example of a strip of the SMI-OOP signals obtained for the measurement of a sinusoidal signal of 20Hz and an amplitude of 40nm. (a) Selection of the OOP of the reference signal. (b)Selection of the OOP of the measurement signal. (c) Focus on a transition of the reference signal showing effects of jitter and shot noise. (d) Focus on a transition of the measurement signal; in this case the transition shows neither jitter nor shot noise.

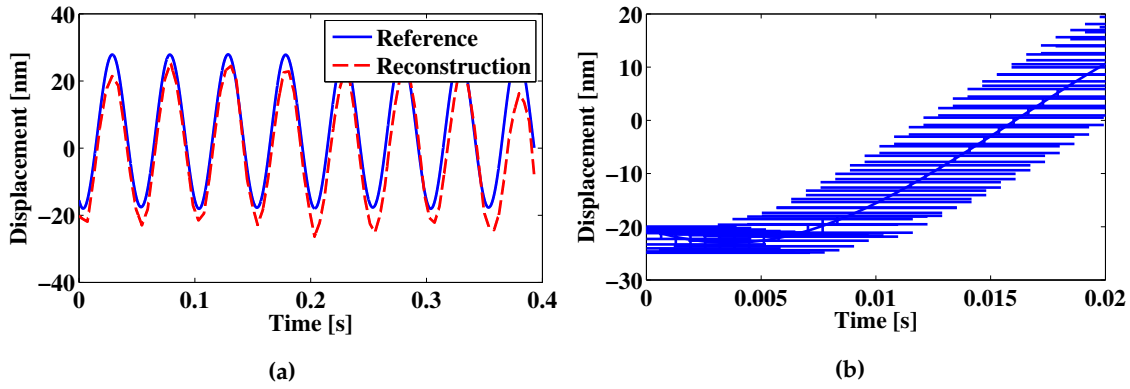

Figure 3.4.6: Reconstruction of a sinusoidal signal of amplitude 50nm and frequency 20Hz . (a) Reconstruction of the displacement (dashed line) compared to original displacement (solid line) . (b) Error bar plot comparing the motion in the period between 0 and 0.02s, the average error in this area shows a variation of 0.68nm.

waveform. This behavior suggests that during certain points of the measurement some type of unstability may have varied the measurement conditions inside the room. This effects were specially observed in the cases where low velocities ($v_{ref} < 76\mu m/s$) were used for the reference displacement.

Therefore, in general it can be stated that the resolution of the method can be considered as $\lambda/100$. It

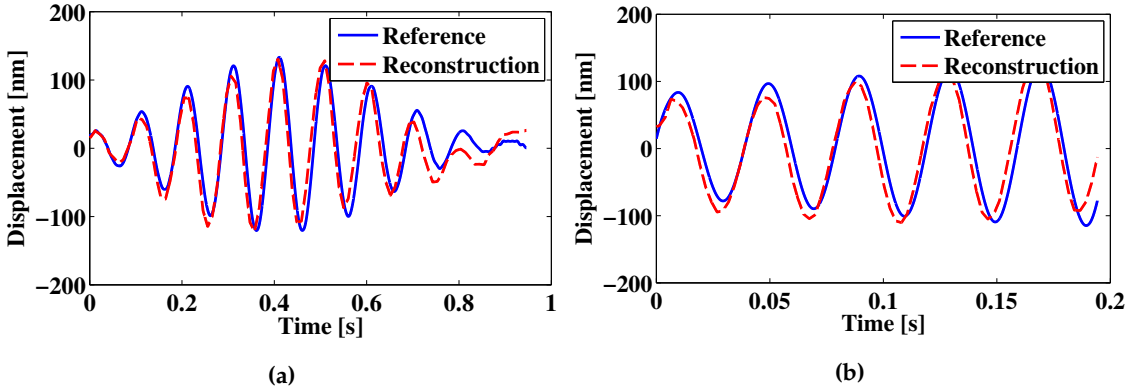

Figure 3.4.7: Example of reconstruction of an amplitude modulated sinusoidal signal for different frequencies. (a) Sinusoidal modulation with 90% modulation depth, maximum displacement 300nm with a reference velocity of 38$\mu m/s$. (b) Sinusoidal modulation with 90% modulation depth, maximum displacement 300nm with a reference velocity of 182$\mu m/s$.

Freq.[Hz]	$\overline{\text{Err}}$[nm]	σ_{Err}[nm]	Err_{RMS}	Err_{Max}
5	0.42 ± 1.56	4.95 ± 1.69	5.21 ± 1.60	10.87 ± 2.84
10	0.78 ± 0.74	4.14 ± 1.49	6.82 ± 2.71	9.06 ± 2.14
20	0.30 ± 0.44	4.05 ± 1.37	4.09 ± 1.36	10.12 ± 1.98
50	0.18 ± 0.16	5.84 ± 2.55	5.85 ± 2.54	20.31 ± 16.30

Table 3.4.3: Detected error after reconstruction of 50nm peak to peak sinusoidal signals with frequencies 5Hz, 10Hz, 20Hz, and 50Hz after removing the reconstruction delay. The result shows an average standard deviation error equal or lower than $\lambda/100$.

should be noticed, nevertheless, that in contrast with the simulations, it was not possible to find an exact correction factor and in all cases it was necessary to apply a fitting of at least order 1 to remove the effects introduced by the difference in wavelength and by the method itself. In addition, in some cases a residual modulation could appear on the reconstructed waveform which would suggest a small variation of the wavelength over time. It is also noticed that the technique has produced good results for displacements of amplitudes close to 300nm, specially in those cases where the DSMI sampling is enough to reconstruct properly the displacement.

While the double LD method shows an important enhancement in terms of attainable resolution when compared with classic SMI reconstruction methods, and enables the measurement of displacements below $\lambda/2$, it also has been observed to require at least two measurement sensors as close as possible, as well as a double amount of processing power. Therefore it has to be wondered if there exists a method to simplify the depicted setup and processing algorithm. In the next section a possible method to face this challenge is described.

3.5 The single laser diode method

From Eq.(3.1.2) one can easily see that the term corresponding to the velocity reference term ($v_r = \lambda_r/2\Delta t_r$) can be substituted by any estimation of the reference velocity. In this work the four following options are considered:

- **Case 1: Use of a reference measurement with a static target.** In this case the measurement takes place in two different instances of time. During the first instance the target is static and the acquisition of the SMI signal is performed for the reference motion only. Once the SMI signal is acquired and stored, the motion to be measured may be triggered and acquired. Next both signals can be processed using the DSMI algorithm described earlier on this chapter. This type of acquisition is only suitable for cases in which the user has some degree of control of the target (e.g. scientific measurements) in which the target can be excited at will. In principle this method could be further expanded to use a stored SMI signal of the given reference motion to simply use it with any target, but we consider that using the same target may introduce some added knowledge for the signal processing, and it may allow the user to know whether the given SMI signal is valid for the process and if any calibration of the optical power may be required.
- **Case 2: Estimation of the average velocity of the SMI OOP signal.** For this case, the SMI measurement signal can be used to estimate the average velocity of the target by using a velocity estimation method based in FFT analysis. Since the DSMI method relies on the use of linear-like displacements, the average velocity during the studied period will stay constant and small variations will not appear in the main harmonic of the FFT. It is to be noticed that this type of processing is only limited to linear reference displacements, since the sign of the velocity is typically not observed for velocity processing, although they may be applicable. Care should be taken to apply the correct velocity signs during the processing to avoid a possible sign inversion in the reconstructed signal. This type of processing may be encouraged when no other sensors on the stage are available and no control over the target is possible.
- **Case 3: Contact sensor attached to the reference displacement stage.** In this case the reference displacement/velocity measurement can be obtained using e.g. a contact sensor (e.g. accelerometer, PZT, etc) with enough resolution placed on the translation stage generating the reference motion. The values obtained by the contact sensor can be used either to calculate the average speed during the motion or to generate an artificial SMI signal to be used as reference. This type of setup can be used in those cases in which the user has no control over the target motion and the stage producing the reference motion contains an internal sensor (e.g a PZT stage). The major drawback of this type of application may be related to possible contact issues between the contact sensor and the reference stage as well as the added electronics and costs entailed by the contact sensor.
- **Case 4: Estimation of the velocity according to the theoretical description of the displacement stage.** This type of configuration assumes some previous knowledge and control over the stage producing the reference displacement. An example of this case is the PZT displacement stages in which the displacement is directly proportional to the applied voltage. Since the driving voltage is controlled by the user, it is possible to model the behavior of the stage and similarly estimate the reference SMI signal. Thus, this model is discouraged for most uses and should be only used if no other option is available. As in the case of the previous two methods, no control over the target is required, but a good understanding of the reference displacement stage is a must. Possible errors on reconstruction may arise as a result of stage dynamics not taken into account on the model.

Each of the solutions poses its own set of advantages and disadvantages as, for instance, they may introduce inaccuracies due to the use of velocity estimators which may vary over time (e.g. due to the mechanics of the displacement stage), the requirement of adding external sensors to measure the reference

Parameter	Symbol	Value	Units
Measurement wavelength	λ_m	785.0	nm
Reference velocity	v_r	38.0	$\mu m/s$
Reference frequency	f_1	1.0	Hz
Displacement amplitude 1	A_{1pp}	30.0	nm
Displacement amplitude 2	A_{2pp}	12.0	nm
Displacement amplitude 3	A_{3pp}	5.0	nm
Distance to the target	D	20	cm
Time window	t_T	0.5	s
Acquisition rate	f_a	250.0	kS/s

Table 3.5.1: Parameters used for the simulation of the mechanically modulated OOP signal processing.

displacement, limitations in terms of resolution and time response of the external sensor, etc. The main advantage of using one of the described options is the simplification of the DSMI setup to a single laser diode, reducing its complexity and the processing time in the reconstruction algorithm as only one OOP signal needs to be analyzed. Besides, a single laser diode reduces the number of effects that may affect the reconstruction as a result of intrinsic LD dynamics since the effects will be limited to a single LD.

In this section, some of the proposed options are studied to test their feasibility and if there exists any improvement in terms of resolution compared to the double LD method. It is important to note that the implementation of this type of setup can be referred as mechanically modulated SMI, as in some cases it could be argued that the analysis does not apply a differential approach.

3.5.1 Simulation

The simulations presented in this section are focused on the second and third options presented above. The first option is not simulated since the results would be the same to the results presented in the double laser diode method, as they would refer to the different effects studied to observe possible errors. The fourth option is also hard to simulate, as it partially contains the processing proposed for the second case, given that our work uses PZT stages to produce the reference motion and assumes that the structure holding the DSMI sensor is properly isolated from mechanical vibrations. The parameters used in this set of simulations is presented in Tab.3.5.1.

As in previous simulations, the target displacement has been obtained adding different sinusoidal signals, in this case using:

$$\Delta D_{exp} = A_{1pp}\sin(2\pi f_1 t) - A_{2pp}\sin(8\pi f_1 t + \pi/5) - A_{3pp}\sin(\pi f_1 t + \pi/3) \tag{3.5.1}$$

As in the case of the DSMI technique based on a double LDs, different tests are performed in order to observe the effects of using different SNR factors as well as the effects of C in the signal analysis. Each analysis is performed for the methods (case 2 and case 3) described above.

3.5.1.1 Case 2: Estimation of the average velocity of the SMI OOP signal

In this case, the reference velocity is estimated by calculating the Fourier spectra of the acquired OOP. After obtaining the reference displacement, the analysis continues using the DSMI formulation. Results of this type of estimation are shown in Tab.3.5.2.

C[AU]	SNR[dB]	$\widehat{\mathbf{v_r}}$[μm/s]	$\overline{\mathbf{Err}}$[nm]	$\sigma_{\mathbf{Err}}$[nm]	$\mathbf{Err_{RMS}}$[nm]	$\mathbf{Err_{Max}}$[nm]
0.98	20	38.47	$(-7.58 \pm 5.85) \times 10^{-14}$	2.47 ± 0.03	2.47 ± 0.03	5.61 ± 0.04
0.98	10	38.47	$(-4.91 \pm 6.74) \times 10^{-14}$	2.46 ± 0.13	2.46 ± 0.13	5.74 ± 0.19
0.98	6	38.47	$(-4.79 \pm 6.58) \times 10^{-14}$	2.53 ± 0.18	2.53 ± 0.18	5.66 ± 0.23
0.98	3	38.47	$(-9.76 \pm 8.85) \times 10^{-14}$	2.37 ± 0.13	2.37 ± 0.13	5.85 ± 0.25
0.98	0	38.47	$(-4.78 \pm 4.96) \times 10^{-14}$	2.57 ± 0.30	2.57 ± 0.30	5.81 ± 0.31
0.98	−3	38.47	$(-8.25 \pm 1.05) \times 10^{-14}$	2.48 ± 0.79	2.48 ± 0.79	6.85 ± 1.23
0.49	20	38.47	$(-4.29 \pm 5.77) \times 10^{-14}$	2.94 ± 0.07	2.94 ± 0.07	5.97 ± 0.14
0.49	10	38.47	$(-12.90 \pm 22.98) \times 10^{-14}$	2.87 ± 0.14	2.87 ± 0.14	6.11 ± 0.27
0.49	6	38.47	$(-5.65 \pm 6.17) \times 10^{-14}$	2.83 ± 0.32	2.83 ± 0.32	6.25 ± 0.24
0.49	3	38.47	$(-6.41 \pm 5.97) \times 10^{-14}$	2.99 ± 0.34	2.99 ± 0.34	6.32 ± 0.38
0.49	0	38.47	$(-4.22 \pm 9.69) \times 10^{-14}$	3.21 ± 0.35	3.21 ± 0.35	6.72 ± 0.50
0.49	−3	38.47	$(-4.19 \pm 7.06) \times 10^{-14}$	2.71 ± 0.62	2.71 ± 0.62	7.72 ± 1.12
0.30	20	38.47	$(-3.63 \pm 1.07) \times 10^{-14}$	3.11 ± 0.08	3.11 ± 0.08	6.22 ± 0.14
0.30	10	38.47	$(-0.64 \pm 28.06) \times 10^{-14}$	3.06 ± 0.16	3.06 ± 0.16	6.29 ± 0.24
0.30	6	38.47	$(-8.99 \pm 7.05) \times 10^{-14}$	2.97 ± 0.36	2.97 ± 0.36	6.58 ± 0.51
0.30	3	38.47	$(-4.61 \pm 5.85) \times 10^{-14}$	3.27 ± 0.61	3.27 ± 0.61	6.83 ± 0.98
0.30	0	38.47	$(-6.09 \pm 6.46) \times 10^{-14}$	3.59 ± 0.44	3.59 ± 0.44	7.83 ± 0.68
0.30	−3	38.47	$(-6.43 \pm 4.63) \times 10^{-14}$	3.88 ± 1.10	3.88 ± 1.10	10.22 ± 2.23
0.10	20	38.47	$(-5.62 \pm 6.51) \times 10^{-14}$	3.18 ± 0.11	3.18 ± 0.11	6.85 ± 0.25
0.10	10	38.47	$(-7.96 \pm 9.22) \times 10^{-14}$	3.19 ± 0.19	3.19 ± 0.19	6.94 ± 0.30
0.10	6	38.47	$(-6.96 \pm 4.46) \times 10^{-14}$	3.38 ± 0.37	3.38 ± 0.37	7.35 ± 0.59
0.10	3	38.47	$(-5.23 \pm 8.80) \times 10^{-14}$	3.21 ± 0.47	3.21 ± 0.47	7.83 ± 1.12
0.10	0	38.47	$(-7.95 \pm 43.39) \times 10^{-14}$	24.93 ± 68.74	24.93 ± 68.74	45.58 ± 1.18
0.10	−3	38.47	$(-1.19 \pm 5.02) \times 10^{-12}$	815.61 ± 552.92	815.61 ± 552.92	1498.59 ± 956.99

Table 3.5.2: Set of results for different parameters affecting a SMI OOP during a measurement based in mechanically modulated SMI.

As in the case of the evaluation of noise effects in the case of a double LD DSMI setup, the results provided in Tab.3.5.2 correspond to the average of ten consecutive simulations in the same conditions of C with white additive noise incorporated on the signal. An increase in the number of simulations did not show a significant difference in the results presented on the table (the variations between individual measurements are in the order of $0.02nm$, and thus are smaller than the expected $\lambda/100$ resolution of the method).

The results obtained using this method show a reduction in resolution when compared to the practical results attained with the DSMI method using two LDs. Again, the values of error in standard deviation tend to be in the order of $3nm$. In contrast with previous results, however, it is observed that a small offset appears on the reconstructed velocity which can be explained by the limits in resolution of the velocity estimation method. Therefore, it is necessary to apply a removal of the mean value of the reconstructed velocity previous to the velocity integration in order to reduce possible the errors on the displacement reconstruction. As a result of this processing step, it is possible to remove the linear fitting step from the algorithm. Nevertheless, this also carries an issue as the measurable bandwidth is decreased as displacements with constant velocity are no longer measurable.

Examples of the resulting reconstructions and errors for a ramp and a triangular displacement are presented in Fig.3.5.1.

It should also be noticed that, in concordance with the results observed previously, the SNR limits the achievable resolution and the capacity of the algorithm to provide a reconstruction. Also the C factor seems

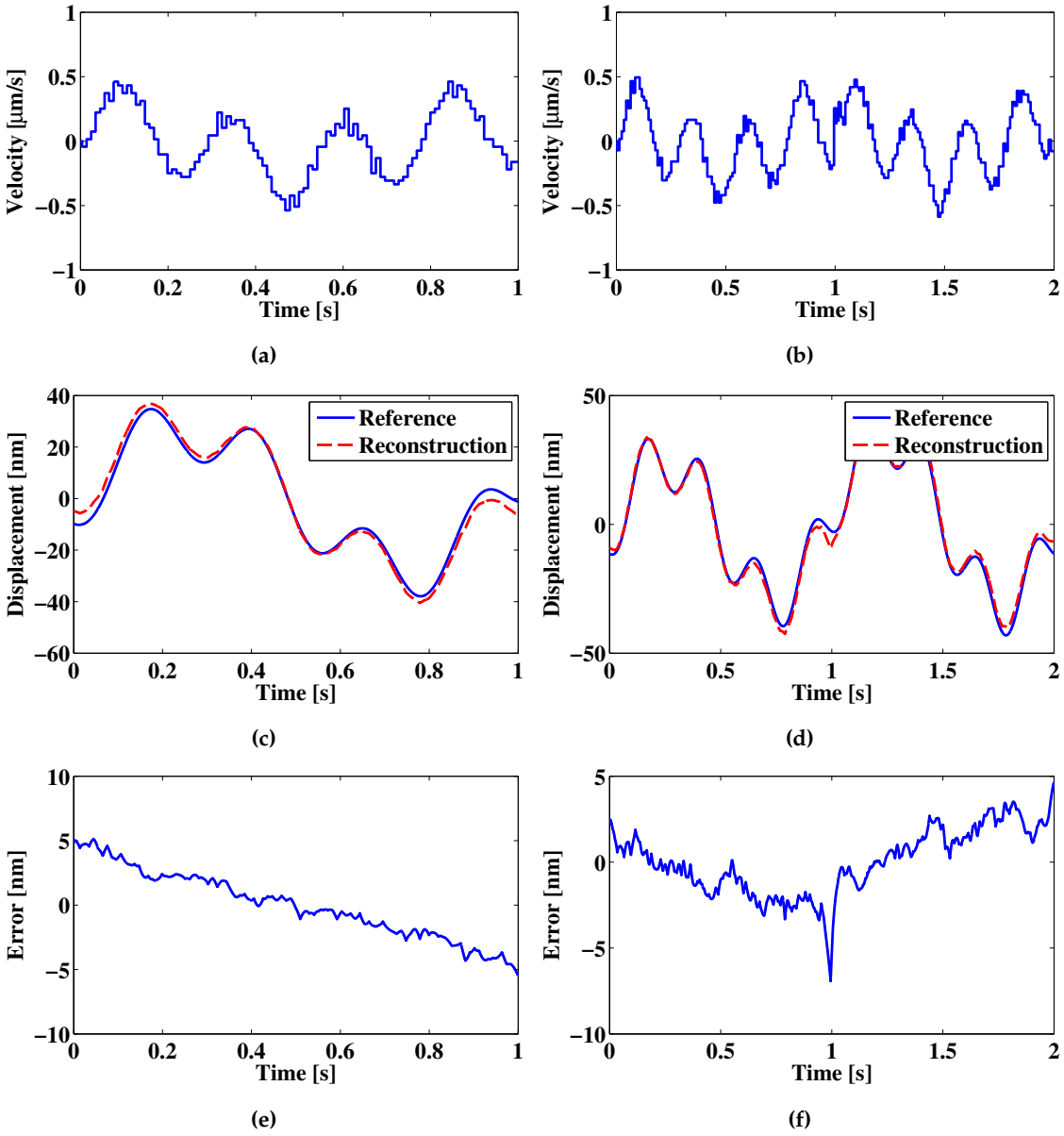

Figure 3.5.1: Example of velocity and displacement reconstructions and obtained errors for the cases of a ramp displacement and triangular displacement for Case 2 with $C = 0.98$ and $SNR = 6dB$. (a) Example of a velocity reconstruction for a ramp displacement reference. (b) Example of a velocity reconstruction for a triangular displacement reference. (c) Example of displacement reconstruction for a ramp displacement reference. (d) Example of displacement reconstruction for a triangular displacement reference. (e) Example of displacement error for a ramp displacement reference. (f)Example of displacement error for a triangular displacement.

to have an impact in this case as it introduces a peak on the error for values of $C \approx 0.10$ with low levels of SNR (0 and $-3dB$).

In the case of a triangular driving reference modulation the observed theoretical error is similar to the case where a ramp-like reference is applied. The main difference in the processing takes place during the transition between the positive and negative ramps, where a small discontinuity appears causing a peak in the error values.

In practice the peak discontinuity may behave "randomly" (as due to mechanical elastic behavior, small transients and non-linear displacements may be expected), which would make hard to predict the overall motion around this area. Thus, the analysis of mechanically modulated signals with ramp-like displacements as a reference should be preferred when this processing method is used.

3.5.1.2 Case 3: Contact sensor attached to the reference displacement stage

As described above, the use of an external sensor can also be used to estimate the velocity of the reference displacement. This could be measured either using directly a velocity sensor, or a displacement sensor, which would require the appropriate conversion to velocity.

In the case of this simulation, a displacement sensor is used for this purpose, to be consistent with the possible setup using the LISA-753.3CD PZT displacement stage. To produce a response similar to that of the PZT, the $2nm$ resolution of the sensor is applied to the simulated displacement, and finally a step behavior according to the limits given by the digital to analogue converter used in the measurement is applied to the signal. Finally, the mechanically modulated signal processing is applied as in the velocity estimation using the OOP signal.

The parameters corresponding to this simulation can be found in Tab.3.5.1. As in the previous examples each simulation is performed at least 10 times. The results of the simulation are presented in Tab.3.5.3. It is observed that after setting the numeric conversion on the displacement ramp, the reference velocity is estimated as the slope of the ramp which has a value $\widehat{v_r} = 38.02\mu m/s$. The signal processing is applied in a similar fashion to the one discussed for Case 2 of the current section.

The results presented in Tab.3.5.3 show good agreement with those obtained for the self reference method based on the estimation of velocity using the OOP signal presented in the previous subsection. As in that case, larger errors can be related to the decrease in C value and SNR.

The use of an external sensor also produces indirect benefits as in some cases there may be issues in the detection of the sign of the transitions. In such cases, it is possible to set the correct sign on the detection by looking at the response of the external sensor. Also, it is observed that errors tend to increase towards the edges of the window with a slope in the order of $10nm/s$ as shown in Fig.3.5.2.

As in the simulations presented for case 2, similar results have been obtained using a triangular reference modulation instead of a ramp modulation. A peak error appears during the change of direction of the triangular driving signal. Again, as a result of possible non-linearities in the displacement when a stage changes its traveling direction, linear ramp-like displacements should be preferred whenever possible.

In comparison to the simulation results of the double LD method presented earlier in this chapter, results show higher error values. This is well in agreement with the expectations of using a single LD, since the number of unknowns in the reference motion is increased, and several calculations depend on a model of displacement of the reference translation stage. Yet, it is also remarked that even with the increased number of unknowns, the estimated resolution rests within a $\lambda/100$ value in simulations, which is worth to test in a practical setup due to the reduction of complexity in the setup.

As depicted in Fig.3.5.2, the reconstructed error tends to be smaller when an external sensor is used than in the case where the velocity is estimated using the SMI measurement signal. This suggests that the resolution of the velocity measurement would play a higher role than expected originally in the displacement estimation. We attribute this variations between the given results to the accuracy in the detection of the reference velocity as in the case of the external sensor the error in the measurement of velocity is in the order of $0.02\mu m/s$, while in the case of the estimation of the OOP signal velocity it is in the order of $0.50\mu m/s$. Thus,

C[AU]	SNR[DB]	$\overline{\text{Err}}$[nm]	σ_{Err}[nm]	Err_{RMS}[nm]	Err_{Max}[nm]
0.98	20	$(-7.20 \pm 7.37) \times 10^{-14}$	2.08 ± 0.04	2.08 ± 0.04	5.15 ± 0.08
0.98	10	$(-5.96 \pm 5.09) \times 10^{-14}$	1.97 ± 0.08	1.97 ± 0.08	5.30 ± 0.18
0.98	6	$(-6.74 \pm 7.53) \times 10^{-14}$	2.02 ± 0.16	2.02 ± 0.16	5.18 ± 0.29
0.98	3	$(-7.90 \pm 6.33) \times 10^{-14}$	2.05 ± 0.19	2.05 ± 0.19	5.26 ± 0.32
0.98	0	$(-1.72 \pm 9.80) \times 10^{-14}$	2.09 ± 0.33	2.09 ± 0.33	5.52 ± 0.42
0.98	−3	$(-9.90 \pm 9.45) \times 10^{-14}$	1.98 ± 0.37	1.98 ± 0.37	6.00 ± 0.77
0.49	20	$(-5.59 \pm 4.59) \times 10^{-14}$	2.67 ± 0.05	2.67 ± 0.05	5.67 ± 0.20
0.49	10	$(-3.77 \pm 10.45) \times 10^{-14}$	2.75 ± 0.15	2.75 ± 0.15	5.69 ± 0.34
0.49	6	$(3.27 \pm 29.56) \times 10^{-14}$	2.83 ± 0.17	2.83 ± 0.17	5.66 ± 0.43
0.49	3	$(-7.95 \pm 5.12) \times 10^{-14}$	2.66 ± 0.20	2.66 ± 0.20	6.02 ± 0.27
0.49	0	$(-3.76 \pm 11.32) \times 10^{-14}$	2.92 ± 0.39	2.92 ± 0.39	6.39 ± 0.53
0.49	−3	$(-4.26 \pm 4.67) \times 10^{-14}$	3.05 ± 0.94	3.05 ± 0.94	8.87 ± 1.46
0.30	20	$(-4.78 \pm 6.75) \times 10^{-14}$	2.85 ± 0.08	2.85 ± 0.08	5.88 ± 0.15
0.30	10	$(-0.64 \pm 11.41) \times 10^{-14}$	2.78 ± 0.12	2.78 ± 0.12	6.01 ± 0.38
0.30	6	$(-5.51 \pm 9.95) \times 10^{-14}$	2.77 ± 0.27	2.77 ± 0.27	6.37 ± 0.44
0.30	3	$(-6.70 \pm 7.59) \times 10^{-14}$	2.91 ± 0.37	2.91 ± 0.37	6.38 ± 0.58
0.30	0	$(-4.75 \pm 8.44) \times 10^{-14}$	3.17 ± 0.40	3.17 ± 0.40	7.08 ± 0.66
0.30	−3	$(-0.10 \pm 16.58) \times 10^{-14}$	3.03 ± 0.64	3.03 ± 0.64	8.70 ± 1.34
0.10	20	$(-7.66 \pm 10.51) \times 10^{-14}$	2.95 ± 0.07	2.95 ± 0.07	6.32 ± 0.29
0.10	10	$(2.55 \pm 17.34) \times 10^{-14}$	2.99 ± 0.19	2.99 ± 0.19	6.38 ± 0.39
0.10	6	$(-6.74 \pm 7.53) \times 10^{-14}$	2.02 ± 0.16	2.02 ± 0.16	5.18 ± 0.29
0.10	3	$(-4.58 \pm 13.97) \times 10^{-14}$	3.07 ± 0.63	3.07 ± 0.63	6.77 ± 1.04
0.10	0	$(-6.24 \pm 9.11) \times 10^{-14}$	3.36 ± 0.54	3.36 ± 0.54	8.50 ± 1.21
0.10	−3	$(-1.17 \pm 8.67) \times 10^{-13}$	182.75 ± 75.10	182.75 ± 75.10	387.42 ± 143.51

Table 3.5.3: Example of measurement errors for a simulation of a mechanically modulated SMI setup based in an external sensor reference measurement.

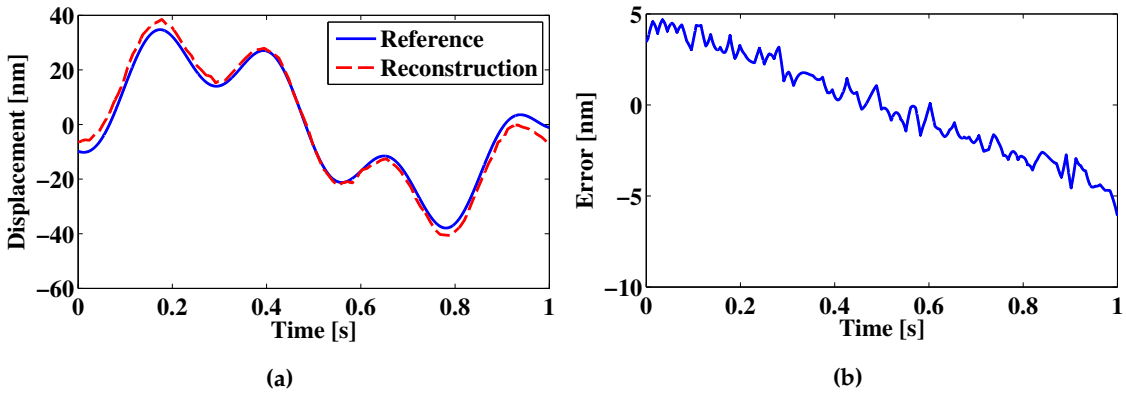

Figure 3.5.2: Example of simulation of Case 3 with $C = 0.5$ and $SNR = 6dB$. (a) Displacement reconstruction. (b) Error on the displacement estimation.

the method of estimation of $\widehat{v_r}$ plays a key role in the case of mechanically modulated SMI measurements.

3.5.2 Experimental result

In the previous subsection, it was illustrated by means of simulation that it might be possible to reduce the DSMI setup while attaining similar resolutions to those obtained in practical laboratory conditions.

To test the proposed methods, different OOP signals were acquired and evaluated using the frequency

Method	$\overline{\text{Err}}[nm]$	σ_{Err}[nm]	Err_{RMS}[nm]	Err_{Max}[nm]
Double LD Setup	0.24	4.29	4.29	14.00
Single LD Case 2	0.24	4.63	4.63	14.45
Single LD Case 3	0.24	4.64	4.64	14.46

Table 3.5.4: Error comparison between the Double LD setups and method case 2 and 3 for the signal presented in Fig.3.5.3. No significant difference in the error magnitudes is observed.

method and the reference displacement method described above. Before the acquisition, all mechanical couplings in the setup were tightened to reduce the mechanical noise, as well as miss-adjustment effects introduced in the measurement. Fig.3.5.3 show a good agreement of the different methods implemented for the reconstruction with the simulations presented in Sec.3.5.1.

The reference motion for the proposed study cases used a ramp like displacement with an estimated velocity of $76.00\mu m/s$. The target motion uses a variable amplitude modulation in an attempt to show that the methods are capable of measuring different amplitudes.

A comparison of the errors obtained for different measurement methods (double LD method, and single LD method case 2 and case 3) of the signal presented in Fig.3.5.3 is shown in Tab.3.5.4. When the estimated velocity for case 2 and 3 is compared, a difference of $0.35\mu m/s$ can be observed ($\widehat{v_r} = 76.80\mu m/s$ for case 2 and $\widehat{v_r} = 76.45\mu m/s$ for case 3). From the results presented in Tab.3.5.4, it is observed that the errors obtained in all the cases have a similar amplitude to that presented by the double LD setup reconstruction. The increase of error found in the measurement corresponds to $0.30nm$, which is well below to the $\lambda/100$ limit considered in all the scenarios studied so far. The better agreement between simulation and experimental results in the single diode setup suggests that laser dynamics may be playing a larger role than expected on the two LD setup. As a result, the reduction of complexity on the setup leads to a similar resolution limit between the double LD and a single LD setup. Furthermore, this suggests that having a better control of the LD dynamics in the 2 LD setup could potentially lead to resolutions closer to the theoretical limit.

From the studied cases, the main limitation in resolution has been observed when the reference stage suffers a degree of variation in its velocity along the ramp displacement, thus not behaving linearly, so only a mean estimation of the reference velocity is available. In such cases, if the variation is large enough, larger errors may be introduced in the measurement. While the displacement information can be extracted by implementing a $4th$ order polynomial fitting in the velocity reconstruction, in such cases it would be recommended to use a double LD setup.

To sum up, the results described in this section have shown the possibility of using a simplified DSMI setup based in only one laser for the estimation of target displacements with amplitudes smaller than $\lambda/2$. The use of this type of setups can reduce the minimum attainable error in reconstruction as a result of mechanical nonlinearities in the mechanical stage, or changes in the dynamic properties of the LD and the OOP signal due to the degradation of the LD over time.

3.6 Conclusion

In this chapter a method to allow the reconstruction of displacements with amplitudes smaller than $\lambda/2$ with a estimated resolution in the order of $\lambda/100$ for typical cases was presented. The method has been named differential self-mixing interferometry since in the first portrayed implementation, two OOP signals are acquired at the same time and the displacement is calculated as a function of the difference in phase

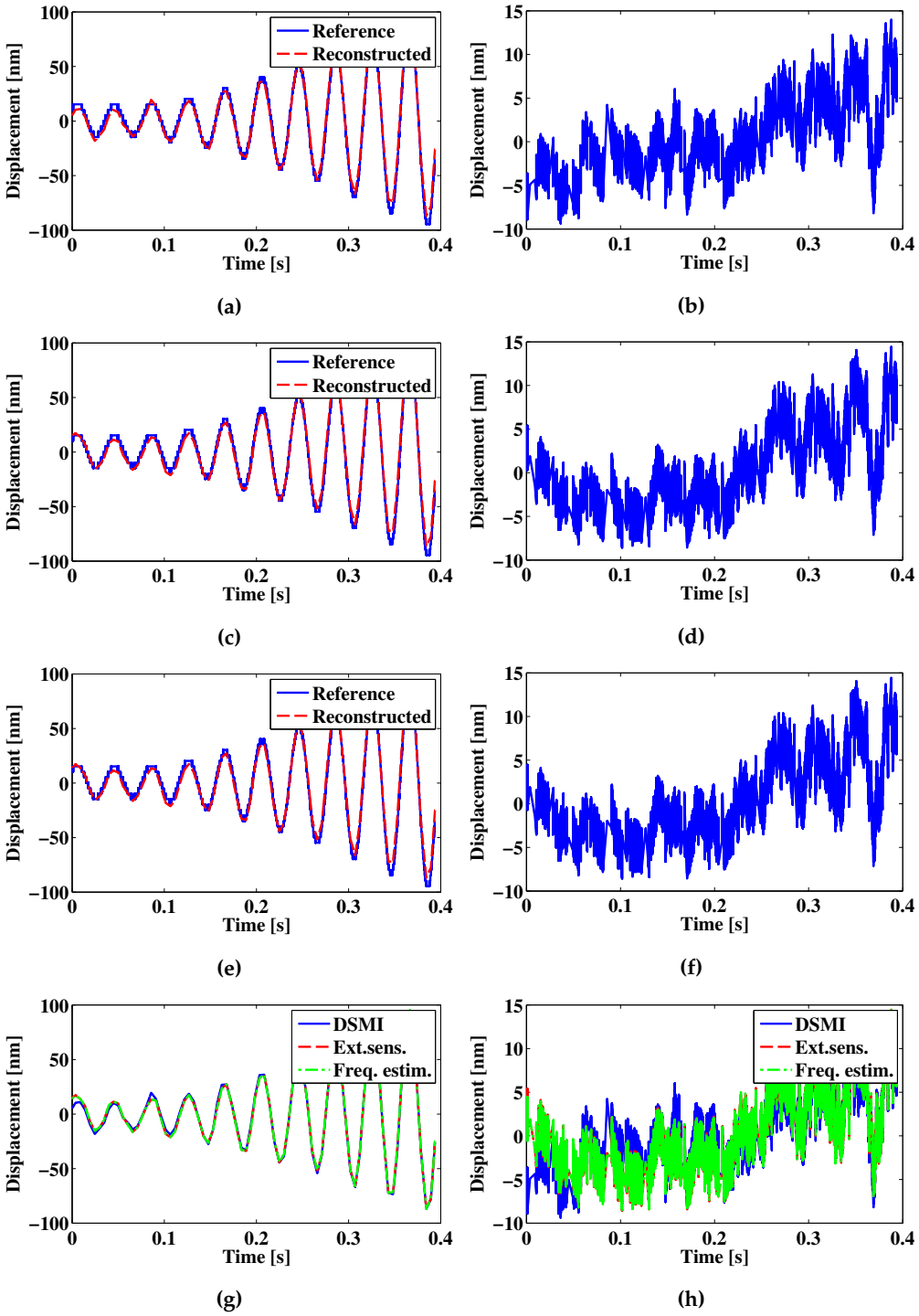

Figure 3.5.3: Examples of reconstruction and error for an experimental amplitude modulated signal. (a,b) Reconstruction of a modulated signal using the DSMI double LD setup and corresponding error, respectively. (c,d) Reconstruction using an external capacitive sensor as velocity reference. (e,f) Reconstruction and corresponding error for a velocity estimation based on the SMI frequency. (g,h) Comparison of the three displacement reconstruction values as well as the corresponding reconstruction error in the three cases discussed.

between a reference and a measurement signals. Later implementations have been renamed as mechanically modulated SMI since this better describes the method's execution and processing.

Along the first section of the chapter, a mathematical model for DSMI has been presented. The model shows that it is possible to calculate displacements of small amplitude by comparing the differences in localized velocities that may happen between detected transitions in a reference signal that has a velocity $v_r(t)$ and a measurement signal with a velocity $v_m(t) = v_r(t) + \Delta v(t)$. From this theoretical model, it has been observed that the resolution of the method is related to several factors such as the sampling acquisition f_a, the reference velocity v_r, and the wavelength of the LD among others.

In the second section, a double LD DSMI setup has been studied using a simulation and a experimental implementation. Simulations showed that in theory the attainable resolution could reach values of $\lambda/2000$ in ideal conditions. When different types of noise and expected effects in the measurement were included in the simulation, the detected error value increased an order above $\lambda/1000$. Also a simulation to test the possibility of reconstruction using a triangular reference signal was tested, showing errors in a similar order of magnitude to those obtained in the ramp displacement measurements. After studying the theoretical performance of the method, a practical implementation was performed. In this case several measurements were acquired and analyzed using the DSMI method and the results were compared to a capacitive sensor response with a resolution of $2nm$. In this case, the deviation errors were within a value of$\lambda/100$. This increase of the error in one order of magnitude is related to different non linearities in the reference displacement, to the presence of experimental noise, as well as the dynamic behavior of the laser during the measurement.

Finally, in the third section, alternative DSMI setups based in the use of a single LD are discussed. In general, the errors obtained in theoretical and practical measurements are comparable to the results observed in the experimental measurements of the double LD setup. Furthermore, similar errors were also found when the measurements were evaluated using two of the suggested implementations (estimation of SMI velocity using the frequency response of the signal, and using an external sensor). In the case of the use of a pre-stored reference OOP signal, an increase of the error by a factor of 2 was found. This increase is attributed to effects caused by delays observed during the triggering of the reference motion and the target stimuli. A better triggering might reduce the error to the levels observed in the rest of the cases.

The results obtained in this chapter suggest that using SMI along with a reference modulation, or other kind of modulation which allows to obtain a reference OOP with a nearly constant time difference between contiguous transitions, can be used to detect variations of the optical path with amplitudes smaller than $\lambda/2$ with a reduced and self-aligned setup. The expected resolution shows a value close to $\lambda/100$ for most of the studied experimental conditions. Also it has been noticed that a large amount of error can appear in practical measurements when a triangular displacement is used as a result of the non linear behavior around the peaks of the driving motion. Thus, even when in theory it is possible to use triangular signals for a reference motion, it is strongly recommended to restrain the characterization of displacements using DSMI to ramp reference motions.

In the next chapter some applications developed during the course of this work are presented. The presented applications have been analyzed using either the DSMI method, in one of its possible implementations, or SMI. The decision to use the former or the later technique is taken as a function of the typical amplitude detected for the corresponding application.

4. Applications

Along the previous chapters, the theoretical state of the art of SMI technique has been presented, and the DSMI technique has been introduced. In both cases, basic examples of the method for its use on "direct" displacement measurements have been presented. Nevertheless, the capabilities of these methods extend far beyond the direct displacement measurement approach. An example of such capabilities is presented e.g. in Sec.2.3.4, where the distance measurement method is modified to map the form of fan blades. As in that case, similar approaches are possible using displacement measurement methods, both for SMI and for DSMI.

In this Chapter, two indirect measurement approaches using the SMI and the DSMI principles are explored. In the two cases the object being measured is subjected to an optical path change by the mechanical change of an interface, or by the change of the medium in which the measurement is taking place. After observing a sample of the resulting equivalent optical path variation for each case, the decision of using SMI or DSMI for the measurement will be taken. The results are presented in the chronological order in which they were obtained.

First, in Sec.4.1, SMI is used for a biophotonics application in order to measure the shape of the arterial pulse wave (*APW*) *in vivo* on a human fingernail. SMI shows its capability to measure with a good degree of accuracy some of the parameters related to the arterial pulse wave, detecting traits such as the dichrotic notch and frequency of the beat which are present in the recovered signal. Attempts to perform the same measurement on direct skin sections were also tested. While it is possible to recover the signal under some experimental conditions, it was not possible to produce a large repeatability of the results under a set of constrained conditions. Moreover, as it is shown in Sec.4.1 the use of SMI on direct skin may pose a threat to a patient depending on the wavelength and the power of the exposure.

Next, in Sec.4.2, an approach to measure the motion of a microcantilever in the nanometric scale is reported. In this case, since the expected amplitude of the cantilever deflection is below the $\lambda/2$ range, the DSMI method is selected. As explained in the section, the use of cantilever based sensors can expand the reach of possible applications for the SMI and DSMI methods allowing to characterize different micrometric scale properties of matter, such as profile, roughness, surface forces, etc. The study shows that the method works well with typical aluminium-coated cantilevers even requiring an amount of de-focusing to provide a measurement signal within the expected feedback regime. As a result, it is proposed that the use of non-coated cantilevers paired with the DSMI method may produce an advantage over other methods, by reducing the bending induced by the bimetallic effect observed in coated cantilevers.

As a closure, the chapter presents some concluding remarks and ideas regarding the applications presented.

4.1 SMI for the measurement of the arterial pulse wave

A continuous effort to increase the quality of preventive healthcare and disease treatment standards has been a trend for several years and is expected to follow on with the increased ageing of the world population

and the higher life standards of the last decades. A quick search on Google Scholar easily shows this trend as only in 2016 around 139000 results can be found showing different types of health-related sensors and applications. Focusing onto heart diseases and vascular health related sensors around 9900 hits can be found in the same website. From these results, more than 50% describe non invasive and non-contact based methods, and about 3400 use optical based technologies, showing the strong push of biophotonic technologies in this particular sector.

Optical sensors are an interesting choice for health detection interfaces because of their high resolution, relatively small size and low cost, together with a variety of measurement principles which may be applied in different situations. Besides, optical based sensors, in many cases, can be assembled into non contact and non invasive devices which significantly increase the quality of patient care. Some examples of this type of technology have been already incorporated in different everyday objects which now are commodities, for instance laser based thermometers, pulse oximeters or exercising wrist bands.

In particular, the development of non-invasive methods for the acquisition and interpretation of cardiovascular signals has gained importance in the last years because of the increase in cardiovascular diseases around the world and the relevance of such diseases in an aging world. Several cardiac waves, and their relationship or delay, are typically subject of study from the clinical point of view as they can provide information regarding the general and localized state of the cardiovascular system of an individual.

As described by O'Rourke and Gallagher in [134], throughout the history of clinical medicine the arterial pulse wave has been a key tool used for cardiovascular examination purposes. As soon as in the late XIXth century, early analysis of the pulse wave showed possibilities in the detection of diseases such as hypertension and chronic nephritis. In many cases, however, the study of the waveform pattern was overlooked, as during the XXth century as measurements from a sphygmomanometer were enough to obtain a reasonable estimation of the blood pressure and pulse repetition. More recently, the introduction of other instruments based on improved technology such as tonometers and optical photopletismograph meters has renewed the interest in the complete analysis of the pulse waveform shape in different parts of the body,and the relationships introduced by their changes in amplitude or their relative delays [134–137].

The pulse wave signal is typically composed by a superposition of two waves [138], as presented in Fig.4.1.1. First, an incident wave $\epsilon_i(t)$ appears as a result of the increase of pressure caused during the left ventricular contraction [139]. Such an increase of pressure exerts a force on the arterial walls as blood travels through the aortic vessel. When a branching point is reached, different waves are back reflected (reflected wave $\epsilon_r(t)$)and transmitted through the arterial walls as a second traveling wave causing a new expansion of the vessel. By measuring the amplitude of expansion and contraction of the arterial walls it is possible to detect, for example, situations of arterial stiffness [138, 140] or arteriosclerosis [141]. Therefore, the implementation of new techniques that allow the complete and precise reconstruction of the pulse wave with a high level of detail and accuracy becomes an interesting field of research for micro displacement measuring methods, specially for those based in optical sensors.

Different optical methods have been proposed for the acquisition of the arterial pulse wave (*APW*). Among them, possibly, the most popular method used today to acquire the waveform is photoplethysmography (*PPG*) [142–144]. Such a method, based on the absorbance of oxigenated and de-oxigenated hemoglobin in different wavelengths, allows the measurement of the pulse wave in different parts of the patient body, with sensors which can be miniaturized and easily implemented e.g. in the fingertip or earlobe clips commonly observed in medical equipment. In addition, such sensors may be used even in non-cooperative patients easily,

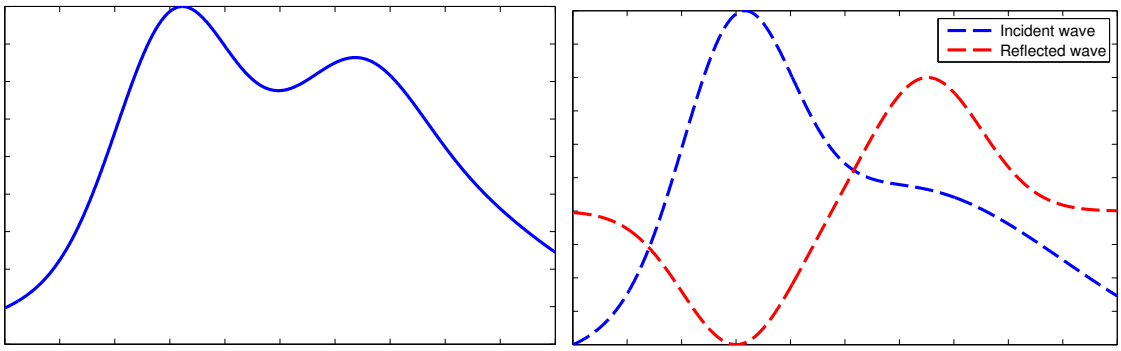

Figure 4.1.1: Artistic representation of an arterial pulse wave as the superposition of two waves. (a) Pulse waveform example. The signal is modeled using Gaussian functions to contain two maxima, the first as a result of the incident wave and the second as a result of the reflected wave. (b) Example of the incident and reflective waves that cause the pulse wave.

In PPG, when a light source is shined at living skin tissue, the interaction between the light and the chemical composition of the media causes a small AC modulation as a result of an absorption processes. According to the information provided in [142], different factors such as blood volume, wall movement, or red cell orientation may affect the amount of light received by the photodetector and, thus, the measurement.

A typical PPG sensor consists of one or two light emitting diodes (*LEDs*) with different wavelengths (usually one of them within or very close to the red wavelengths and another one around NIR wavelengths, so they both penetrate well inside the tissue). Each LED is turned on and off alternatively, allowing a single photodiode (which is placed in front or beside the LEDs) to differentiate between each wavelength response.

Another usual solution for the acquisition of the pulse wave is based in Doppler methods [145]. In this case, a laser diode vibrometer (*LDV*) is used to estimate the velocity curves of the concerned artery. According to the data provided by the European Society of Hypertension, a pulse velocity of $12m/s$ may be considered as a threshold of organic damage [145]. The main problem with this type of implementation is the size of the setup, as it might be bulky and require positioning sensors in uncomfortable places for the patient. More recently the size of the setup has been compacted to provide on-chip measurements as described in [145].

Self-mixing interferometry, mainly in its LDV configuration, has been assessed by different authors as a method to detect different medical constants [146]. While some applications have focused, for instance, in the detection of extra corporeal blood flow velocity [147], and mechanomyography [148], some other authors have shown interest in applications related to the arterial pulse wave.

In [149], for instance, Meigas et al. proposed the use of a LDV SMI sensor to detect different pulse related parameters. In this work they use a LD coupled to a fiber, which is then used to point at the target. In the case of APW measurements, the fiber is clamped to a measurement point on the arm and signals are recorded using a sampling frequency of $10kHz$ during $10s$. The signals are then pre-processed using a 128-point Hanning sliding window and a power spectrum is calculated every $0.8ms$ recording the maximum amplitude. The resulting waveform shows some of the traits of the pulse wave in terms of velocity. Nevertheless, with this method, the direct amount of motion of the artery is not assessed in terms of displacement. Moreover. the requirement of using a fiber in the sensor may introduce issues during the

measurement, as strain due to temperature,or to other mechanical effects may bias the measurement, as typically strain will induce some degree of birefringence in the fiber.

Hast, in his PhD Thesis [150] also proposed methods to analyze the pulse wave in the radial artery using a SMI sensor. In this case, the sensor is placed on a $3\times4\,cm$ chip placed on the arm of the patient by means of a plastic watchband. The captured SMI signal is filtered using an analogue band pass filter with a high cut off frequency of $f_{high} = 100Hz$ and a variable low cut off frequency (1, 2 , 4 ,$6kHz$) which is selected using an analogue multiplexer. The laser optical power is operated in values which range form $0.2mW$ to $16mW$,and no reference to other optical elements is described in the document. From their results, it is possible to conclude that using a reconstruction process similar to the one presented in [149], the waveform obtained by an FFT method has a high degree of relation to the derivative of the pressure pulse (dP/dt).

In this section, however, a more direct interpretation of the SMI signal is pursued, focusing in the amplitude of the signal instead of its frequency. This is expected to allow a direct reconstruction of the arterial pulse shape and, in theory, of the associated pressure wave.

For the present analysis, and inline with what has been considered by other authors ([149, 150]), the cardiovascular pulse is considered as a pressure wave which induces changes in the radius of the arterial wall. Such changes may induce a small displacement in the order of a few microns over the skin surface, which can be captured by a SMI interferometer.

One of the main differences in this analysis relative to the studies discussed above is the placement and contact of the LD probe. For the experiments presented in this work, the measurements will be acquired on nail tissue instead of directly over the skin, and dislpacement measurements (not velocity) will be considered. The hypothesis presented is that the movement caused by the arterial vessels in the skin produces micro or nanoscale motions which are transmitted to the studied nail. By measuring on nail tissue rather than the skin, it is expected to reduce the possibility of laser skin damage, and at the same time to have a better control of the target as healthy nail tissue seems to present a more homogeneous structure when compared to skin tissue.

In the following section, the elements required to implement the proposed method are introduced. In Sec.4.1.2 some of the main aspects of the processing algorithm for SMI, as well as some guidelines taken into account to ensure an efficient readout of the pulse waveform, are described. In Sec.4.1.3, a summary of results attained for artificially simulated pulses and in vivo measurements over the skin are presented. Results of measurements obtained over skin tissue are also presented as well as a short analysis on optical power limitations according to current normative.

4.1.1 Setup and materials

As described above, the main objective of this section is to develop a system capable of measuring the APW over a fingernail *in vivo*. A possible setup is shown in Fig.4.1.2. The system is composed by a LD SMI sensor in the photodiode current detection mode using a displacement scheme. After the SMI signal is generated, it is pre-processed using the analogue band pass filter and the resulting AC signal is amplified and fed into a PC for post processing after the analog to digital conversion. In parallel, if required, the pulse rate of the test subject is registered using a wristband to provide a comparison with the results of APW measurements obtained after the signal reconstruction stage.

The experimental setup built for fingernail measurements is presented in Fig.4.1.3. The setup uses a $LT230220P-B$ Thorlabs focusing tube equipped with a $C220230P-B$ aspheric lens pair with a numerical

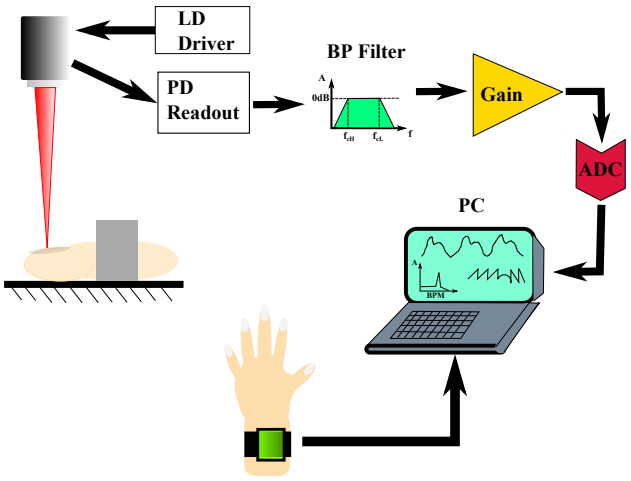

Figure 4.1.2: Schematic setup used for the measurement of APW over a human fingernail.

aperture $NA_1 = 0.55$ and $NA_2 = 0.25$ for each lens; focal lengths were $f_{A1} = 4.51mm$ and $f_{c2} = 11mm$ respectively.

A LD is fixed inside the focusing tube using a holding ring with a screw for adjusted positioning. The tube is then fixed to a mechanical aluminum support attached to a mechanical screw fixation to a $PI - LISA753.3CD$ transducer attached to an optical board placed vertically. The position of the laser is adjusted to provide a distance to the target of approximately $10cm$. All the elements, as well as an adjustable finger mechanical fixation are placed on an optical table to reduce some of the artifacts resulting from an *in vivo* noncontact measurement.

The measurements, unless specified, were carried out using a Hitachi FP LD GaAlAs HL7851G with nominal wavelength of $785nm$ and maximum output power of $50mW$. The LD optical power was controlled using the electronic card presented in Sec.3.1.3, limiting the maximum output power to values between $6mW$ to $20mW$ by adjusting the resistance in the control potentiometer. The recovered SMI signal is preconditioned using an analog band-pass filter with a fixed high-pass cutoff frequency in the order of $16Hz$, and an initial low-pass cutoff frequency in the order of $1MHz$.

After an analog amplification stage, the signal is digitized using a Tektronix $DPO2024B$ oscilloscope with windows of $125kS$. The time duration of the acquisition window was varied using $1s$, $2s$, $4s$, and $10s$ to observe potential effects in the reconstruction, acquisition and results. Finally, a second analogue low pass filter stage provided by the Tektronix oscilloscope was applied to the SMI signal to remove some of the high frequency noise effects observed in the signal.

Previous to the initial data capture, the right hand of the test subject is placed in a prone position and one of the fingers is fixed to the optical table using the adjustable finger fixation. This type of mechanical fixation is used to reduce some of the artifacts caused by involuntary movements of the subject during acquisition. Next, the laser spot is adjusted to produce the required SMI signal, preferably in a $C \sim 1$ condition. It is possible to automate this calibration process by applying one of the methods proposed by Atashkhooei [107]. Once the system is calibrated, the OOP signals are stored in an external drive for an offline processing analysis. It is possible to provide an online analysis in a limited way using the Matlab script, which uses the oscilloscope as an ADC. All acquired signals are finally processed in a PC as shown in Fig.4.1.2.

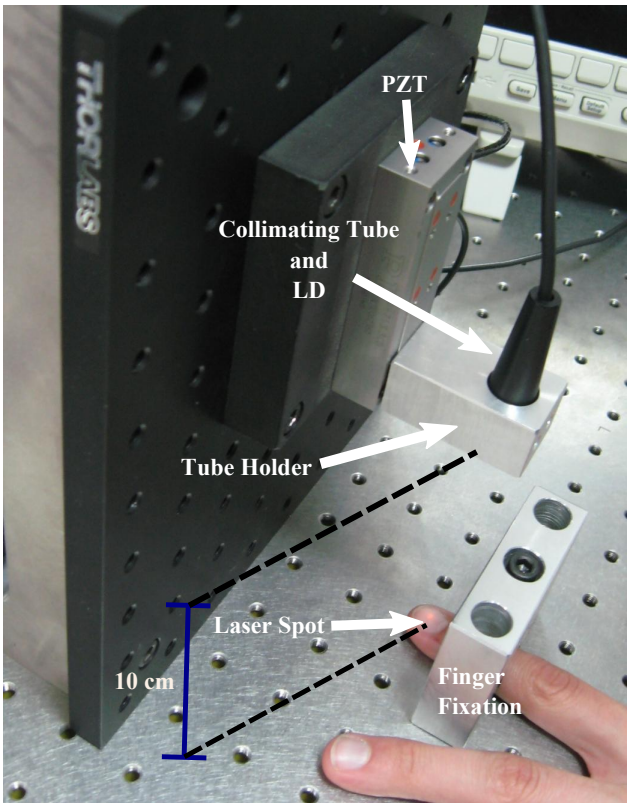

Figure 4.1.3: Experimental setup for the measurement of the APW. A focused or collimated laser beam is pointed onto the fingernail of the test subject.

4.1.2 Signal processing

As described earlier, in this study we use a vibration or displacement approach of the SMI method rather than the Doppler approach typically used in biomedical studies. The use of this type of measurement allows the retrieval of the complete APW contour, not limiting the application to the detection of the velocity in the blood flow.

The most common approach for the reconstruction of the SMI signal is the fringe counting algorithm (FCA),already discussed in Ch.2. The FCA typically recovers the target displacement in three steps: first, the acquired OOP is transformed into phase by means of an arccosine function; next, the derivative of the phase signal, after normalization, is compared to arbitrary threshold values ($thr > 0.5$ for high SNR signals) to detect the transitions of the SMI signals; and finally, a discrete step of $\lambda/2$ is set at every transition according to the sign of the transition. A smoothing process may be applied over the reconstructed signal to reduce the stepwise shape of the reconstruction. If higher resolution is required, other reconstruction processes may be applied such as the ones discussed in [114, 123].

The FCA is highly efficient in the measurement of nearly flat and smooth surfaces with displacements below $100\mu m$, given a signal close to the moderate feedback level is achieved. In other cases, for instance in the cases of lower feedback values, or in the case of irregular surfaces with high granularity, (such as the skin and other biological tissue), the FCA can produce faulty displacement results, which are typically attributed to the presence of speckle [106] in the SMI signal. If speckle phenomena is present in the acquired SMI signal, the use of a continuous threshold level throughout the analyzed period of the SMI signal leads to misdetection of some of the transitions, and as a consequence to loss of information. While some methods

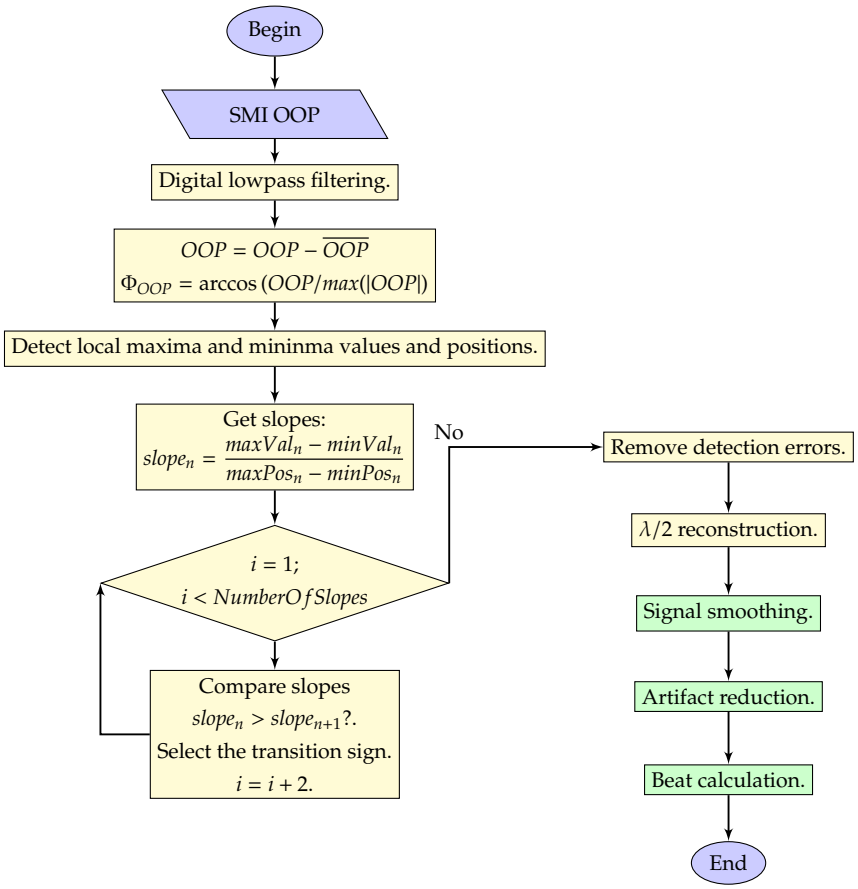

Figure 4.1.4: Flow diagram for the MFCA algorithm used in pulse wave reconstruction. The steps corresponding to the reconstruction algorithm are presented in a yellow background and those corresponding to a post processing stage are presented in a green background.

have already been proposed in order to reduce the influence of speckle [109, 151], for this work a simple modification of the FCA algorithm is proposed.

For the proposed FCA method which will be applied, further on referred to as modified fringe counting algorithm (*MFCA*), the obtained SMI signal should preferably be in a feedback level close to the moderate regime ($C \simeq 1$). After the signal acquisition is performed using the electronics described in Sec.4.1.1 the signal is postprocessed following the flow diagram presented in Fig.4.1.4. The proposed MFCA algorithm, thus, can be described using the following steps:

1. A digital low pass filter in the order of $1kHz$ is applied to the SMI signal to reduce high frequency noise effects. A nonlinear median filter might be also introduced to remove erratic trends on the signal.
2. The local minima and maxima of the signal are selected by means of a low threshold value relative to the amplitude of the SMI signal. Each of the positions and values of the maxima and the minima are stored in vectors.
3. The local minima and maxima values are normalized to one.
4. The slopes for each minima and maxima pair are computed.
5. The slopes are compared by pairs selecting the one that has the higher absolute value as the correct transition. A correction of the transition position is computed as the median position between the

Wavelength [nm]		Duration [s]		Calculation
λ_{min}	λ_{max}	t_{min}	t_{max}	
		1×10^{-9}	100×10^{-9}	$200C_A$ $[J/m^2]$
400	1400	100×10^{-9}	10	$11C_A t^{0.25}$ $[kJ/m^2]$
		10	30×10^3	$2.0C_A$ kW/m^2

Table 4.1.1: Laser radiation exposure times for skin in the visible and NIR range as presented in [153]. Care should be taken in the calculation for apertures smaller than $1mm$.

corresponding minimum and maximum, and a value of 1 or -1 (according to the sign of the slope) is stored in a vector at the estimated position.

6. The sign of the contiguous transitions is analyzed. If a solitary transition is detected, it is removed from the transition detection vector (e.g. if the transition detection vector is defined as $\mathbf{x} = [1, 1, 1, -1, 1, 1]$, after the error detection, it becomes $\mathbf{x} = [1, 1, 1, 1, 1]$ and the corresponding position is also removed from the position vector.
7. After removing the errors in the transition, a $\lambda/2$ step reconstruction is applied to the transition vector.
8. A bandpass filter between $0.5Hz$ and $10Hz$ is applied to the recovered displacement. According to [152], the use of a high-pass filter with a cutoff frequency around $0.5Hz$ reduces the effects of involuntary tremors over the measurement. The low pass filter produces a smoothing effect and removes unnecessary frequencies, as the expected range of the pulse falls in a range between $[45, 180]BPM$ ($[0.75, 3]Hz$).
9. Finally, the beat frequency may be detected using a FFT, or some other frequency determination method.

4.1.3 Results

After looking at the results of other research groups previously dealing with the problem [145,146,149,150], it can be concluded that the APW displacement over the skin should be in the order of the micrometric scale. The use of the laser directly over the skin, however, may entail different issues in practice as the exposition time should be kept within the regulations given in the norm ANSI Z136.1, UNE EN60825, and according to the guidelines presented by the International Commission on Non Ionizing Radiation Protection [153], where the limits are expressed as a function of the exposure duration as presented in Tab.4.1.1. In the table, the value C_A depends upon the wavelength, and for the range between $700nm$ and $1050nm$, it is stated as $C_A = 10^{0.002(\lambda)-700}$ where λ is given in nm.

As it can be seen in Tab.4.1.2 even in the case of low power LDs ($P_o \leq 50mW$) for wavelengths in a range between $780nm$ and $850nm$, the maximum permissible exposure (MPE)can be easily reached if a the laser spot used for the measurement has a small diameter (Φ). It is to be observed that for $P_o \approx 40mW$ the minimum spot diameter should be larger than $5mm$, which in some cases might result in issues to recover enough feedback to produce an exploitable SMI signal. Furthermore, the calculated limit, even in the case of $\Phi = 5mm$ spots, is too close to the designated limit, which might be considered risky specially in the design of medical monitoring apparatus. A way to work around this limitation would be to reduce P_o in the LD, which may entail problems as the desirable working power might be too close to the LD threshold, potentially causing instability in the measurement. Also, the use of smaller optical powers may cause issues

λ [nm]	Φ_{Spot} [mm]						MPE [W/m^2]	OOP[mW]
	1.0	2.0	2.5	3.0	5.0	10.0		
	5.09×10^4	1.27×10^4	8.15×10^3	5.66×10^3	2.04×10^3	5.09×10^2		40
785.0	1.27×10^4	3.18×10^3	2.04×10^3	1.41×10^3	5.09×10^2	1.27×10^2	2.96×10^3	10
	1.27×10^3	3.18×10^2	2.04×10^2	1.41×10^2	5.09×10	1.27×10		1
	5.09×10^4	1.27×10^4	8.15×10^3	5.66×10^3	2.04×10^3	5.09×10^2		40
830.0	1.27×10^4	3.18×10^3	2.04×10^3	1.41×10^3	5.09×10^2	1.27×10^2	3.64×10^3	10
	1.27×10^3	3.18×10^2	2.04×10^2	1.41×10^2	5.09×10	1.27×10		1
	5.09×10^4	1.27×10^4	8.15×10^3	5.66×10^3	2.04×10^3	5.09×10^2		40
850.0	1.27×10^4	3.18×10^3	2.04×10^3	1.41×10^3	5.09×10^2	1.27×10^2	3.99×10^3	10
	1.27×10^3	3.18×10^2	2.04×10^2	1.41×10^2	5.09×10	1.27×10		1

Table 4.1.2: Calculation of Maximum permissible exposure (MPE) for three values of emitted optical output power (OOP) on human skin. The values are calculated for the wavelengths of 785, 830, and 850nm, as taking into account the spot size. Green cells show values valid for exposures in a range between 10s and 8.3h. Similarly, in red, values where the exposure is larger than the permitted value according to the information in [153].

in the recovery of the proper feedback level, which would result in the need to reduce the distance between the LD and the target, which also impacts the type of SMI signal obtained.

As a result of the issues noted above, it is proposed that the SMI acquisition of the pulse wave is performed over a fingernail instead of the skin. Hypothetically, measuring in this conditions would limit the incidence of direct optical power over the skin, as the main reflective power (minimum spot area) would be placed on the outer layer of the nail, and the power would be diffused until it reaches the top layer of the dermis, as the expected penetration within the wavelength range used should be in the range of 2mm or lower [154].

It is also important to remark that, typically, relying on direct measurements over the skin using the SMI approach results in noisy measurements that are difficult to process and may lead to an inaccurate reconstruction of the APW as it has been assessed by other authors [149,150]. In part, our hypothesis is that measuring over the fingernail may remove partially some of the "parasitic" motion related to involuntary muscle movement which results in a bias of the measurement, and would also allows to have a better control on the feedback since the nail surface is smoother than the skin, which, in turn, would result in a better overall SNR. Thus, the fingernail would act as a mechanical mass-spring system which interacts with the skin motion producing a decrease on the total displacement amplitude observed at the skin interface as a result of possible mechanical miscouplings. This damping effect would reduce additive noise produced by involuntary muscle movement, as commented before, which during the signal capture may show up as the appearance of multiple fringes, or as high frequency noise, depending on the limits of the electronic acquisition card. Thus, an initial capture (Fig.4.1.5) was obtained to validate the different hypothesis and set the valid measurement strategy.

After setting the measurement spot over the fingernail, it was necessary to decide the correct acquisition method since it was not clear whether the displacement over the nail would have the required amplitude for DSMI ($A_{pp} < \lambda/2$), or it would show amplitudes larger than $\lambda/2$ pushing the measurement method to conventional SMI. While some examples of pulse wave measurements over skin have shown displacements larger than 5μm (as observed for instance in the second lobe of the pulse wave displayed at Fig. 9 of [149]), the initial hypothesis of this test was that the measurement over the fingernail would result in a decrease of the total displacement.

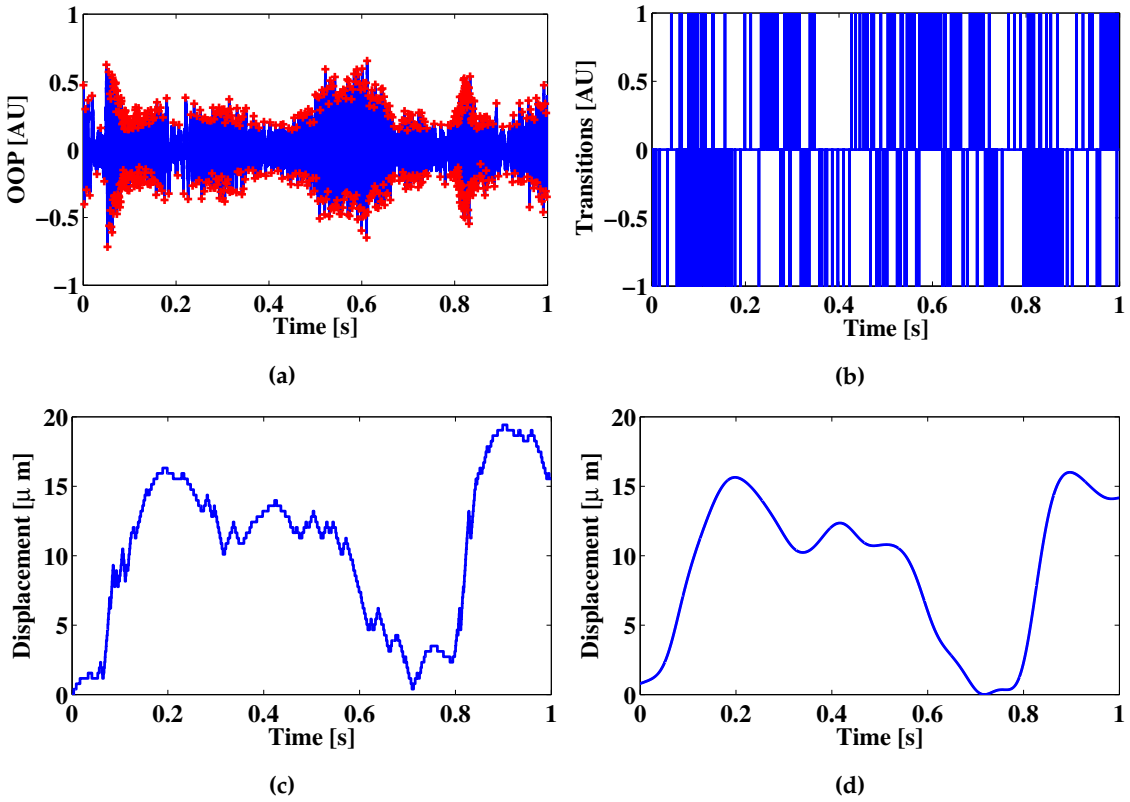

Figure 4.1.5: Initial test signal of a pulse wave measurement using a SMI approach, the signal shows two well defined sections with an initial estimated amplitude of $15\mu m$ in the initial slope. (a) SMI signal in blue, with detected peaks in red. (b) Detected transitions in the signal after applying the proposed algorithm. (c) Initial reconstruction before smoothing filters. (d) Reconstructed pulse wave signal after smoothing and low-pass filtering.

After an initial test, shown in Fig.4.1.5, it was observed that the acquired pulse signal (Fig.4.1.5a), presents a large number of transitions, including a region with high frequency of the fringes, close to the start of the pulse, which should correspond to the systole of the cycle, followed by a change in direction and a slight decrease in the frequency of the SMI signal. After reconstruction, it is estimated that the pulse amplitude (systole maximum) was in the order of $15\mu m$. Therefore, it was concluded that classic SMI methods were sufficient for the measurement. This initial test enabled also to confirm that a relevant problem in this type of measurements is the bias introduced by involuntary movements of the patient with amplitudes larger than $\lambda/2$.

It can be appreciated that the pulse wave, even before smoothing, can be divided into different sections. In a first section a rapid increment of the signal is observed for approximately a $1/7th$ of the total period of the pulse. The steep slope in this section shows a good relationship with the appearance of high frequency transitions in the SMI signal (e.g.Fig.4.1.5b in the section between $0.05s$ and $0.2s$), as well as with the expected form of the APW. Also, it is to be noticed that the envelope of the SMI signal presents some traits of the type of displacement as an initial incremental behavior can be observed in (Fig.4.1.5a). A similar observation was also provided by Hast in [150].

After this initial section of the signal, the rate of appearance of the transitions drops significantly and produces a change in the sense of the displacement, causing the appearance of the first maximum which can be related to the incident pulse pressure wave as presented in Fig.4.1.1. The amplitude of the signal

continues dropping until a new saddle point is reached (*dicrotic notch*) which is used in some analysis to discriminate between the systolic pulse phase (between the first minimum point and the dicrotic notch) and the diastolic phase (between the dicrotic notch and the first minimum of the following pulse). After the dicrotic notch a second peak of smaller amplitude correspondent to the reflected pulse pressure wave is observed on the reconstructed signal. Next, the signal amplitude decays again during the remaining period.

In general, it is observed that the appearance of a transition point during the amplitude reduction in the diastolic phase tends to have a lower fringe appearance than that of the positive slope of the systolic phase. As a result, it is possible to say that the APW captured over a human fingernail produces a SMI signal with different frequencies, showing a higher frequency close to the beginning of the pulse, followed by a change of sense of movement and a decrease of the SMI transition frequency. It is also clear that a small number of transitions is to be expected around the end of the systolic slope and in the area around the dicrotic notch. This test also allows to calculate an initial estimation for filters and sampling requirements, as it is possible to estimate that the pulses may fall within a range of $20\mu m$ of amplitudes with a typical set of frequencies between 0.75 and $3Hz$.

To select the required bandwidth, the APW pulse is divided into two zones, considering the peak in the systolic point as the discriminator between the two sections. To ease the frequency estimation, it is considered that the velocity behaves quasi-linearly along both slopes. Therefore it is possible to equate:

$$f_{lim} = 2k_{adj}\frac{A_{APW}}{\lambda T_{case}}, \tag{4.1.1}$$

where, $A_{APW} = 20\mu m$ is the amplitude of the APW, $\lambda = 785nm$ is the LD wavelength, T_{case} is the period of the worst case predictable APW, and k_{adj} is a constant coefficient to take into account the Nyquist theorem. As a result and considering the worst case scenarios for high-pass cutoff frequency as $f_{limH} = 13.37Hz$ with $k_{adj} = 0.5$ and $T_{case} = (1/0.45)(6/7)$, and $f_{limL} = 2751.59Hz$ with $k_{adj} = 2$ and $T_{case} = (1/3)(1/7)$ for the low-pass cut off frequency. If the SNR of the signal is high, it can be possible to increase the value of k_{adj} for the low-pass cutoff frequency up to 10 to increase the reconstruction capacities of the algorithm, allowing to increase the sharpness of the SMI transitions.

4.1.3.1 Simulated target

In order to test possible errors in the APW reconstruction procedure or in the proposed setup, an artificial APW signal is simulated using the LISA 753.3CD PZT stage shown in Fig.4.1.3. The PZT is fed with an electrical signal with an amplitude and frequency comparable to that of the APW showing the initial quick rise observed during the systole, followed by a decrease of the amplitude until a secondary peak with an amplitude in the order of 80% of the systolic peak is shown. The frequency is selected to be $1Hz$ ($60BPM$) to simulate a test subject in a relaxed state. Other frequencies can be easily tested by changing the repetition rate in the signal generator. The main limitation in terms of reproduction of the signal is related to the DAC capabilities of the Tektronix signal generator AFG3102C, as in the case of low frequencies it introduces steps in the displacement rather than the desired continuous motion, which would prevent the correct interpretation of the SMI phenomenon.

Previous to the start of the test, the focus lens is adjusted to produce a SMI signal close to the moderate regime to allow a correct reconstruction. The signal is then low pass filtered ($f_c = 12.2kHz$), and acquired by a Tektronix DPO2024B oscilloscope for different acquisition periods ($2s$, $4s$, $10s$, and $20s$) using a $125kS$

window. After the acquisition the signals are stored in a CSV file which is then recovered and analyzed using a Matlab script using the process described in Sec.4.1.2. The results are shown in Fig.4.1.6.

As observed in Fig.4.1.6, for all presented cases it is possible to recover the APW pulse wave. The analysis of the resulting signal suggests that the the reconstruction might be limited around the window boundaries, as the maximum error tends to rapidly increase around these regions. It is also noticed that as the sampling frequency f_s decreases the detected error increases. In this case, the maximum error values are observed around the simulated systolic rise. This, however, is an expected behavior since the detection capabilities of the fringe analysis algorithm may be decreased as a result of the step resolution used to calculate the slope between corresponding maxima and minima points.

The error values for all cases show $\sigma_{Err} \approx Err_{RMS} \leq 2.82\mu m$(better than 15% of the total amplitude) and a mean error value close to zero. For the largest sampling frequency studied ($62.5kHz$) a $\sigma_{Err} = 0.74\mu m$ is observed.

While the APW signal reconstruction tends to show better results for shorter sampling windows (meaning higher sampling frequency), the beat detection shows, in the presented cases, a tendency to improve the accuracy in the detection of the beat frequency as the sampling window period increases.

This result is clearly shown in Fig.4.1.7, where the larger period window ($20s$) shows the most well-defined Fourier peak as a result of the appearance of more independent pulses in the reconstructed signal. This result is reasonable as a consequence of the limited number of APW forms observed by the FFT in the shorter time windows. Thus, as in many other cases, a balance between frequency acquisition and memory management will be necessary to provide an efficient measurement. The use of a high frequency sampling should also result in an accurate beat frequency measurement, however this would require the use of a massive amount of memory, which in most cases is not an option, especially if a portable device was to be designed.

In the case of smaller sampling frequencies containing a larger number of APW forms within the measurement window, it should be noticed that even when the frequency peak is easier to detect due to the decrease of the amplitude in the side-bands, a lobe in lower frequencies is observed, which corresponds to the increment of error in the reconstructed signal.

Regarding beat frequency detection, the relevant parameter to consider is the minimum detectable step required to provide a measured value accurate enough. If such valid step value was to be around $\pm 1BPM$, then the minimum detectable frequency step should be below $1BPM/60s = 0.017Hz$.

This in turn would require at least a sampling frequency of $125Hz$ for a 1 minute window (approximately 60 pulses on a relaxed individual). This value suggests that after reconstruction, the obtained APW can be downsampled and still produce valid values with a FFT analysis. At the same time it is possible to obtain similar results with larger frequencies at the cost of an increase of memory consumption.

A second test was proposed using the setup shown in Fig.4.1.8, to test the possibility of using the sensor directly over the skin. To do this, and for safety reasons, the FP LD was replaced with a Finisar HFE4093-332 VCSEL LD placed inside of the Thorlabs LT230220P-B tube, equipped with a C230P-B focusing lens for focusing purposes. It is to be observed that the use of the VCSEL LD shows an output power in the order of $0.8mW$, several times smaller than the $20mW$ to $50mW$ output power of the FP LD. To try to evaluate the effects in different types of skin, two different measurements were proposed. The first one pointed the laser towards a black surface, to check the feasibility of the measurement under conditions of low reflectivity. The second approach pointed the laser against a sample of ear pig skin obtained at a local butchery. All signals are acquired for a window of 1 minute using a $10kHz$ sampling frequency. A polarizer was added to

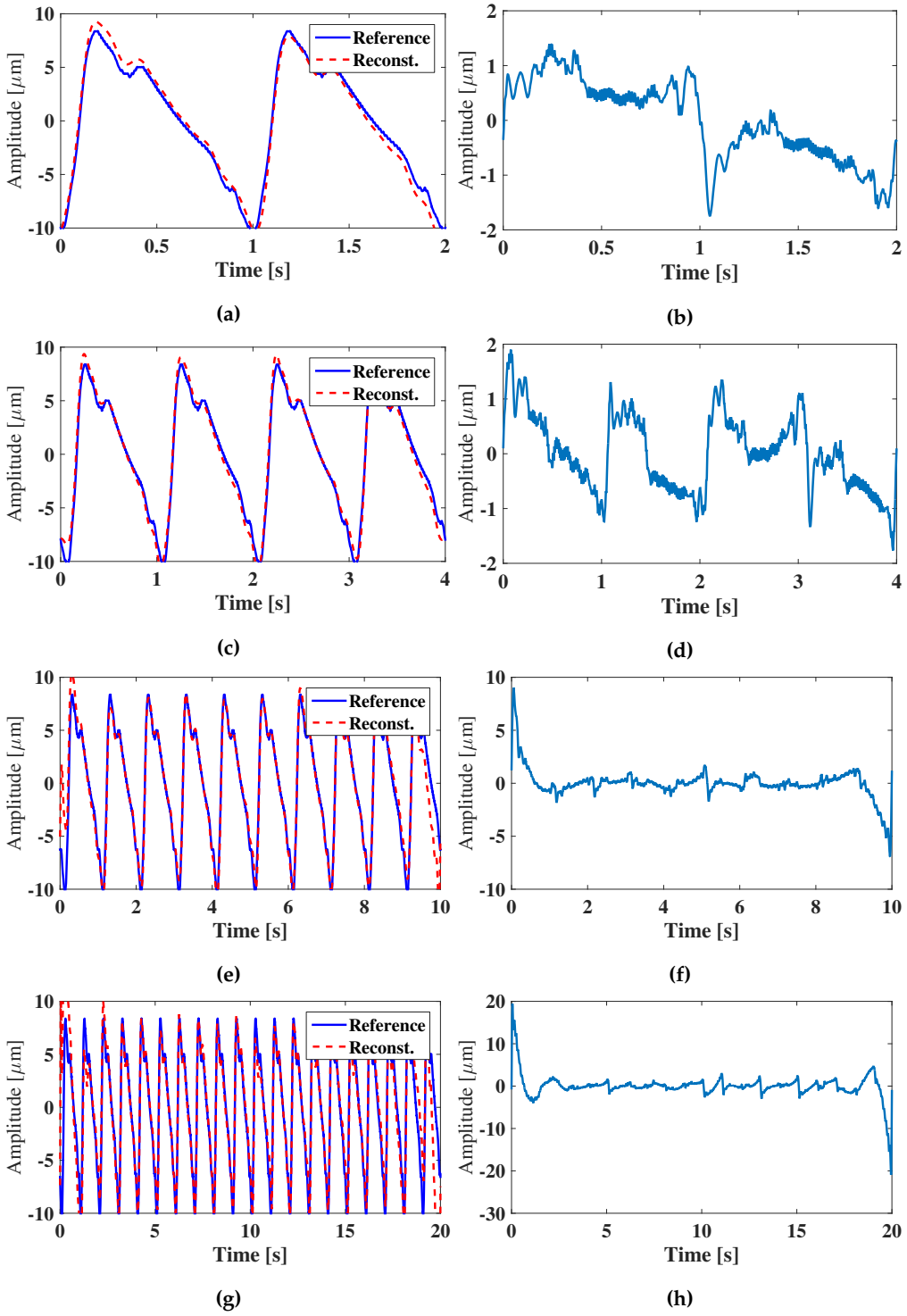

Figure 4.1.6: Comparison of reconstructed and simulated APW forms over a PZT target. The acquired SMI signal is processed and the output is compared to the internal capacitive sensor of the PZT. All windows correspond to $nSamp = 125kS$ windows resulting in $f_s = T_{acq}/N_s$, where N_s is the number of samples, and T_{acq} the acquisition period. (a) Comparison for a 2s window. (b) Measured error for a 2s window. (c) Comparison for a 4s window. (d) Measured error for a 4s window. (e) Comparison for a 10s window. (f) Measured error for a 10s window. (g) Comparison for a 20s window. (h) Measured error for a 20s period.

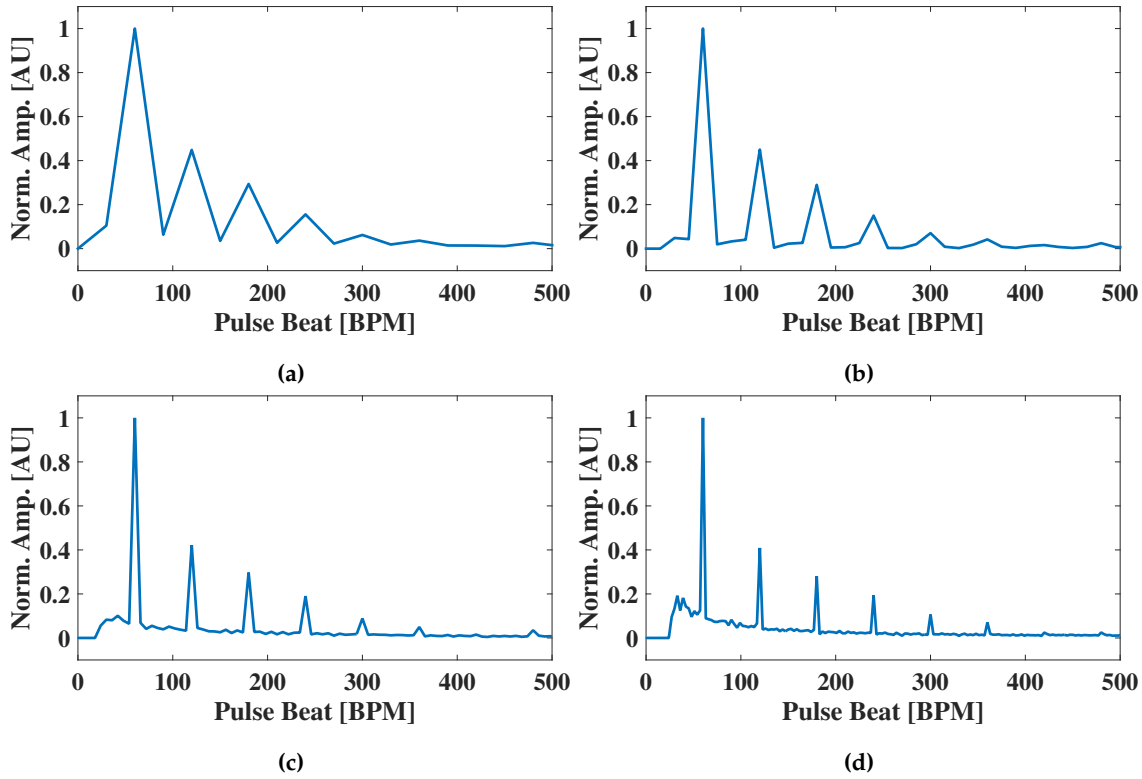

Figure 4.1.7: Fourier spectra corresponding to the reconstructed pulses: (a) 2s window, (b) 4s window, (c) 10s window, (d) 20s window.

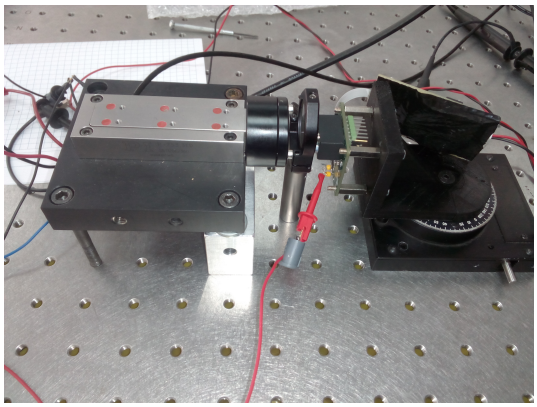

Figure 4.1.8: Self mixing setup for the measurement of a simulated APW using a VCSEL LD. The setup includes a polarizer to reduce the effects of unpolarized light in the PD.

.

the setup in order to filter diffuse light from internal regions of the skin. The results of both tests are shown in Fig.4.1.9.

For the case using the black surface, the measurement shows a correct reconstruction with peak errors in the order of 4μm, which seem to correspond with the expected decrease of the sampling frequency. The test, however, is not successful for the measurement over pig skin showing errors in the order of 10μm. The test was repeated several times only obtaining successful results randomly, which lead us to think that this type of measurement might not be possible with the depicted setup on skin.

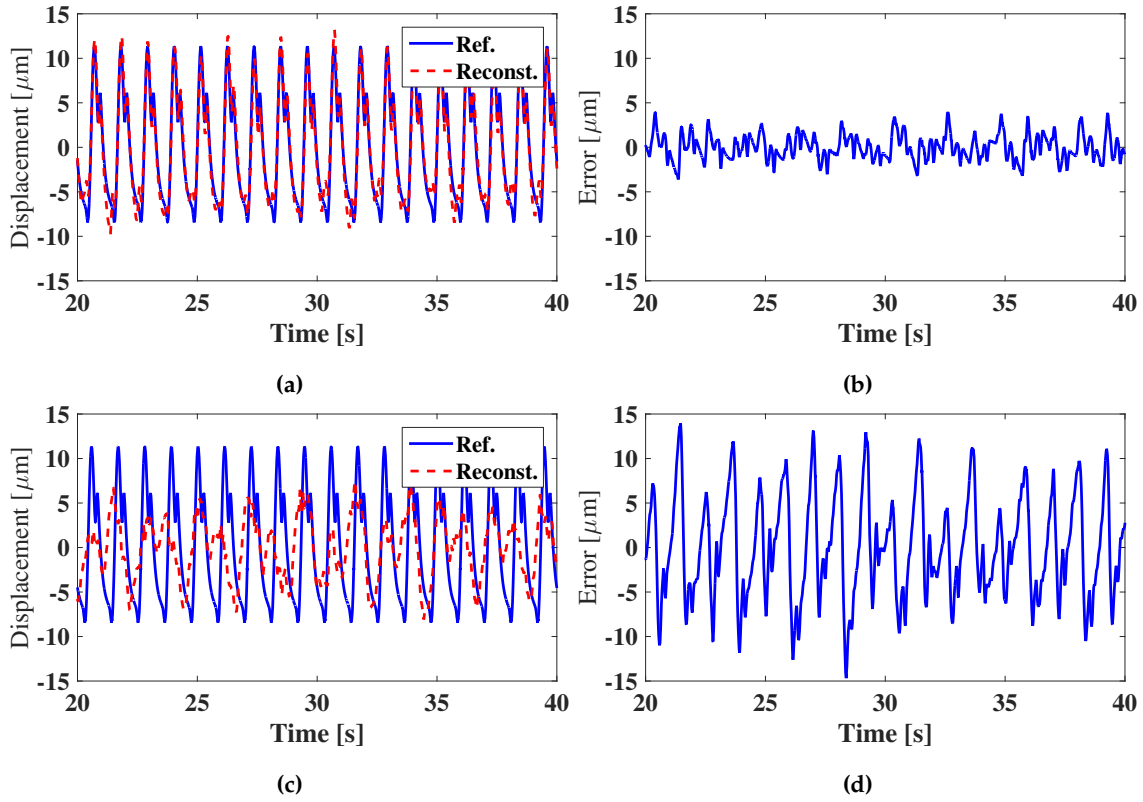

Figure 4.1.9: Results of simulated APW reconstruction using a setup with VCSEL and polarizer, and different types of sample. (a) Reconstruction of the simulated APW signal on a black sample. (b)Error of the reconstruction on a black sample. (c) Reconstruction of the APW signal on pig skin. (d) Error of the reconstruction on pig skin.

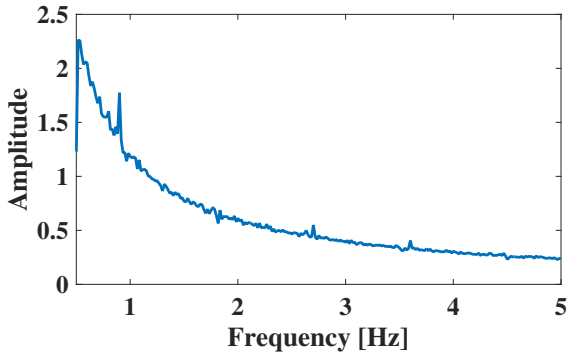

Figure 4.1.10: Example of power spectra of the reconstructed SMI-APW signal from a measurement over pig skin.

Even when the reconstruction does not allow to extract the pulse pattern information, it still allows to extract the frequency of the APW signal from the FFT spectra in all cases. Nevertheless, as a result of the amount of noise in the signal, it may be necessary to introduce an special algorithm to detect the real peak of the signal as low frequency noise seems to be prevalent in the spectra (Fig.4.1.10).

In our opinion, in order to obtain better results it might be necessary to increase the output power of the LD and to measure in a region with a smoother surface such as the nail. The use of higher power, as it was explained earlier, may introduce risks for the patient skin specially in the case of long exposure times. Therefore, for in vivo measurements, it is better to perform the measurement over the nail and limit

the test to short exposure times to stay well below the limitations of current normative. The use of other wavelengths may also benefit this type of measurement in order to increase the overall measuring time.

A possible option to increase the reliability of the measurement over the skin may be to attach a reflective or partially diffusive sticker over the skin in the measurement zone, which might increase the SNR of the OOP and at the same time provide a more controlled measurement setup. However, this solution may produce unwanted artifacts associated to the mechanical coupling between the sticker and the skin. Care should be taken on the selection of the sticker as a mirror-like surface may produce a loss of the SMI signal as a result of the incident angle between the LD beam and the sticker, or as a result of reaching the chaotic regime as a result of a too large feedback.

4.1.3.2 In-vivo arterial pulse wave measurement

Once that it was observed that the algorithm was able to comply with the expected frequency ranges for the simulated sets, different measurements in voluntary test subjects were obtained. The test subjects were healthy young adults with no cardiac history to their knowledge. The tests were performed in a relaxed environment with the subjects at rest. In all cases the tests are performed during measurement intervals shorter than 1 minute, therefore staying well within the allowed radiation levels for NIR radiation.

During the test, the finger of the test subject is partially fixed to the setup to reduce its motion. After the finger is positioned, the SMI power is adjusted onto the fingernail using the focus lens, and different measurements are acquired following the oscilloscope acquisition frequencies investigated in the simulation section. An example of a reconstructed signal using a $31.25kHz$ sampling rate is presented in Fig.4.1.11

As observed in Fig.4.1.11, once the SMI signal is acquired the signal processing algorithm is used to detect the transitions in the signal and its corresponding direction, to generate the reconstruction. It is important to remark that, even when a small amount of speckle may be observed in the SMI signal in the modulation of the envelope of the signal, it was still possible to perform a correct detection of all the interferometric fringes. It is easy to observe how the zones with high positive fringe density correspond to the beginning of the arterial pulse wave, and the lower density zones with negative fringes correspond to the line of descent. If the measurement is performed under the moderate feedback regime (large SNR) with the finger at rest (no movement artifacts), good results reducing the possibility of misdetection can be obtained. As shown in Fig.4.1.11c, reconstructed pulses are well characterized presenting a fast ascent, a decrease towards the dicrotic notch, and finally descending to the base of the next pulse.

Nevertheless, special care should be taken for the cases where the SNR of the signal is low or where the speckle noise is large, as this may limit the quality of the measurement. In some cases, as a result of the combination of the noise it might not be possible to perform a correct reconstruction. In those cases a frequency analysis might still be obtained to provide an estimate of the pulse rate.

Other tests have also shown erratic patterns, showing in some cases the loss of amplitude in one of more of the pulses (Fig.4.1.12). However, we consider this a normal condition in *in vivo* measurements, as even in commercial pulse-oximeters a variability of the pulse amplitude might be observed. It is also to be noted that when the SMI signal is in a moderate feedback regime, the SMI pulse envelope may present, to some extent, the pattern of the APW signal, which could be exploited in some cases to increase the quality of the transition detection algorithm. Nevertheless, this situation could not be granted for all the tests so such an approach was considered beyond the scope of the present work.

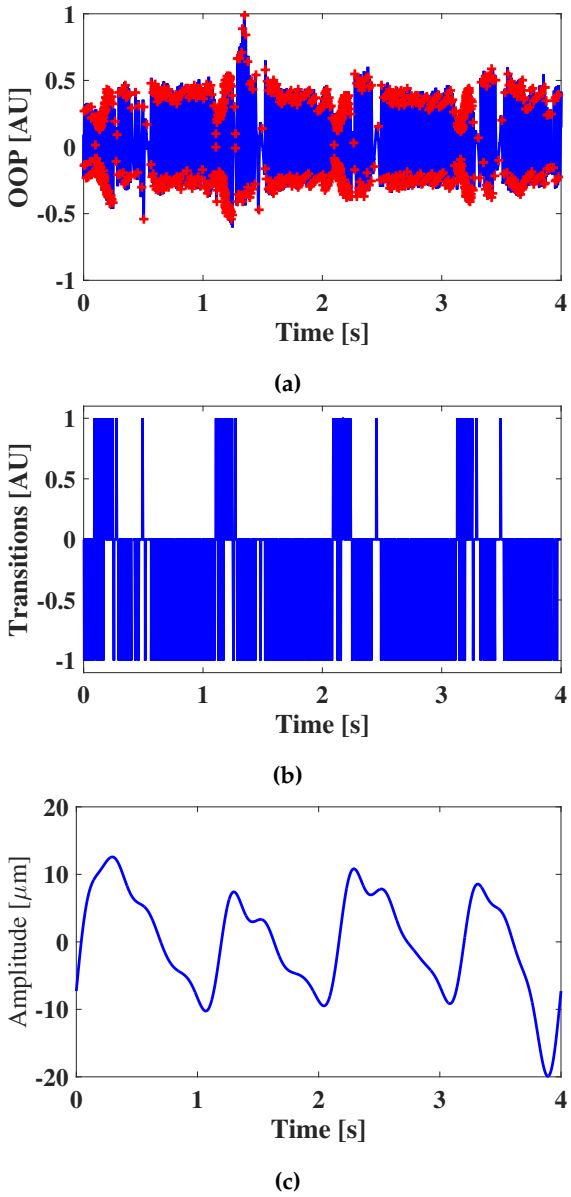

Figure 4.1.11: Reconstructed APW acquired over the left hand index fingernail of a test subject. (a) Acquired SMI signal. (b) Transition interpretation of the SMI signal. (c) Reconstructed APW waveform.

4.1.3.3 Estimation of the pulse beat

The resolution of the method, as explained above, is conditioned by the sampling frequency and the number of pulses acquired in the analyzed reconstruction window. Thus, a larger acquisition time typically results in a better correspondence to the pulse beat of the patient. This type of effect is easily observed by doing a simple FFT analysis of the signal. While in many cases a simple FFT analysis can be enough for the estimation, in cases when only 4 or less pulses are acquired, it is possible to perform a estimation of the pulse beat in the time domain by calculating the local minima of the APW waveform and getting the inverse of the time difference between this two points. In case of multiple pulses, it is possible to implement an average of the inverse period of the represented pulses.

Another option to estimate the pulse beat is to subsample the reconstructed APW waveform to a

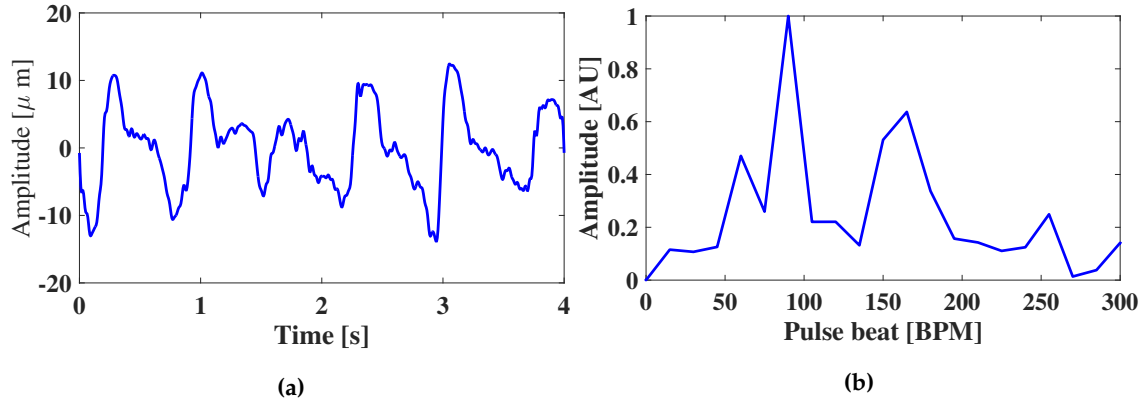

Figure 4.1.12: Example of a reconstructed pulse with a varying amplitude (a). The pulse shows amplitudes of $20\mu m$ in different sections of the reconstruction, and in the third pulse a large amplitude drop is observed. The repetition rate, however does not appear to be altered by the drop in amplitude (b).

frequency in the order of hundreds of Hz. After the subsampling algorithm a zero padded FFT can be applied, which allows to increase the resolution of the FFT at the cost of losing the accuracy shown for example in Fig.4.1.12b. This is better demonstrated in Fig.4.1.13, where the FFT of a $4s$ reconstructed and subsampled APW is analyzed. As observed, the region around the maximum peak widens but at the same time allows a better quantification of the real position of the maximum.

To prove the capacity of the method for capturing the beat of the APW, a comparison with an available commercial wrist pulse meter was performed. During the test, the subject is asked to wear the pulse meter in the left wrist and he is asked to exercise until his pulse beat reaches a frequency in the region of one hundred Hz. Next, a series of recordings are performed in both the SMI based sensor and the pulse meter. The record of the signals is captured at the same time in order to minimize differences between the measurements. A comparison of the results obtained by the pulse-meter and the SMI method is depicted in Fig.4.1.14.

As it is observed in Fig4.1.14 the measurements obtained with the commercial pulse meter and the SMI sensor show good agreement with a ratio very close to one. After fitting the data, it is observed that the relation between the pulse-meter and the SMI sensor is given by the function:

$$f(x) = 0.9828x + 0.7554, \tag{4.1.2}$$

where $f(x)$ corresponds to the estimated measured pulse beat value using the SMI sensor and x is the value of the measurement using a pulse-meter, with a correlation coefficient $r^2_{adj} = 0.9834$. The error at higher pulse values shows a maximum difference of $3BPM$ which is typically in the order of resolution of commercial pulse-meters. At lower pulse beats the error value is close to $1BPM$, which is negligible for most practical applications.

4.1.4 Conclusion

In this section, a potential use for SMI sensors in biomedical signal detection is assessed. The obtained results show good agreement with previous SMI measurements performed by other authors [146,147,149]. The results show good agreement (in terms of waveform) with measurements acquired using the PPG method. In both cases, it is possible to detect both the form and the beat frequency of the signal. SMI measurements, however, present the advantage of quantifying the displacement of the arterial wall, which

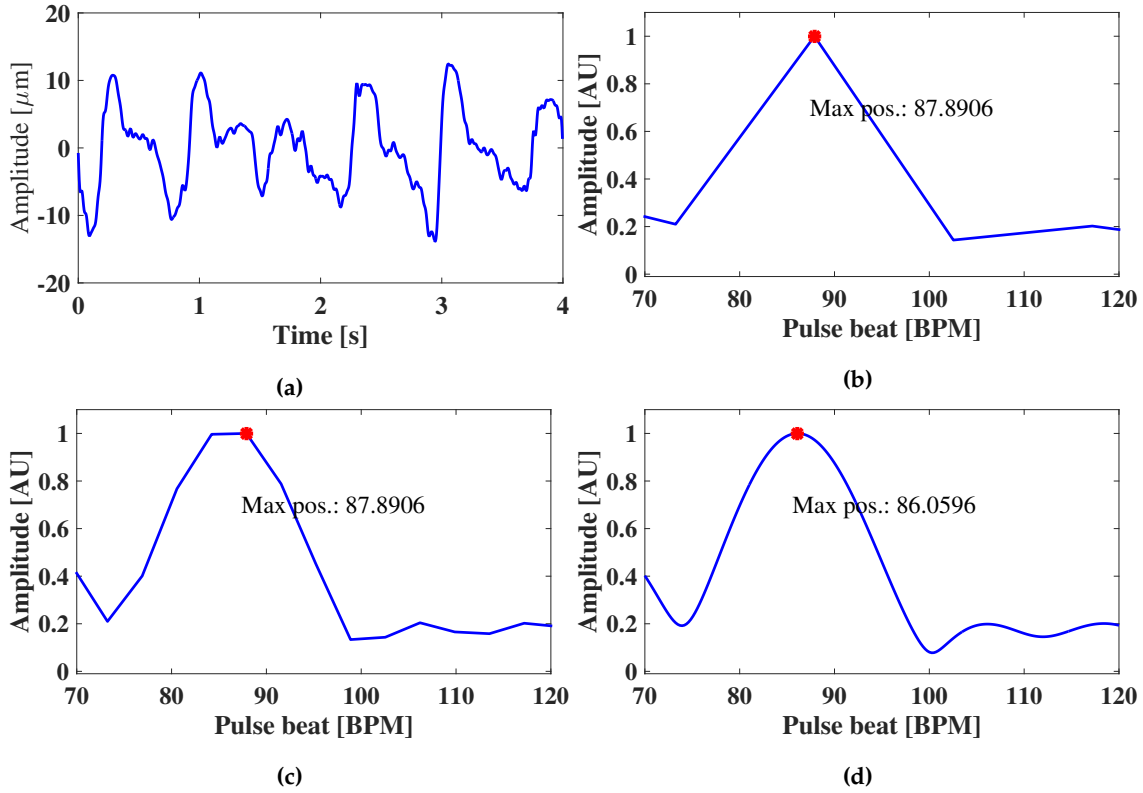

Figure 4.1.13: Example of the result of different zero padding conditions in the estimation of the APW pulse beat in a subsampled signal. (a) Subsampled reconstructed APW signal at 250Hz. (b) FFT of the APW (1kS window) using a zero padding up to 1024. (c) FFT of the APW signal with a zero padding up to 2^{12}. (d) FFT of the APW signal with a zero padding up to 2^{16}. The region around the maximum shows an increase in width, but at the same time enables to define with better resolution the real value of the pulse beat.

might be added information for a further analysis of the biomedical signal. At this point, nevertheless, it is not possible for us to conclude on the possible implications of a varying amplitude in the detected motion as a clinical study with medical supervision would be necessary to provide further information on the usefulness, or lack thereof of the data. This, however, is out of the scope of the present work and becomes an interesting topic for future research.

From the experimental point of view, a laboratory test bench has been presented and discussed in this section. The setup is compact, and it allows an easy adjustment of most of the components needed for the measurement. Besides, it is a very low cost setup. It is observed that in all cases the sensor probe does not have direct contact with the skin or the fingernail, increasing the complexity of the measurement due to different voluntary or involuntary movements of the test subject. The finger holder in the setup is proposed as an effort to minimize such error sources. In many cases however it can be observed that the reconstructed signal can be modulated by low frequency components (smaller than 0.5Hz), and in some cases variations on the peak to peak amplitude can be measured. This low frequency modulations can be attributed to other biological signals present, such as the respiratory rate for example. Since most of the signals acquired present a short span of time, it was not possible to analyze whether the bias motion presented periodic patterns which would be attributed to longer period signals, or if the bias was just a result of random motion of the finger during the measurement.

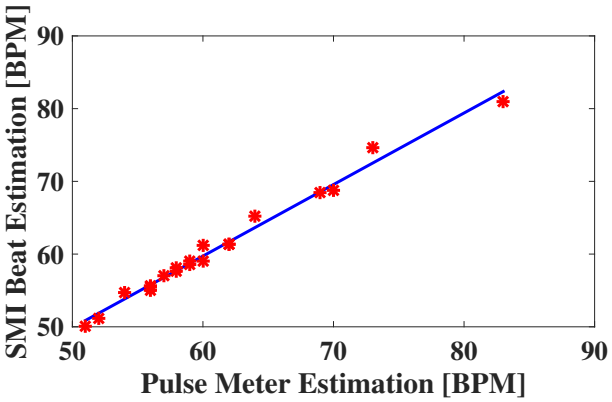

Figure 4.1.14: Comparison between heart beat measurement obtained by a commercial pulse-meter and the proposed SMI method.

In terms of signal reconstruction, the tests performed show that it is possible to reconstruct the APW waveform as long as the sampling frequency, and SMI signal requirements are met. From our experience measuring over the fingernail presents larger possibilities of producing a correct reconstruction when compared to measurements produced over the skin.

The reconstructed data shows that in some case errors within the resolution of the SMI method can be obtained. The reconstruction errors for the obtained measurements vary as a function of the sampling frequency, showing the smaller peak to peak errors (in the order of $400nm$ to $1\mu m$ for larger sampling frequencies. This is shown even further with the tests performed using the reference PZT, where the higher discrepancies between the reconstruction and the pulse are coincident with the changes in direction of the pulse amplitude. In our opinion, these errors may be reduced using more sophisticated methods such as phase unwrapping. Even with this limitations, it is possible to obtain a good representation of the waveform to detect interest points such as the local maxima and the dicrotic notch.

The value of the beat of the signal also presents a point of interest in the measurement, as it is, possibly, the easiest to repeat. It has been observed, as expected, that analyzing a window which includes a larger number of pulses will provide a more accurate match with the actual heart beat rate. This however will present a degree of lag in the measurement, which is tolerable in most common applications. The use of windows with a fewer number of pulses also allows a good estimation, but especial processing strategies such as subsampling followed by zero padding may be required to increase the actual resolution of the measurement. If only one or two pulses are available in the measurement window then the inverse of the period between two consecutive global minimum values can be used for the estimation. Overall, when the method is compared with a commercial pulsemeter, results show a very good correspondence, with a fit proportional constant close to a value of 1.

To sum up, SMI can be used as a non-contact instrument for the acquisition of APW signals. It is suggested that skin measurements are avoided both for instability and safety reasons. If it is not possible to avoid taking measurements over the skin, it is suggested that low power LD's (VCSEL) are used. Measurements on the fingernail have shown to be more stable than those over the skin. Even in such a case, a relatively careful alignment may be necessary to produce good signal reconstruction results. The beat of the signal is possibly the most repeatable characteristic and in many cases can be obtained even without processing the signal, as it would be present in the envelope of the SMI signal. In order to take the experimental setup to a clinical environment further work is still necessary, but the use of SMI presents an interesting

opportunity as a complementary technique to current available methods as it provides information (a quantified displacement) which, to our knowledge, is not provided by other techniques.

4.2 Proof of concept of DSMI sensors for the measurement of micro-cantilever motion

In previous chapters, SMI and DSMI were described as two methods capable of measuring displacement phenomena in the micro and nano scale, respectively. In both cases, limiting conditions are ultimately related to the SNR and the achievable bandwidth given by the electronic acquisition system (this is, the SMI signal conditioning stage and ADC). In the particular case of DSMI measurements, the mechanical modulation used to produce the reference SMI signal also introduces limitations on the measurement bandwidth as described in Ch.3.

The measurement of displacements and small angle variations using SMI has been previously exploited as a method for characterizing surface profile and material deformation by different authors [79, 155]. Material deformation, in particular, can be an interesting field of study in the micro and nano scale since deformation in such scales can be related to superficial force interactions. In order to compute such forces some basic knowledge of the material e.g. area of cross section, length, and Young modulus are necessary to translate accurately deformation into force.

The aim of this section is to present DSMI as an alternative method for measuring deflection on cantilever-based sensors. Cantilever sensors are usually applied on techniques such as Atomic Force Microscopy (*AFM*), although they have also been proposed for the measurement of bio-electrical currents and other small changes at the cellular scale [156, 157]. As discussed earlier DSMI, in its single LD configuration, presents several desirable characteristics (compact-size, high-resolution, low cost) for its implementation in scientific instruments which require optical path change measurements with large resolution.

To begin the analysis, an overview of AFM from its technical and historical perspective is proposed. This introduction does not discuss in depth all the details corresponding to the state of the art in AFM methods, as such topic would require a too lengthy description which would deviate from the main focus of this Thesis. Nevertheless, it is deemed necessary to present some of the basic principles of cantilever sensors used in AFM and other cantilever methods, as it relates to possible further implementations of the proposed technique.

Next, a short theretical review of the cantilever sensor and the spring-mass cantilever model is exposed. The proposed review will be focused in the mechanics of rectangular cross section cantilevers. It is to be noted that the theoretical propositions presented in the following pages can also be applied to other types of cantilevers (e.g. V shaped cantilevers). Nevertheless, the use of other type of cantilevers would require to modify the mechanical mass spring model used for calculations.

After covering the basics of cantilever sensor mechanics, an explanation of the experimental setup is presented. The acquisition method and a detailed scheme of the signal processing techniques are also depicted. As it will be shown, an automated acquisition system was programmed using Visual C++ .Net 2010. The signals are then processed offline by a custom interpretation algorithm using Matlab 2010b.

Once the basic aspects of the method are covered, discussion of the most relevant results obtained using the experimental setup proposed based in DSMI is carried out. The obtained results show that it is possible to recover the displacement of cantilevers within the expected resolution using DSMI. The limitations of the

setup, however, prevent from obtaining the same quality of results as the ones obtained in the presented simulations. Further mechanical isolation, or a reconfiguration of the measuring direction of the setup could provide better results in terms of noise performance and measuring capabilities. Some observations of the effects of SMI signal with respect to the cantilever velocity signal will also be discussed.

Finally, a discussion on the feasibility and interest of a DSMI-based AFM is presented. Possible changes that could enhance the feasibility of the setup and the work of the DSMI-AFM sensor are also discussed.

4.2.1 Atomic Force Microscopy: Historical Overview

In the decade of 1980, in part encouraged by requirements of characterization in electronic production, several efforts pursuing to image objects in the nanometric scale were undertaken. As a result, different scanning probe microscopy methods (*SPM*) [158, 159] were developed. Among these methods, Atomic Force Microscopy (*AFM*) is, possibly, the most representative. Over 1.4 million manuscripts, not including patents nor cites, can be found by making a quick search in Google scholar (December, 2016), from which at least 48.9 thousand have been published in the last year demonstrating the impact of this technology in current research and technology.

Atomic Force Microscopy was first proposed in 1986 by Binning et al. [160] in an effort to produce an instrument capable of measuring the topographic structure of the surface of bulk insulators. In this seminal work, Binning used a cantilever sensor composed of a gold foil and a $25\mu m$ diamond tip which acted as a spring-mass system that reacted to surface forces. In order to reduce mechanical noise coming from the building structure, the resonance frequency of the cantilever was chosen to be larger than $2kHz$. The manuscript also describes four possible modes for applying AFM in practice:

1. First mode - The sample is modulated at its resonance frequency in the z-direction modulating the tunneling current on the feedback circuitry.

2. Second mode - The lever is oscillated at its resonance frequency and the amplitude changes of the tunneling current are used to drive the feedback circuitry.

3. Third mode - The lever is driven at its resonance frequency and the phase changes of the tunneling current are used as inputs of the feedback circuitry.

4. Fourth mode - The tunneling gap is maintained constant by changing the force on the stylus.

From these methods, the one that later became to be known as AFM contact mode (*AFM-CM*), proved to be the more stable obtaining values with a vertical resolution of 1Å and a lateral resolution of 30Å. The deflection of the cantilever was measured using Scanning Tunneling Microscopy (*STM*), resulting in a complex system largely affected by the roghness of the surface of the cantilever. It was also predicted that the instrument sensitivity could reach values ranging from $10^{-18}N$ to $10^{-15}N$ in largely controlled environment conditions. This values are well below the inter-atomic interaction forces, which range from $10^{-12}N$ in the case of Van der Waals forces, to $10^{-7}N$ in the case of ionic bonds.

Later in 1987, non-contact AFM, otherwise known as frequency modulation AFM (*FM-AFM*) [161], was demonstrated by Martin et al. [162], reducing the risk of damaging the sample. In the experiments, a cantilever, made out of a wire and a Tungsten tip, is driven to resonance frequency by a piezoelectric. In these conditions, it was possible to perform measurements at a sample distance ranging from $3nm$ to $18nm$. Martin also commented on the advantages of using an optical sensor (a heterodyne interferometer) over the

tunneling detection proposed by Binning. The use of the interferometer reduced alignment and rugosity issues caused by the STM sensing method. The following year, the use of optical interferometry on AFM was also supported by Erlandsson et al. [163] reaching a 50Å lateral resolution.

Another AFM cantilever sensing method was presented in 1989 by Alexander et al. [164]. The method, known as optical lever, uses a laser which is focused at an aluminum coated cantilever and then reflected to a quadrant position sensitive detector (*PSD*). The deflection is then detected as a function of the reflected beam spot position on the PSD. According to Fujisawa et al. [165], the optical lever deflection method allows the detection of surface corrugation and friction forces while the optical interferometer only permits the measurement of surface corrugation.

New changes were introduced by Ducker et al. [166] in 1991 by changing the cantilever pyramid tip for a colloidal probe. The use of colloidal probes [167] enhanced AFM biological measurement capabilities by reducing the stress applied to the sample during the contact phase at the cost of decreasing the lateral resolution of the instrument. In the same year, true atomic resolution was demonstrated by Giessibl and Binning under Ultra High Vacuum (*UHV*) conditions [168].

Afterwards, in 1993, Zhong et al. [169] defined tapping mode AFM, also known as amplitude modulation AFM (*AM-AFM*) [161], in order to reduce the problem of tip sticking. In this type of AFM, a relatively stiff cantilever with a large spring constant, in the order of $40N/m$, subject to oscillations with an amplitude in the order of $100nm$ for the cantilever tip were suggested. In the same year, AFM piezo resistive cantilever sensors were also introduced [170]. This type of sensors were embedded on the cantilever body and allowed deflection measurement with a resolution of 0.1Å rms in a bandwidth going from $10Hz$ to $1kHz$, making them suitable for CM-AFM.

Next, about 10 years after the invention of AFM, in 1996, Erlandsson et al. [171] demonstrated that AFM allows differentiating inequivalent atoms, adatoms and holes of the same species by imaging a unit of silicium $Si(111)$ using FM-AFM under UHV conditions. For the experiments, Erlandsson used a cantilever etched from tungsten wires which were oscillated with a maximum amplitude of 16Å. The authors concluded that the image contrast was caused by the relaxation of the outermost surface atoms due to the finite force between tip and sample during a small fraction of the cantilever oscillation. Also chemical reactivity was suggested as a possible cause of the relaxation, opening new paths of research for a technique which is becoming the reference in surface and material science.

4.2.2 Measuring cantilever motion in the micro and nano scale

To measure the cantilever motion, different types of sensors and technologies have been proposed [172]. Typically, optical sensors are preferred over other technologies, since they do not exert any external loading over the cantilever, thus preventing possible bias i ^{o}n the measurement.

The optical lever technique [173] is possibly one of the most commonly used methods for measuring microcantilever deflection. This technique allows a high sensitivity of the cantilever deflection angle by sensing the position of a laser spot relative to the central position of a four quadrant photodiode. The main problems of this technique are related to the requirement of a metal coated cantilever (which may induce deformations due to the bimetallic effect [174, 175]) and the need of a careful alignment between the three elements involved in the AFM measurement (laser, cantilever and PD).

Classical interferometric methods have also been suggested for the characterization of cantilever motion. They provide high resolution, usually below 1Å, at the expense of an expensive and bulky setup, which often proves difficult to align. To partially solve this issue, particularly in the microscale, optical fiber

interferometers were proposed, even though the use of optical fibers may induce additional errors in the shape of thermal drifts in low time scales [176], and it will also require special handling to prevent stress during the positioning.

Self mixing interferometry has been previously explored as a method for the estimation of cantilever deflection. In [177], Ovryn and Andrews measured micrometric scale displacements on a millimetric length cantilever using a phase shifting approach. In this method, a calibration for different amplitudes and frequencies is performed using an electro-optic modulator. After a calibration and a phase unwrapping process in the cases where amplitudes are larger than half-wavelength ($\lambda/2$), the net peak amplitude of the deformation is obtained. According to their results, it is possible to achieve similar results to those obtained with holographic interferometry in terms of peak to peak amplitude and main resonance frequency.

Another method was proposed by Larsson et al. in [34]. They proposed to use a combined VCSEL LD and an external PD to characterize the vibration of a polymer micrometric-sized cantilever. In their experiment, the VCSEL is placed at approximately $35\mu m$ from the cantilever. The cantilever is then oscillated by a piezoelectric actuator in a range of $1.2\mu m$. The SMI signal was then recovered using a voltage junction approach [73], and, at the same time, it is also recovered using the external PD placed above the cantilever. As a result of the motion, a cyclic sinusoidal-like behavior correspondent to SMI is observed. In some sections of the displacement reconstruction, linear regions with an equivalent slope of $45mV/nm$ for the PD measurements were observed. This ratio, however, is only found in small intervals of the measurement ($\pm 25nm$), thus requiring locking the measurement region around this point to provide a linear response for the cantilever deflection.

In comparison to the method presented in [177], DSMI presents a more compact setup, which, due to the decrease in the number of optical elements, reduces the alignment constraints. Furthermore, the complexity of the method is reduced, as the technique depicted in [177] requires at least five intensity measurements. Comparing DSMI to the method described in [34], DSMI reduces the need of an external photodiode and increases the measurement range, as the method allows estimating displacements up to a range of $\lambda/2$, while the linearity region shown in [34] is limited to $\lambda/8$ approximately.

4.2.2.1 Rectangular cantilever sensors

As explained above, the AFM sensor can be divided into two parts: a mechanical transducer, which typically behaves as a mass-spring system, and the deflection sensor which acquires the given displacement. Once the deformation signal is acquired and translated into its equivalent displacement (deflection), different processing algorithms can be applied to reconstruct the required variable.

In micro cantilever sensors, the deflection of the cantilever can be related to the surface stress induced by the effects of surface forces. These deflections can range from a few tenths to a few hundredths of nanometers, depending on the dimension and the spring constant of the cantilever.

As a result of requiring two transducer stages, in AFM it is not enough to have a displacement transducer with high resolution, but also a well characterized mechanical interface (cantilever). If one of this conditions fails to be met, the results provided by the given AFM method can be deemed as faulty. Thus, it is necessary to accurately characterize ("calibrate") the mechanical cantilever used for each measurement.

In literature, different methods depending on the geometry of the cantilever have been proposed for this purpose. In this work, however, the description will be limited to methods used for the calibration of rectangular profile cantilevers [178–180]. From these methods, possibly the Sader dynamic technique [180] is one of the best known.

In the Sader method, the spring constant of a rectangular cross section cantilever is measured by comparing a cantilever vibration between a medium with a known viscosity and void conditions. The difference in frequency between the two measurements is then related to the spring constant of the cantilever. In practice, the Sader method involves the shift in the resonant frequency in vacuum ω_{vac} compared to the resonance frequency in a fluid ω_{0f}.

In order to perform the measurement on the oscillator, it is necessary to take into account the quality factor Q of the resonance system which describes the ratio between the resonance frequency of the cantilever and twice its damping factor as described in [181]. Considering a Q factor that exceeds 1 (which describes an underdamped oscillator typically achievable in air [180]), it is possible to relate ω_{vac} and ω_{0f} by:

$$\omega_{vac} = \omega_{0f}\left(1 + \frac{\pi\rho_f W}{4\rho_c H}\Gamma_r(\omega_{0f})\right)^{\frac{1}{2}}, \tag{4.2.1}$$

where W is the cantilever width, and the area mass density $\rho_c h$ is given by:

$$\rho_c h = \frac{\pi\rho_f W}{4}[Q\Gamma_i(\omega_{0f}) - \Gamma_r(\omega_{0f})], \tag{4.2.2}$$

with ρ_f the density of the fluid, and Γ_r and Γ_i are the real and imaginary components of the hydrodynamic function Γ, which only depends on the Reynolds number $Re = \rho_f \omega W^2/(4\eta)$, where η is the viscosity of the surrounding fluid. Thus, it is possible to characterize the cantilever spring constant as a function of its physical dimensions (L length and W width), the quality factor and the resonance frequency as

$$k = 0.1906\rho_f W^2 L Q\Gamma_i(\omega_f)\omega_{0f}^2. \tag{4.2.3}$$

It is to be noted that Eq.(4.2.3) is only valid for cases where $Q \gg 1$, which minimizes the effects of the product $\Gamma_r\omega_{0f}$ on the spring constant estimation.

The overall goal of selecting the correct mechanical properties of a cantilever sensor is to improve the SNR of the deflection measurements. In order to improve the SNR, the resonance frequency of the cantilever ω_{0f} should be as high as possible to minimize the effects of external vibrations on the cantilever. The use of polymer cantilevers can also increase the SNR of the measurement by increasing the attainable deflection. Nevertheless, it is important to notice that polymer based cantilevers are more sensitive to temperature changes, which may induce a bias in the measurement. Another way to improve the sensitivity in cantilever sensors is to increase the deflection by changing the shape of the cantilever, thus reducing its moment of inertia.

4.2.3 Experimental AFM setup using a DSMI method

As discussed in Sec.3.5, the concept of DSMI can be applied to single LD setups, such as the one depicted in Fig.4.2.1. For the sake of clarity, this type of setup can also be referred to as mechanically-modulated SMI as the comparison between the two SMI signals is not performed in the same instant. As described in detail in Sec.3.5, even in such type of configuration the proposed sensor is able to reproduce displacements with a resolution better than $\lambda/2$.

In the proposed configuration for cantilever measurements, the LD is pointed towards the target (the top surface of a rectangular cantilever) and subjected to a reference motion during the whole measurement process. The measurement is divided into two steps. First, as shown in Fig.4.2.1a, an SMI signal with $C \simeq 1$ is acquired for a known PZT reference motion against a static target. Next, in a second step, shown in

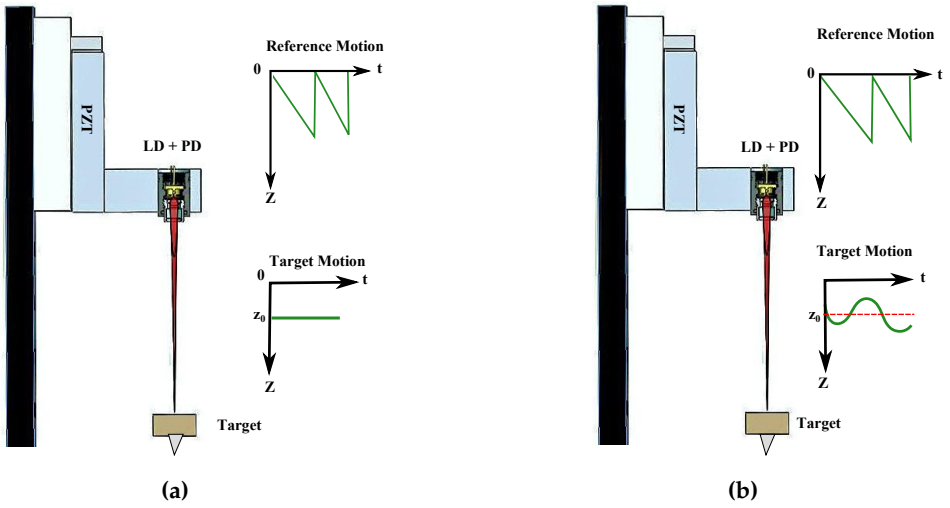

Figure 4.2.1: Example of a mechanically-modulated SMI setup. (a) Reference signal acquired while the target is in a static position with respect to the Y axis; (b) The measurement signal is acquired while both the target and the PZT are in motion

.

Fig.4.2.1b, the measurement signal is acquired while the target undergoes a sub-$\lambda/2$ motion, while the PZT keeps the motion used during the reference acquisition.

Although the depicted setup is bulky compared to the original SMI setup because of the mechanical system needed to create the reference motion, the sensor can still be built in a reduced area compared to other interferometric approaches. Moreover, the size of the sensor may be reduced even further by using an electrically modulated version of DSMI, such as the one suggested by Jha et al. in [182]. For the current implementation, however, the mechanical modulation might present an advantage over the electronic modulation due to its lower dependence on the distance to generate sampling fringes. A more detailed description of the specific methods used in this work to produce the reference signal will be presented in Sec.4.2.3.3.

4.2.3.1 Setup

To test the capabilities and limitations of the DSMI single LD setup for cantilever measurements, the proof of concept setup shown in Fig.4.2.2b was built. As observed in the scheme in Fig.4.2.2a, the sensor performs the measurement along the Z axis, while it is pointing to the tip of the cantilever, which is displaced along that same axis. The description of the setup is divided into three main groups of components: positioning elements, the DSMI sensor, and the digital acquisition equipment.

The positioning elements comprise 2 PI XY LS-120 stepper motor displacement tables (labeled as **(1)** in Fig.4.2.2b) with a step resolution of $0.2\mu m$ and a maximum travel length of $40mm$, which is used to change the relative position between a sample surface and the cantilever probe. The position is tracked by the custom software described in Sec.4.2.3.2. A PI M-227.50 translation stage (labeled as **(2)**) is used to control the Z-axis positioning of the cantilever with a resolution of $50nm$. A PI-LISA PZT stage (labeled as **(3)**) with a maximum travel length of $25\mu m$ is used to generate a sinusoidal motion for the cantilever holder (labeled as **(4)**) and the cantilever. As in the tests performed in Ch.3, the internal capacitive sensor of the PZT stage with a maximum resolution of $2nm$ is used in the measurement for comparison purposes. For all tests the

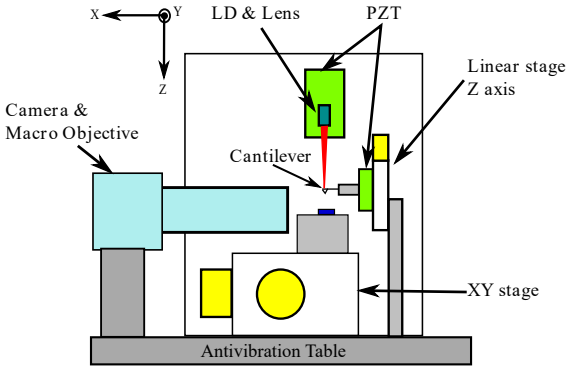

(a)

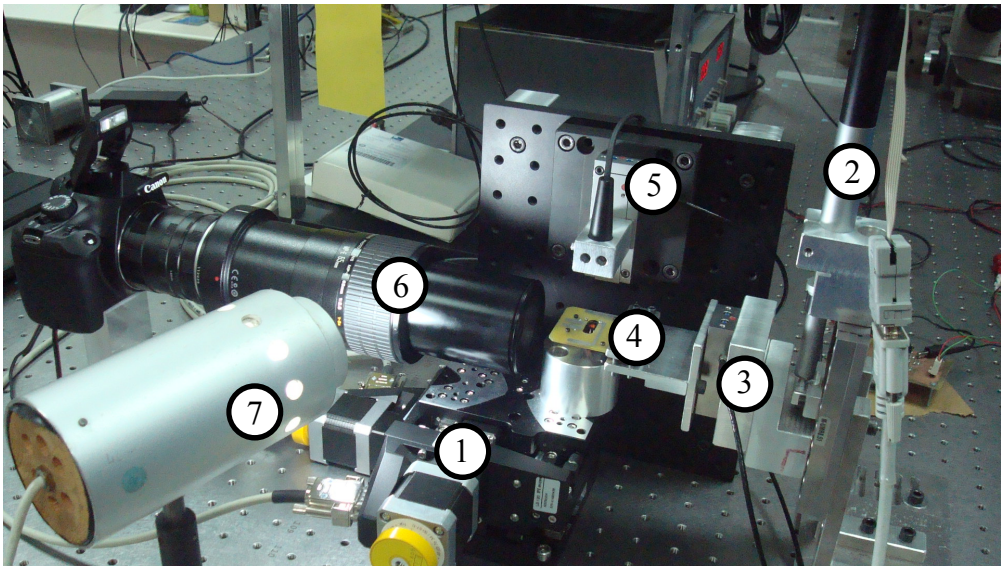

(b)

Figure 4.2.2: (a) Schematics of the mechanically-modulated DSMI setup for AFM measurements; (b) Photograph of the implemented experimental setup: **(1)** XY translation stage for the sample; **(2)** Z-axis translation stage; **(3)** Piezoelectric vibration displacement stage; **(4)** Cantilever holder; **(5)** DSMI sensor; **(6)** Camera with macro objective for pointing and imaging; **(7)** White light source providing the required illumination for imaging.

sample presented in Fig.4.2.3 is used as a target (see Ann.D for a complete technical detail of the target). The sample consists of different steps of 100nm height with different cross sections, and the detail of the distribution of the steps may be found in Annex D . The measurements are attempted on section A of the sample (it is important to remark that although the sample is used as part of the setup, it is not possible to validate a direct measurement on the sample as different mechanical tolerances in the setup account for values larger than the 100nm step size).

A rectangular cross section cantilever *AppNano SHOCONA* with aluminum coating is used as target and experimentally characterized yielding an experimental resonance frequency of 45.29kHz, a quality factor on air of $Q = 108.70$, length of $L = 225\mu m$, width of $W = 46\mu m$ and thickness of $1\mu m$. The nominal characteristics of the cantilever used in the experiments can be consulted in Annex C. The resonance characteristics, however, required to be obtained experimentally as the range provided by the manufacturer is too wide to be used in any computation.

The calibration of the cantilever was performed using the previously mentioned Sader method at the

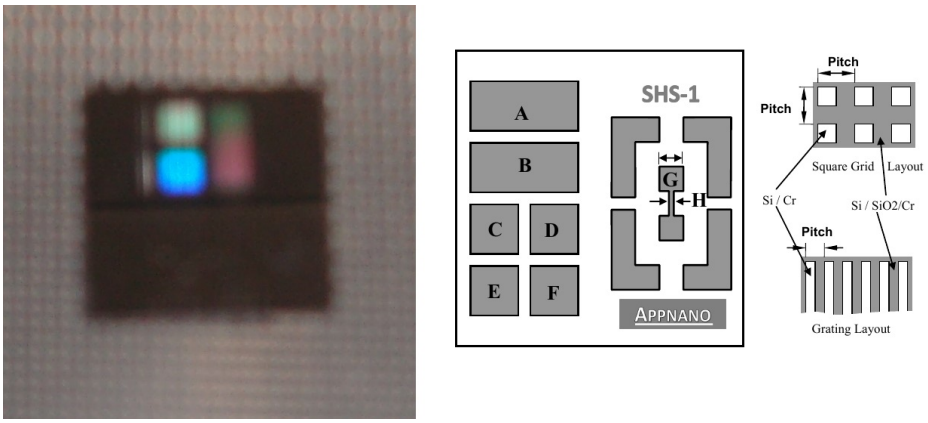

Figure 4.2.3: Target used for the experimental DSMI-AFM setup. Specific details about the target are described in the technical specification presented in Ann.D.

Sample	f_r [kHz]	Q	L [μm]	W [μm]	k [N/m]
1	45.29	108.70	225.00	46.00	0.95
2	46.62	125.16	225.00	46.00	1.14
3	45.24	111.54	225.00	46.00	0.97

Table 4.2.1: Experimental values for the calibration of three cantilever samples with rectangular cross section. The represented values correspond to the resonance frequency f_r, the quality factor Q, the cantilever length L, the cantilever width W and the cantilever stiffness k.

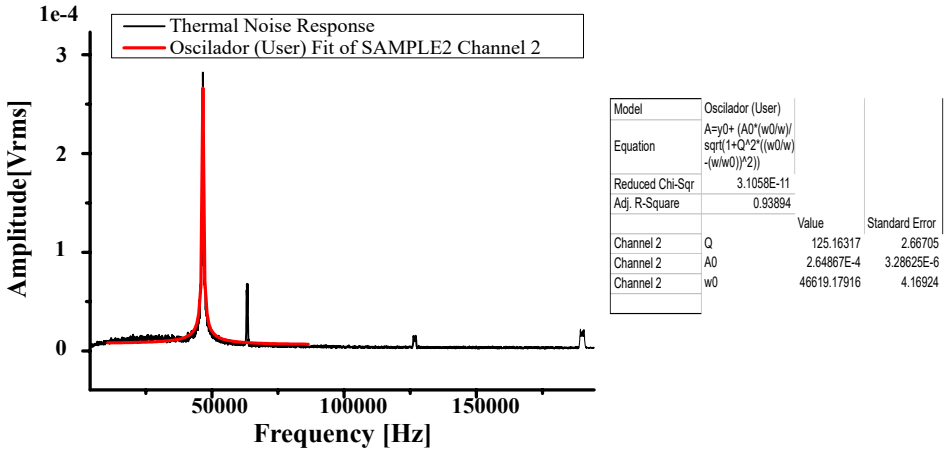

Figure 4.2.4: Example of resonance frequency fit for the cantilever sample labeled as 2.

facilities of the Barcelona Microelectronics Institute of the National Microelectronics Centre-CSIC (*IMB-CNM-CSIC*). The measurement was performed using a Michelson interferometer with a HeNe laser (λ = 633nm) to measure the motion of the tip of the cantilever. All measurements were performed in standard room temperature conditions (T_c = 25^{o}C). During the calibration three samples were measured making a linear fit of the resonance frequency and a post processing using Sader's online calibration method [183]. The results and an example of the obtained resonance frequency are shown in Tab.4.2.1 and Fig.4.2.4 respectively

The DSMI sensor **(5)** is composed of a *Hitachi HL7851G* multi-quantum well Fabry–Perot laser diode with λ = 783.5 nm measured using *Instrument System's SPECTRO 320(D)R5*. As in previous instances, the LD is

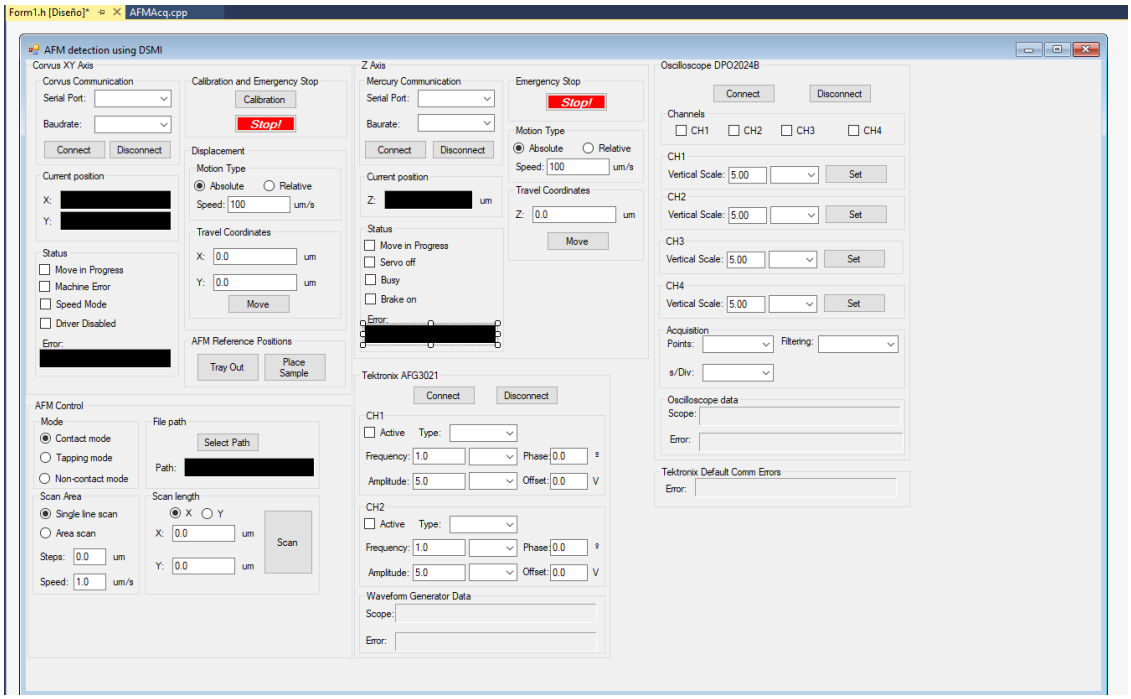

Figure 4.2.5: PC GUI interface to control experimental AFM-DSMI setup.

mounted on a Thorlabs *LT230220P-B* collimating tube equipped with a *C230220-B* aspheric lens pair with numerical aperture $NA = 0.55/0.25$. The tube is then attached to another PI-LISA PZT with a maximum travel length of $38\mu m$ using a custom aluminum support, which is used to oscillate the laser and create the interference fringes. The sensor is placed at an approximate distance of $100mm$ from the cantilever. The LD is then connected to a custom-made electronic card, which collects the PD current (I_{PD}) and sends it to a current mirror allowing to obtain two duplicates of I_{PD}. One of the signals is sent to the LD driver and the second one to a passive TIA with an approximate transimpedance gain of 2200. After the conversion to voltage, the signal undergoes a high pass filter with a cutoff frequency in the order of $15Hz$ to remove the DC part of the signal. Finally, the signal is subjected to a gain stage whose output is fed into the acquisition stage.

The acquisition stage uses a *Tektronix DPO2024B* oscilloscope using one channel to recover the SMI signal and a second channel to retrieve the displacement of the $25\mu m$ LISA PZT from its reference capacitive sensor. For the proposed application, the ADC conversion is limited to 8 bit values in order to minimize issues in the data transfer between the oscilloscope and the PC. While an option has been integrated in the custom software to use 10 bit values, after several acquisitions, it was observed that the use of a 10 bit representation did not enhance significantly the reconstruction capabilities of the post-processing algorithm, while the acquisition was slower and more prone to data transfer errors.

A custom-made interface developed on VC++ 2010 .NET is used to control the whole setup as shown in Fig.4.2.5. The interface also allows the control the parameters of a *Tektronix AFG3022B* signal generator, and also commands the XYZ stage positioning. The interface can also be used with other Tektronix oscilloscopes as the implementation uses the VISA command set for the RS-232 communication. Similarly the PI platform control uses at its base the PI proprietary communication language which in principle would allow to easily modify the setup to use other stages from the same manufacturer.

A *Canon EOS1100D* camera equipped with a *MP-E 65mm f/2.8* macro objective **(6)** and a white light

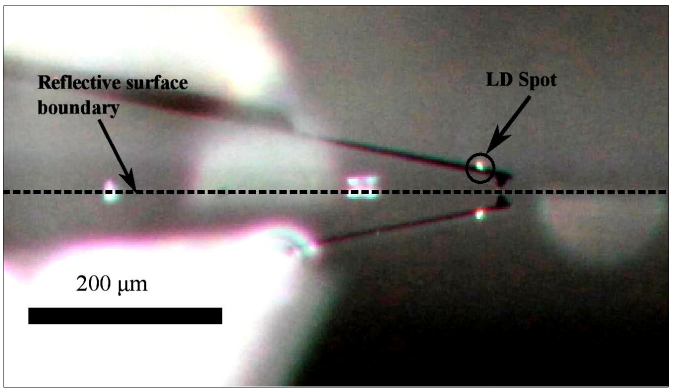

Figure 4.2.6: Microcantilever SHOCONA aligned to the LD. Spot from the SMI sensor is visible.

source **(7)** is used to provide visual feedback regarding the vertical position of the cantilever. It is important to notice that even with the use of the MP-E 65mm macro objective it was not possible to directly observe the cantilever as a result of its lateral dimensions. To solve this issue, a $10cm$ tube extender was placed between the camera and the macro objective, enabling to observe the cantilever at the cost of losing some definition in the obtained image.

4.2.3.2 Scanning and Signal Acquisition

Previous to the start of the measurement, a SHOCONA cantilever is placed on a cantilever holder, which is then fixed on a custom mechanical support connected to the PZT, as shown in Fig.4.2.2b **(3)** and **(4)**, then, the LD is focused on the cantilever. The alignment between the cantilever and the laser beam is confirmed by looking at the reflection of the laser spot on the cantilever through the camera, as shown in Fig.4.2.6. Once the proper alignment is confirmed, the XY table is calibrated and set at its origin until a sample is placed on the stage for measurement. After displacing the sample holder and the sample to the measurement coordinates, the cantilever is moved to the required working distance from the sample, and an offline test is performed to check that the SMI signal is working under the desired feedback regime ($C \simeq 1$). After moving up the cantilever to prevent a collision with the sample, the XY table is moved to the initial scanning position. At this point, it is possible to change the starting scanning position relative to the initial preset coordinate. Next, the cantilever is approached as close as possible to the sample surface. The approach is controlled manually using custom software with the visual aid of the camera.

Once the cantilever and sample are at the initial measurement position, a reference measurement is taken by inducing a ramp mechanical modulation on the SMI sensor.

The acquisition in arranged so the captured signal corresponds only to the positive ramp of the PZT displacement. After storing the reference measurement, a sinusoidal vibration in the range of $10Hz$ to $200Hz$ is induced on the cantilever by means of the PZT shown in Fig.4.2.2b. The start of the acquisition for the measurement signals is launched using the rising edge of a square transistor-transistor logic (TTL) signal that is matched with the start of the positive ramp translation of the PZT, and it is stopped on the falling edge of the TTL signal. After each acquisition, the signals are automatically saved in a PC for further offline signal processing.

After each measurement, the sample is displaced either in the X or Y axis in order to test the effects of the raster scanning functionality to be used in further developments. Once the sample is set in its new position, the vibration process is restarted using the parameters previously selected by the user. The

process is repeated for the equidistant number of points selected in the software interface, resulting in the final distance scanned. In the case of XY displacements the scan is performed using an S type pattern in which all the positions of the X scan direction are covered followed by a Y step displacement and a reversal of the direction of the X motion. This is repeated until the specified final coordinate is met.

4.2.3.3 Signal Processing

As discussed in Sec.3.5, the implemented method uses a mechanically-modulated SMI sensor. The reference OOP signal can thus be obtained using any of the four possible ways mentioned in Sec.3.5. For the results presented below, a reference signal was acquired for each sample set with a static target. In the case of simulations, however, the frequency spectra of the mean velocity method is evaluated, as this is the most suitable implementation in the case that no other type of reference signal is available. Although, as it is discussed above, any of the methods discussed in Sec.3.5 is valid for this application, capturing the reference signal allows us to validate the procedure and whether the cantilever oscillation is within the expected $\lambda/2$ range. In the case of simulations, the use of the frequency method simplifies the initial steps of the signal processing reducing the requirements (memory and time) to produce a result with a long data sequence.

After the acquisition, the measurement sample is band-pass filtered using an FFT-based filter with cutoff frequencies at $f_{SMI}/5$ and $10 \times f_{SMI}$, where f_{SMI} is the main frequency of the SMI signal. Next, the filtered SMI signal is processed using a fringe detection algorithm. In this stage the SMI signal is first normalized, then an arc-cosine function is applied to work in the phase domain and finally the signal is differentiated and normalized to one. After this initial preprocessing the fringe detection is performed using a threshold comparison method. The threshold is calculated as the RMS of the differentiated signal. To ensure a correct detection of the fringe sign and to prevent fringe loss, after the initial fringe detection, a zero crossing algorithm is applied on the filtered SMI signal. The detected positions are compared to those in the differentiated signal to confirm proper detection. The fringes are finally selected as the common output of both algorithms.

After the fringe detection process, the time intervals between consecutive fringes in the measurement and reference signals are calculated, as well as the corresponding velocity given that the distance between two fringes is fixed as $\lambda/2$. After obtaining the velocity waveform, the signal is integrated using the cumulative trapezoidal method described in [184]. This process is repeated for each of the positions of the acquired scan.

4.2.4 Simulation

A simulation of the detection of the sinusoidal motion of a cantilever using the mechanically-modulated SMI method was performed in order to optimize the performance of the sensor. The SMI algorithm solves the excess phase Equation (Eq.2.2.42) using the Schröeder root finding method and bracketed with the intervals described in [185]. The parameters of the simulation are presented in Tab.4.2.2.

The chosen parameters were selected to provide a $C \simeq 1$ ($C = 0.976$) to optimize the performance of the method. A positive ramp-like displacement with a constant velocity $v_r = 380\ \mu m/s$ is chosen as a reference for the SMI signal. All simulated displacement vectors, as well as the corresponding SMI signals are composed by $125kS$ to match the length of the acquisition vectors in the experimental measurements.

For the cantilever motion, a harmonic modulation is calculated using as reference the mass-spring

Parameter	Value	Units
Wavelength (λ)	783.50	nm
Reference velocity (v_r)	380.00	μm/s
Feedback attenuation (ϵ)	0.06	
Feedback factor (C)	0.98	
Distance to cantilever (D)	100.00	mm
Cantilever displacement (ΔD)	100.00	nm
Cantilever frequency (f)	100.00	Hz
Cantilever reflectance (R_e)	0.90	
Distance sample-cantilever 1 (d_{z1})	100.00	nm
Distance sample-cantilever 2 (d_{z2})	0.50	nm
Cantilever stiffness (k_c)	0.95	N/m
Cantilever quality factor (Q_c)	108.70	
Cantilever resonance frequency (f_{rc})	45.29	kHz

Table 4.2.2: Parameters for cantilever displacement simulation.

resonator equation:

$$F_{ext} + F_d \times sin(2\pi f t) = m_{eff}\frac{d^2z}{dt^2} + f_v\frac{dz}{dt} + k_c z \tag{4.2.4}$$

where the effective mass m_{eff}, the damping factor f_v and the stiffness k_c are parameters describing the mechanical performance of the cantilever in terms of the displacement z and its time derivatives, F_d is the amplitude of the driving force, and F_{ext} accounts for the van der Waals (VdW) force interaction using as reference the Derjaguin–Muller–Toporov (DMT) model [186]. The simulation is tested for two cantilever tips which sample minimum distances $d_{z1} = 100nm$ and $d_{z2} = 0.50nm$. The cantilever displacement profiles behave following a harmonic motion with a variation in amplitude when the cantilever tip is closer to the sample, as illustrated in Fig.4.2.7. The cantilever displacement is only considered for the cantilever tip in a motion parallel to the axis of the laser beam. When available, the parameters of the calibrated cantilever presented in the previous section have been used.

The resulting SMI signal contains the information of the reference velocity, as well as that of the target displacement, as displayed in Fig.4.2.8b by the frequency peaks induced over the spectra due to the Doppler effect. It should also be noted that the normalized amplitude of the frequency peaks caused by the motion of the tip is dependent on the force, resulting in a value of $0.4383AU$ for d_{z1} and $0.4389AU$ for d_{z2}. For the presented simulation, the frequency resolution is limited to $10Hz$. In the case where the FFT resolution is not sufficient to represent the result, the peaks caused by the cantilever vibration become wider, and, as in the previous case, their amplitude also changes as a function of their proximity to the simulated sample.

After analyzing the spectral effects, the simulated mechanically-modulated SMI signal is subjected to the algorithm discussed in Sec.4.2.3.2. In the case of the $d_{z1} = 100nm$ sample distance, the reconstruction follows the simulated cantilever displacement with an RMS error of $7.66nm$ and a standard deviation of $7.70nm$, as illustrated in Fig.4.2.9. In the case of a distance of $d_{z2} = 0.50nm$, no significant differences are observed in the reconstruction; however, the RMS error and standard deviation increase in the order of $0.002nm$ which may be related to numerical limits in the simulation. The errors in the reconstruction can be related to non-linearities induced by large displacements. This is best observed if we double the velocity of the ramp reference displacement in the d_{z1} case, which results in an error of $3.84nm$ and a standard deviation of $3.86nm$, respectively. This is also observed when a $1nm$ amplitude displacement is applied as a cantilever motion in the simulation. The resulting RMS error in the reconstruction is reduced to a change in path

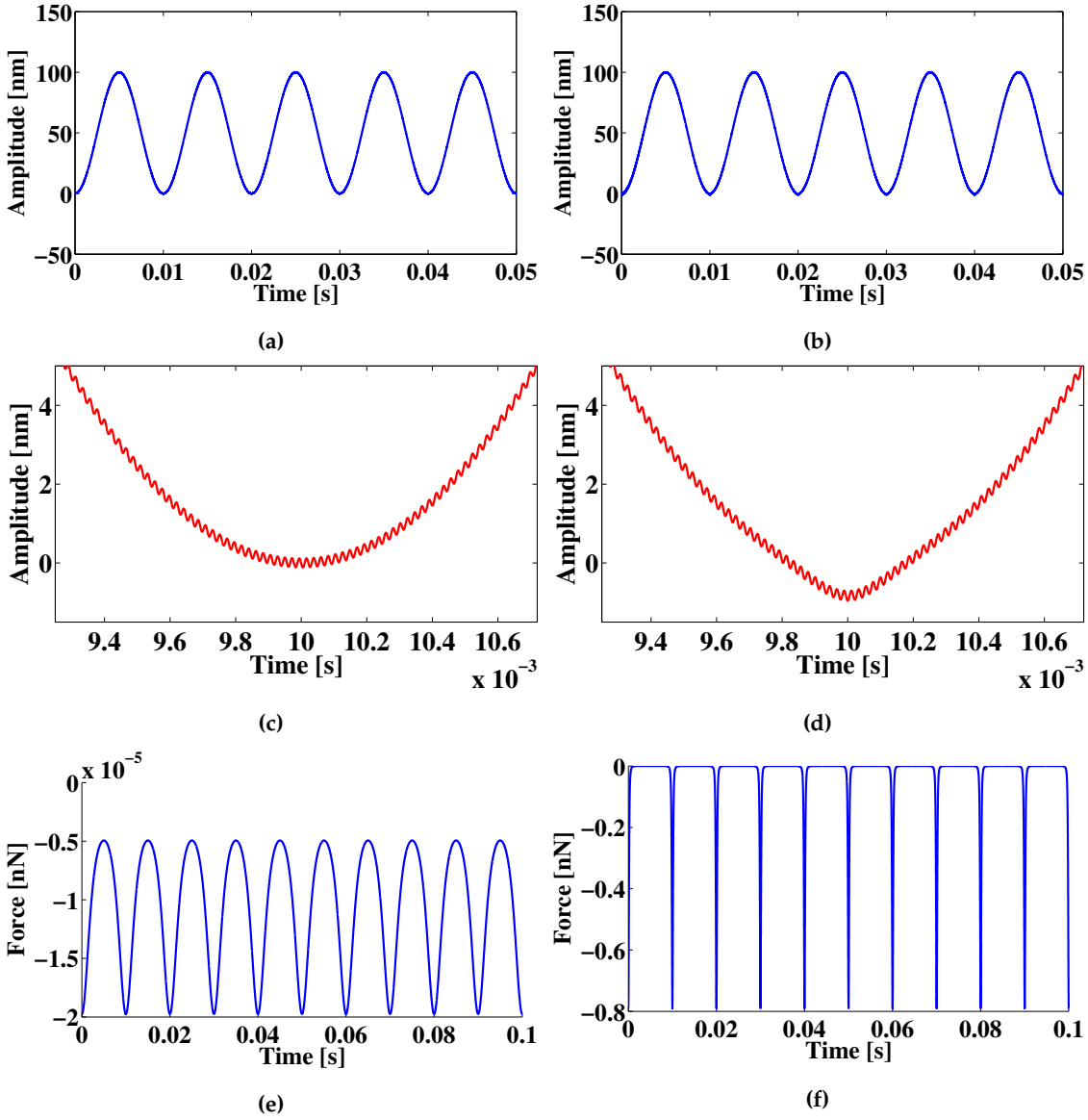

Figure 4.2.7: Simulated behavior of the cantilever tip due to an applied harmonic motion. (a,b) Amplitude representation of a harmonic displacement with the tip placed for d_{z1} (left) and d_{z2} (right) respectively; (c,d) Zoom of the displacement amplitude around the region where the tip is closer to the sample; a deformation of the harmonic motion increases as the minimum tip to sample distance is reduced; (e,f) Corresponding force effect for d_{z1} (left) and d_{z2} (right).

length of 0.16nm and a standard deviation of 0.16nm.

4.2.5 Experimental Results

As a first test, a set of mechanically-modulated SMI measurements was obtained in regular lab working conditions at a room temperature of 25 $°C$. A 100nm peak to peak oscillation was induced on the cantilever, and the signals were retrieved following the steps described in Sec.4.2.3.2, resulting in the waveform shown in Fig.4.2.10. Reconstruction errors can be attributed to three major sources: (1) the linearity of the reconstruction algorithm; (2) mechanical fixation issues; and (3) mechanical noise caused by acoustic and mechanic vibration of the building and the environment itself. Low SNR signals may also induce errors

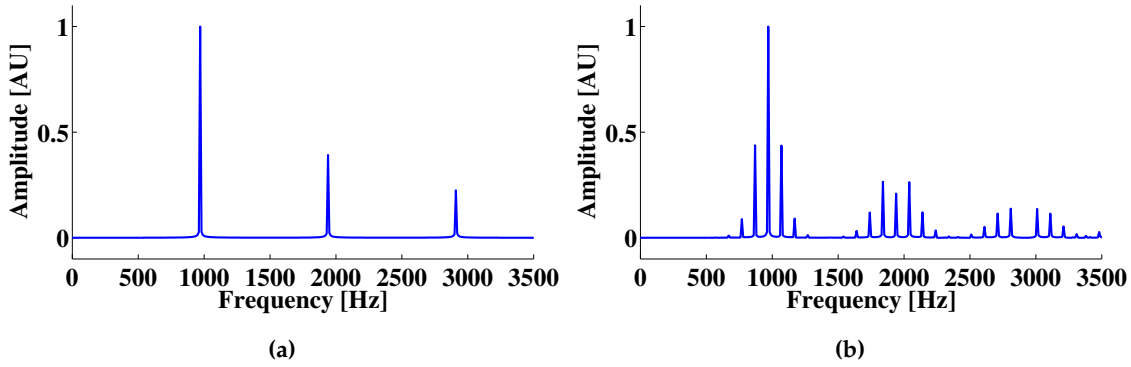

Figure 4.2.8: (a) Frequency spectra of a simulated mechanically-modulated SMI sensor signal without target motion; (b) Effect of the cantilever motion over the frequency spectra; different peaks are observed around the main SMI frequency and its corresponding harmonics; the frequency difference between the main SMI peak and the highest amplitude peak around it equals the frequency of vibration of the target.

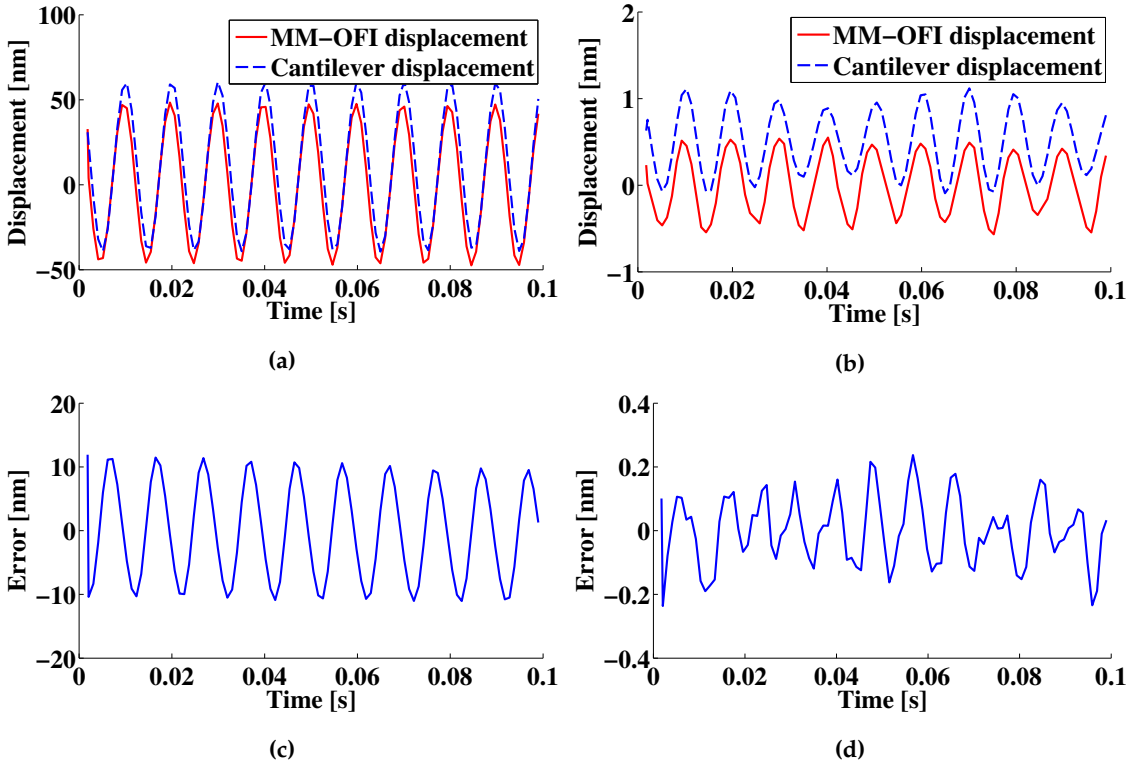

Figure 4.2.9: (a,b) Reconstructed displacements and (c,d) Reconstruction errors for a 100nm and 1nm simulated amplitude displacements at the tip of the cantilever. In (a), a 10nm offset is included on the 100nm displacement for visibility purposes. Similarly, in (b), a 1nm offset is included on the 1nm displacement. The legend MM-SMI is used to refer to the mechanically-modulated SMI signal.

because of the increased difficulty to detect the position of the SMI signal fringes. This effect, however, is limited for the measurements presented in this work, as the sensor is calibrated to work close to $C = 1$ in all cases.

For the case presented, the difference between the PZT sensor response and the mechanically-modulated SMI measurement can be explained by mechanical fixation issues between the PI-LISA PZT and the can-

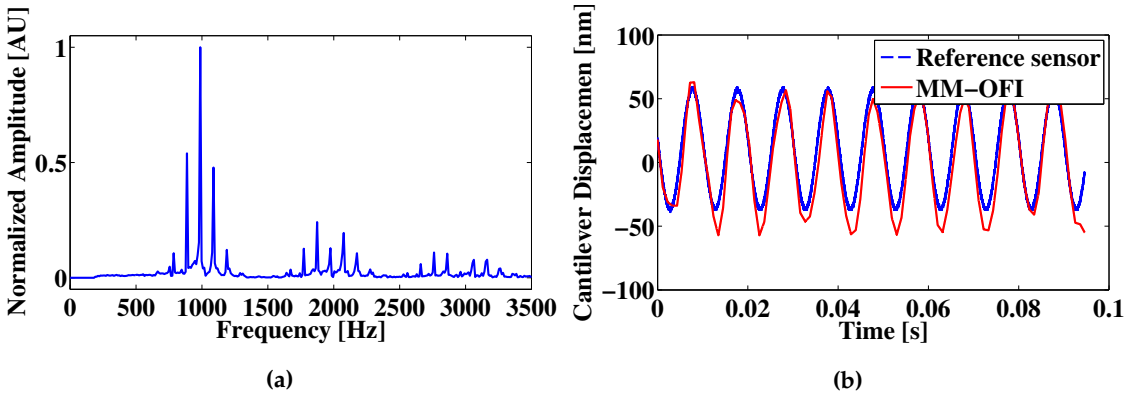

Figure 4.2.10: (a) Frequency analysis of a experimental mechanically-modulated SMI signal with the cantilever vibrating at 100 Hz with a peak to peak amplitude of 100nm; (b) Comparison between the internal capacitive sensor response of the PI-LISA PZT (dashed line) and the mechanically-modulated SMI sensor (solid line).

tilever holder and by possible linearity issues in the reconstruction method. Another possible explanation to the difference might be the detection of surface forces over-imposed on the reference displacement as they are within the 20 to 30nm range, which would represent forces in the range of 0.3nN to 18nN. It should be noted that the frequency spectra displayed in Fig.4.2.10a shows two peaks at 886Hz and 1088Hz around the expected 987Hz frequency. The difference between the central frequency and any of these peaks corresponds to the main driving frequency of the sinusoidal modulation (100Hz). These peaks also appear as the second and third harmonic of the SMI spectra (1975Hz and 2962Hz), with a smaller amplitude than those corresponding to the SMI signal.

In order to remove some of the issues observed in the previous measurement and improve the performance of the system, the holder grip mechanism was modified increasing the stiffness of the mechanical structure. After a new calibration process, a new set of measurements was acquired under normal laboratory conditions, which include the presence of random mechanical noise and acoustic vibrations, even if the environmental conditions (air flow, etc) were minimized within available possibilities. An example of signals acquired for a reference oscillation of amplitude 100nm and frequency 100Hz in the Z-axis, with steps of 0.5μm in the X-axis for a length of 50μm (100 measurement positions) is presented in Fig.4.2.11. As observed, there exist different punctual events, which cause errors in the reconstructed measurement, in some cases with amplitudes circa λ, as shown in Fig.4.2.11b. In most cases, the measurement holds the expected 100nm amplitude value, as observed in Fig.4.2.11c. This stability in the detected amplitude and frequency is also confirmed in the representation of the Fourier spectra for each of the SMI acquired measurements (Fig.4.2.11d). Spectra do not show any discernible variations in the amplitude of the signal (which can be obtained by multiplying by $\lambda/4$ the normalized amplitude), showing a mean value of 92nm with a standard deviation of 8nm for 100 measurements. This, again, has good agreement with the response of the reference capacitive sensor.

A new set of measurements was acquired under even more controlled conditions. In this case the system was automatized to perform the measurements automatically while there was no one in the room, to prevent vibration and unwanted air flows, thus reducing possible sources of acoustic noise during the measurement, and also the presence of mechanical noise induced by footsteps in the room. Again, signals were acquired for a 50μm displacement with steps of 0.5μm in the X-axis as presented in Fig.4.2.12. As shown in Fig.4.2.12a and Fig.4.2.12c, no spikes of amplitude larger than 100nm are now visible. A random variation on the

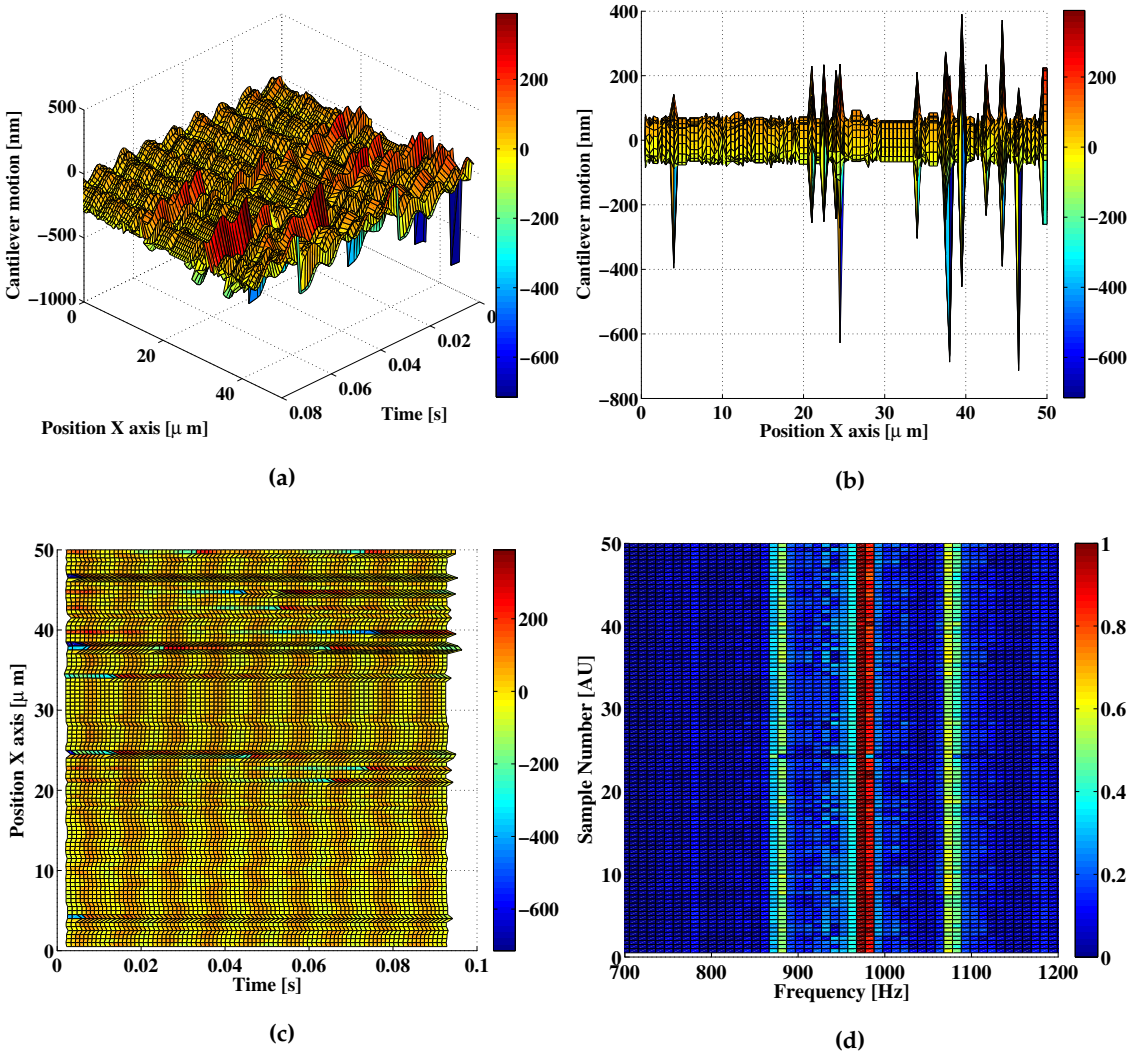

Figure 4.2.11: Example of an experimental $A = 100nm$ cantilever displacement reconstruction under uncontrolled acoustic and mechanical noise conditions. The displacement is shown in different projections: (a) 3D; (b) lateral and (c) top view; (d) The top view of the Fourier spectra around the main harmonic of the SMI measurement signal for each of the points acquired in the X-axis.

detected amplitude is observed in Fig.4.2.12b, leading us to believe that the proximity to the sample surface may be having an effect on the measurement. These variations, nonetheless, cannot be quantified at the moment. In most cases, however, the measurement holds the expected $100nm$ amplitude value as observed in Fig.4.2.12c. The stability in the detected amplitude and frequency is also confirmed in the representation of the Fourier spectra for each of the SMI acquired measurements (Fig.4.2.12d). The Fourier spectra of the signals shows a mean value of $92nm$ with a standard deviation of $8nm$ for 100 measurements which again is in good agreement with the results of the capacitive sensor.

The off-line computing time for each signal containing takes in average $0.695s$, which shows feasibility for an on-line signal processing using the proposed mechanically modulated DSMI method.

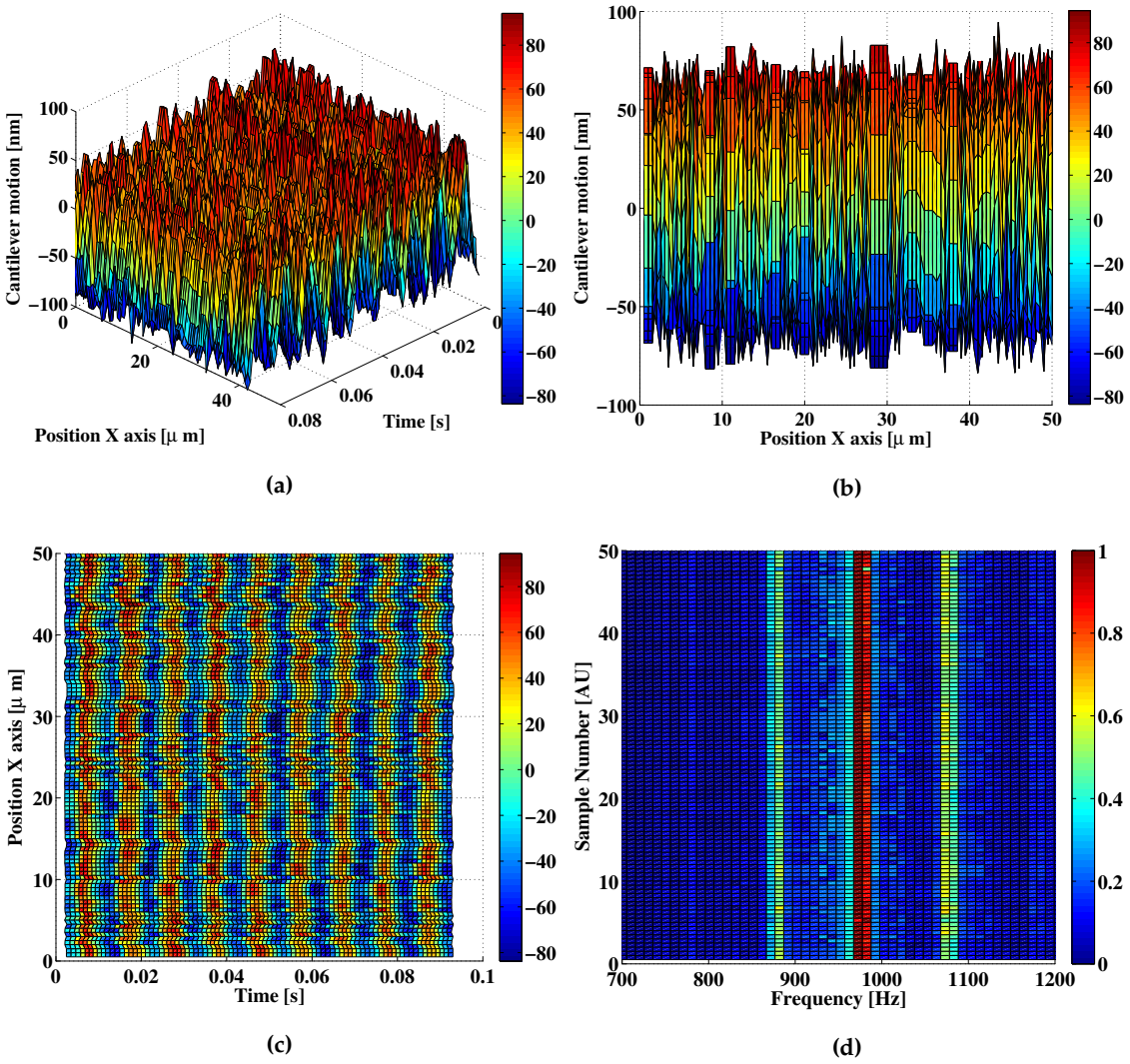

Figure 4.2.12: Example of an experimental $A = 100nm$ cantilever displacement reconstruction after improved mechanical stiffness of the support of the cantilever and automated acquisition to minimize noise sources . The displacement is shown in different projections: (a) 3D; (b) lateral and (c) top view; (d) Top view of the Fourier spectra around the main harmonic of the SMI measurement signal for each of the points acquired in the X-axis.

4.2.6 Discussion

The results obtained in the previous section show the feasibility of a mechanically-modulated DSMI sensor for detecting a cantilever sinusoidal motion with peak to peak amplitudes going from 100 to 200nm. This results agree with the measurements presented in Ch.3 and [184] where it is shown that a practical resolution of 3nm can be reached, thus allowing the capture of 10nm amplitudes with detail enough.

While the test show that it is possible to measure the displacement of cantilevers with dimensions as the ones presented in the experimental section, it is suggested that better results may be obtained with cantilevers of larger dimensions. The use of larger cantilevers would decrease the resonance frequency of the cantilever which would have a better match with the current limitations of the MM-DSMI method. Working closer to the resonance frequency of the cantilever would also help to reduce effects of noise associated to structural vibration and increase the amplitude of the total cantilever oscillation, therefore

making easier its detection.

By means of simulation, it has also been shown that it is possible to reproduce the displacement of lower figures, such as is the case of the $1nm$ displacement shown in Fig.4.2.9, since the linearity of the sensor is increased for smaller changes. Similar results are also shown in [177], where it is observed that the SMI readings behave linearly for small changes. Therefore, in practical experiments it is critical to isolate mechanically the structure of the DSMI and cantilever system to avoid including errors in the measurement. In particular, it has been observed that the system is extremely sensitive to mechanical and acoustic fluctuations in the room. Therefore, it is required to increase the isolation of the system to the room acoustic and environmental conditions, which might be achieved by casing the system in a sound-proof box.

External vibrations can also be reduced by setting the system on an absorbent material (e.g., marble), which would reduce the amount of vibrations transmitted from the floor into the instrument, even through the optical table. Another possibility would be to work on vibration amplitudes with frequencies larger than $200Hz$ to reduce possible vibrations inherent to the building structure.

In terms of mechanical noise reduction, it is also possible to change the measurement direction towards the X- or Y-axis. This, however, may introduce an issue with sample handling in the case of liquid-based media.

In terms of electrical noise, it has been observed that the system is capable of obtaining low errors if the SNR of the signal is larger that $10dB$; for lower values, the signal tends to degrade, reducing the fringe visibility and, thus, affecting the fringe occurrence time detection. For SNRs above $10dB$, detected RMS errors on the signal typically stay below $\lambda/100$. The signals presented in this work presented a minimum SNR in the order of $20dB$.

As mentioned before, the normalized Fourier spectra of the mechanically-modulated SMI signal also contains relevant practical information of the displacement, as it can be used to detect the information of the mean velocity used to generate the reference signal and also to compute the main frequency of the sample displacement in the case of the harmonic motion. It should also be noted that for the case where the cantilever was subjected to forces smaller than $1nN$, a change on the peak amplitude at the corresponding Doppler frequency shift with a value of 0.0006 units was detected. In principle, this variation is negligible; however, it should be expected that as the sample frequency is increased and reaches values closer to the cantilever resonance frequency, the detected amplitude will be larger.

It is also to be noticed that this work focuses on measurements at low frequencies compared to typical measurements in the area, that typically work over the kHz range. It is stressed that the work described is to prove the feasibility of the mechanically-modulated SMI method on the detection of microcantilever displacement in the nanometric scale. The measurements were performed taking into account the limitations of the mechanical systems used to provide both the reference modulation and the cantilever modulation. While working within the selected frequency range can be partially the cause of the noise induced over the measurement, the obtained results show that, nonetheless, it is possible to retrieve a cantilever displacement with nanometric amplitudes using a MM-DSMI method. The use of a frequency analysis could, in principle, improve the amplitude estimation, as this value could be obtained by calculation the ratio between the main frequency and harmonic peaks shown in the FFT. This would be particularly useful in the case of purely sinusoidal motions, but may entail some degree of error for more complex displacements as in the current experiments it was not possible to decouple extra information from other harmonics in the Fourier spectra.

4.2.7 Conclusion

In this section, the feasibility of using MM-DSMI sensors for the measurement of microcantilever motion has been shown. The technique, as it has been presented, is able to recover the motion of a commercial microcantilever of the type usually employed in AFM systems, suggesting that the sensor can detect the motions of micrometric cantilevers, as long as the displacement is within the resolution of the device. While experimental conditions and available materials did not allow testing the method for amplitudes below $100nm$, larger amplitude motions show good agreement with the theory and simulations presented. Furthermore, the frequency analysis shows good correspondence with the theory showing the appearance of secondary peaks in the Fourier spectra with the correct amplitude relative to the normalized amplitude of the principal SMI harmonic and with a shift in frequency corresponding to the main frequency of the cantilever motion.

There are, however, several factors that require further work before creating a practical MM-DSMI sensor for the measurement of cantilever motion. First of all, a better isolation system to mechanical and acoustic noise beyond the optical table is required since, as observed in Fig.4.2.11, some noise sources may drastically hamper the results on the measurements. Some possible solutions to achieve this isolation are described in Sec.4.2.6. Furthermore, the change of some conditions on the tip holder and the tip itself may benefit the measurement. These changes include reducing the angle between the tip and the horizontal plane and removing the aluminum coating on the cantilever. In the first case, a reduction on the possible fringe detection errors during the signal processing caused by the angle of the cantilever is to be expected. In the second case, the aluminum coating of the cantilever can cause issues due to the bimetallic effect, which introduces strain on the cantilever, causing some degree of bending due to the difference of thermal expansion coefficients between the reflective and substrate materials of the cantilever. This has also been remarked by other authors, e.g., in [175, 177] as an issue with classic cantilevers. Even more problematic for the SMI case is the large reflectivity of aluminum, which may change the SMI working point to a strong feedback regime. In the measurements proposed above, a small amount of defocusing has been allowed removing the issue at the cost of having a larger spot size and lower SNR, which also may limit the accuracy of the method.

Regading a profile reconstruction algorithm, further work is required to perform a complete interpretation of the acquired data. For these purposes, a tip force characterization system needs to be included in the processing. The method may largely benefit from the use of other types of SMI setups, such as the one discussed in [182], as they work closer to the bandwidth frequency of more classical commercial instruments. It is important to remark that in its current setup, the sensor is limited by the mechanical modulation imposed by a PZT, thus limiting the working frequency of the reference signal as a function of the displacement amplitude. In principle, the sensor described in this paper should be able to measure displacements with frequencies in the order of 1 to $2kHz$ with high definition and up to $10kHz$ with a smaller definition.

5. Conclusions and Future Work

The work presented along this Thesis started with the aim of improving the resolution of self-mixing interferometry (*SMI*) as part of the developments in optical metrology developed at CD6. In our view, characterizing an providing a method based on SMI with an improved resolution would allow to provide solutions previously out of reach of SMI sensors as a result of the resolution limit of $\lambda/2$ inherent to them. Furthermore, this work continued the line of research on SMI at CD6 and set the basis of further works to be carried out in this area.

The main contribution of this work resides around the idea of differential self-mixing interferometry presented in Ch.3. Along Ch.3 the DSMI concept has been presented and it has been shown that the method is capable of attaining better resolutions than other classic SMI displacement methods while keeping the cost of the technique lower than other interferometric systems. The simulation model used to characterize the method, in which the effects of different variables on the measurement resolution were analyzed (e.g. the feedback regime and wavelength difference, among others), shows that in ideal measuring conditions resolutions better than $\lambda/1000$ might be attainable.

Furthermore, experimental measurements using a calibrated piezoelectric device equipped with a capacitive displacement sensor with $2nm$ resolution further proved the assertion that the proposed method is able to measure oscillatory vibration values with a resolution better than the typical resolution for SMI displacement systems ($\lambda/2$), even if the amplitude of the displacement is well below $\lambda/2$. According to our results in ordinary room conditions, it would be possible to recover displacements with a resolution in the order of $3nm$. It is remarked that this results it was not possible to produce results with a resolution better than $\lambda/200$ for any of the studied cases as this may have required special isolation equipment which is currently not available, and goes beyond the scope of this Thesis. The use of further specialized equipment to improve the complete physical isolation of the system would, in our opinion, remove the simplicity and cost factors which make the SMI and DSMI methods attractive for applications outside a laboratory space.

In our opinion, the difference in one order of magnitude in the resolution between the model and the experimental conditions may be explained by non-linearities existing in the LD as a result of small temperature changes which could result in jitter for the SMI signal. Also, it has been noticed that the reference displacement stage might have been limited in terms of linearity as a result of the quantization steps produced by the reference signal generator which in a closed loop function may have induced additive errors within the resulting resolution of the system.

A second contribution in this work, and still within the DSMI topic, is the proposal of a DSMI setup using a single LD system. The main aim of the single LD DSMI method is to reduce the overall cost of the setup as well as to reduce any mechanical complexity in the construction of a DSMI apparatus. While the single LD DSMI setup may entail a higher degree of complexity in the signal acquisition, we consider that in a long run the use of this type of method may present an advantage over a two LD DSMI setup as a result of the reduction of non linearities dependent upon laser dynamics and differences in the LDs. Furthermore, simulation and experimental results show that using this type of configuration provides a similar resolution to that obtained using the double LD setup. The major downside observed during experimentation is related to temporal drifts in the LD behavior which might result in errors when reconstructing displacements with

a net zero frequency during the measurement interval.

As part of this work two real-world applications, one for SMI and another for DSMI, were explored: arterial pulse wave measurement *APW*, and cantilever displacement sensing, respectively. In the case of APW, it was found that the resolution of DSMI was too high to measure the process as displacements values with a typical amplitude larger than $20\mu m$ were found. As a result an analysis based on SMI was preferred. An important contribution here is related to the review of literature on laser safety which is typically not considered for SMI studies. The research showed that measurements with LDs in the NIR range should be limited in time and power. It is suggested that in case of skin exposure for more than $10s$ the spot should have a diameter larger than $2.5mm$ and with a power lower than $2mW$. Also we have presented the possibility of producing APW measurements over nail tissue using SMI. According to our results the measurement of the APW over the nail may be more stable in the case of the SMI technique as a result of the presence of different artifacts which make APW skin measurements unstable and unreliable. It is to be noted, nonetheless, that the frequency of the APW can be correctly recovered in both the skin and nail cases.

The last contribution of this work is focused on the use of DSMI as a sensing tool for cantilever sensors. It was found that the main limitation of the technique is related to its use in noisy environments, inherent to the small displacements which are to be measured. In such a case the sensitivity of the technique acts as a drawback to itself. To try to solve this issue, mechanical isolation and the use of a horizontal measuring strategy can result in a large reduction of noise. In some cases it has been shown that it is possible to measure along the vertical axis, e.g. in AFM like features, however this practice is discouraged as the likelihood of acquiring noise during the measurement increases significantly. After different tests, it is considered that the method would be better suited to measure displacement of cantilevers of relatively larger dimensions. This would allow to decrease the resonance frequency of the cantilever, thus allowing the sensor to work in more favorable conditions. Otherwise it would be recommended to use other type of stimuli to produce the reference SMI signal. In such a case it should be possible to reduce possible sources of noise which can be directly associated to the structural vibration of the place where the measurement is being performed. It is critical to carefully isolate mechanically the structure of the DSMI and cantilever system to avoid including errors in the measurement. It is observed nonetheless, that we were able to correctly reproduce cantilever motions with an amplitude of $100nm$ and lower. It is also important to remark that the provided frequency analysis has a good agreement with the proposed theory. The use of a frequency analysis could, in our opinion, improve the amplitude estimation, as this value could be obtained by observing the ratio between the main frequency and harmonic peaks shown in the FFT. This however may entail a drawback when the complete translation of the target is required.

5.1 Future work

After several years of work and after getting to know the major benefits and drawbacks of a given method, it is impossible, in a personal opinion, not to consider what things could have been changed during the experimentation, what other tests could have been performed, or what other applications may be suitable for the proposed technique.

At the beginning of this work different ideas came on possible applications for a high resolution system. At that point only small considerations regarding to the limits of the technique in terms of bandwidth were considered. After further studying the approach it was possible to come out with some of the applications described earlier in the text, and to get into a deep knowledge of the different features of the technique.

From the point of view of the method, one of its main current limitations is its reachable bandwidth. This issue is related to the type of modulation used to create the reference SMI signal. The use of a mechanical modulation severely limits the type of events which may be oberverd. The use of an electrical modulation of the intensity of the laser diode, for instance, as suggested in [187] is a suitable approach which may significantly improve the bandwidth of the technique. Other possibilities of improvement are related to the use of other types of modulation, such as electro-optical modulators. This, however, increases the relative cost and complexity of the setup, which is one of its main attributes, and thus would not be desirable. Nonetheless, this could be further studied in applications where the cost and complexity of the complete system may be increased.

Other considerations to be taken into account are related to the stability of the LD. In most of the cases considered in this work, the measurements were performed using FP LDs. It is worth exploring the use of other types of technologies with better stability (e.g. DFBs), which may perform with better stability, repeatability and reliability than in the case of the results presented in this Thesis.

Another interesting approach is the use of the SMI voltage junction read-out method instead of the PD approach used throughout this work. Such a method could reduce some amount of noise induced in the PD conversion as well as saturation effects caused by parasitic light sources. In any case, the results obtained after a larger amplification stage should be similar to the ones obtained in this work, allowing to have a wider selection of LDs suitable for the implementation of the technique in other applications. This would be also important in terms of system miniaturization as it would reduce the number of required on-chip elements. Nonetheless, at this point it is not possible to foresee if there might be other drawbacks related to the use of the voltage scheme on the measurement.

The use of temperature regulators to increase the reliability of the setup is also a relevant line of research in order to further increase the stability of the measurements. The main drawback of this type of elements in the presented configurations is related, in my opinion, to the large increase of size and mass of the setup, which would also limit the range of speeds available in a system driven by a piezoelectric actuator. Thus a temperature controller design with a minimized area would be required for this type of setups. Similarly, a temperature controller of reduced size would contribute to keep the sensor size as small as possible, and possibly should be combined with electrical modulation schemes to skip bandwidth limitations.

In terms of applications, much of the work related to improvements of the method should be aimed at increasing the quality of the isolation to reduce mechanical noise, acoustic perturbations, and environmental problems such as air flows. As observed along the work, although the technique shows its proper performance in a number of experiments, an improved mechanical isolation beyond the optical table would play a crucial role in the repeatability and accuracy of the measurements. Also, other type of sensor isolation (e.g. pressure, temperature, CO_2 content, etc.) would improve the performance of the sensor and potentially increase the number of suitable applications for the method.

From the applications presented here, the one with better chances of technical success is the measurement of cantilever-like sensors. There exists a large number of methods relying on cantilever motion to characterize a wide variety of physical processes, from surface quality to bioelectricity. Each cantilever technique uses cantilevers of different size, thus opening the possibility of finding a technique with optimal characteristics for DSMI. In this sense it is important to set priority in applications with a measurement direction along the horizontal plane. This could be performed for example in magnetic spring systems like the one characterized in [188].

Another possibility would be to analyze the use of DSMI in refractive index measurement. Some initial

simulation results show that it may be possible to obtain results with resolutions better than $10 \times^{-7}$ *RIU* (Refractive index units) for small variations in a localized refractive index. Nonetheless, this topic should be handled with care as a large amount of isolation may be required, which, as discussed before, may be a drawback when talking about SMI.

Finally, in the case of other applications that might be explored, there are a wide variety of them, which as a result of cost or time were out of the scope of this Thesis. Examples of this possibilities of research are the measurement of low frequency magnetic fields using magnetostrictive materials, measurement of displacement of spring type sensors subjected to Lorentz force, or the design of sub-sonic microphones and geo-phones for the detection of low frequency seismic waves.

Common symbols and acronyms

α - Linewidth enhancement factor.

κ - Coupling factor.

λ - Laser diode wavelength.

ω - Angular frequency.

ϕ_0 - Laser wave phase.

ϕ_f - Laser wave phase under feedback.

c - Speed of light in vacuum.

C - Optical feedback coefficient.

n - Refractive index.

N - Carrier density.

$\mathfrak{R}$ - Real part of a complex number.

$\mathfrak{I}$ - Imaginary part of a complex number.

AFM - Atomic force microscopy.

APW - Arterial pulse wave.

DSMI - Double self-mixing interferometry.

DOFI - Differential optical feedback interferometry.

LD - Laser diode.

MPE - Maximum permissible exposure.

OFI - Optical feedback interferometry.

OOP - Optical output power.

PD - Photodiode.

PZT - Piezoelectric transducer.

SMI - Self-mixing interferometry.

SNR - Signal to Noise Ratio.

List of publications

Journal Articles

1. Francisco J. Azcona, Ajit Jha, Carlos Yáñez, Reza Atashkhooei and Santiago Royo, "Microcantilever Displacement Measurement Using a Mechanically Modulated Optical Feedback Interferometer," *Sensors*, vol. 16, no. 7, pp. 997-1–17, Jun. 2016, DOI:10.3390/s16070997.
2. Francisco J. Azcona, Reza Atashkhooei, and Santiago Royo, "Differential optical feedback interfeometry for the measurement of nanometric displacements," *Opt. Pura Apl.*, vol. 47, no. 1, pp.19–25, 2014.
3. A. Arasanz, F. J. Azcona, S. Royo, A. Jha, and J. Pladellorens, "A new method for the acquisition of arterial pulse wave using self-mixing interferometry," *Opt. & Las. Tech.*, vol. 60, pp.98–104, Nov. 2014, DOI: 10.1016/j.optlastec.2014.04.004.
4. Francisco J. Azcona, Reza Atashkhooei, Santiago Royo, Jorge Méndez Astudillo, and Ajit Jha, "A Nanometric Displacement Measurement System Using Differential Optical Feedback Interferometry," *IEEE Photon. Technol. Lett.*, vol. 25, no. 21, pp. 2074–2077, Nov. 2013, DOI: 10.1109/LPT.2013.2281269.
5. Ajit Jha, Francisco J. Azcona, and Santiago Royo, "Frequency-Modulated Optical Feedback Interferometry for Nanometric Scale Vibrometry," *IEEE Photon. Tech. Lett.*, vol. 28, no. 11, pp. 1217–1220, Jun. 2016, DOI: 10.1109/LPT.2016.2531790.
6. Julien Perchoux, Adam Quotb, Reza Atashkhooei, Francisco J. Azcona, Evelio E. Ramírez-Miquet, Olivier Bernal, Ajit Jha, Antonio Luna-Arriga, Carlos Yanez, Jesus Caum, Thierry Bosch, and Santiago Royo, "Current Developments on Optical Feedback Interferometry as an All-Optical Sensor for Biomedical Applications," *Sensors*, vol. 16, no. 5, May 2016, DOI: 10.3390/s16050694.
7. Ajit Jha, Francisco J. Azcona, Carlos Yañez, and Santiago Royo, "Extraction of vibration parameters from optical feedback interferometry signals using wavelets," *App. Opt.*, vol. 54, no. 34, pp. 10106–10113, Nov. 2015, DOI: 10.1364/AO.54.010106
8. Reza Atashkhooei, Santiago Royo, and Francisco J. Azcona, "Adaptive autofocus technique for speckle control in optical feedback interferometry," *Sens. and Act. A: Phys*, vol. 216, pp. 243–248, Sep. 2014, DOI:10.1016/j.sna.2014.06.003.
9. Reza Atashkhooei, Santiago Royo, and Francisco J. Azcona, "Dealing With Speckle Effects in Self-Mixing Interferometry Measurements," *IEEE Sens. J.*, vol. 13, no. 5, pp. 1641–1647, May 2013, DOI: 10.1109/JSEN.2013.2240156.

Conference proceedings

1. Francisco J. Azcona, Ajit Jha, Carlos Yáñez, and Santiago Royo, "Medida de Desplazamiento Nanométrico en Microcantilévers utilizando Interferometría Realimentada Diferencial," XI Reunión Nacional

de Óptica, Resúmenes de las Contribuciones, Salamanca, Spain, 1–3 Sep. 2015.

2. Ajit Jha, Francisco J. Azcona, Carlos Yáñez, and Santiago Royo, "Vibrometría de alta resolución utilizando interferometría óptica retroalimentada diferencial por modulación electrónica,", *IX Optoelectronic Spanish Meeting Libro de Comunicaciones*, Salamanca, Spain, 13–15 Jul. 2015.
3. Francisco J. Azcona, Ajit Jha, Carlos Yáñez, and Santiago Royo, "Differential self-mixing interferometry for micro-cantilever motion sensing," *Proc. of SPIE 9529, Optical Methods for Inspection, Charactrization, and Imaging of Biomaterials II*, pp.95291B Munich, Germany, 22–25 Jun 2015, DOI: 10.1117/12.2184725.
4. Ajit Jha, Francisco Azcona, and Santiago Royo, "Ultracompact vibrometry measurement with nanometric accuracy using optical feedback interferometry," *Proc. of SPIE 9525 Optical Measurement Systems for Industrial Inspection IX"*, pp.95251Y, Munich, Germany, 22–25 Jun 2015, DOI: 10.1117/12.2184730.
5. Francisco J. Azcona, Santiago Royo and Ajit Jha, "Towards atomic force microscopy measurements using differential self-mixing interferometry," *Proc. IEEE Sens. 2014*, pp. 766-770, Valencia, Spain, 2–5 Nov. 2014, DOI:10.1109/ICSENS.2014.6985112.
6. Ajit Jha, Santiago Royo, Francisco Azcona, and Carlos Yañez, "Extracting vibrational parameters from the time-frequency map of a self mixing signal: An approach based on wavelet analysis," *Proc. IEEE Sens. 2014*, pp.1881–1184, Valencia, Spain, 2-5 Nov. 2014, DOI: 10.1109/ICSENS.2014.6985396.
7. Francisco J. Azcona, Reza Atashkhooei, Santiago Royo, Jorge Méndez, and Ajit Jha, "Differential Optical Feedback Interferometry: a New Method to Measure Nanometer Displacements," *OPTOEL 2013 VIII Reunión Española de Optoelectrónica*, Alcalá de Henares, Spain, 10–12 Jul. 2013.
8. Francisco J. Azcona, Reza Atashkhooei, Santiago Royo, Jorge Méndez Astudillo, and Ajit Jha, "A method to measure sub nanometric amplitude displacements based on optical feedback interferometry," *Proc. SPIE 8789 Modeling Aspects in Optical Metrology IV*, pp. 878908, Munich, Germany, 13–16 May 2013, DOI: 10.1117/12.2019992.
9. Francisco J. Azcona, Reza Atashkhooei, Santiago Royo, Lluis Gil, Joseph Pladellorens, "Interferometría Autorrealimentada para la Medición de Deformación en Materiales Estructurales Sometridos a Cargas Dinámicas," *Conference Proceedings X Reunión Nacional de Óptica 2012*, Zaragoza, Spain, 2012
10. Reza Atashkhooei, Francisco J. Azcona, Santiago Royo, Lluis Gil, "Optical feedback interferometry for measuring dynamic stress deformation of beams," *10th International Conference on Vibration measuremt by laser and noncontact techniques (AIVELA 2012), AIP Conference Proceedings 1457*, pp. 132–138, Ancona, Italy, Jun. 2012, DOI: 10.1063/1.4730551.
11. Reza Atashkhooei, Santiago Royo, Francisco J. Azcona, and Usman Zabit, "Analysis and control of speckle effects in self-mixing interferometry," *Proc. IEEE Sens. 2011*, pp. 978-1–4, Limerick, Ireland, 28–31 Oct. 2011, DOI: 10.1109/ICSENS.2011.6127054.
12. Reza Atashkhooei, Usman Zabit, Santiago Royo, Francisco J. Azcona, and Irina Sergievskaya, "Adaptive feedback control in self-mixing interferometry using active optical elements," *AOIM Droplets*, Murcia, Spain, Jun 2011.

Patents

1. Santiago Royo, Reza Atashkhooei, and Francisco J. Azcona, "A method of measuring a displacement-related parameter using a laser self-mixing measuring system, and a laser self-mixing measurement

system," *Patent WO/2012/049561*, Oct. 2012.

2. Santiago Royo, Francisco J. Azcona and Ajit Jha, "A method of measuring a change in an optical path length using differential laser self-mixing interferometry and a differential laser self-mixing interferometry measuring system," *Patent WO/2015/092498*, Jun. 2015.
3. Santiago Royo, Francisco J. Azcona, Ajit Jha, and Javier Bezares, "Method, device and computer programs for measuring a fetal arterial pulse wave," *Patent EP 3001946 A1*, Apr. 2016.

Other

Oral presentation

1. Francisco J. Azcona, Ajit Jha, Carlos Yáñez, and Santiago Royo, "Medida de Desplazamiento Nanométrico en Microcantilévers utilizando Interferometría Realimentada Diferencial," XI RNO, 2 Sep. 2015, Salamanca, Spain.
2. Ajit Jha, Francisco Azcona, and Santiago Royo, "Ultracompact vibrometry measurement with nanometric accuracy using optical feedback interferometry," SPIE Optical Metrology, 25 Jun 2015, Munich, Germany.
3. Francisco J. Azcona, Ajit Jha, Carlos Yáñez, and Santiago Royo, "Differential self-mixing interferometry for micro-cantilever motion sensing," SPIE Optica Metrology, 24 Jun 2015, Munich, Germany.
4. Francisco J. Azcona, Santiago Royo and Ajit Jha, "Towards atomic force microscopy measurements using differential self-mixing interferometry," IEEE Sensors, 4 Nov. 2014, Valencia, Spain.
5. Francisco J. Azcona, "Towards DSMI for the Measurement of Refraction Index Changes," BM1205 Cost Meeting, 30 Apr. 2014, Valleta Malta.
6. Francisco J. Azcona, Reza Atashkhooei, Santiago Royo, Jorge Méndez Astudillo, and Ajit Jha, "A method to measure sub nanometric amplitude displacements based on optical feedback interferometry," SPIE Optical Metrology, 13 May 2013, Munich, Germany.
7. Francisco J. Azcona, Reza Atashkhooei, Santiago Royo, Lluis Gil, Joseph Pladellorens, "Interferometría Autorrealimentada para la Medición de Deformación en Materiales Estructurales Sometridos a Cargas Dinámicas," X RNO, 5 Sep. 2012, Zaragoza, Spain.
8. Reza Atashkhooei, Francisco J. Azcona, Santiago Royo, Lluis Gil, "Optical feedback interferometry for measuring dynamic stress deformation of beams," AIVELA 2012, 27 Jun. 2012, Ancona, Italy.

Poster presentation

1. Francisco J. Azcona, Reza Atashkhooei, Santiago Royo, Jorge Méndez, and Ajit Jha, "Differential Optical Feedback Interferometry: a New Method to Measure Nanometer Displacements," VIII Optoel, 12 Jul. 2013, Alcalá de Henares, Spain.

Appendix A. Hitachi HL7851G Laser Diode Technical Specifications

opnext Powered by HITACHI

HL7851G

GaAlAs Laser Diode

ODE-208-062A (Z)
Rev.1
Dec. 04, 2006

Description

The HL7851G is a high-power 0.78 μm band GaAlAs laser diode with a multi-quantum well (MQW) structure. It is suitable as a light source for optical disk memories, levelers and various other types of optical equipment. Hermetic sealing of the package assures high reliability.

Features

- Visible light output: λp = 785 nm Typ
- Small beam ellipticity: 9.5:23
- High output power: 50 mW (CW)
- Built-in monitor photodiode

Package Type
• HL7851G: G2

Internal Circuit

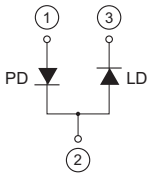

Absolute Maximum Ratings

(T_C = 25°C)

Item	Symbol	Ratings	Unit
Optical output power	P_O	50	mW
Pulse optical output power	$P_{O(pulse)}$	60 *	mW
LD reverse voltage	$V_{R(LD)}$	2	V
PD reverse voltage	$V_{R(PD)}$	30	V
Operating temperature	Topr	–10 to +60	°C
Storage temperature	Tstg	–40 to +85	°C

Note: Maximum 50% duty cycle, maximum 1 μs pulse width.

Optical and Electrical Characteristics

(T_C = 25°C)

Item	Symbol	Min	Typ	Max	Unit	Test Conditions
Threshold current	Ith	—	45	70	mA	
Slope efficiency	ηs	0.35	0.55	0.7	mW/mA	40 (mW) / ($I_{(45mW)}$ – $I_{(5mW)}$)
LD Operating current	I_{OP}	—	135	165	mA	P_O = 50 mW
LD Operating voltage	V_{OP}	—	2.3	2.7	V	P_O = 50 mW
Lasing wavelength	λp	775	785	795	nm	P_O = 50 mW
Beam divergence (parallel)	θ//	8	9.5	12	°	P_O = 50 mW, FWHM
Beam divergence (perpendicular)	θ⊥	18	23	28	°	P_O = 50 mW, FWHM
Monitor current	I_S	30	45	150	μA	P_O = 5 mW, $V_{R(PD)}$ = 5 V
Astigmatism	As	—	5	—	μm	P_O = 5 mW, NA = 0.4

opnext Powered by HITACHI

HL7851G

Typical Characteristic Curves

Optical Output Power vs. Forward Current

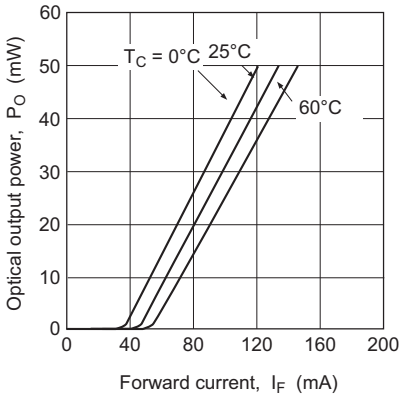

Threshold Current vs. Case Temperature

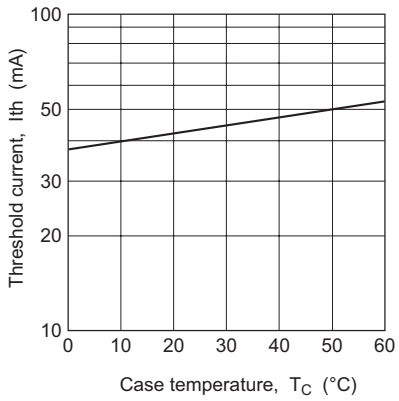

Slope Efficiency vs. Case Temperature

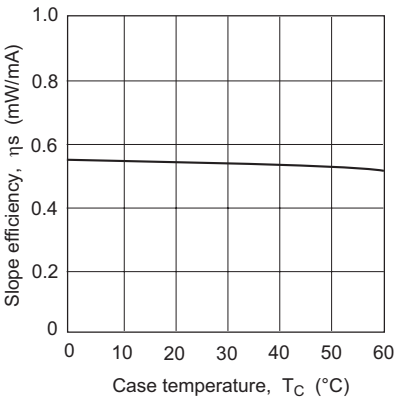

Monitor Current vs. Case Temprature

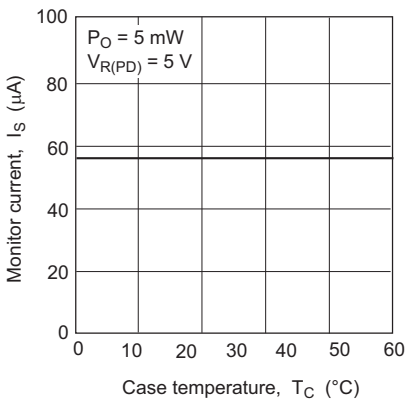

Lasing Wavelength vs. Case Temperature

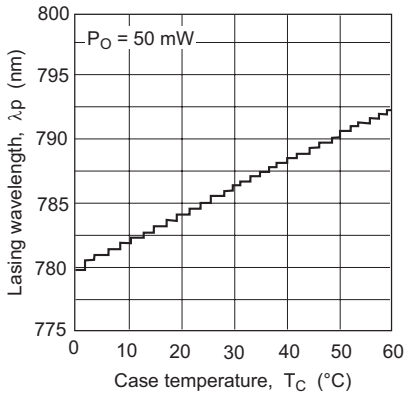

Far Field Pattern

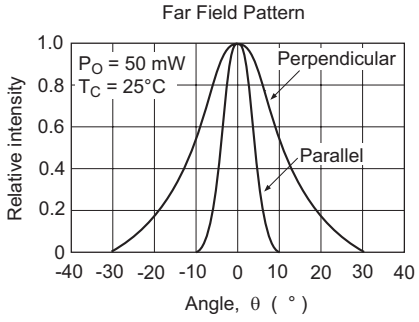

HL7851G

Package Dimensions

Unit: mm

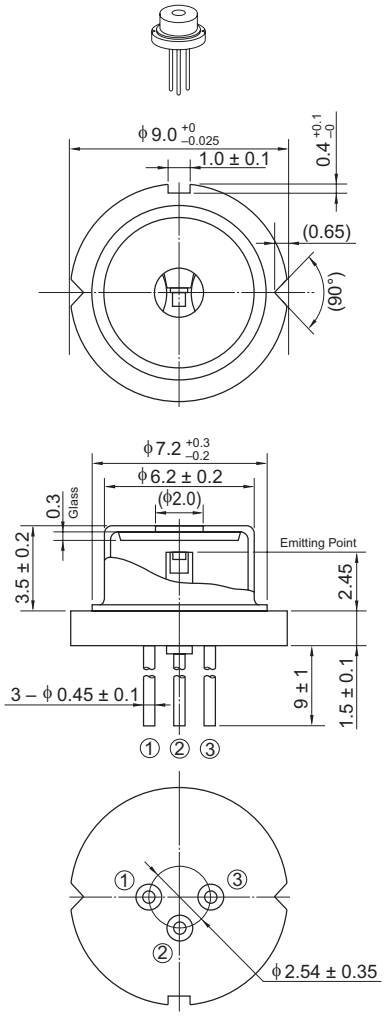

OPJ Code	LD/G2
JEDEC	—
JEITA	—
Mass (reference value)	1.1 g

Cautions

1. Opnext Japan,Inc.(OPJ) neither warrants nor grants licenses of any our rights or any third party's patent, copyright, trademark, or other intellectual property rights for information contained in this document. OPJ bears no responsibility for problems that may arise with third party's rights, including intellectual property rights, in connection with use of the information contained in this document.
2. Products and product specifications may be subject to change without notice. Confirm that you have received the latest product standards or specifications before final design, purchase or use.
3. OPJ makes every attempt to ensure that its products are of high quality and reliability. However, contact our sales office before using the product in an application that demands especially high quality and reliability or where its failure or malfunction may directly threaten human life or cause risk of bodily injury, such as aerospace, aeronautics, nuclear power, combustion control, transportation, traffic, safety equipment or medical equipment for life support.
4. Design your application so that the product is used within the ranges guaranteed by OPJ particularly for maximum rating, operating supply voltage range, heat radiation characteristics, installation conditions and other characteristics. OPJ bears no responsibility for failure or damage when used beyond the guaranteed ranges. Even within the guaranteed ranges, consider normally foreseeable failure rates or failure modes in semiconductor devices and employ systemic measures such as fail-safes, so that the equipment incorporating OPJ product does not cause bodily injury, fire or other consequential damage due to operation of the OPJ product.
5. This product is not designed to be radiation resistant.
6. No one is permitted to reproduce or duplicate, in any form, the whole or part of this document without written approval from OPJ.
7. Contact our sales office for any questions regarding this document or OPJ products.

1. The laser light is harmful to human body especially to eye no matter what directly or indirectly. The laser beam shall be observed or adjusted through infrared camera or equivalent.
2. This product contains gallium arsenide (GaAs), which may seriously endanger your health even at very low doses. Please avoid treatment which may create GaAs powder or gas, such as disassembly or performing chemical experiments, when you handle the product.
   When disposing of the product, please follow the laws of your country and separate it from other waste such as industrial waste and household garbage.
3. Definition of items shown in this CAS is in accordance with that shown in Opto Device Databook issued by OPJ unless otherwise specified.

Sales Offices

opnext
Powered by HITACHI

Device Business Unit Opnext Japan, Inc.
Takagi Bldg., 3F, 1-3-9, Iwamoto-cho, Chiyoda-ku, Tokyo 101-0032 Japan
Tel: (03) 3865-5591

For the detail of Opnext, Inc., see the following homepage:
Japan (Japanese) http://www.opnext.com/jp/products/
Other area (English) http://www.opnext.com/products/

Appendix B. Specifications of piezoelectric actuator LISA P-753.2CD and P-753.3CD

PI

LISA Linear Actuator & Stage

HIGH- DYNAMICS, VERY STABLE PIEZO NANOPOSITIONER

P-753

- Versatile design: Flexure stage or actuator
- Travel range to 38 µm
- Resolution 0.05 nm
- Direct- drive design for fastest response
- Highest linearity and stability with capacitive sensors

Specifications

	P-753.1CD	P-753.2CD	P-753.3CD	Unit	Tolerance
Active axes	X	X	X		
Motion and positioning					
Integrated sensor	Capacitive	Capacitive	Capacitive		
Closed- loop travel	12	25	38	µm	
Closed- loop / open- loop resolution	0.05	0.1	0.2	nm	typ., full travel
Linearity error, closed- loop	0.03	0.03	0.03	%	typ.
Repeatability	±1	±2	±3	nm	typ.
Pitch / yaw	±5	±7	±10	µrad	typ.
Mechanical properties					
Stiffness in motion direction	45	24	16	N/ µm	±20 %
Unloaded resonant frequency	5.6	3.7	2.9	kHz	±20 %
Resonant frequency @ 200 g	2.5	1.7	1.4	kHz	±20 %
Push / pull force capacity in motion direction	100 / 20	100 / 20	100 / 20	N	max.
Load capacity (vertical / horizontal mounting)	10 / 2	10 / 2	10 / 2	kg	max.
Drive properties					
Ceramic type	PICMA® P-885	PICMA® P-885	PICMA® P-885		
Electrical capacitance	1.5	3.1	4.6	µF	±20 %
Dynamic operating current coefficient	12	15	15	µA / (Hz × µm)	±20 %
Miscellaneous					
Operating temperature range	-20 to 80	-20 to 80	-20 to 80	°C	
Material	Steel	Steel	Steel		
Dimensions	44 mm × 30 mm × 15 mm	44 mm × 30 mm × 62 mm	44 mm × 30 mm × 80 mm		
Mass	0.16	0.215	0.26	kg	±5 %
Cable length	1.5	1.5	1.5	m	±10 mm
Sensor / voltage connection	Sub- D Special	Sub- D Special	Sub- D Special		

The resolution of PI piezo nanopositioning systems is not limited by friction or stiction. Value given is noise- equivalent motion with the E-503 piezo amplifier module

Versions with LEMO connector available as P-753.x1C.
Vacuum- compatible versions to 10^{-9} hPa available as P-753.xUD.
Non- magnetic versions available as P-753.xND.

Ask about custom designs!

Order Information

Versions with Sub- D connector

P-753.1CD
LISA High- Dynamics Nanopositioning System, 12 µm, Direct Metrology, Capacitive Sensor, Sub- D Connector(s)
P-753.2CD
LISA High- Dynamics Nanopositioning System, 25 µm, Direct Metrology, Capacitive Sensor, Sub- D Connector(s)
P-753.3CD
LISA High- Dynamics Nanopositioning System, 38 µm, Direct Metrology, Capacitive Sensor, Sub- D Connector(s)

Versions with LEMO connector

P-753.11C
LISA High- Dynamics Nanopositioning System, 12 µm, Direct Metrology, Capacitive Sensor, LEMO Connector(s)
P-753.21C
LISA High- Dynamics Nanopositioning System, 25 µm, Direct Metrology, Capacitive Sensor, LEMO Connector(s)
P-753.31C
LISA High- Dynamics Nanopositioning System, 38 µm, Direct Metrology, Capacitive Sensor, LEMO Connector(s)

Vacuum versions

P-753.1UD
LISA High- Dynamics Nanopositioning System, 12 µm, Direct Metrology, Capacitive Sensor, Sub- D Connector(s), Vacuum- Compatible to 10^{-9} hPa
P-753.2UD
LISA High- Dynamics Nanopositioning System, 25 µm, Direct Metrology, Capacitive Sensor, Sub- D Connector(s), Vacuum- Compatible to 10^{-9} hPa
P-753.3UD
LISA High- Dynamics Nanopositioning System, 38 µm, Direct Metrology, Capacitive Sensor, Sub- D Connector(s), Vacuum- Compatible to 10^{-9} hPa

Non- magnetic versions available as P-753.xND.

Ask about custom designs!

Controllers / Drivers / Amplifiers

E-753 Digital Piezo Controller
E-509 Signal Conditioner / Piezo Servo Module
E-625 Piezo Servo- Controller & Driver

Related Products

P-752 High Precision Nanopositioning Stage
P-620.1 – P-629.1 PIHera Piezo Linear Stage
P-601 PiezoMove Flexure- Guided Linear Actuator

Drawings / Images

P-753.1 dimensions in mm, max. torque at M2.5 threads: 30 Ncm

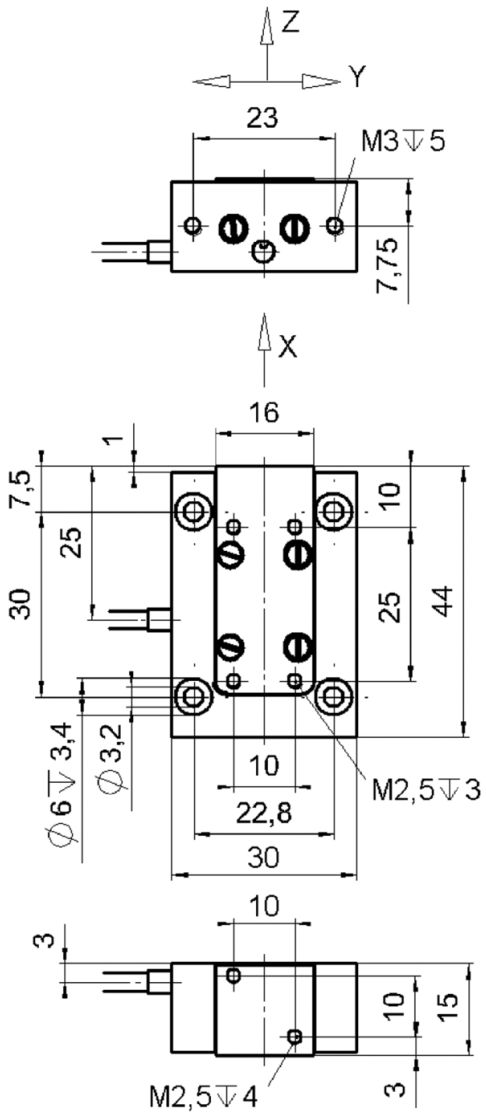

P-753.2 dimensions in mm, max. torque at M2.5 threads: 30 Ncm

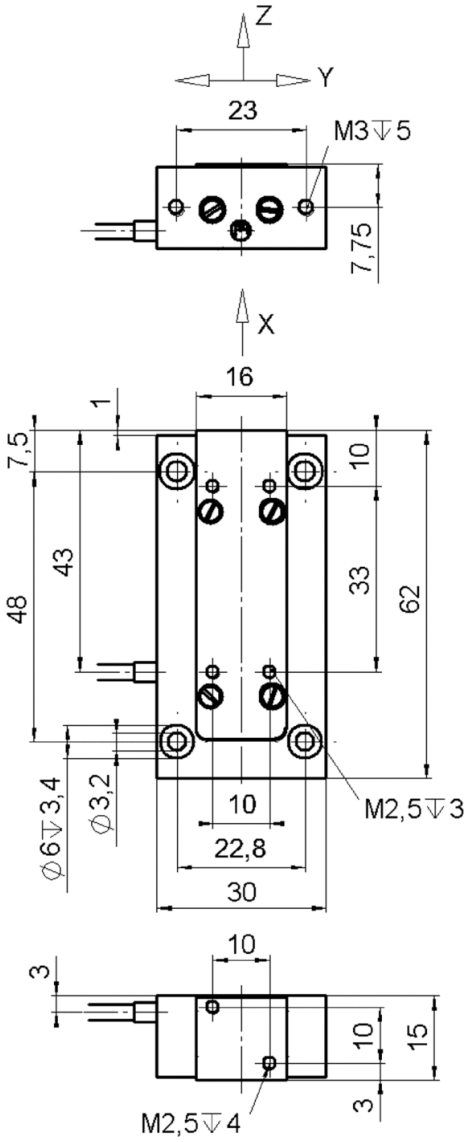

P-753.3 dimensions in mm, max. torque at M2.5 threads: 30 Ncm

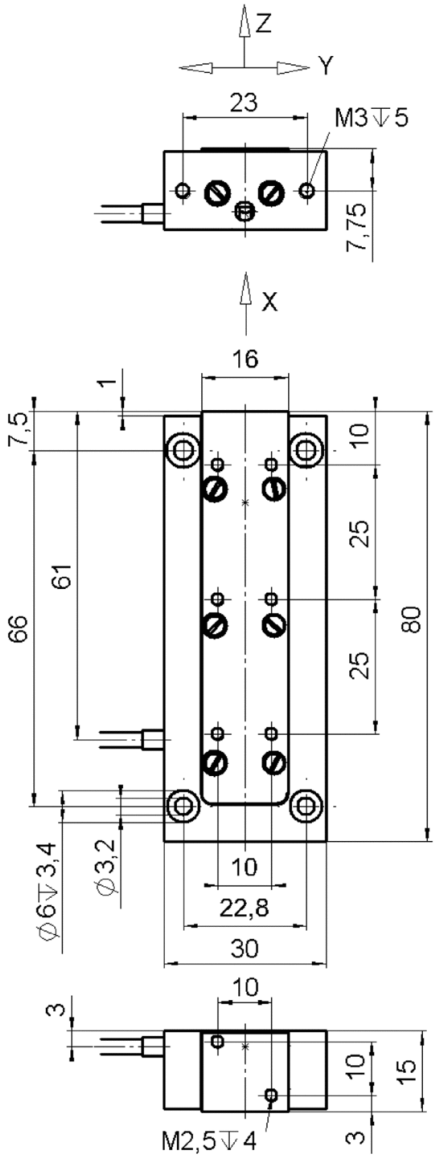

Performance Test Protocol
P-753.3CD - Linearity

PI
Piezo · Nano · Positioning

File: 112062360_linearity_x.cal
Protocol No.: FM 7.5-16 A4

13:33 2012-11-13

Order Info

Customer	MIcos Iberia
Customer Ref No.	
PI Order No.	

System Setup

Stage	P-753.3CD
Ser. No.	112062360
Commanded Axis	X
Measured Axis	X
Feedback Sensor	CAP SENSOR
Sensor Bandwidth	3000 Hz
Design	Standard
Nominal Oper. Voltage	-20V...+120V
Nominal Expansion	38 µm
Controller	E-665.CR, #112060398
Calibration Type	Standard, via digital interface

Measurement Setup

Measurement Device	SIOS SP 120 D
Meas. Device Type	Laser Interferometer
Temperature	20.0 °C
Air Pressure	989.0 mbar
Humidity	50.0 %
Measurement Date	13:31:42, 2012-11-13
Meas. Program	PZTCalib 7.6.0.1
Examiner	HGR
Min. Ctrl Input	0.0 µm
Max. Ctrl Input	38.0 µm
Step Size	1.9 µm
Time Delay	0.5 s

Measurement Results

Ctrl In [µm]	Output + [µm]	nonlin [µm]	nonlin [%]
0.0000	0.0000	0.0000	0.0000
1.9000	1.8979	-0.0021	-0.0057
3.8000	3.7962	-0.0038	-0.0100
5.7000	5.6966	-0.0034	-0.0091
7.6000	7.5969	-0.0031	-0.0082
9.5000	9.4968	-0.0033	-0.0086
11.4000	11.3962	-0.0039	-0.0103
13.3000	13.2955	-0.0046	-0.0120
15.2000	15.1959	-0.0042	-0.0111
17.1000	17.0963	-0.0038	-0.0101
19.0000	18.9976	-0.0025	-0.0066
20.9000	20.8990	-0.0011	-0.0030
22.8000	22.7998	-0.0003	-0.0008
24.7000	24.7002	0.0000	0.0001
26.6000	26.6016	0.0014	0.0037
28.5000	28.5024	0.0023	0.0059
30.4000	30.4033	0.0031	0.0082
32.3000	32.3022	0.0020	0.0051
34.2000	34.2015	0.0013	0.0034
36.1000	36.1014	0.0012	0.0030
38.0000	38.0003	0.0000	0.0000

Control Function:
Expansion = 1.000007*Ctrl_In + 0.0000 µm

Displacement Curves

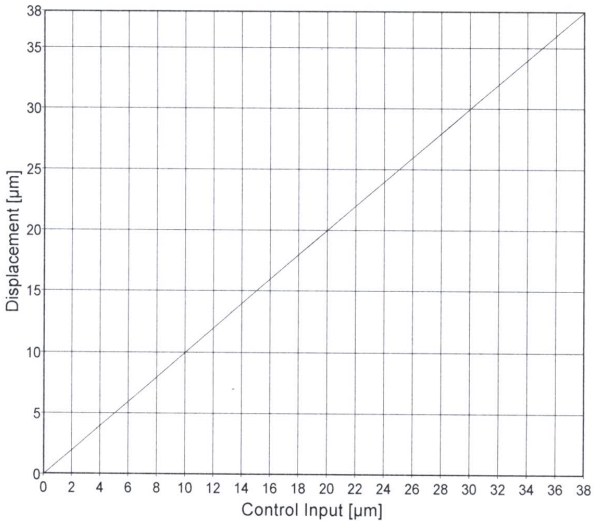

Linearity

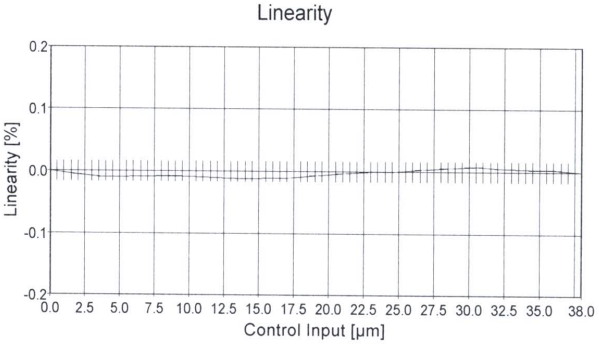

Physik Instrumente (PI) GmbH & Co. KG, Auf der Römerstraße 1, 76228 Karlsruhe - Phone (+49) 721-4846-0, Fax (+49) 721-4846-100, e-mail info@pi.ws

Appendix C. Shocona cantilever specification

Technical Specifications Sheet — Probe Model: SHOCONA

APPNANO probes are compatible with most commercially available SPMs. These probes are nanofabricated using highly doped single crystal silicon with unparalleled reproducibility, robustness and sharpness for consistent high resolution imaging capabilities.

SHOCONA Probes are designed for contact mode applications with a shorter length, providing better sensitivity without compromising on spring constant requirements. The reflex side is coated with aluminum for increased laser signal quality.

Handle Chip Specifications	
L x W x T	3.4 mm x 1.6 mm x 315 µm
Alignment Grooves	YES

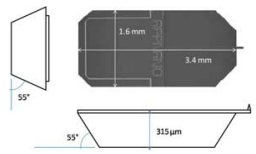

Tip Specifications	
Shape	Pyramidal
Height (µm)	14 - 16
ROC (nm)	6
Coating	None

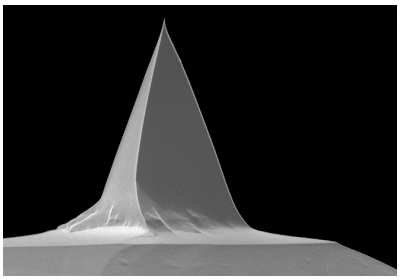

Cantilever Specifications	
Material	Si
Shape	Rectangular
Reflex Side Coating	Al, 50 nm ± 5 nm

Parameter	Value		
	Nominal	Minimum	Maximum
Spring Constant (N/m)	0.14	0.01	0.60
Frequency (kHz)	21	8	37
Length (µm)	225	215	235
Width (µm)	46	41	51
Thickness (µm)	1.0	0.5	1.5

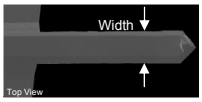

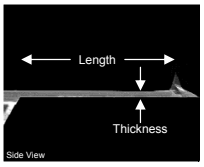

Ordering Information	
Part Number	Probes
SHOCONA-10	10
SHOCONA-20	20
SHOCONA-50	50
SHOCONA-200	200
SHOCONA-W	410 - 424

NOTES:

1. The specification range is **guaranteed**. The values of spring constant and frequency are calculated using mathematical formulation
2. These probes feature **alignment grooves** compatible with all alignment chips available in the market.
3. Please contact our **distributor** in your area to **order** the probes.
4. For more technical information, please contact either our distributor in your area or e-mail us directly at info@appnano.com

Applied NanoStructures, Inc.
415 Clyde Avenue, Suite 102, Mountain View, CA 94043, USA
Tel: 1 650 988 9880 Fax : 1 408 516 4917
E-mail : info@appnano.com

APPNANO **www.appnano.com**

Appendix D. 100nm Step Target specification

Technical Specifications Sheet **SHS: Step Height Standards**

Applied NanoStructures' Step Height Standards are uniquely designed for X,Y, and Z calibration of scanning probe microscopes and profilometers. Our Step Height Standard features are defined in thermally grown silicon dioxide on silicon substrate. A layer of Cr is deposited to harden the surface. Our step height standards are available in two heights.

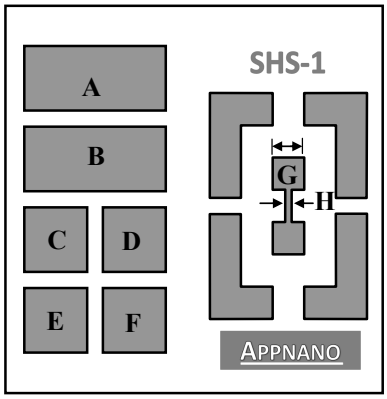

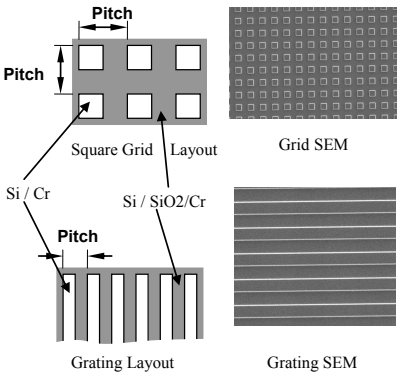

Feature	Description	Details
A	Square grid	3 µm pitch
B	Square grid	10 µm pitch
C	Grating	10 µm pitch
D	Grating	3 µm pitch
E	Grating	50 µm pitch
F	Grating	20 µm pitch
G	Square Pad	1000 µm x 1000 µm
H	Rectangular line	1000 µm x 200 µm

Ordering Information		
Part #	No of Chips	Step Height
SHS – 1	1	1 µm
SHS – 0.1	1	100 nm

NOTES:

1. The values are nominal.
2. The feature step height and pitch are not calibrated.
3. Please contact our Distributor in your area to order the products.
4. For more technical information, please contact either our distributor in your area or e-mail us directly at info@appnano.com.

Applied NanoStructures, Inc.
1700 Wyatt Dr. Suite 12, Santa Clara, CA 95054, USA
Tel: 1 408 567 0115 Fax : 1 408 516 4917
E-mail : info@appnano.com

APPNANO www.appnano.com

Bibliography

[1] T. Young, "The bakerian lecture: On the theory of light and colours," *Phil. Tran. R. Soc. Lond.*, vol. 92, pp. 12–42, Jan 1802.

[2] R. Barakat, "Analytic proofs of the Arago-Fresnel laws for the interference of polarized light," *J. Opt. Soc. Am. A.*, vol. 10, no. 1, pp. 180 – 185, 1993.

[3] A. A. Michelson and E. W. Morley, "Influence of motion of the medium of the velocity of light," *Am. J. Sci.*, vol. 31, no. 185, pp. 377–386, 1886.

[4] A. A. Michelson and E. W. Morley, "On the relative motion of earth and luniniferous ether," *Am. J. Sci.*, vol. 34, no. 203, pp. 333 – 345, Nov 1887.

[5] A. A. Michelson, "On the application of interference methods to astronomical measurements," *Astrophysical Journal*, vol. 51, no. 5, pp. 257–262, Jun 1920.

[6] A. Bergamin, G. Cavagnero, and G. Mana, "A displacement and angle interferometer with subatomic resolution," *Rev. Sci. Instrum.*, vol. 64, no. 11, pp. 3076–3081, Nov 1993.

[7] M. Zhu, H. Wei, X. Wu, and Y. Li, "Fabry-perot interferometer with picometer resolution," *Opt. Laser Eng.*, vol. 63, pp. 128–134, Dec 2014.

[8] ZYGO, visited: August 4th 2015, 11:17 GMT +1. [Online]. Available: www.zygo.com/?/met/markets/stageposition/zmi/interferometers

[9] A. L. Schawlow and C. H. Townes, "Infrared and optical masers," *Phys. Rev.*, vol. 112, no. 6, pp. 1940–1949, Dec 1958.

[10] T. H. Maiman, "Optical and microwave-optical experiments in ruby," *Phys. Rev. Lett.*, vol. 4, no. 11, pp. 564 – 566, Jun 1960.

[11] J.-M. Liu, *Photonic Devices*, 1st ed. Cambridge University Press, 2005, ch. 10 Laser Amplifiers, pp. 613–664.

[12] P. G. R. King and G. J. Steward, "Metrology with an optical maser," *New Sci.*, vol. 17, no. 323, p. 182, Jan 1963.

[13] J. W. Crowe and R. M. C. Jr., "Gaas laser linewidth measurements by heterodyne detection," *Appl. Phys. Lett.*, vol. 5, no. 4, pp. 72–74, 1964.

[14] M. J. Rudd, "A laser doppler velocimeter employing the laser as a mixer-oscillator," *J. Phys. E.*, vol. 1, no. 7, pp. 723–726, Jul 1968.

[15] O. Hirota and Y. Suematsu, "Noise properties of injection lasers due to reflected waves," *IEEE J. Quantum Electron.*, vol. 15, no. 3, pp. 142–149, Mar 1979.

[16] G. P. Agrawal, N. A. Olsson, and N. K. Dutta, "Effect of fiber-far-end reflections on intensity and phase noise in ingaasp semiconductor lasers," *Appl. Phys.*, vol. 45, no. 6, pp. 597–599, Sep 1984.

[17] H. Temkin, N. A. Olsson, T. H. Abeles, R. A. Logan, and M. B. Panish, "Reflection noise index guided ingaasp lasers," *IEEE J. Quantum Electron.*, vol. 22, no. 2, pp. 286–293, Feb 1986.

[18] D. Lenstra, B. Verbeek, and A. D. Boef, "Coherence collapse in single-mode semiconductor lasers due to optical feedback," *IEEE J. Quantum Electron.*, vol. 21, no. 6, pp. 674–679, Jun 1985.

[19] R. D. Dupuis, "An introduction to the development of the semiconductor laser," *IEEE J. Quantum Electron.*, vol. 23, no. 6, pp. 651–657, Jun 1987.

[20] R. N. Hall, G. E. Fenner, J. D. Kingsley, T. K. Soltys, and R. O. Carlson, "Coherent light emission of radiation from gaas junctions," *Phys. Rev. Lett.*, vol. 9, no. 9, pp. 366–368, Nov 1962.

[21] M. I. Nathan, W. P. Dumke, G. Burns, F. H. D. Jr., and G. Lasher, "Stimulated emission of radiation from ga-as p-n junctions," *Appl. Phys. Lett.*, vol. 1, no. 3, pp. 62–64, Nov 1962.

[22] N. H. Jr. and S. F. Bevacqua, "Coherent (visible) light emission from Ga($As_{1-x}P_x$) junctions," *Appl. Phys. Lett.*, vol. 1, no. 4, pp. 82–83, Dec 1962.

[23] T. M. Quist, R. H. Rediker, R. J. Keyes, W. E. Krag, B. Lax, A. L. McWhorter, and H. J. Zeiger, "Semiconductor maser of gaas," *Appl. Phys. Lett.*, vol. 1, no. 4, pp. 91–92, Dec 1962.

[24] R. Lang and K. Kobayashi, "External optical feedback effects on semiconductor injection laser properties," *IEEE J. Quantum Electron*, vol. 16, no. 3, pp. 347–355, Mar 1980.

[25] P. Spencer, P. Rees, and I. Pierce, "Theoretical analysis," in *Unlocking Dynamical Diversity*, 1st ed. John Wiley & Sons,Ltd, 2005, ch. 2, pp. 23 – 54.

[26] A. Dandridge, R. O. Miles, and T. G. Giallorenzi, "Diode laser sensor," *Electron. Lett.*, vol. 16, no. 25–26, pp. 948–949, Dec 1980.

[27] J. H. Churnside, "Laser doppler velocimetry by modulating a co_2 laser with backscattered light," *Appl. Opt.*, vol. 23, no. 1, pp. 61–66, Jan 1984.

[28] S. Shinohara, A. Mochizuki, H. Yoshida, and M. Sumi, "Laser doppler velocimeter using the self-mixing effect of a semiconductor laser diode," *Appl. Opt.*, vol. 25, no. 9, pp. 1417–1419, May 1986.

[29] E. T. Shimizu, "Directional discrimination in the self-mixing type laser doppler velocimeter," *Appl. Opt.*, vol. 26, pp. 4541–4544, Nov 1987.

[30] S. Donati, G. Giuliani, and S. Merlo, "Laser diode feedback interferometer for measurement of displacements without ambiguity," *IEEE J. Quantum Electron.*, vol. 31, no. 1, pp. 113–119, Jan 1995.

[31] S. Donati and R.-H. Horng, "The diagram of feedback regimes revisited," *IEEE J. of Sel. Top. Quantum Electron.*, 2013.

[32] S. Donati, "Responsivity and noise of self-mixing photodetection schemes," *IEEE J. Quantum Electron.*, vol. 47, no. 11, pp. 1428–1433, Nov 2011.

[33] P. Dean, A. Valavanis, J. Keeley, K. Bertling, Y. L. Lim, R. Alhathool, S. Chowdhury, T. Taimre, L. H. Li, D. Indjin, S. J. Wilson, A. D. Rakić, E. H. Linfield, and A. F. Davies, "Coherent three-dimensional terahertz imaging through self-mixing in a quantum cascade laser," *App. Phys. Lett.*, vol. 103, no. 18, pp. 181 112–1–3, Oct 2013.

[34] D. Larsson, A. Greve, J. M. Hvam, A. Boisen, and K. Yvind, "Self-mixing interferometry in vertical-cavity surface-emitting lasers for nanomechanical cantilever sensing," *App. Phys. Lett.*, vol. 94, no. 9, pp. 091 103–1–3, Mar 2009.

[35] J. Perchoux, H. E. Dougan, F. Bony, and A. D. Rakić, "Photodiode-free doppler velocimeter based on self-mixing effect in commercial vcsels," in *Sensors, 2008 IEEE*, IEEE. IEEE, 2008, pp. 290–293.

[36] T. Pereira, P. Vaz, T. Oliveira, I. Santos, A. Leal, V. Almeida, H. Pereira, C. Correia, and J. Cardoso, "New optical probe approach using mixing effect in planar photodiode for biomedical applications," in *Optical Sensors 2013*, F. Baldini, J. Homola, and R. Lieberman, Eds., vol. Proc. of SPIE vol. 8774. SPIE, May 2013, pp. 87 840U–1–8.

[37] S. Radovanović, A. Annema, and B. Nauta, "Physical and electrical bandwidths of integrated photodiodes in standard cmos technology," in *Electron Devices and Solid-State Circuits, 2003 IEEE Conference on*. IEEE, 2003, pp. 95–98.

[38] G. H. M. van Tartwijk and D. Lenstra, "Semiconductor lasers with optical injection and feedback," *Quantum Semiclass. Opt.*, vol. 7, no. 2, pp. 87–143, Apr 1995.

[39] G. Giuliani, M. Norgia, S. Donati, and T. Bosch, "Laser diode self-mixing technique for sensing applications," *J. Opt. A: Pure Appl. Opt.*, vol. 4, no. 6, pp. S283–S294, Nov 2002.

[40] Y. Yu, G. Giuliani, and S. Donati, "Measurement of the linewidth enhancement factor of semiconductor lasers based on the optical feedback self-mixing effect," *IEEE Photon. Technol. Lett.*, vol. 16, no. 4, pp. 990–992, Apr 2004.

[41] Y. Yu, J. Xi, J. F. Chicharo, and T. Bosch, "Toward automatic measurement of the linewidth-enhancement factor using optical feedback self-mixing interferometry with weak optical feedback," *IEEE J. Quantum Electron.*, vol. 43, no. 7, pp. 527–534, Jul 2007.

[42] J. R. Tuckker, A. D. Rakić, C. J. O'Brien, and A. V. Zvyagin, "Effect of multiple transverse modes in self-mixing sensors based on vertical-cavity surface-emitting lasers," *Appl. Opt.*, vol. 46, no. 4, pp. 611–619, Feb 2007.

[43] W. M. Wang, W. J. O. Boyle, K. T. V. Grattan, and A. W. Palmer, "Self-mixing interference in a diode laser: experimental observations and theoretical analysis," *Appl. Opt.*, vol. 32, no. 9, pp. 1551–1558, Mar 1993.

[44] A. P. Bogatov, P. G. Eliseev, L. P. Ivanov, A. S. Logginov, M. A. Manko, and K. Y. Senatorov, "Study of the single-mode injection laser," *IEEE J. Quantum Electron*, vol. 9, no. 2, pp. 392–394, Feb 1973.

[45] Y. Mitsuhashi, T. Morikawa, K. Sakurai, A. Seko, and J. Shimada, "Self-coupled optical pickup," *Opt. Commun.*, vol. 17, no. 1, pp. 95–97, Apr 1976.

[46] T. Taimre, M. Nikolić, K. Bertling, Y. L. Lim, T. Bosch, and A. D. Rakić, "Laser feedback interferometry: a tutorial on the self-mixing effect for coherent sensing," *Adv. Opt. Photon.*, vol. 7, no. 3, pp. 570–631, Aug 2015.

[47] G. Giuliani and S. Donati, "Laser interferometry," in *Unlocking Dynamical Diversity*, 1st ed. John Wiley & Sons,Ltd, 2005, ch. 7, pp. 217–255.

[48] C. H. Henry, "Theory of Linewidth of Semiconductor Lasers," *IEEE J. Quantum Electron.*, vol. QE-18, no. 2, pp. 259–264, Feb 1982.

[49] P. J. de Groot, G. M. Gallatin, and S. H. Macomber, "Ranging and velocimetry signal generation in a backscatter-modulated laser diode," *Appl. Opt.*, vol. 27, no. 21, pp. 4475–4480, Nov 1988.

[50] M. H. Koelink, M. Slot, F. F. M. de Mul, J. Greve, R. Graff, A. C. M. Dassel, and J. G. Aarnoudse, "Laser doppler velocimeter based on the self-mixing effect in a fiber-coupled semiconductor laser: theory," *Appl. Opt.*, vol. 31, no. 18, pp. 3401–3408, Jun 1992.

[51] K. Petermann, *Laser Diode Modulation and Noise*. Kluwer Academic, 1988.

[52] W. M. Wang, K. T. V. Grattan, and A. W. Palmer, "Self-mixing interference inside a single-mode diode laser for optical sensing applications," *J. Lightw. Technol.*, vol. 12, no. 9, pp. 1577–1587, Sep 1994.

[53] U. Zabit, "Optimisation of a self-mixing laser displacement sensor," PhD. Thesis, University of Toulouse, Jul 2010.

[54] J. A. Roumy, J. Perchoux, Y. L. Lim, T. Taimre, A. D. Rakić, and T. Bosch, "Effect of injection current and temperature on signal strength in a laser diode optical feedback interferometer," *App. Opt.*, vol. 54, no. 2, pp. 312–318, Jan 2015.

[55] G. A. Acket, D. Lenstra, A. J. D. Boef, and B. H. Verbeek, "The influence of feedback intensity on longitudinal mode properties and optical noise in index-guided semiconductor lasers," *IEEE J. Quantum Electron.*, vol. 20, no. 10, pp. 1163–1169, Oct 1984.

[56] R. W. Tkach and A. R. Chraplyvy, "Regimes of feedback effects in 1.5-μm distributed feedback lasers," *J. Lightw. Technol.*, vol. 4, no. 11, pp. 1655–1661, Nov 1986.

[57] C. Bès, "Conception d'un sistème laser de mesures de déñolacements par interférométrie à rétroinjection optique dans le cas de feedbacks faible et modéré," Ph. D. Thesis, Institut National Polytechnique de Toulouse, Oct 2006.

[58] S. Donati and M. T. Fathi, "Transition from short-to-long cavity and from self-mixing to chaos in a delayed optical feedback laser," *IEEE J. Quantum Electron.*, vol. 48, no. 10, pp. 1352–1359, Oct 2012.

[59] Y. Yu, J. Xi, and J. F. Chicaro, "Measuring the feedback parameter of a semiconductor laser with external optical feedback," *Opt. Exp.*, vol. 19, no. 10, pp. 9582–9593, May 2011.

[60] G. Plantier, C. Bès, and T. Bosch, "Behavioral model of a self-mixing laser diode sensor," *IEEE J. Quantum Electron.*, vol. 41, no. 9, pp. 1157–1167, Sep 2005.

[61] J. Fan, S. Jia, W. Lu, and Z. Wang, "Application of lvdt sensor data acquisition system based on pci-1716," in *2011 IEEE International Conference on Computer Science and Automation Engineering (CSAE)*, vol. 3. IEEE, Jun 2011, pp. 548–552.

[62] H. Li, J. Ding, B. Chu, and X. Zhao, "A contact stress sensor based on strain gauge," *Instruments and Experimental Techniques*, vol. 58, no. 2, pp. 288–296, Apr 2015.

[63] M. Kim, W. Moon, E. Yun, and K.-R. Lee, "A new capacitive displacement sensor with high accuracy and long range," *Sensor Actuat. A-Phys*, vol. 130–131, pp. 135–141, Aug 2006.

[64] S. Duric, L. Nad, B. Biberdzić, and L. Zivanov, "Planar inductive sensor for small displacement," in *26th Internation Conference on Microelectronics*. IEEE, May 2008, pp. 11–14.

[65] K.-M. Lee and D. Zhou, "A Real Time Optical Sensor for Simultaneous Measurement of Three-DOF Motions," *IEEEASME Trans. Mechatronics*, vol. 9, no. 3, pp. 499–507, Sep 2004.

[66] E. Higurashi, R. Sawada, and T. Ito, "Monolithically integrated optical displacement sensor based on triangulation and optical beam deflection," *Appl. Opt.*, vol. 38, no. 9, pp. 1746–1751, Mar 1999.

[67] L. M. Smith and C. C. Dobson, "Absolute displacement measurements using modulation of the spectrum of white light in a Michelson interferometer," *Appl. Opt.*, vol. 28, no. 16, pp. 3339–3342, Aug 1989.

[68] L. A. Coldren and T. L. Koch, "Analysis and Design of Coupled-Cavity Lasers – Part I: Threshold Gain Analysis and Design Guidelines," *IEEE J. Quantum Electron.*, vol. 20, no. 6, pp. 659 – 670, Jun 1984.

[69] M. Pisani, "A homodyne Michelson interferometer with sub-picometer resolution," *Meas. Sci. Technol.*, vol. 20, pp. 1–6, Jun 2009.

[70] G. C. A. Bergamin and G. Mana, "A displacement and angle interferometer with subatomic resolution," *Rev. Sci. Instrum.*, vol. 64, no. 11, pp. 3076–3081, Nov 1993.

[71] T. Bosch and N. Sarvagent, "Optical feedback interferometry for sensing applications," *Opt. Eng.*, vol. 40, no. 1, pp. 20–27, Jan 2006.

[72] U. Zabit, T. Bosch, and F. Bony, "Adaptative transition algorithm for a self-mixing displacement sensor," *IEEE Sensors J.*, vol. 9, no. 12, pp. 1879–1886, Dec 2009.

[73] T. Taimre, M. Nicolić, K. Bertling, Y. L. Lim, T. Bosch, and A. D. Rakić, "Laser feedback interferometry: a tutorial on the self-mixing effect for coherent sensing," *Adv. Opt. Photonics*, vol. 7, no. 3, pp. 570–631, September 2015.

[74] M. A. Hauptmann, K. T. V. Grattan, A. W. Palmer, H. Fritsch, R. Lucklum, and P. R. Hauptmann, "Silicon resonator sensor systems using self-mixing interferometry," *Sensor Actuat. A. Phys*, vol. 55, no. 2–3, pp. 71–77, Jul 1996.

[75] M. Y. Tsai and T. S. Liu, "Sliding mode based fuzzy control for positioning of optical pickup head," *International Journal on Smart Sensing and Intelligent Systems*, vol. 3, no. 2, pp. 304–321, Mar 2010.

[76] M. Dabbico, A. Intermite, and G. Scamarcio, "Laser-self-mixing fiber sensor for integral strain measurement," *J. Lightw. Technol.*, vol. 29, no. 3, pp. 335–340, Feb 2011.

[77] A. N. Lukashkin, M. E. Bashtanov, and I. J. Russel, "A self-miing laser-diode interferometer for measuring basilar membrane vibrations without opening cochlea," *J. Neurosci. Methods*, vol. 148, no. 2, pp. 122–129, Oct 2005.

[78] G. Giuliani, S. Bozzi-Pietra, and S. Donati, "Self-mixing laser diode vibrometer," *Meas. Sci. Technol.*, vol. 14, no. 1, pp. 24–32, Nov 2003.

[79] R. Atashkhooei, F. J. Azcona, S. Royo, and L. Gil, "Optical feedback interferometry for measuring dynamic stress deformation on beams," in *AIP Conf. Proc.*, vol. 1457, no. 1, AIVELA. AIP, Jun 2012, pp. 132–138.

[80] R. Atashkhooei, J.-C. Urresty, S. Royo, J.-R. Riba, and L. Romeral, "Runout tracking in electric motors using self-mixing interferometry," *IEEE/ASME Trans. Mech.*, vol. 19, no. 1, pp. 184–190, Nov 2012.

[81] L. Campagnolo, "Optical feedback interferometry sensing technique for flow measurements in microchannels," Ph. D. Thesis, University of Toulouse, Apr 2013.

[82] S. K. Özdemir, I. Ohno, and S. Shinohara, "A comparative study for the assessment on blood flow measurement using self-mixing laser speckle interferometer," *IEEE Trans. Instrum. Meas.*, vol. 57, no. 2, pp. 355–363, Feb 2008.

[83] J. R. Tucker, Y. L. Lim, K. Bertling, A. V. Zvyagin, and A. D. Rakić, "Fluid flow rate measurement using the change in laser junction voltage due to the self-mixing effect," in *Conference on Optoelectronic and Microelectronic Materials and Devices COMMAD 2006*. IEEE, Dec 2006, pp. 192–195.

[84] M. Nagahara, Y. Tamaki, A. Tomidokoro, and M. Araie, "In vivo measurement of blood velocity in human major retinal vessels using the laser speckle method," *Investigative Ophtalmology & Visual Science*, vol. 52, no. 1, pp. 87–92, Jan 2011.

[85] M. Norgia, A. Pesatori, and L. Rovati, "Low-cost optical flowmeter with analog front-end electronics for blood extracorporeal circulators," *IEEE Trans. Instrum. Meas.*, vol. 59, no. 5, pp. 1233–1239, May 2010.

[86] L. Scalise and N. Paone, "Laser doppler vibrometry based on self-mixing effect," *Opt. Las. Eng.*, vol. 38, no. 3–4, pp. 173–184, Sep–Oct 2002.

[87] H. Wang, J. Shen, B. Wang, and B. Y. an Y. Xu, "Laser diode feedback interferometry in flowing brownian motion system: a novel theory," *Appl. Phys. B*, vol. 101, no. 1–2, pp. 173–183, May 2010.

[88] H. Wang and J. Shen, "Power spectral density of self-mixing signals from a flowing brownian motion system," *Appl. Phys. B*, vol. 106, no. 1, pp. 127–134, Jan 2012.

[89] A. Mowla, T. Taimre, Y. L. Lim, K. Bertling, S. J. Wilson, T. W. Prow, H. P. Soyer, and A. D. Rakić, "Concurrent Reflectance Confocal Microscopy and Laser Doppler Flowmetry to Improve Skin Cancer Imaging: A Monte Carlo Model and Experimental Validation," *Sensors*, vol. 16, no. 9, pp. 1–19, Sep 2016.

[90] S. Donati, "Developing self-mixing interferometry for instrumentation and measurements," *Las. Photon. Rev.*, vol. 6, no. 3, pp. 393–417, May 2012.

[91] M. Norgia, G. Giuliani, and S. Donati, "Absolute distance meaurement with improved accuracy using laser diode self-mixing interferometry in a closed loop," *IEEE Trans. Intrum. Meas.*, vol. 56, no. 5, pp. 1894–1900, Oct 2007.

[92] G. Beheim and K. Fritsch, "Range finding using frequency-modulated laser diode," *Appl. Opt.*, vol. 25, no. 9, pp. 1439–1442, May 1986.

[93] S. Shinorara, H. Yoshida, H. Ikeda, and K. Nishide, "Compact and high-precision range finder with wide dynamic range using one sensor head," in *8th IEEE Instrumentation and Measurement Technology Conference IMTC-91*. IEEE, May 1991, pp. 126–130.

[94] F. Goaux, N. Servagent, and T. Bosch, "Absolute distance measurement with an optical feedback interferometer," *Appl. Opt.*, vol. 37, no. 28, pp. 6684–6689, Oct 1998.

[95] K. Kou, X. Li, L. Li, H. Li, and T. Wu, "Absolute distance estimation with improved genetic algorithm in laser self-mixing scheme," *Opt. Las. Tech.*, vol. 68, pp. 113–119, May 2015.

[96] D. Guo and M. Wang, "Self-mixing interferometry based on a double-modulation technique for absolute distance measurement," *Appl. Opt.*, vol. 46, no. 9, pp. 1486–1491, Mar 2007.

[97] T. Suzuki, S. Hirabayashi, and T. Maruyama, "Self-mixing type of phase-locked laser diode interferometer," *Opt. Eng.*, vol. 38, no. 3, pp. 543–548, Mar 1999.

[98] T.-D. O. C. U. a Self-Mixing Type Scanning Laser Range Finder, "Ieee trans. instrum. meas." •, vol. 47, no. 5, pp. 1326–1329, Oct 1998.

[99] T. Bosch, "An overview of self-mixing sensing applications," in *2004 Conference on Optoelectronic and Microelectronic Materials and Devices COMMAD 2004*. IEEE, Dec 2005, pp. 385–392.

[100] C. Zakian and M. Dickinson, "Laser Doppler imaging through tissues phantoms by using self-mixing interferometry with a laser diode," *Opt. Lett.*, vol. 32, no. 19, pp. 2798–2800, Oct 2007.

[101] Y. L. Lim, M. Nikolic, K. Bertling, R. Kliese, and A. D. Rakić, "Self-mixing imaging sensor using a monolithic vcsel array with parallel readout," *Opt. Exp*, vol. 17, no. 7, pp. 5517–5525, Mar 2009.

[102] Y. L. Lim, R. Kliese, K. Bertling, K. Tanimizu, P. A. Jacobs, and A. D. Rakić, "Self-mixing flow sensor using a monolithic VCSEL array with parallel readout," *Opt. Exp.*, vol. 18, no. 11, pp. 11 720–11 727, May 2010.

[103] R. Kliese, Y. L. Lim, E. Stefan, and J. Perchoux, "Rapid scanning flow sensor based on the self-mixing effect in a vcsel," in *2010 Conference on Optoelectronic and Microelectronic Materials and Devices (COMMAD) 2010*. IEEE, Dec 2010, pp. 7–8.

[104] R. Ocaña and T. Molina, "Mapping a vibrating surface by using laser self-mixing interferometry," in *Proc. of SPIE*, vol. 9132. SPIE, May 2014, pp. 913 213–1–10.

[105] J. W. Goodman, "Some fundamental properties of speckle," *J. Opt. Soc. Am.*, vol. 66, no. 11, pp. 1145–1150, Nov 1976.

[106] S. Donati, G. Martini, and T. Tambosso, "Speckle pattern errors in self-mixing interferometry," *IEEE J. Quantum Electron.*, vol. 49, no. 9, pp. 798–806, Sep 2013.

[107] R. Atashkhooei, S. Royo, F. J. Azcona, and U. Zabit, "Analysis and control of speckle effects in self-mixing interferometry," in *2011 IEEE Sensors*. IEEE, Oct 2011, pp. 1390–1393.

[108] M. Norgia and S. Donati, "A displacement-measuring instrument utilizing self-mixing interferometry," *IEEE Trans. Instrum. Meas.*, vol. 52, no. 6, pp. 1765–1770, Dec 2003.

[109] R. Atashkhooei, S. Royo, and F. J. Azcona, "Dealing with speckle effects in self-mixing interferometry measurements," *IEEE Sens. J.*, vol. 13, no. 5, pp. 1641–1647, May 2013.

[110] R. Atashkhooei, S. Royo, and F. J. Azcona, "Adaptive autofocus technique for speckle control in optical feedback interferometry," *Sens. Actuator A*, vol. 216, pp. 243–248, Sep 2014.

[111] A. L. Arriaga, "Analysis and implementatin of algorithms for embedded self-mixing displacement sensors design," Ph. D. Thesis, Université de Toulouse, Jul 2014.

[112] N. Servagent, T. Bosch, and M. Lescue, "Design of a phase-shifting optical feedback interferometer using an electrooptic modulator," *IEEE J. Sel. Topics Quantum Electron.*, vol. 6, no. 5, pp. 798 – 802, Sept – Oct 2000.

[113] J. Hast, M. Okkonen, H. Heikkinen, L. Kreut, and R. Myllylä, "Nanometer-scale displacement sensing using self-mixing interferometry with a correlation-based signal processing technique," *Opto-electronic Rev.*, vol. 14, no. 2, pp. 129–134, Jun 2006.

[114] C. Bès, G. Plantier, and T. Bosch, "Displacement measurements using a self-mixing laser diode under moderate feedback," *IEEE Trans. Instrum. Meas.*, vol. 55, no. 4, pp. 1101 – 1105, Aug 2006.

[115] O. D. Bernal, U. Zabit, and T. Bosch, "Study of Laser Feedback Phase Under Self-Mixing Leading to Improved Phase Unwrapping for Vibration Sensing," *IEEE Sens. J.*, vol. 13, no. 12, pp. 4962–4971, Aug 2013.

[116] L. Wei, J. Xi, Y. Yu, and J. Chicaro, "Phase unwrapping on self-mixing signals observed in optical feedback interferometry for displacement measurement," in *International Simposium on Intelligent Signal Processing Communications, 2006. ISPACS' 06.* IEEE, December 2006, pp. 780 – 783.

[117] L. Fei and S. Zhang, "The discovery of nanometer fringes in laser self-mixing interference," *J. Opt. Comm.*, vol. 273, no. 1, pp. 226–230, May 2007.

[118] C. Jiang, Z. Zhang, and C. Li, "Vibration measurement based on multiple self-mixing interferometry," *J. Opt. Comm.*, vol. 367, no. 1, pp. 227–233, 2016.

[119] S. Donati and M. Norgia, "Self-mixing interferometry for biomedical signals sensing," *IEEE J. Sel. Top. Quantum Electron.*, vol. 20, no. 2, pp. 6 900 108–1–8, Mar/Apr 2014.

[120] G. Giuliani, S. Bozzi-Pietra, and S. Donati, "Self-mixing laser diode vibrometer," *Meas. Sci. Technol.*, vol. 14, no. 1, pp. 24–32, Oct 2003.

[121] A. Jha, "Continuous wave frequency modulated optical feedback (CWFM-OF): theory and applications," Ph.D. dissertation, Universitat Politècnica de Catalunya, Nov 2016.

[122] U. Zabit, F. Boni, T. Bosch, and A. D. Rakic, "A self-mixing displacement sensor with fringe-loss compensation for harmonic vibrations," *IEEE Photon. Techno. Lett.*, vol. 22, no. 6, pp. 410 – 412, Mar 2010.

[123] F. J. Azcona, R. Atashkhooei, S. Royo, J. M. Astudillo, and A. Jha, "A method to measure sub nanometric amplitude displacements based on optical feedback interferometry," in *SPIE Proceedings Vol. 8789: Modeling Aspects in Optical Metrology IV*, B. Bodermann, K. Frenner, and R. M. Silver, Eds., vol. Proc. SPIE 8789. Munich: SPIE, May 13 2013, pp. 878 908–1–8.

[124] N. Semiconductors, "Bcm61b npn/npn matched double transistor," NXP Semiconductors, Product Specification Rev. 02, Aug 2009.

[125] N. Semiconductors, "Bcm62b ppn/pnp matched double transistor," NXP Semiconductors, Product Specification Rev. 02, Aug 2009.

[126] iC Haus, "iC-WJ, iC-WJZ laser diode driver," iC-Haus, Product Specification Rev. C1, 2006.

[127] T. Instruments, "Opax22x high precision, low noise operational amplifiers," Texas Instruments, Product Specification SBOS110B, Jun 2015.

[128] T. R. Scavo and J. B. Thoo, "On the geometry of Halley's method," *Amer. Math. Monthly*, vol. 102, no. 5, pp. 417–426, May 1995.

[129] E. W. Weissten, "Schröeder's method," Mathworld – A Wolfram Web Resource, Last accessed: August 25th 2016 10:39 GMT-1 2016. [Online]. Available: http://mathworld.wolfram.com/SchroedersMethod.html

[130] R. Kliesse, T. Taimre, A. A. A. Bakar, Y. L. Lim, K. Bertling, J. Perchoux, T. Bosch, and A. D. Rakić, "Solving self-mixing equations for arbitrary feedback levels: a concise algorithm," *Applied Optics*, vol. 53, no. 17, pp. 3723 – 3736, 2014.

[131] OpNext, "HL7851G GaAlAs Laser Diode," OpNext, Technical Specifications Rev. 1 ODE-208-062A (Z), Dec 2006.

[132] OpNext, "HL8337MG GaAlAs Laser Diode," OpNext, Product Specifications Rev. 1 ODE-208-065A (Z), May 2007.

[133] Finisar, "850nm Single Mode VCSEL TO-46 Package HFE4093-332," Finisar, Product Specifications Rev. B00, Oct 2014.

[134] M. F. O'Rourke, A. Pauca, and X.-J. Jiang, "Pulse wave analysis," *Br. J. Clin. Pharmacol.*, vol. 51, no. 6, pp. 507–522, Jun 2001.

[135] L. Peter, N. Noury, and M. Cerny, "A review of methods for non-invasive and continuous blood pressure monitoring: Pulse transit time method is promising?" *IRBM*, vol. 35, no. 5, pp. 271–282, Oct 2014.

[136] T. Pereira, C. Correia, and J. Cardoso, "Novel methods for pulse wave velocity measurement," *J. Med. Biol. Eng.*, vol. 35, no. 5, pp. 555–565, Oct 2015.

[137] M. . Ariza-García, J. F. Zurita, D. P. Piñero, J. F. Rodriguez-Matas, and B. Calvo, "Couple biomechanical response of the cornea assessed by non-contact tonometry. a simulation study," *J. PONE*, vol. 10, no. 3, pp. 1–15, March 2015.

[138] M. Saito, M. Matsukawa, T. Asada, and Y. Watanabe, "Noninvasive assessment of arterial stiffness by pulse wave analysis," *IEEE Trans. Ultrason. Ferroelectr*, vol. 59, no. 11, pp. 2411–2419, Nov 2012.

[139] I. Codreanu, M. D. Robson, O. J. Rider, T. J. Pegg, B. A. Jung, C. A. Dasanu, K. Clarke, and C. J. Holloway, "Chasing the reflectec wave back into the heart a new hypothesis while the jury is still out," *Vasc. Health Risk Manag.*, vol. 7, pp. 365–373, Jun 2011.

[140] S. R. Alty, N. Angarita-James, S. C. Millasseau, and P. J. Chowienczyk, "Predicting arterial stiffness from the digital volume pulse waveform," *IEEE Trans. Biomed. Eng.*, vol. 54, no. 12, pp. 2268–2275, Nov 2005.

[141] M. Brand, A. J. Woodwiss, F. Michael, H. L. Booysen, M. G. Veller, and G. R. Norton, "A mismatch between aortic pulse pressure and pulse wave velocity predicts advanced peripheral arterial disease," *Eur. J. Vasc. Endovasc*, vol. 46, no. 3, pp. 338–346, Sep 2013.

[142] J. Allen, "Photoplethysmography and its application in clinical physiological measurement," *Physiol. Meas.*, vol. 28, no. 3, pp. R1–R39, Feb 2007.

[143] G. Cennini, J. Arguel, K. Aksit, and A. van Lest, "Heart rate monitoring via remote photoplethysmography with motion artifacts reduction," *Opt. Exp.*, vol. 18, no. 5, pp. 4867–4875, Feb 2010.

[144] J. Zheng, S. Hu, V. Azorin-Peris, A. Echiadis, V. Chouliaras, and R. Summers, "Remote simultaneous dual wavelength imaging photoplethysmography: a further step towards 3-d mapping of skin blood microcirculation," in *Multimodal Biomedical Imaging III*, F. S. Azar and X. Intes, Eds., vol. Proc. SPIE 6850, SPIE. San Jose, CA: SPIE, Feb 2008, pp. 6850S–1–6850S–8.

[145] Y. Li, P. Segers, J. Dirckx, and R. Baets, "On-chip laser doppler vibrometer for arterial pulse wave velocity measurement," *Opt.Exp*, vol. 4, no. 7, pp. 1229–1235, Feb 2013.

[146] S. Donati and M. Norgia, "Self-mixing interferometry for biomedical signals sensing," *IEEE J. Sel. Top. Quant.*, vol. 20, no. 2, pp. 6 900 108 1–8, Mar–Apr 2014.

[147] M. Norgia, A. Pesatori, and L. Rovati, "Self-Mixing Laser Doppler Spectra of Extracorporeal Blood flow: A Theoretical and Experimental Study," *IEEE Sens. J.*, vol. 12, no. 3, pp. 552–557, Mar 2012.

[148] A. Courteville, T. Gharbi, and J. Y. Cornu, "Noncontact MMG Sensor Based on the Optical Feedback Effect in a Laser Diode," *J. Biomed. Opt.*, vol. 3, no. 3, pp. 281–285, Jul 1998.

[149] K. Meigas, H. Hinrikus, R. Kattai, and J. Lass, "Self-mixing in a laser diode as a method for cardiovascular diagnosis," *J. Biomed. Opt.*, vol. 8, no. 1, pp. 152–160, Jan 2003.

[150] J. Hast, "Self-mixing interferometry and its applications in noninvasive pulse detection," PhD Thesis, Department of Electrical and Information Engineering, University of Oulu, Apr. 2003.

[151] M. Norgia, S. Donati, and D. d'Alessandro, "Interferometric measurements of displacement on a diffusing target by speckle tracking technique," *IEEE J. Quantum Electron*, vol. 37, no. 6, pp. 800–806, Jun 2001.

[152] J. Allen and A. Murray, "Effects of filtering multi-site photoplethysmography pulse waveform characteristics," in *Computers in Cardiology,2004*, vol. 31, Long Beach, CA, Sept 2004, pp. 485–488.

[153] International Commission On Non Ionizing Radiation Protection, "ICNIRP guidelines on limits of exposure to laser radiation of wavelength between 180nm and 1000 μm," *Health Physics*, vol. 105, no. 1, pp. 271–295, Jan 2013.

[154] T. A. Henderson and L. D. Morries, "Near-infrared photonic energy penetration: can infrared phototherapy effectively reach the human brain?" *Neuropsychiatr Dis Treat*, vol. 11, pp. 2191–2208, Aug 2015.

[155] N. Servagent, T. Bosch, and M. Lescure, "A laser displacement sensor using the self-mixing effect for modal analysis and defect detection," *IEEE Transactions on Instrumentation and Measurement*, vol. 46, no. 4, pp. 847–850, August 2002.

[156] R. Raiteri, M. Grattarola, H.-J. Butt, and P. Skládal, "Micromechanical cantilever-based biosensors," *Sens. and Act. B: Chem*, vol. 79, no. 2–3, pp. 115–126, Oct 2001.

[157] B. Reid and M. Zhao, "Measurement of biolectric current with a vibrating probe," *J. Vis. Exp.*, vol. 47, pp. 1–6, Jan 2011.

[158] M. A. Poggi, E. D. Gadsby, and L. A. Bottomley, "Scanning probe microscopy," *Analytical chemistry*, vol. 76, no. 12, pp. 3429–3444, June 2004.

[159] S. M. Salapaka and M. V. Salapaka, "Scanning probe microscopy," *IEEE Control Systems Magazine*, vol. 28, no. 2, pp. 65–83, April 2008.

[160] G. Binning, C. F. Quate, and C. Gerber, "Atomic force microscope," *Physical Review Letters*, vol. 56, no. 9, pp. 930–934, March 1986.

[161] R. García and R. Pérez, "Dynamic atomic force microscopy methods," *Surface Science Reports*, vol. 47, no. 6–8, pp. 197–301, September 2002, 10.1016/S0167-5729(02)00077-8.

[162] Y. Martin, C. C. Williams, and H. K. Wickramasinghe, "Atomic force microscope-force mapping and profilling on a sub 100-Å scale," *Journal of Applied Physics*, vol. 61, no. 10, pp. 4723–4729, May 1987.

[163] R. Erlandsson, G. M. McClelland, C. M. Mate, and S. Chiang, "Atomic force microscopy using optical interferometry," *Journal of Vacuum Science & Technology A*, vol. 6, no. 2, pp. 266–270, March/April 1988.

[164] S. Alexander, L. Hellemans, O. Marti, J. Schneir, V. Elings, P. K. Hansma, M. Longmire, and J. Gurley, "An atomic-resolution atomic-force microscope implemented using an optical lever," *Journal of Applied Physics*, vol. 65, no. 1, pp. 164–167, January 1989.

[165] S. Fujisawa, M. Ohta, T. Konishi, and Y. Sugawara, "Difference between the forces measure by an optical lever deflection and by an optical interferometer in atomic force microscopy," *Review of Scientific Instruments*, vol. 65, no. 3, pp. 644–648, March 1994.

[166] W. A. Ducker, T. J. Senden, and R. M. Pashley, "Direct measurement of colloidal forces using an atomic force microscope," *Nature*, vol. 353, pp. 239–241, September 1991.

[167] C. Neto and V. S. J. Craig, "Colloid probe characterization: Radius and roughness determination," *Langmuir*, vol. 17, no. 7, pp. 2097–2099, February 2001.

[168] F. J. Giessib, "Advances in atomic force microscopy," *Reviews of Modern Physics*, vol. 75, no. 3, pp. 949–983, July 2003.

[169] Q. Zhong, D. Innis, K. Kjoller, and V. B. Elings, "Fractured polymer/silica fiber surface studied by tapping mode atomic force microscopy," *Surface Science*, vol. 290, no. 1–2, pp. L688–L692, June 1993.

[170] M. Tortonese, R. C. Barret, and C. F. Quate, "Atomic resolution with an atomic force microscope using piezoelectric detection," *Journal of Applied Physics*, vol. 62, no. 8, pp. 834–836, February 1993.

[171] R. Erlandsson, L. Olsson, and P. Mårtensson, "Inequivalent atoms and imaging mechanisms in ac-mode atomic-force microscopy of Si(111)7×7," *Physical Review B*, vol. 54, no. 12, pp. R8309–R8312, September 1996.

[172] R. Raiteri, M. Grattarola, H.-J. Butt, and P. Skládal, "Micromechanical cantilever-based biosensors," *Sensors and Actuators B: Chemical*, vol. 79, no. 2–3, pp. 115–126, Oct 2001.

[173] C. A. J. Putman, B. G. D. Grooth, N. F. V. Hulst, and J. Greve, "A detailed analysis of the optical beam deflection technique for use in atomic force microscopy," *J. Appl. Phys.*, vol. 72, no. 1, pp. 6–12, Jul 1992.

[174] T. Thundat, R. J. Warmack, G. Y. Chen, and D. P. Allison, "Thermal and ambient-induced deflections of scanning force microscope cantilevers," *Appl. Phys. Lett.*, vol. 64, p. 2894, March 1994.

[175] D. Ramos, J. Mertens, M. Calleja, and J. Tamayo, "Study of the origin of bending induced by bimetallic effect on microcantilever," *J. Sensors*, vol. 7, no. 9, pp. 1757–1765, September 2007.

[176] D. Rugar, H. J. Mamin, and P. Guethner, "Improved fiber-optic interferometer for atomic force microscopy," *Appl. Phys. Lett.*, vol. 55, no. 25, pp. 2588 – 2590, Dec 1989.

[177] B. Ovryn and J. H. Andrews, "Measurement of changes in optical path length and reflectivity with phase-shifting laser feedback interferometry," *App. Opt.*, vol. 38, no. 10, pp. 1959–1967, April 1999.

[178] N. A. Burnham, X. Chen, C. S. Hodges, G. A. Matei, E. J. Thoreson, C. J. Roberts, M. C. Davies, and S. J. B. Tendler, "Comparison of calibration methods for atomic-force microscopy cantilevers," *Nanotechnology*, vol. 14, no. 1, pp. 1–6, 2003.

[179] C. P. Green, H. Lioe, J. P. Cleveland, R. Proksch, P. Mulvaney, and J. E. Sader, "Normal and torsional spring constants of atomic force microscope cantilevers," *Rev. Sci. Instrum.*, vol. 75, no. 6, pp. 1988–1996, 2004.

[180] J. E. Sader, J. W. M. Chon, and P. Mulvaney, "Calibration of rectangular atomic force microscope cantilevers," *Rev. Sci. Instrum.*, vol. 70, no. 10, pp. 3967–3969, 1999.

[181] Purdue Education, visited: February 4th, 2018 15:17 GMT +1. [Online]. Available: https://www.purdue.edu/discoverypark/prism/assets/pdfs/Posters%202009/Quality-Factor-for-Cantilever-Beams.pdf

[182] A. Jha, F. J. Azcona, and S. Royo, "Frequency modulated optical feedback interferometry for nanometric scale vibrometry," *IEEE Photon. Technol. Lett.*, vol. 28, no. 11, pp. 1217–1219, June 2016.

[183] J. Sader, "Atomic force microscopy (calibration method of sader)," May 2015, http://www.ampc.ms.unimelb.edu.au/afm/calibration.html#normal.

[184] F. J. Azcona, R. Atashkhooei, S. Royo, and J. Mendez-Astudillo, "A nanometric displacement measurement system using differential optical feedback interferometry," *IEEE Photon. Technol. Lett.*, vol. 25, no. 21, pp. 2074–2077, Nov 2013.

[185] R. Kliese, T. Taimre, A. A. A. Bakar, Y. L. Lim, K. Bertling, M. Nikolić, J. Perchoux, T. Bosch, and A. D. Rakić, "Solving self-mixing equations for arbitrary feedback levels: a concise algorithm," *App. Opt.*, vol. 53, no. 17, pp. 3723–3736, Jun 2014.

[186] B. V. Derjaguin, V. M. Muller, and Y. P. Toporov, "Effect of contact deformations on the adhesion of particles," *J. Colloid Interface Sci.*, vol. 53, no. 2, pp. 314–326, Nov 1975.

[187] A. Jha, "Continuos wave frequency modulated optical feedback (cwfm-of):theory and applications," Ph.D. dissertation, Universitat Politècnica de Catalunya, Nov 2016.

[188] J. Abadie, E. Piat, S. Oster, and M. Boukallel, "Modeling and experimentation of a passive low frequency nanoforce sensor based on diamagnetic levitation," *Sens. Act. A. Phys.*, vol. 173, no. 1, pp. 227–237, Jan 2012.